Systèmes optiques interférentiels et incertitudes

Olivier Vasseur

UNIVERSITÉ PARIS SUD | FACULTÉ DES SCIENCES D'ORSAY

Habilitation à diriger des recherches

Discipline : Physique

Présentée par

Olivier VASSEUR

Systèmes optiques interférentiels et incertitudes

Rapporteurs :

Xu LIU	Université de Zhejiang
Jean-Louis MEYZONNETTE	Institut d'Optique
Jean-Claude SIMON	ENSSAT

Soutenue le 7 septembre 2012 à l'Université Paris-Sud devant le jury composé de :

François FLORY	Ecole Centrale Marseille
Yves JAOUËN	Télécom ParisTech
Jean-Louis MEYZONNETTE	Institut d'Optique
Pascal PERNOT	Université Paris-Sud
Michelle SERGENT	Université d'Aix-Marseille
Jean-Claude SIMON	ENSSAT

ONERA
THE FRENCH AEROSPACE LAB

Remerciements

Je tiens tout d'abord à remercier Xu Liu, Jean-Louis Meyzonnette et Jean-Claude Simon pour m'avoir fait l'honneur d'être rapporteur de ce travail de synthèse de mes activités de recherche rédigé pour l'obtention de l'habilitation à diriger des recherches.

J'adresse mes remerciements à Michelle Sergent, François Flory, Yves Jaouën, Jean-Louis Meyzonnette, Pascal Pernot et Jean-Claude Simon pour avoir accepté de faire partie de mon jury.

Cette synthèse de mes activités de recherche est en partie le fruit de tentatives de mêler des méthodologies ou savoirs de domaines différents, tentatives qui constituent une mise en pratique de contre-règles selon Paul Feyerabend. Je remercie donc d'autant plus chaleureusement mes rapporteurs et membres du jury de s'être attelés avec enthousiasme à la lourde tâche de juger un travail mêlant différentes méthodologies de plusieurs domaines scientifiques.

Je tiens à remercier tous ceux qui m'ont encouragé à entreprendre ce travail : mon épouse France, Michel Cathelinaud, Pierre Bourdon, Véronique Jolivet, Dominique Grenier, Anne Durécu, Agnès Dolfi-Bouteyre, Abou Ndiaye, Solange Barrachina, Jacques Blanc-Talon, Xavier Briottet, Xianghua Zhang et André Mysyrowicz.

Je remercie Franck Lefèvre, directeur du Département d'Optique Théorique et Appliquée pour son soutien dans cette démarche.

Je ne saurais oublier d'adresser mes remerciements à Georges Rasigni qui dès 1995 me conseillait fortement de rédiger mon HDR et à Anne Sauvageot qui renouvelait ce conseil dès la soutenance de ma thèse de Sociologie en 2003. Aussi, j'exprime ma reconnaissance à Georges Rasigni et Charles Vassallo pour leur soutien dans mes premiers travaux de recherche menés en freelance après ma thèse de Physique.

Ce travail est le fruit d'activités de recherche menées à l'Onera avec mes collègues laseristes : Guillaume Canat, Laurent Lombard, Didier Goular, Didier Fleury, Matthieu Valla, Christophe Planchat et Xavier Orlik de l'Onera mais aussi Reinhard Ebert, Bernd Eberle, Helge Bürsing et Georges Boudebs. D'importants acquis ont été obtenus grâce aux doctorants que j'ai encadrés : Jean-Michel Ponzo, Baya Bennaï, Magali Durand et Adrian Azarian. Dans le domaine des couches minces, les fructueuses discussions lors de congrès avec Angus Macleod qui fut rapporteur de ma thèse de Physique, Xu Liu, Michel Cathelinaud, François Flory et Claude Amra ont également contribué à ma réflexion. Dans le domaine des mathématiques appliquées, mes travaux ou discussions scientifiques avec Gérard Bakouche, Laurent Mugnier, Sandrine Fauqueux, Patricia Klotz, Fabrice Poirion, François-Henri Leroy, Manuel Samuelidès, Roger Phan-Tan-Luu, Magalie Claeys-Bruno, Bernard Corre, Jessica Franco, Roland Rabeau, Fabrice Gaudier, Régis Lebrun, Luc Pronzato, Jean-Pierre Gauchi, Jean-Marc Martinez ont été également riche d'enseignements. Les discussions avec les membres du comité de pilotage du Réseau Optique et Photonique et ceux du Réseau Mesures, Modèles et Incertitudes du CNRS furent également enrichissantes. Je leur adresse à tous mes remerciements.

J'adresse également mes remerciements à tous mes collègues de recherche qui ont été associées plus ou moins directement à ce travail, en particulier Béatrice Augère, Claudine Besson, Yves-Michel Frederic, Marie-Thérèse Velluet, Catherine Jolly, Valérie Delrue, Evelyne Valet, Thierry Gaudo et Chantal Appriou.

SOMMAIRE

Avant propos

La première période de mes activités de recherche s'est inscrite dans les domaines de la microélectronique et de l'optique. En effet, l'objectif de mes travaux consistait à améliorer le processus de gravure des composants microélectroniques au moyen de la mise en place d'une détection de fin de gravure performante par l'identification de raies d'émission pertinentes du plasma lorsque la zone gravée ne représentait qu'une très faible surface du wafer. Ces travaux se caractérisaient principalement par l'étude de plasmas d'émission de mélanges gazeux comportant des produits de réactions chimiques non connues dans des conditions de pressions non standards. Ces travaux ont abouti à la définition et à la réalisation d'un filtre multidiélectrique bi-bande double onde, ce qui a constitué une première mondiale.

La seconde période de mes activités de recherche m'a permis de travailler simultanément dans le domaine des couches minces et de l'optique guidée. J'ai effectué une thèse de physique qui a consisté à définir et réaliser les traitements optiques multicouches antireflets pour diodes laser monomodes afin d'obtenir des amplificateurs à onde progressive[1] au profit du CNET Lannion. Ces travaux constituait un double défi : réaliser des antireflets dont les performances n'avaient jamais été atteintes d'une part et déposer les différentes couches sur des substrats non homogènes du fait de la structure guidante de la diode d'autre part, en tenant compte des contraintes technologiques de réalisation d'un empilement de couches minces[2]. La connaissance des techniques de fabrication et des incertitudes résiduelles associées m'a permis de

[1] Onde amplifiée en un seul passage.

[2] Notamment les incertitudes sur les valeurs d'indices des matériaux en couche mince et sur les épaisseurs des couches minces.

concevoir les premiers filtres multicouches performants et robustes aux incertitudes de fabrication.

La troisième phase de mes activités de recherche s'est inscrite dans le domaine dans le domaine de la simulation technico-opérationnelle de systèmes. Mes travaux ont porté sur l'exploration de codes de calculs ayant un grand nombre de paramètres d'entrée, la propagation des incertitudes dans ces codes et la cohérence entre les différents modèles physiques et systèmes pris en compte dans une simulation.

La quatrième phase de mes activités de recherche portant sur l'étude de l'image dans la technoscience s'est déroulée sur une période de cinq ans dans le cadre d'une thèse de sociologie, en parallèle de mes activités professionnelles qui consistaient principalement à orienter des activités de recherche dans le domaine de l'optronique. L'objectif de ce travail a été d'étudier l'usage et l'influence de l'image dans le monde technoscientifique, principalement dans les domaines de la recherche appliquée, de la modélisation et de la simulation.

La dernière phase de mes activités de recherche se déroule à l'Onera au sein du Département d’Optique Théorique et Appliquée. Mes travaux portent principalement sur les systèmes laser utilisant sur la combinaison cohérente de sources laser fibrées, les applications des sources laser femtoseconde, l’analyse de sensibilité, l’exploration d’espaces de paramètres de grande dimension, les métamodèles et la qualification des plans d’expériences. Plusieurs résultats acquis sur ces thèmes ont constitué des premières mondiales. Enfin, mes activités, qui mettent en synergie l'ensemble des acquis des travaux de recherche antérieurs, ont ouvert de nouveaux axes de recherche sur la caractérisation du phénomène de speckle généré lors de l’interaction faisceau laser/cible ou lors de la propagation en atmosphère turbulente, et plus généralement sur la caractérisation de la variabilité spatiale de phénomènes stochastiques dans le domaine optique.

L'ensemble de ces activités de recherche me conduit à élaborer ce travail de synthèse sur les systèmes optiques interférentiels et leur sensibilité aux incertitudes.

Savoir qu'on sait quand on sait, et savoir qu'on ne sait pas quand on ne sait pas, c'est là, la vraie connaissance.

Confucius, *Entretiens*.

I. Introduction

Les interférences lumineuses sont le résultat de l'interaction de deux ou plusieurs ondes lumineuses cohérentes qui, par l'addition de leurs amplitudes, produit un éclairement global différent de la somme incohérente des éclairements des ondes individuelles. Ces interférences lumineuses permettent une observation commode de très petites variations de distances au moyen de mesures différentielles qui donnent un écart de phase par rapport à une référence : déplacement par rapport à une origine ou déformation par rapport à une surface de référence par exemple. L'apparition des lasers, du fait de leur extrême cohérence, a rendu commune l'observation d'interférences et a contribué en particulier à l'usage des interférences lumineuses comme moyen de contrôle industriel par le développement des techniques d'interférométrie de speckle [1], [2]. En effet, le speckle se manifeste dès que la surface rugueuse d'un objet diffusant est éclairée par un laser en générant un système d'interférences complexe dans l'espace du fait de la superposition cohérente des ondes lumineuses provenant des divers éléments éclairés de la surface rugueuse.

Les développements technologiques permettent aujourd'hui l'élaboration de systèmes optiques interférentiels composés d'un grand nombre de composants. Ainsi, des formules de filtres diélectriques multicouches comportant plusieurs dizaines ou centaines de couches minces ont été proposées [3]. La combinaison cohérente de plusieurs dizaines à plusieurs centaines de sources laser fibrées fait également l'objet

de nombreux travaux de recherche [4], **[5]**[3]. De même, d'autres systèmes comme les réseaux diffractifs bi et tridimensionnels composés d'un grand nombre d'ouvertures peuvent être étudiés [6].

L'évaluation de la robustesse de tels systèmes interférentiels aux incertitudes de fabrication constitue un enjeu important mais d'autant plus difficile que le nombre de paramètres décrivant le système est grand. En effet, il est alors nécessaire de quantifier l'influence des incertitudes de chacun des paramètres caractéristiques du système interférentiel considéré ainsi que les synergies critiques entre certains paramètres sur les performances souhaitées du système. Cette évaluation est réalisée par des expérimentations numériques avec les codes de calcul modélisant ces systèmes. L'analyse de sensibilité globale, qui étudie comment la variabilité des paramètres d'entrée d'un modèle se répercute sur celle de la sortie, permet d'identifier les facteurs caractéristiques les plus influents et ceux qui interagissent entre eux [7]. Cette analyse détermine la part de variance de la variable de sortie due à chaque paramètre d'entrée ou ensemble de paramètres d'entrée. Toutefois, le nombre élevé de paramètres considéré (plusieurs dizaines à plusieurs centaines) exige de disposer d'outils statistiques d'exploration d'espaces mathématiques de grandes dimensions efficaces d'une part et des outils aptes à identifier des interactions entre des paramètres, les systèmes interférentiels étant par construction le fruit de telles interactions d'autre part. En définitive, l'évaluation de la robustesse de systèmes interférentiels décrits par un grand nombre de paramètres aux incertitudes liées à leur réalisation constitue un enjeu majeur pour identifier les caractéristiques critiques d'un système et pour choisir, parmi les solutions de systèmes envisageables, celui qui offre le meilleur potentiel de réalisation et de performances.

Dans ce document de synthèse, sont rappelés, dans un premier temps, les méthodologies liés aux plans d'expériences numériques et les résultats concernant leur qualité d'exploration des espaces de grandes dimensions au moyen de la méthode développée lors de mes travaux de recherche qui est basée sur la construction d'un

[3] Une référence en gras signifie que cette référence est le fruit de travaux que j'ai initiés, dirigés et auxquels j'ai contribué.

graphe : l'arbre de longueur minimale. Dans une seconde partie, l'analyse de l'influence des incertitudes des paramètres d'entrée de systèmes interférentiels sur leurs performances est illustrée au moyen de deux applications : les filtres interférentiels multidiélectriques et la combinaison cohérente de sources laser fibrées. La méthodologie mise en oeuvre permet notamment d'identifier les incertitudes et les synergies les plus critiques au sein du système tout en construisant des métamodèles représentatifs. A partir de ces acquis, la caractérisation spatiale du speckle de surfaces rugueuses et plus généralement la caractérisation de la variabilité spatiale de phénomènes optiques sont explicitées dans la partie IV. Enfin, les perspectives scientifiques issues de l'ensemble de ces acquis et de mes travaux de recherche depuis ma thèse de physique sont mises en exergue dans la dernière partie.

II. Les plans d'expériences numériques.

Les codes de calcul qui modélisent ou simulent des phénomènes complexes sont de plus en plus réalistes et même si la puissance des ordinateurs augmente sans cesse, les temps de calcul demeurent importants et peuvent limiter l'utilisation des techniques de Monte-Carlo. Ces dernières exigent en effet un nombre important d'évaluation du code de calcul pour obtenir une bonne précision. Pour cette raison, ont été développées des méthodes alternatives qui visent à organiser, de manière plus efficace à l'aide de plans d'expériences, les évaluations du code de calcul afin de converger plus rapidement vers la solution [8], [9]. Ainsi, lorsque les relations entre les sorties et les entrées du code de calcul sont complexes, les plans d'expériences numériques sont utilisés pour explorer l'espace des variables d'entrée[4] de manière efficace afin de répondre à des objectifs variés : criblage, analyse de sensibilité, construction de métamodèles… Le développement de métamodèles permet alors de remplacer le simulateur par un outil plus "simple" construit à partir du simulateur complexe [10]. Ces métamodèles ou surfaces de réponse sont en général des fonctions obtenues à l'aide de méthodes d'interpolation ou d'approximation à partir d'un nombre limité d'exécutions du simulateur sur des jeux de paramètres constituant le plan d'expériences numériques. Du fait des caractéristiques non linéaires et/ou non paramétriques des codes de modélisation ou simulation, il est nécessaire de répartir les points dans l'espace le plus uniformément possible de façon à capter au mieux le comportement du simulateur. Ainsi, l'exploration du code gagne en efficacité et les

[4] Compte tenu de la diversité des termes employés dans le domaine de la physique et de la statistique, les termes variables d'entrée, paramètres d'entrée et facteurs ont un sens équivalent. De même, pour la variable de sortie d'un modèle, le terme réponse pourra être employé avec un sens identique.

métamodèles construits seront plus robustes. C'est ce mode de répartition uniforme des points que cherchent à proposer les plans d'expériences Space Filling Designs (SFD).

L'étude des plans d'expériences numériques SFD pour identifier les plus performants a pour objectif de fournir des plans permettant d'explorer efficacement des espaces dont le nombre de variables d'entrée est supérieur à quelques dizaines dans un premier temps mais peut atteindre plusieurs centaines ultérieurement. Ces plans sont alors utilisés pour étudier des systèmes optiques interférentiels c'est-à-dire des systèmes présentant des interactions fortes entre les variables d'entrée.

1) Les plans d'expériences numériques

Les plans d'expériences numériques sont basés sur la démarche des plans d'expériences utilisés dans le domaine de l'expérimentation pour organiser au mieux un nombre minimal d'essais tout en obtenant des résultats fiables avec une bonne précision [11], [12].

1. Les plans classiques pour l'expérimentation

Dans le domaine de l'expérimentation, l'utilisation des plans d'expériences répond à des objectifs variés tels que :

- l'identification des régions d'intérêt dans une étape de recherche exploratoire,

- l'identification des facteurs les plus influents,

- la quantification des effets produits par les différents facteurs et leurs interactions sur la réponse du système ou processus étudié,

- la construction de métamodèles ou surfaces de réponse,

- l'optimisation du système ou processus étudié.

Une grande variété de plans a été proposée pour répondre à ces objectifs tout en tenant compte des spécificités du phénomène étudié : plans factoriels, plans factoriels fractionnaires, matrice d'Hadamard, plans de Doehlert... De même, différents critères ont été introduits pour qualifier l'optimalité des plans d'expériences [12]-[14]. Il est à

noter que ces plans sont limités à l'exploration d'un nombre de facteurs limités donc à l'exploration d'espaces de faibles dimensions.

Dans la pratique expérimentale, les essais définis par le plan d'expériences choisi peuvent être réalisés dans un ordre aléatoire pour limiter l'influence de biais expérimentaux ou être répliqués pour déterminer la variance de la réponse pour un même choix de valeurs des paramètres d'entrée. Dans le domaine de l'expérimentation numérique ces pratiques s'avèrent inutiles, chacune des expériences numériques étant déterministe.

2. Les plans de type "Space Filling Design"

Dans le domaine de l'expérimentation numérique, il est nécessaire d'utiliser des plans permettant de remplir au mieux l'espace exploré pour détecter des non-linéarités et d'étudier un grand nombre de paramètres d'entrée. Les caractéristiques exigées des plans SFD sont une répartition uniforme des points dans l'espace étudié et une répartition uniforme des projections des points dans les sous-espaces. Ainsi, les plans de type carré latin LHD[5] pour l'étude de *p* facteurs avec *n* expériences répondent à cette exigence et autorisent l'exploration d'espaces de grandes dimensions. Ils sont construits de la manière suivante :

- division des plages de variation de chacun des *p* facteurs en *n* intervalles,

- tirage aléatoire d'un point dans chaque strate.

Il résulte de ce procédé que chacun des niveaux est pris une fois et une seule par chaque facteur.

Comme dans le cas de l'expérimentation, différents critères sont utilisés pour apprécier la qualité de ces plans.

[5] LHD : Latin Hypercube Design

a) Les critères classiques d'appréciation de la qualité d'un plan.

Les principaux critères d'appréciation de la répartition des points dans l'espace reposent sur l'évaluation des distances entre deux points de l'espace pour déterminer les distances minimale et maximale d'un point à son plus proche voisin d'une part et l'évaluation de la discrépance qui est la différence entre le nombre de points d'une suite x(n) = {x1,.. , xn} contenus dans les pavés P d'un espace X = $[0, 1]^d$ et les volumes de ces pavés[6] d'autre part [15]. Ainsi, le souhait de répartir au mieux un ensemble limité de points dans l'hypercube unité se traduit, par exemple, par la recherche de la distance maximale entre un point donné et son plus proche voisin lors de l'utilisation d'un critère distance. Une répartition uniforme se traduit dans le cas de l'utilisation de la discrépance par la recherche du plus faible écart entre la proportion de points contenus dans un pavé donné et son volume relativement à l'espace total, c'est-à-dire en définitive que la densité de points dans un pavé donné doit être la plus proche possible de la densité de points dans l'espace total. Les caractéristiques de la distribution des points dans l'espace définissent la qualité intrinsèque du plan numérique.

[6] Les pavés considérés pouvant être construits de différentes manières, il existe donc plusieurs discrépances. Par exemple, les centres des pavés peuvent correspondre au centre du domaine exploré ou, au contraire, contenir systématiquement le point origine.

b) Les principaux plans SFD

Les plans d'expériences SFD les plus connus sont les carrés latins, les carrés latins optimisés, les plans minimax, les plans maximin et les plans construits sur des suites à faible discrépance [16]. D'autres plans ou des améliorations de plans existants sont régulièrement proposés et étudiés. Ainsi, dans le cadre du consortium DICE (Deep Inside Computer Experiments)[7], les plans WSP[8] [17] et les plans de Strauss[9] [16] ont été caractérisés.

A titre d'illustration, la Figure 1 présente quelques plans classiques en dimension 2 et permet notamment d'observer que la répartition des points issus d'une loi de densité uniforme génère une répartition composée de points très proches et de larges zones vides (cf. Plan aléatoire). Le plan factoriel à 6 niveaux s'avère trop régulier et ne fournit pas une répartition uniforme des points projetés sur les deux axes. Toutefois, un léger déplacement des points du plan factoriel permet d'améliorer considérablement le plan comme l'illustre la répartition "Grille". Mais cette démarche basée sur l'utilisation de plans factoriels multiniveaux est vouée à l'échec en grande dimension du fait du très grand nombre de calculs qu'impose l'utilisation d'une grille.

[7] Ce consortium a réunit des différents partenaires universitaires, industriels ou institutions publiques pour avancer sur les thèmes de l'exploration et de l'optimisation des grands codes de calcul (2006-2009). Les organismes représentés étaient : École des Mines de Saint-Etienne, EDF, IRSN, Onera, Renault, Total, Université Joseph Fourier, Université d'Orsay et Université Paul Cézanne.

[8] Le but de l'algorithme WSP est d'extraire, dans un ensemble de points candidats, un sous-ensemble de points répartis uniformément. Les points de l'espace sont choisis de telle façon qu'ils sont à la fois au moins à une distance minimale (Dmin) de chaque point déjà inclus dans le plan et également, aussi près que possible du centre de l'hypercube unité.

[9] Ce plan SFD est défini à l'aide d'un processus de Strauss. Les n expériences sont vues comme la photographie à un instant donné de n particules de même charge électrique en mouvement dans une boîte d-dimensionnelle (hors gravité).

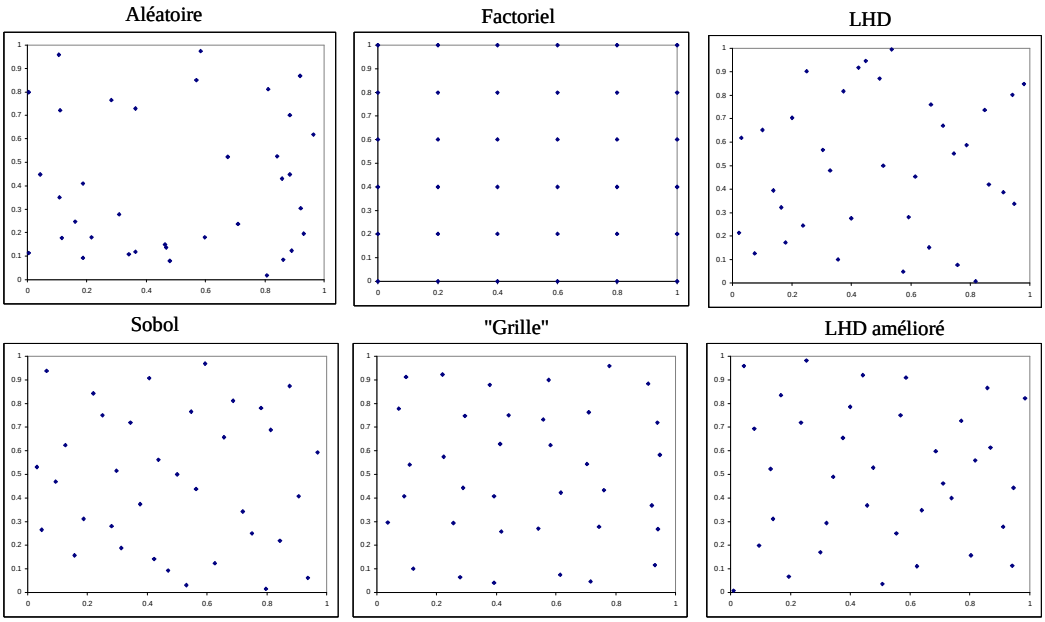

Figure 1 : Exemples de plans de 36 points en dimension 2.

Le Tableau 1 fournit une comparaison quantitative de ces plans confirmant les impressions visuelles d'une part mais également la difficile qualification des plans d'autre part. En effet, le critère *MinDist* qui exprime l'écartement minimal entre deux points voisins souligne la supériorité du plan factoriel et du plan "Grille". Le plan aléatoire qui a des points beaucoup trop proches et de larges zones vides a la valeur *MinDist* la plus faible. En ce qui concerne les valeurs des discrépances C^2 et L^2 [15], [18], qui doivent être les plus faibles possibles, les plans factoriel et aléatoire montrent une piètre qualité.

	MinDist	Discrépance C2	Discrépance L2
Factoriel	0.2000	0.1113	0.0338
Aléatoire	0.0143	0.1296	0.0322
"Grille"	0.1013	0.0439	0.0147
LHD	0.0358	0.0280	0.0128
LHD amélioré	0.0690	0.0247	0.0115
Sobol	0.0663	0.0370	0.0119

Tableau 1 : Valeurs de la distance minimale entre deux points (MinDist) et de discrépances pour les plans présentés en Figure 1.

Compte tenu de l'ensemble des critères présentés, les carrés latins (LHD et LHD amélioré) et le plan basé sur une suite à faible discrépance (Sobol) réalisent un bon

compromis entre les critères. On remarquera d'ailleurs sur cet exemple que le LHD amélioré présente le meilleur compromis : les plus faibles discrépances et une valeur MinDist élevée. Il est à noter également que la hiérarchie des plans LHD et Sobol est modifiée selon la discrépance choisie. Ainsi la multiplication des critères basés sur la discrépance peut rendre difficile la qualification et la hiérarchisation des plans SFD.

2) L'arbre de longueur minimale et la qualification des plans d'expériences numériques

La caractérisation de l'uniformité d'une distribution de points utilisant des critères de discrépance ou de calculs de distances entre les points s'avère insuffisante. Comme illustré précédemment en dimension 2 (Figure 1et Tableau 1), le choix de la discrépance peut conduire à des résultats très variables et difficilement interprétables en grande dimension et l'évaluation de la distance minimale d'un point à son plus proche voisin ne fournit qu'une information locale. Dussert et al. [19] ont montré que la construction d'un arbre de longueur minimale (ALM) sur un ensemble de points en dimension 2 permettait de qualifier la répartition des points à partir de la longueur moyenne m des branche de l'arbre et de l'écart-type σ des longueurs de branche : la répartition de points peut alors être aléatoire, régulière, quasi-régulière, en amas ou en gradient. Un exemple de construction d'un arbre de longueur minimale sur des amas de points dans le plan est présenté sur la Figure 2 et les différentes zones délimitant les typologies de répartition des points dans le plan (m,σ) sont présentées sur la Figure 3.

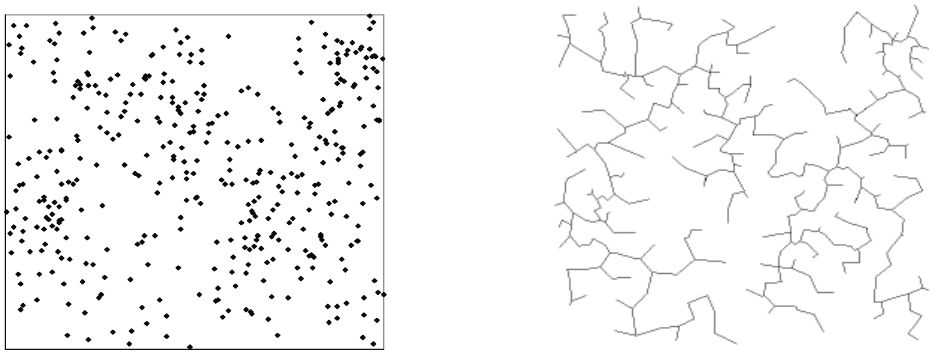

Figure 2 : Construction d'un ALM sur un ensemble de 400 points en dimension 2.

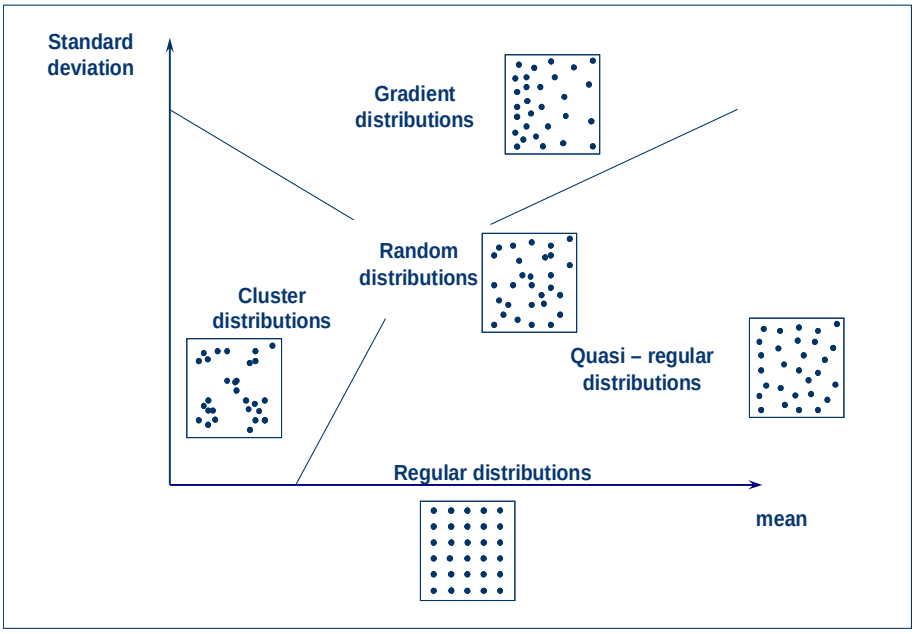

Figure 3 : Représentation de la répartition des distributions dans le plan (m, σ)

J'ai proposé d'utiliser cette démarche, qui s'est avérée la plus performante pour qualifier des répartitions de points en dimension 2 [20], [21], pour évaluer la qualité de répartition des points d'un plan d'expériences dans un espace multidimensionnel i.e. de classer ces plans selon leur structure, ce que ne permettent pas les autres critères couramment utilisés **[22]**, **[23]**.

Tous les plans d'expériences évoqués dans la partie précédente permettent d'obtenir de très bonnes répartitions dans le cas d'espaces de faibles dimensions. Ainsi, sur la Figure 4, on peut constater que tous les plans se situent dans la zone des plans quasi-périodiques en dimension 2. On peut également remarquer, qu'en ce qui concerne les exemples de plans de 36 points en dimension 2, les meilleurs plans pour le critère ALM sont les plans LHD amélioré et "Grille".

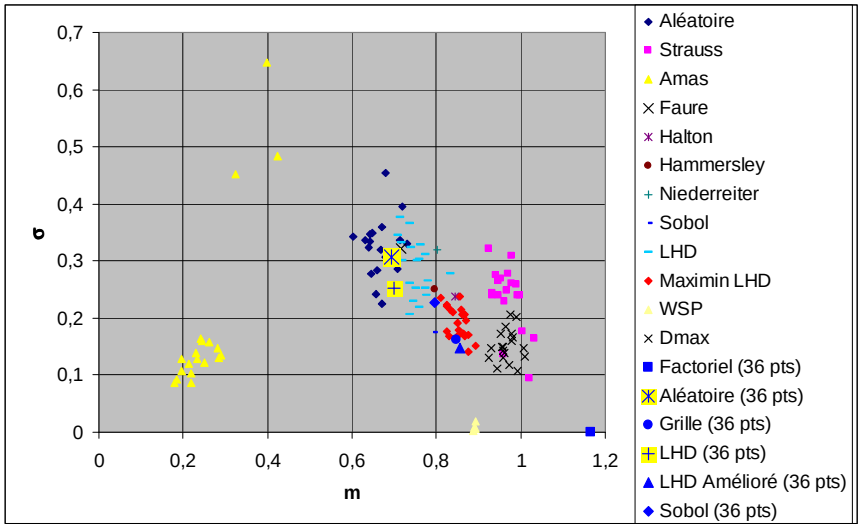

Figure 4 : Représentation de la longueur moyenne et de l'écart-type des longueurs de branches de l'ALM pour différents plans SFD de 20 points et 36 points en dimension 2.

En dimension 5, les plans classiques se situent encore dans la zone quasi-périodique du plan (m, σ) même si plusieurs types de plans sont désormais plus proches de la zone des plans aléatoires (Figure 5).

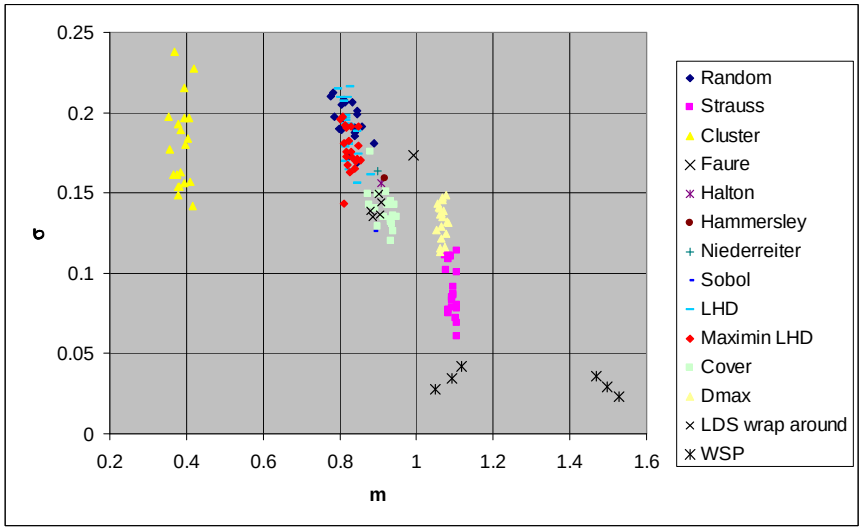

Figure 5 : Représentation de la longueur moyenne et de l'écart-type des longueurs de branches de l'ALM pour différents plans SFD de 100 points en dimension 5.

Si les performances des plans SFD classiques permettent d'obtenir des répartitions satisfaisantes en faibles dimensions, cela n'est plus le cas en grandes dimensions. Il est important de retenir que la structure quasi-périodique est nécessaire pour ne pas avantager certaines dimensions dès lors qu'on réalise une démarche exploratoire pour déterminer un zone d'intérêt avec peu de connaissances a priori, ce

qui est généralement le cas lorsqu'on désire construire un métamodèle sur un code complexe ou réaliser une analyse de sensibilité. Ainsi, les plans quasi-périodiques seront qualifiés comme des plans disposant d'une bonne qualité intrinsèque.

3) L'exploration d'espaces de grandes dimensions

L'exploration des espaces de grande dimension soulève des difficultés importantes. En effet, l'usage de plans de type Factoriel ou "Grille"[10] est absolument exclu compte tenu du nombre d'expériences numériques n à réaliser : $n = k^p$ avec k le nombre de niveaux par paramètres et p le nombre de paramètres. Lors de l'utilisation de plans SFD pour l'exploration d'espaces de grandes dimensions, l'efficacité d'exploration est d'autant plus cruciale que la dimension est grande, le nombre d'expériences numériques nécessaires étant plus importants. Ainsi Loepky [24] a proposé de manière empirique la relation $n = 10*p$ mais cette règle semble être pertinente uniquement pour le cas des dimensions inférieures à 20 comme l'ont montré nos résultats d'analyse de sensibilité avec 27 ou 29 facteurs dans le cas de filtres multidiélectriques[11]. L'utilisation de plans SFD s'accompagne d'une exigence implicite d'une qualité d'exploration meilleure que celle obtenue par des plans aléatoires. Dans ce cadre, l'utilisation du point au centre du domaine d'étude que proposent certains plans SFD peut présenter un intérêt. En définitive, la qualité de répartition des points dans l'espace (remplissage et quasi-régularité) est cruciale. L'arbre de longueur minimale permet d'apprécier ces deux caractéristiques. En effet, un écart-type des longueurs de branche suffisamment faible permet d'assurer la régularité de la distance entre les points et une valeur de longueur moyenne des branches élevée permet une exploration de l'espace efficace. L'analyse des propriétés de différents plans SFD permet de mettre en évidence que les plans bâtis sur des suites à discrépance faible, hormis le plan Sobol, s'avèrent peu appropriés au-delà de la dimension 20 (Figure 6 et Figure 7). Ces résultats peuvent s'inscrire dans les efforts de

[10] Ces plans correspondent dans un premier temps à des plans factoriels multiniveaux.

[11] Travaux effectués dans le cadre du consortium DICE et résultats confirmés dans le cas de la combinaison cohérente de sources laser fibrées **[30]**.

recherche concernant l'évaluation de la qualité des méthodes Quasi-Monte Carlo [25]-[27].

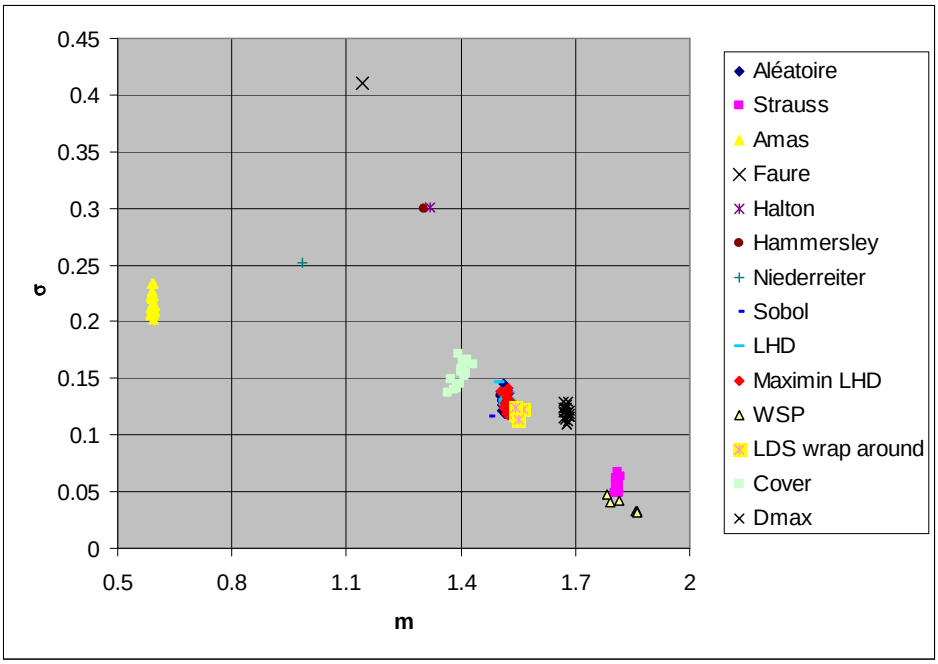

Figure 6 : Représentation de la longueur moyenne et de l'écart-type des longueurs de branches de l'ALM pour différents plans SFD de 400 points en dimension 20.

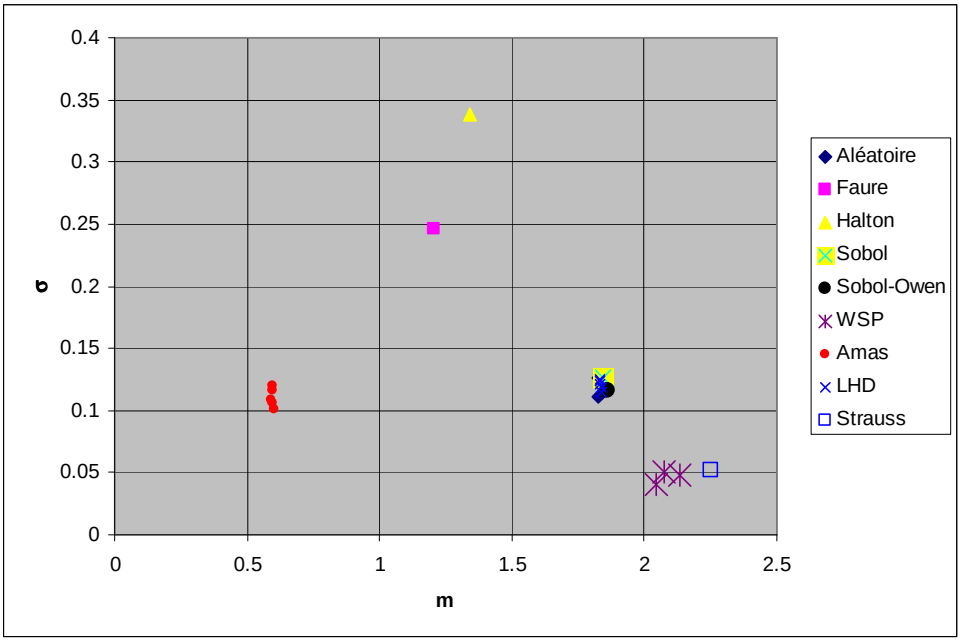

Figure 7 : Représentation de la longueur moyenne et de l'écart-type des longueurs de branches de l'ALM pour différents plans SFD de 614 points[12] en dimension 29.

[12] Deux plans WSP comportent 598 points.

Il est à noter que certains plans SFD (ex : Sobol, WSP) présentent une densité de points plus importantes au centre du domaine. Cette propriété, qui peut présenter un intérêt, est malheureusement perdue dès lors qu'un scrambling est effectué lors de la construction du plan, comme c'est le cas pour le plan Sobol-Owen.

4) De l'usage des projections dans des sous-espaces et de ses limites

L'exploration d'un grand nombre de variables d'entrée d'un code de calcul conduit à considérer des espaces de grandes dimensions. Souvent les propriétés des projections des points dans les sous-espaces de dimensions 1 ou 2 participent à l'évaluation de la qualité de ces plans. En effet, si l'une des variables n'a aucune influence, il est souhaitable que les expériences numériques soient le plus utiles possibles pour étudier les autres variables : il est donc nécessaire que les projections des points dans les sous-espaces satisfassent aux critères des plans SFD. Le fait qu'une variable n'ait aucune influence sur la sortie du code de calcul correspond à réduire la dimension du système étudié en ne retenant que les variables influentes et à considérer en définitive une dimension effective plus faible [28]. Cette exigence sur les projections conduit à exclure les plans très réguliers d'une part mais également à rechercher une répartition uniforme des points dans l'espace de projection d'autre part. Pour cette raison, le critère du "Radial Scanning Statistics" a été proposé [29] mais ce critère, tout en présentant des informations visuelles très utiles sur la plus mauvaise projection, fournit des informations quantitatives délicates à exploiter **[30]**. La qualification des plans par l'ALM peut être également réalisée dans tous les sous-espaces de l'espace original pour en déterminer les structures et compléter l'analyse de la qualité des plans SFD. Par exemple, les résultats obtenus dans les 406 sous-espaces de dimensions 2 des plans 29-D mettent en évidence une distribution aléatoire des points projetés pour les plans quasi-périodiques ou aléatoires (WSP, Aléatoire, LHD) mais de grande disparités de structure pour le plan Sobol et le plan Sobol-Owen (Figure 8) **[30]**. Ce comportement très particulier des plans basés sur les suites à faible discrépance de Sobol peut fournir des éléments pour comprendre la disparité observée des performances de ces suites sur des cas d'application très différents. Ainsi, les

résultats obtenus sur les systèmes interférentiels s'avèrent peu satisfaisants contrairement aux résultats obtenus à l'aide de fonctions mathématiques de test [27].

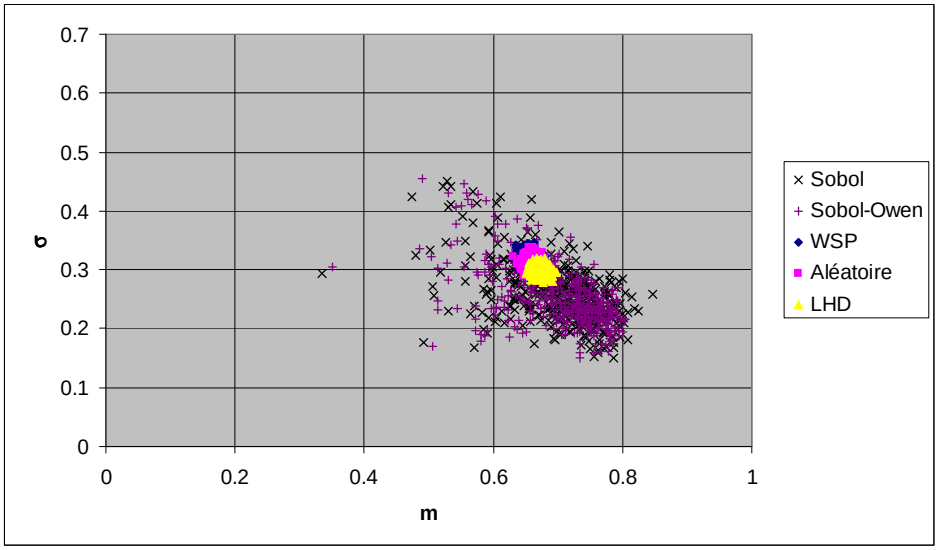

Figure 8 : Représentation dans le plan (m, σ) des plans SFD en dimension 29 dans les 406 sous-espaces de dimension 2 : mise en évidence de structures particulières pour les plans Sobol et Sobol-Owen et d'une distribution aléatoire pour les autres plans.

L'intérêt de l'utilisation des projections dans des sous-espaces de dimension 1 ou 2 est manifeste et l'appréciation d'un plan SFD par ses projections s'avère insuffisante pour déterminer sa qualité intrinsèque et l'évaluation globale du plan d'expériences dans l'espace d'origine est fondamentale. Il en résulte que l'ALM constitue un critère incontournable pour évaluer la qualité intrinsèque des plans d'expériences numériques.

5) Conclusion

A partir de cette analyse des propriétés des plans SFD pour l'exploration des espaces de grandes dimensions, l'ALM constitue un critère indispensable pour qualifier les plans d'expériences numériques. Diverses voies d'amélioration de ces plans sont actuellement étudiées afin de disposer de plans numériques de grande qualité intrinsèque et ainsi explorer de manière efficace des espaces de très grandes dimensions. La qualité intrinsèque des plans d'expériences numériques et la compréhension des spécificités de ces plans sont fondamentales pour explorer avec confiance des codes de calcul complexes comportant de nombreuses variables d'entrée dont certaines interagissent entre elles. La partie suivante présente une synthèse des

résultats obtenus avec ces plans pour l'étude de l'analyse de sensibilité globale de systèmes optiques interférentiels et complète l'analyse de la qualité des plans SFD.

III. L'analyse de sensibilité globale de systèmes optiques interférentiels.

Les plans d’expériences numériques présentés précédemment doivent constituer un outil efficace pour conduire des analyses de sensibilité des systèmes optiques interférentiels composés d'un grand nombre de variables d'entrée. Ainsi, les plans SFD de grande qualité intrinsèque doivent constituer un moyen d’identifier efficacement les variables d’entrée et leurs interactions critiques dans le cas de filtres interférentiels composés d’un grand nombre de couches minces en tenant compte des incertitudes ou des erreurs de fabrication. De même, l’analyse de sensibilité de la combinaison cohérente de fibres laser doit permettre de mettre en évidence les facteurs les plus critiques en fonction des bruits de phase résiduels, de la structure géométrique envisagée et des moyens de contrôle de la phase utilisés. Ces résultats d’analyse de sensibilité sont particulièrement utiles pour la conception robuste de tels systèmes optiques interférentiels.

De plus, la confrontation des résultats acquis avec des structures de filtres interférentiels bien connus permet d’établir un lien entre la qualité intrinsèque des plans SFD et leurs qualités extrinsèques sur des cas d’applications réels présentant de fortes interactions entre les variables d’entrée. Enfin, la détermination des variables les plus influentes constitue une première étape pour l'optimisation ultérieure des caractéristiques du système considéré ou encore l'élaboration de métamodèles représentatifs de la propagation des incertitudes dans le système.

1) Les filtres interférentiels multidiélectriques

La description des propriétés d’un filtre optique diélectrique monocouche dans le cas d’une onde plane arrivant sur une couche homogène et isotrope est réalisée au

moyen du formalisme matriciel tenant compte de la continuité des composantes tangentielles des champs électrique et magnétique à l'interface [31], [32]. Avec ce formalisme, il est alors possible de déterminer le profil spectral d'un empilement ou encore l'évolution du profil spectral lors de la fabrication du filtre comme le présente la Figure 9.

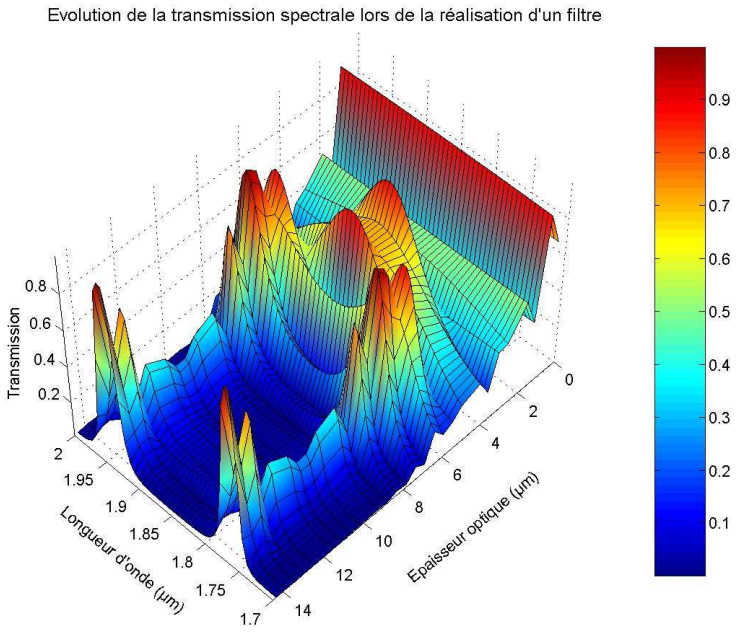

Figure 9 : Evolution de la transmission spectrale lors de la fabrication d'un filtre de 27 couches quart d'onde.

Le principe de la démarche est illustré au moyen des résultats obtenus avec quelques filtres dont les propriétés bien connues ont servi à évaluer la qualité des plans numériques SFD sur ces cas d'application présentant de fortes interactions. La cohérence des diverses analyses autorise alors l'exploration de configurations moins connues que nous évoquerons.

Si le criblage et l'analyse de sensibilité peuvent être conduits pour différentes sorties ou fonctions d'intérêt, l'analyse porte principalement sur l'évolution de la transmission d'un filtre sur un domaine spectral et sur la comparaison de deux méthodes de fabrication des filtres en fonction des incertitudes inhérentes à leur fabrication. L'écart de profil spectral entre le filtre théorique parfait et le filtre simulé en tenant compte des incertitudes est généralement évalué au moyen d'une fonction de mérite F du type :

$$F = \sqrt{\sum_i (T(\lambda_i) - T_p(\lambda_i))^2} \text{ ou } F = \sum_i (T(\lambda_i) - T_p(\lambda_i))^2 \text{ ou } F = \sum_i \left| T(\lambda_i) - T_p(\lambda_i) \right|$$

où $T(\lambda_i)$ est le facteur de transmission à la longueur d'onde λ_i dans l'expérimentation numérique (avec des incertitudes sur les valeurs des facteurs d'entrée : indice de réfraction et épaisseur de chacune des couches) et $T_p(\lambda_i)$ est le facteur de transmission du filtre parfait.

Ainsi, la fonction de mérite *F* évalue l'influence des valeurs des paramètres d'entrée sur le facteur de transmission dans un domaine spectral. L'influence de chacun des paramètres et de leurs interactions est évaluée au moyen d'une fonction polynomiale du second ordre :

$$f(X_1,...,X_n) = a_0 + \sum_{k=1}^{n} a_k . X_k + \sum_{k=1}^{n} b_k . X_k^2 + \sum_{0<i<j\leq n} c_{ij} . X_i . X_j \qquad (1)$$

où chaque X_i représente un paramètre caractéristique du système étudié (indice de réfraction *n* de la couche *i*, épaisseur *e* de la couche *i*, ou incertitude δ_i de l'indice de réfraction *n* et/ou de l'épaisseur *e* de la couche *i*). Les termes X_iX_j représentent les interactions du 1er ordre entre les paramètres considérés de la couche *i* et de la couche *j*. Pour les différents paramètres, les valeurs des variations considérées pour l'indice de réfraction et l'épaisseur d'une couche sont fournies par le plan d'expériences dont les valeurs δ appartiennent à l'intervalle $[-\Delta ; \Delta]$[13]. Ce type de polynôme est choisi du fait de la présence d'un minimum au centre du domaine étudié : lorsqu'il n'y a pas d'erreurs ou d'incertitudes sur la fabrication du filtre ($\delta = 0$), la valeur de la fonction de mérite *F* est nulle.

1. Les paramètres et interactions critiques de filtres passe bandes.

Le principe de la démarche a notamment été illustré par l'étude de l'influence des incertitudes des valeurs d'indice de réfraction de chaque couche sur le filtre 29-couches suivant **[33]** :

[13] Les incertitudes maximales considérées dans ces travaux sont souvent de l'ordre de 1% à 2,5% ce qui correspond à l'ordre de grandeur des incertitudes considérées pour évaluer un filtre dans le domaine des couches minces ou aux incertitude rencontrées lors de la fabrication de te filtres couches minces.

Substrat/HBHB4HBHBH B HBHB4HBHBH B HBHB4HBHBH/air

où H et B sont des couches quart d'onde à λ_0 = 1µm d'indice de réfraction haut (H; n=2,35) et bas (B; n=1,3) respectivement.

Cette approche peut correspondre à l'utilisation d'un contrôle par quartz piézoélectrique pour la fabrication des couches en considérant que l'épaisseur de chaque couche fabriquée correspond à celle déterminée pour le filtre parfait. La Figure 10 présente l'influence de variation des valeurs d'indice sur le profil spectral du facteur de transmission. On constate que les incertitudes sur les valeurs d'indices peuvent considérablement modifier le profil spectral du filtre initial souhaité.

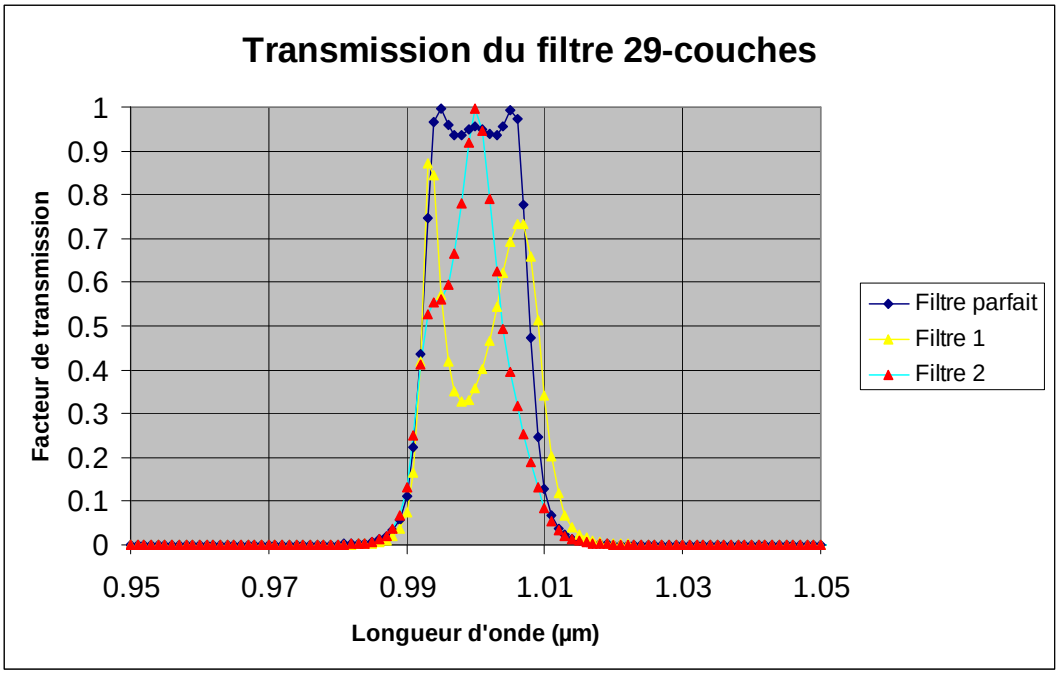

Figure 10 : Facteur de transmission spectral du filtre parfait et de deux filtres avec des incertitudes sur les valeurs d'indice (Filtre 1 et Filtre 2).

La qualité des résultats obtenus avec les différents plans est appréciée au moyen des critères suivants:

- Coefficient de détermination: R^2

- Identification des interactions les plus critiques c_{ij} d'un tel filtre (couches des blocs B4HB et entre les couches 4H de chacun des blocs) : $c_{5,15}$, $c_{15,25}$, $c_{5,25}$, $c_{4,5}$, $c_{5,6}$, $c_{14,15}$, $c_{15,16}$, $c_{24,25}$, $c_{25,26}$.

- Valeur du coefficient a_0 (métamodèle de type quadratique). Dans le cas d'absence de variation des valeurs d'indice, la valeur de la variable de sortie est nulle et par conséquent la valeur du coefficient constant a_0 devrait être 0.

A l'aide de ces critères, la qualité de l'identification des couches les plus influentes et la qualité du métamodèle construit sur l'échantillonnage du plan d'expériences peuvent être évaluées pour chacun des plans d'expériences utilisés. Les plans quasi-périodiques WSP fournissent d'excellents résultats dans ce cas d'application en 29-dimensions **[30]**. La même qualité d'analyse a été obtenue dans le cas de l'étude d'un filtre optique de 39 couches avec un plan WSP de 1485 points **[33]**.

La mise en oeuvre de notre démarche, qui s'attache simultanément à construire un métamodèle et à identifier et évaluer l'influence des paramètres les plus critiques fournit des résultats qui sont corroborés par l'approche classique de calcul des indices de Sobol en analyse de sensibilité. Ainsi, par exemple, le calcul des indices de Sobol totaux et du 1er ordre permet de mettre en évidence les paramètres les plus influents et ceux pour lesquels existent de fortes interactions (Figure 11 et Figure 12).

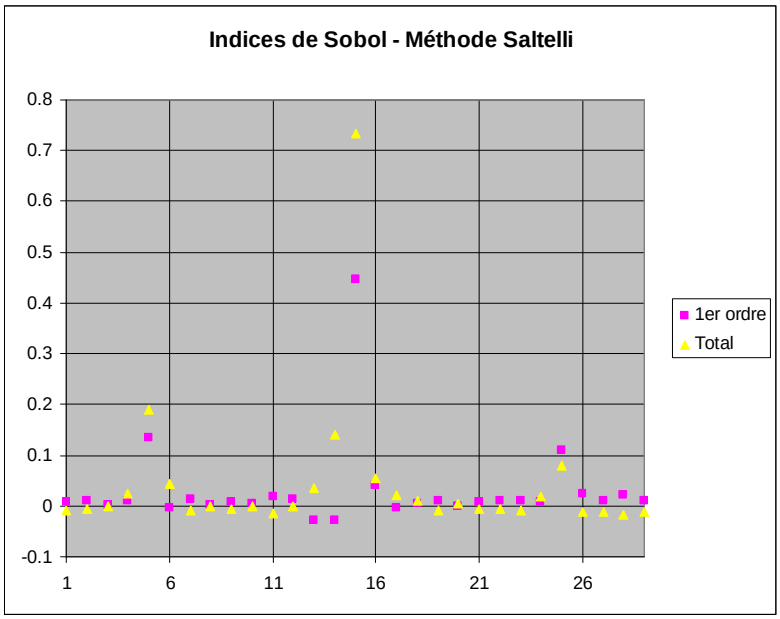

Figure 11 : Valeurs des indices de Sobol de chacune des 29 couches déterminées directement sur le modèle étudié par la méthode Saltelli implémentée dans le package R "Sensitivity"[34]. Valeurs des indices déterminées au moyen de 31000 évaluations du code de calcul.

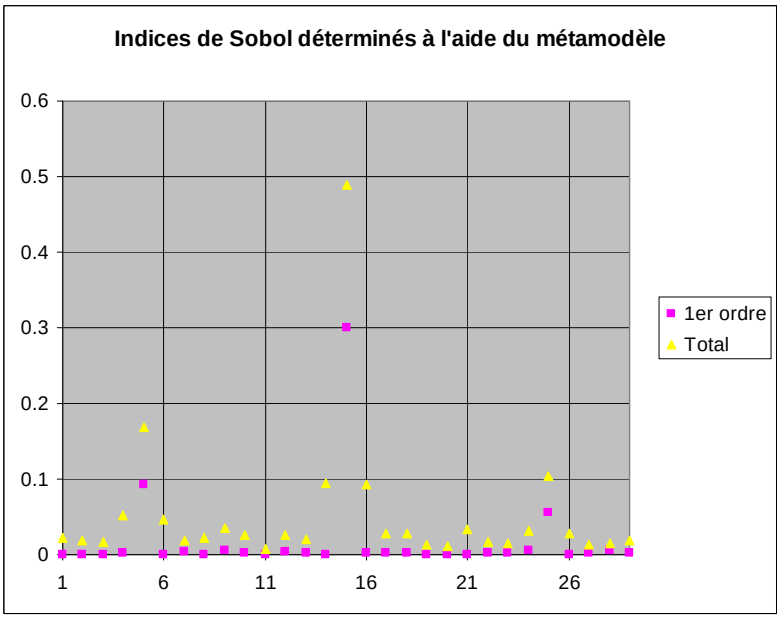

Figure 12 : Valeurs des indices de Sobol de chacune des 29 couches déterminées analytiquement à partir du métamodèle [35]. Valeurs des indices déterminées au moyen de 614 évaluations du code de calcul.

La convergence vers les valeurs des indices de Sobol du 1er ordre et totaux par la méthode Saltelli est très lente: le graphique de la Figure 11 a été obtenu avec 31000 évaluations du code de calcul alors que l'utilisation d'un métamodèle construit avec un plan d'expériences quasi-périodique WSP fournit de bien meilleurs résultats avec

seulement 614 évaluations du code (Figure 12). En effet, les 31000 évaluations du code donnent des résultats aberrants : ainsi, un coefficient du 1er ordre ne peut être supérieur à l'ordre total (cf. couche n°25) et certains indices ont une valeur négative (cf. couches n° 14 et 26 par exemple). Il serait donc nécessaire de réaliser plus d'évaluations du modèle numérique pour obtenir des résultats plus cohérents. La détermination de ces coefficients de Sobol ne permet pas d'identifier toutes les interactions : pour cela, il faudrait calculer l'ensemble des indices de Sobol ce qui nécessiterait encore plus d'évaluations du modèle. Cette détermination de tous les indices de Sobol s'avère pratiquement impossible dès lors que le système étudié comporte un grand nombre de facteurs d'entrée (>20).

Il en résulte que la démarche visant à évaluer les paramètres critiques d'un système dont certains composants sont en forte interaction et à quantifier leur importance tout en construisant un métamodèle satisfaisant à l'aide de plans d'expériences numériques SFD de grande qualité s'avère particulièrement performante.

2. Comparaison de deux méthodes de fabrication de filtres interférentiels multidiélectriques.

Nous considérons, à titre d'exemple, deux méthodes de fabrication de filtres interférentiels afin de comparer l'influence de leurs incertitudes sur les performances et la hiérarchie des interactions les plus critiques.

Dans la première technique de contrôle (TC1) qui correspond à l'utilisation d'un contrôle par quartz piézoélectrique, la détermination des couches plus influentes et de leurs interactions a été présentée dans la partie précédente. Pour la seconde technique de contrôle (TC2), l'utilisation d'un contrôle optique durant la fabrication des couches implique que la valeur de l'indice de réfraction $n^* = (1+\delta).n$ est compensée par la modification de l'épaisseur de la couche à la longueur d'onde λ_0 via la relation $e' = \frac{\lambda_0}{4.n^*}$.

La comparaison des paramètres et/ou interactions identifiés comme étant les plus critiques pour chacune de ces techniques de fabrication met en évidence une

hiérarchisation complètement différente **[36]**, **[37]**. Les processus mis en oeuvre pour fabriquer un filtre ont une conséquence directe sur la criticité des paramètres.

Les résultats acquis soulignent notamment que, pour une formule de filtre donnée, il n'est pas possible de déterminer les paramètres les plus critiques de manière absolue. En effet, les paramètres et leurs interactions qui se révèlent les plus influents dépendent étroitement des critères de performances utilisés (fonctions de mérite) et des méthodes de fabrication mises en œuvre.

L'analyse de sensibilité des filtres optiques prenant en compte des incertitudes sur les valeurs d'indice de réfraction *n* et d'épaisseur des couches *e,* ce qui constitue le cas le plus proche de la réalité, est également possible **[37]**. Pour la technique TC1 les incertitudes sur les valeurs d'indice de réfraction *n* et d'épaisseur des couches *e* sont indépendantes : $n^* = (1+\delta)n$ et $e^* = (1+\delta)e$. Pour la seconde technique de contrôle (TC2), les valeurs des épaisseurs des couches sont corrélées aux valeurs des indices de réfraction par les relations : $e' = \frac{\lambda_0}{4.n^*}$ et $e^* = (1+\delta)e'$. Les résultats obtenus lors de l'analyse de sensibilité de différents types de filtres diélectriques multicouches mettent en évidence que les interactions les plus critiques ne concernent que des interactions entre des épaisseurs de couches dans le cas de l'utilisation d'un contrôle optique (TC2) **[37]**, **[38]**. Ainsi, l'influence des incertitudes d'indice des différentes couches lors de la fabrication du filtre sur l'ensemble du domaine spectral considéré est considérablement réduite voire neutralisée. La corrélation des variables d'entrée caractéristiques de chacune des couches constitue ainsi un moyen d'améliorer la fabrication des filtres optiques.

L'évaluation de l'influence des incertitudes représentatives du processus de fabrications d'un filtre permet d'identifier les paramètres et les interactions les plus influents de ce filtre multidiélectrique. Pour que cette analyse soit efficace dans l'étape de conception d'un filtre interférentiel, il est fondamental que le modèle numérique exploré par un plan d'expériences prenne en compte la méthodologie de fabrication, la hiérarchisation des paramètres les plus critiques d'un filtre multidiélectrique dépendant étroitement des critères et processus utilisés.

3. Conclusion sur la qualité extrinsèque des plans SFD.

L’analyse de sensibilité des filtres optiques au moyen de plans d’expériences numériques et de métamodèles permet d’identifier efficacement les paramètres caractéristiques (indice ou épaisseur) et/ou leurs interactions les plus critiques en tenant compte de la méthode de fabrication.

Enfin, l’excellent accord entre la qualité intrinsèque des plans d’expériences utilisés et leur qualité extrinsèque sur des cas d’application de filtres bien connus ainsi que l’examen complémentaire avec les indices de Sobol a permis de mettre en place des moyens méthodologiques efficaces pour étudier des systèmes optiques interférentiels, c'est-à-dire des systèmes qui présentent par essence des interactions fortes entre paramètres.

La démarche mise en oeuvre pour l'analyse de sensibilité des filtres interférentiels a permis d'identifier les paramètres et les interactions les plus critiques dans le cas d'une onde plane incidente. La même analyse peut être réalisée pour une onde plane en incidence oblique ou sur des propriétés différentes que le facteur de transmission ou réflexion. Ces acquis ouvrent désormais la voie à l'identification des paramètres et des interactions les plus cruciales dans le cas d'un substrat inhomogène comme un guide d'onde diélectrique plan ou circulaire.

4. Les filtres multidiélectriques en extrémité de guides.

A l'extrémité d'un guide d'ondes diélectrique, l'onde lumineuse se propageant dans le guide est en partie transmise vers le milieu extérieur et en partie réfléchie dans le guide. Dans ce dernier cas, l'onde lumineuse réfléchie se répartira entre une propagation guidée sur des modes guidés et une propagation non guidée sur des modes rayonnants (Figure 13).

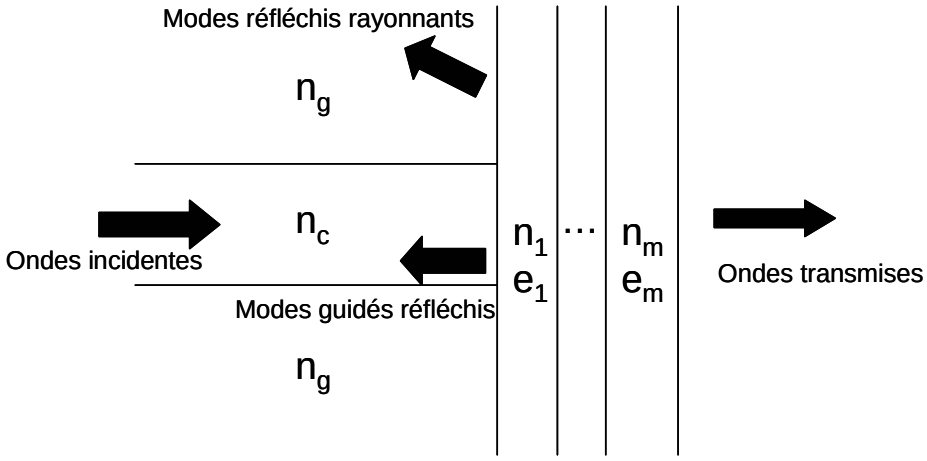

Figure 13 : Schéma de principe de l'étude des filtres déposés en extrémité de guides. n_c représente l'indice de réfraction du cœur, n_g l'indice de réfraction de la gaine, n_1 à n_m les indices de réfractions des couches minces et e_1 à e_m les épaisseurs des couches minces.

Les caractéristiques de la répartition d'énergie lumineuse lors de la réflexion en extrémité de guide dépendent fortement de la structure du guide d'ondes diélectrique d'une part et des valeurs d'indices réfractifs des différents milieux. Le problème de la discontinuité entre un milieu guidant et un milieu homogène a fait l'objet de nombreuses études qui ont souvent porté sur le guide plan [39]-[41]. Différentes approches théoriques ont été développées et souvent l'objectif de ces études était d'accroître l'énergie lumineuse transmise vers le milieu homogène tout en diminuant l'énergie réfléchie dans le mode guidé [41], **[42]**. L'approche basée sur la décomposition du champ incident en onde plane et le remplacement de la structure guidante par un milieu homogène a permis de définir et de réaliser des antireflets modaux de très grande performance dans le cas du guidage faible $\Delta = (n_1/n_2 - 1) << 1$ **[42]**-[44]. Cette approche a été étendue au cas des fibres monomode et multimodes et a permis d'obtenir les premiers résultats décrivant la propriété spectrale de filtres en extrémité de guide 3-D **[45]**, [46].

La décomposition en ondes planes du champ et le formalisme décrivant les propriétés optiques d'un empilement de couches minces permettent d'appliquer directement notre démarche pour identifier les paramètres les plus influents sur les propriétés modales et en énergie du filtre pour une structure d'onde particulière.

5. Perspectives

L’identification de plans d’expériences efficaces et la démarche développée pour l’analyse de sensibilité de filtres interférentiels ont été notamment appliquées pour la détermination des paramètres et/ou de leurs synergies les plus influents sur les facteurs de transmission ou de réflexion des filtres dans un domaine spectral donné par rapport au profil désiré du filtre.

Dans le domaine de la conception robuste de filtres interférentiels, l’étude de l’impact des incertitudes sur d’autres propriétés des filtres est également envisageable. Par exemple, les travaux concernant l’élaboration de miroirs dispersifs destinés au domaine des lasers femtoseconde utilisent comme variables d’intérêt simultanément le facteur de réflexion du miroir et la dispersion de la vitesse de groupe et ces miroirs comportent un grand nombre de couches [47]. La détermination des solutions les plus robustes aux incertitudes résiduelles des méthodes de fabrication constitue un domaine d’application de notre méthodologie et de nos plans qualifiés par l'ALM.

L'ensemble des acquis concernant les propriétés des filtres interférentiels en extrémité de guides et l'exploration efficace d'espaces de grandes dimensions ouvrent également la voie à la conception robuste de filtres multidiélectriques sur des structures guidantes beaucoup plus élaborées telles les guides microstructurés.

2) La combinaison cohérente de sources laser fibrées

Le développement de sources laser solides de forte énergie se heurte inévitablement aux limites de tenue au flux du milieu amplificateur. Le développement des sources laser fibrées et des amplificateurs à fibres sont soumis aux mêmes limitations physiques mais a favorisé les travaux permettant d’atteindre de très fortes énergies par la combinaison cohérente des faisceaux laser d’un ensemble de fibres. Les travaux conduits à l'Onera porte sur la combinaison cohérente par contrôle actif de la phase dont le schéma de principe est rappelé sur la Figure 14.

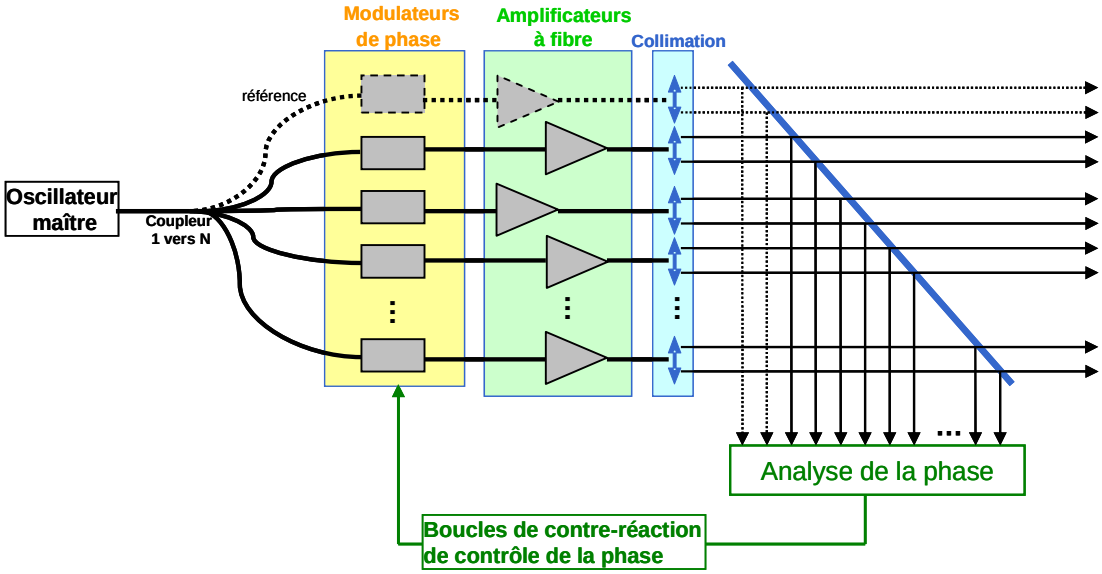

Figure 14 : Principe de la combinaison cohérente par contrôle actif de la phase.

Outre le développement de sources laser de haute énergie, la combinaison cohérente offre la possibilité de sculpter le front d'onde du faisceau laser donc d'obtenir une répartition de l'intensité lumineuse particulière (Figure 15), de défléchir le faisceau laser et de compenser en partie la turbulence atmosphérique **[48]**, **[49]**. Cette sculpture du front d'onde est effectuée directement au sein de la source laser par déphasage de certains faisceaux ce qui évite l'utilisation d'une optique adaptative devant la source laser et accroît finalement la compacité du système global. Pour le développement de sources laser de haute énergie, la fragmentation de la fonction source laser sur différents amplificateurs fibrés permet d'envisager également une meilleure gestion de la chaleur des différents composants et d'accroître la fiabilité de l'ensemble de la source par rapport à un seul milieu laser.

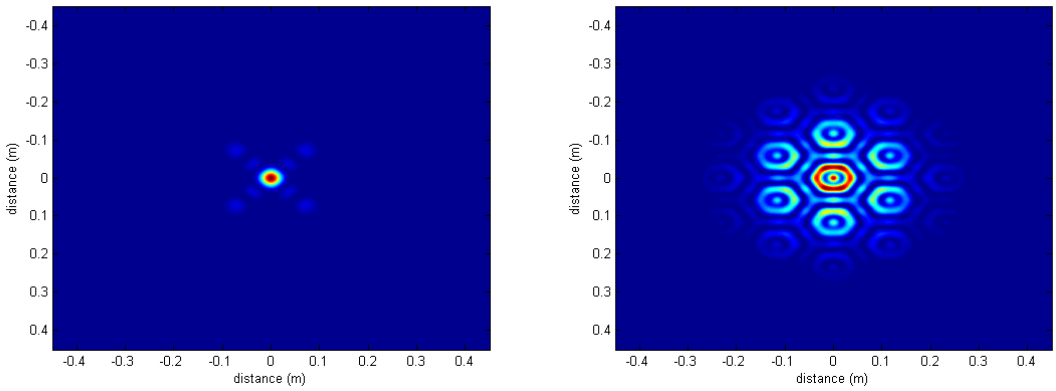

Figure 15 : Différentes formes de faisceau en champ lointain obtenues pour un réseau de 9 fibres (gauche) et 19 fibres (droite) disposées en hexagone.

Dans cette partie sont rappelées les principales caractéristiques des résultats obtenus lors de travaux d'évaluation de ces sources pour des applications à grandes distances, c'est-à-dire dans le cas d'une propagation dans l'atmosphère et par conséquent en présence de turbulence atmosphérique.

1. Critères de qualité de la combinaison cohérente

La qualité de la combinaison cohérente est généralement évaluée en laboratoire par le rapport de Strehl **[50]**. Toutefois ce critère qui n'évalue la combinaison cohérente que sur un point de la répartition d'intensité dans un plan à une distance fixée ne fournit aucune information sur la répartition d'intensité dans une zone donnée. Pour cette raison, la DARPA[14] a proposé d'utiliser le Beam Propagation Factor (BPF) afin d'évaluer l'énergie contenue dans le lobe central du faisceau laser **[50]**. L'utilisation combinée de tels critères permet d'apprécier la qualité de la combinaison cohérente à partir des caractéristiques de la source laser[15] mais ne répond pas à la pertinence de la combinaison cohérente réalisée pour une application donnée. Il est alors nécessaire de compléter cet ensemble de critères par d'autres, construits sur les caractéristiques de l'objet illuminé par le faisceau. Ainsi le Mask Encircled Power (MEP) permet d'apprécier la quantité d'énergie ou de puissance reçue dans une zone déterminée de la surface de l'objet pour une configuration donnée (distance laser-

[14] DARPA : Defense Advanced Research Projects Agency.

[15] D'autres critères du même type peuvent être proposés.

objet). L'examen de la répartition de la densité de puissance au sein de cette zone peut également être utile **[49]**, **[50]**.

Dès lors que la réalisation d'une source laser reposant sur la combinaison cohérente de faisceaux élémentaires est envisagée pour répondre à des applications concrètes d'emploi, la qualité de la combinaison cohérente de sources laser doit être nécessairement appréciée au moyen de multiples critères. Le respect de cette exigence est d'autant plus crucial pour la conception robuste du système laser. Cette démarche limitera l'impact des incertitudes résiduelles des différents paramètres de la source laser et des variations non contrôlables des caractéristiques de l'environnement d'emploi[16] sur les performances exigées de la combinaison cohérente des faisceaux à grande distance de la source laser.

Il est à noter que les critères proposés sont scalaires. L'analyse de la répartition d'intensité dans le plan bénéficierait grandement d'une caractérisation de l'organisation spatiale de l'intensité comme nous le développerons dans la partie IV. Une caractérisation fonctionnelle de la répartition de l'intensité peut également être envisagée. Toutefois, la prise en compte de sorties fonctionnelles fait l'objet de nombreux travaux et ne fournit pas encore tous les outils adéquats. Cependant, notre méthodologie basée sur l'analyse de sensibilité et la construction de métamodèle autorise l'utilisation de plusieurs critères scalaires judicieux et l'obtention de résultats satisfaisants.

2. La détermination des paramètres critiques.

L'identification des paramètres de la source laser dont les incertitudes résiduelles ont une influence déterminante sur les performances de la combinaison cohérente est effectuée au moyen de différents types de plans d'expériences : plans de criblage, analyse de sensibilité et construction de métamodèles.

Dans un premier temps, l'analyse de l'influence des facteurs géométriques de la source et des paramètres optogéométriques des fibres en sus des différences de phase

[16] Par exemple, la turbulence atmosphérique.

entre les faisceaux issus des différentes fibres a permis de confirmer que les facteurs les plus influents étaient les différences de phase entre chacune des fibres et une fibre de référence **[50]**. Il en résulte que les analyses de sensibilité doivent identifier les architectures de sources laser les plus pertinentes pour atteindre les performances souhaitées sur les différents critères. Il est également nécessaire d'identifier les paramètres les plus critiques pour concevoir, de manière robuste, le système.

La disposition de moyens efficaces en terme d'exploration d'espaces mathématiques de grandes dimensions et les résultats obtenus sur les filtres interférentiels permettent désormais d'étudier la combinaison cohérente d'un grand nombre de sources laser. Les travaux ont été conduits en utilisant la même fonction polynomiale (Equation 1 p. 29) que pour les filtres interférentiels et en utilisant les critères de qualité pour le métamodèle : R^2 et a_0 (a_0 doit être un maximum). Bien que ces études n'ont pas pu bénéficier directement de cas étalons comme dans le cas des filtres interférentiels, le critère du rapport de Strehl a permis d'évaluer la démarche et la qualité des métamodèles obtenus (R^2 >0.999) de conforter les analyses **[30]**.

Les résultats d'analyse de sensibilité concernant les déphasages résiduels entre les différentes fibres de la source mettent en évidence une hiérarchie différente en fonction des critères d'appréciation de la mise en phase. Ainsi, pour le critère du rapport de Strehl qui est couramment utilisé mais peu représentatif d'applications potentielles, toutes les fibres ont la même influence sur le critère. En revanche, pour les autres critères, certaines interactions entre fibres s'avèrent beaucoup plus critiques que d'autres (Figure 16) **[5]** et la hiérarchie de ces interactions peut varier selon ces critères.

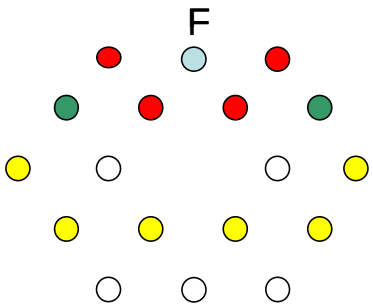

Figure 16 : Hiérarchie des interactions de la fibre F avec les autres. Rouge : interactions les plus fortes. Vert : interactions 2 à 3 fois inférieures à rouge. Jaune : interactions 6 à 10 fois inférieures à rouge. Blanc : 50 à 60 fois inférieures à rouge.

De plus, dans le cas du critère MEP qui est représentatif de l'application, la taille de la zone retenue entraîne des ajustements de hiérarchies. Ainsi, dans le cas de 19 fibres placées en hexagone et pour un MEP large, les termes b_i correspondant aux fibres placées sur l'extérieur de la structure ont des valeurs plus élevées que dans le cas de l'utilisation d'un MEP étroit.

La maîtrise des déphasages entre les fibres les plus critiques doit alors être garantie avec une attention particulière pour développer des sources laser performantes et robustes.

3. Perspectives pour la combinaison cohérente

La détermination des paramètres critiques de la combinaison cohérente de sources laser fibrées en fonction des critères adaptés à l'application visée autorise désormais l'étude des architectures robustes aux incertitudes non contrôlables liées à l'environnement du système lors de son utilisation comme, par exemple, la turbulence atmosphérique. Les travaux correspondants sont d'autant plus nécessaire que la démonstration de la correction des effets de turbulence à grande distance sur le trajet laser-cible a permis de mettre en évidence la possibilité "d'incorporer" le miroir adaptatif au sein de la source laser par rapport au cas d'un système composé d'une source laser monolithique **[48]**, **[49]**.

L'évaluation des performances et de la robustesse de la combinaison cohérente de plusieurs centaines de fibres laser est désormais accessible. Mais la réalisation

pratique peut se heurter au nombre de fréquences nécessaires pour moduler chacune des voies laser. L'utilisation de codes de marquage sur les fréquences en remplacement des modulations sinusoïdales permet, alors, de limiter le nombre de fréquences nécessaires pour réaliser la combinaison cohérente **[51]**. Il s'agit alors d'apprécier la sensibilité de la qualité de la combinaison cohérente aux différents codes pour identifier le meilleur compromis entre le nombre de fréquences utilisé et la longueur des codes de marquage.

L'étude la combinaison cohérente dans le domaine continu a permis de mettre en place les outils fondamentaux qui favorisent le développement de nouvelles orientations. Ainsi, dès lors que la dérive de phase s'avère négligeable pendant une impulsion nanoseconde, la mise en phase de faisceaux impulsionnels est possible. Il suffit de disposer d'un signal de faible puissance permettant d'assurer la mise en phase avant le début de l'impulsion **[52]**.

Si la "neutralisation" de l'influence de la turbulence atmosphérique s'avère être une exigence importante pour la mise en oeuvre d'un système laser dans un contexte d'emploi hors du laboratoire, les progrès actuels auxquels nous avons contribués permettent aujourd'hui de proposer des solutions. Ainsi la combinaison cohérente apporte des solutions pour des systèmes continus et impulsionnels **[49]**, **[52]**, [53]. Dans le cas des très hautes puissances (TW), la filamentation de faisceaux laser femtoseconde assure une moindre sensibilité à la turbulence atmosphérique **[54]**.

4. Evolution des concepts

En plus des travaux sur l'organisation des systèmes de sources laser envisageables, de nouvelles orientations de recherche apparaissent concernant la structure guidante. En effet, jusqu'à présent, les fibres considérées au sein du système sont toutes identiques. Il est nécessaire d'envisager l'utilisation de fibres différentes et de ré-interroger l'apport des fibres multimodes **[50]**, **[55]**, [56]. De même, le remplacement des fibres par d'autres structures guidantes (carré, rectangulaire par exemple) et, à défaut, la modification de la géométrie de l'extrémité des fibres doivent être étudiés. L'examen de ces perspectives bénéficiera alors des acquis des études

portant sur la modélisation d'une onde arrivant en extrémité de guide (cf. § III.1)4) et, dans le cas de guides multimodes, de la détermination des couplages modaux.

Les méthodologies mises en œuvre peuvent être utilisées pour combiner de manière incohérente plusieurs sous-ensembles d'amplificateurs laser fibrés combinés de manière cohérente. L'architecture de tels systèmes définie à partir des applications envisagées peut alors être évaluée et optimisée par l'analyse de la robustesse des performances et l'identification des interactions ou synergies entre les différents sous-systèmes. Le développement de tels systèmes mêlant combinaison cohérente et incohérente peut compléter la panoplie des sources laser à large bande spectrale : OPO (Oscillateur Paramétrique Optique), super-continuum, laser femtoseconde.

3) Perspectives

La méthodologie mise en place et la qualification des plans d'expériences pour réaliser l'analyse de sensibilité de systèmes optiques interférentiels composés d'un grand nombre de composants permettent aujourd'hui d'identifier les facteurs du système et leurs synergies les plus influents de manière efficace et d'apprécier leurs conséquences sur les performances du système laser.

La qualité des résultats acquis constitue le socle indispensable pour aborder désormais la dynamique de ces systèmes. Ainsi, dans le cas des filtres interférentiels, il faut envisager l'intérêt d'un processus dynamique de correction des défauts de fabrication des couches déposées par la modification de la structure du filtre restant à fabriquer pour répondre aux exigences de performance. Dans le domaine de la mise en phase de sources laser, la simulation de l'ensemble des boucles de contre-réaction et de la propagation laser dans l'atmosphère constitue un nouveau challenge pour identifier les formes de faisceaux les plus adaptées aux applications. Ces orientations exigent désormais d'étudier de manière plus approfondie l'influence des incertitudes de variables corrélées comme cela a été initié avec les filtres interférentiels. De plus, l'étude de l'évolution temporelle des cartographies d'interactions entre les différents composants (couches minces et fibres) constitue un nouveau challenge pour maîtriser intégralement la dynamique du système.

Dans le cas de l'élaboration de métamodèles, il s’agit désormais de remplacer les fonctions de mérite scalaires actuelles par la sortie vectorielle correspondant à l’évolution des propriétés spectrales pour chacune des longueurs d’onde dans le cas des filtres interférentiels d'une part et d'utiliser la sortie matricielle de la répartition d’intensité dans le cas de la mise en phase de sources laser fibrées d'autre part. Plus généralement, ces travaux doivent s’accompagner de l’intégration des acquis des travaux de recherche actuels concernant la prise en compte d'entrées ou de sorties fonctionnelles pour l'exploration de codes de calculs.

IV. De la caractérisation du speckle à la caractérisation de la variabilité spatiale de phénomènes optiques

Les travaux sur la mise en phase conduisent inévitablement à s'intéresser au speckle engendré par la propagation en atmosphère turbulente et/ou par la surface illuminée. Ainsi, le système de détection installé dans la boucle d'asservissement pour effectuer la combinaison cohérente utilise une partie du speckle réfléchi **[48]**. Il pourrait être envisagé de réaliser la combinaison cohérente en déterminant les corrections de phases à utiliser à partir de la figure de speckle. Si la loi de distribution des intensités est bien connue [57], la répartition spatiale de la l'intensité n'a pas été étudiée. Nous présentons l'intérêt de cette approche à partir de l'outil ALM, que nous avons utilisé pour la détermination de la qualité des plans d'expériences, dans le cas de l'application à l'étude de la transition gaussienne[17]. Si la caractérisation spatiale n'est pas aisée, l'ALM a montré son efficacité pour décrire des typologies d'organisation de points et même permis d'appréhender la perception humaine de répartitions "aléatoires" dans le plan **[58]**.

1) La caractérisation du speckle laser

La figure de speckle générée par une surface est engendrée par le nombre de cellules élémentaires et les déphasages introduits par ces différentes cellules. L'analyse de la fonction de probabilité représentant la distribution statistique de l'intensité du speckle optique a permis à Goodman de montrer que la distribution de sa densité de probabilité suit une loi exponentielle négative [57], [59], [60] :

[17] La transition gaussienne correspond à l'étude de l'évolution des figures de speckle en fonction du nombre de cellules illuminées de la surface.

$$p(I) = \frac{1}{I_m}\exp(-\frac{I}{I_m})$$ avec I_m l'intensité moyenne et I > 0.

Toutefois, l'existence d'une telle distribution d'intensité entre pixels ne traduit pas forcément l'existence d'une figure de speckle et ne permet pas d'apprécier la répartition spatiale d'intensité dans une zone donnée. Ainsi, la Figure 17 présente des répartitions spatiales d'intensité extrêmement différentes mais qui respectent la même distribution de densité de probabilité.

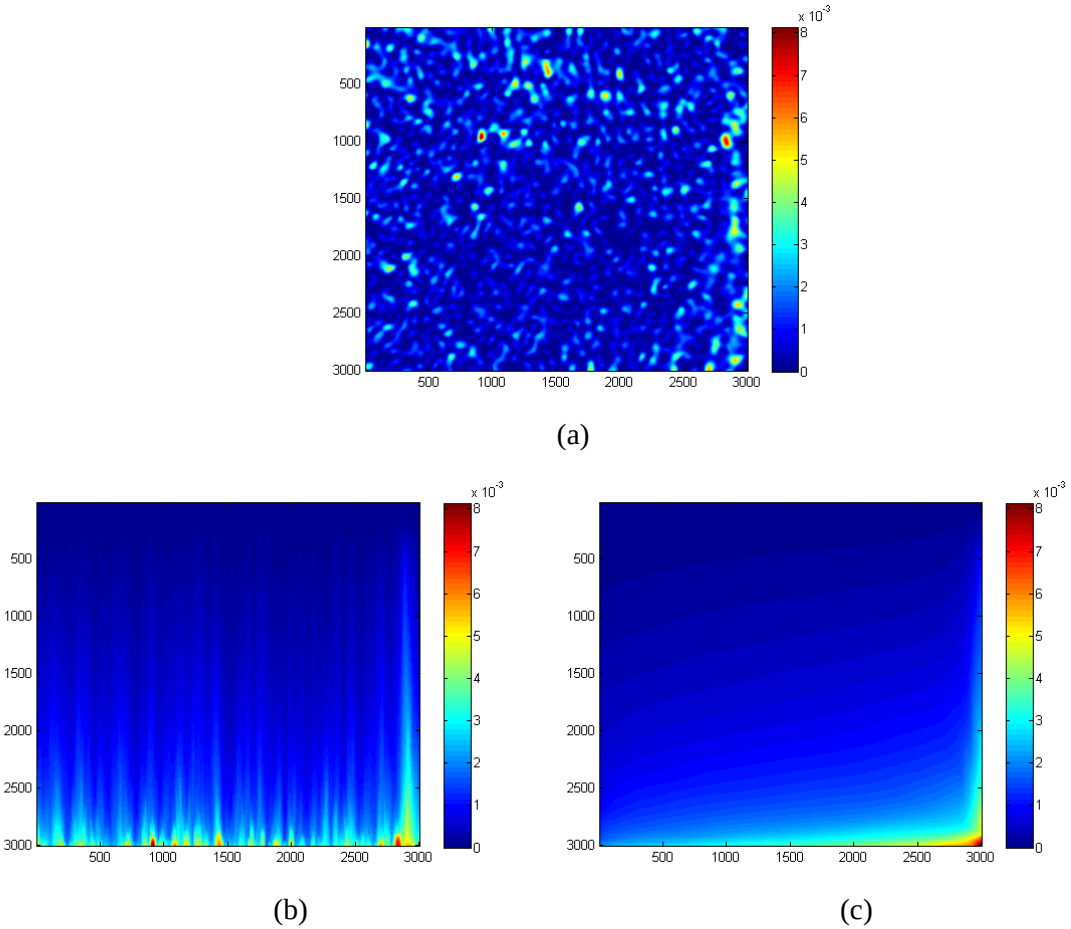

(a)

(b) (c)

Figure 17 : Différentes répartitions spatiales d'intensité ayant la même distribution de densité de probabilité : image de speckle originale (a), image modifiée spatialement : les pixels de l'image (a) sont triés par colonne selon une intensité croissante du haut vers le bas (b) puis triés par ligne selon une intensité croissante de gauche à droite (c).

La qualification de la répartition spatiale de l'intensité dans l'image constitue donc un complément utile à l'étude du speckle. La qualification de la répartition de points en dimension 2 [19], qui a permis de qualifier les plans d'expériences en grande

dimension, constitue un moyen de compléter la description du speckle par un critère spatial sur l'analyse des maxima d'intensité.

2) Première application : la transition gaussienne

La démarche proposée a été appliquée à l'étude de la transition gaussienne en utilisant les maxima et minima d'intensité dans l'image **[61]**, **[62]**. Dans un premier temps, il a été constaté que la variabilité statistique des surfaces illuminées se traduisait par des localisations voisines des représentations dans le plan (m, σ) : ainsi, la variabilité entre différentes images de speckle correspondant à des caractéristiques physiques déterminées est bien caractérisée par l'ALM. La Figure 18 présente différentes images de speckle et l'ALM construit sur les points correspondant aux maxima pour différentes valeurs du nombre de cellules illuminées (n_c)[18].

[18] $n_c = \frac{\omega_0^2}{L_{corr}^2}$ où ω_0 est le waist de l'amplitude gaussienne du faisceau laser illuminateur et L_{corr} est la longueur de corrélation de la distribution gaussienne de hauteur de la surface éclairée. La valeur est modifiée par la variation de la valeur L_{corr}. La surface est éclairée au niveau du waist du faisceau laser.

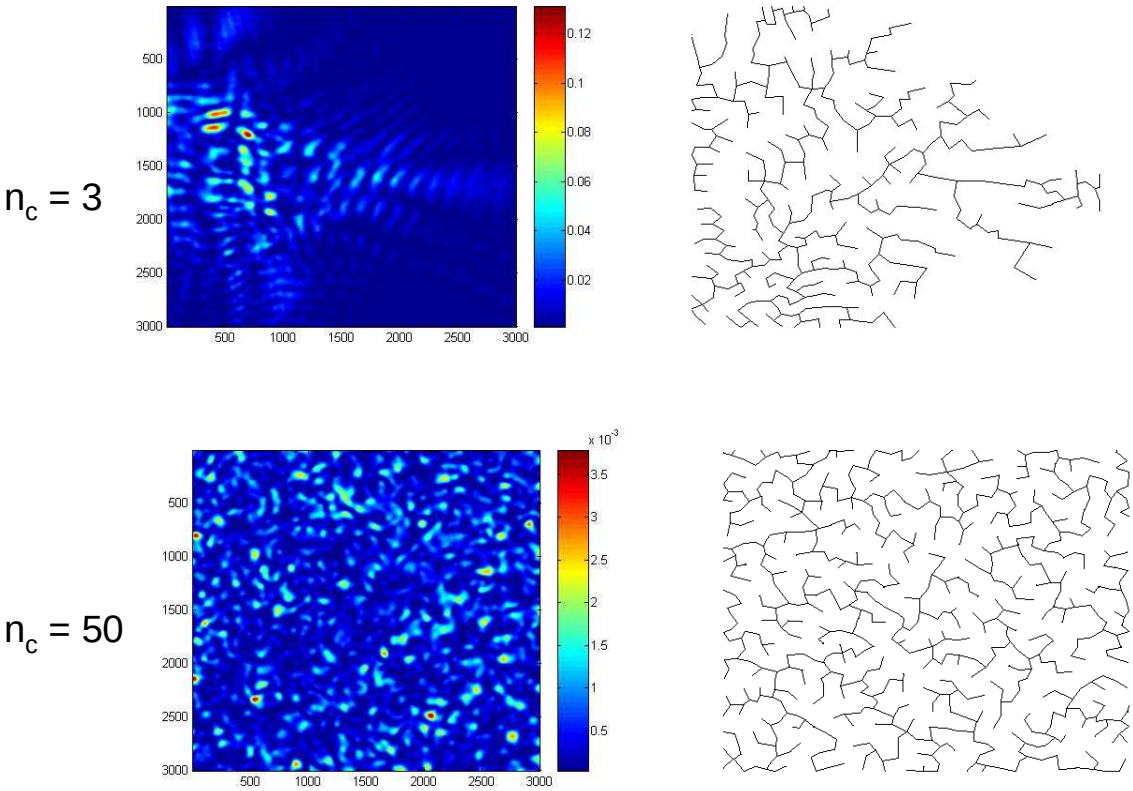

Figure 18 : Images de speckle et ALM correspondant construit sur les maxima dans le cas de 3 et 50 cellules illuminées.

L'évolution des caractéristiques des ALMs peut alors être observée dans le plan (m, σ) (Figure 19).

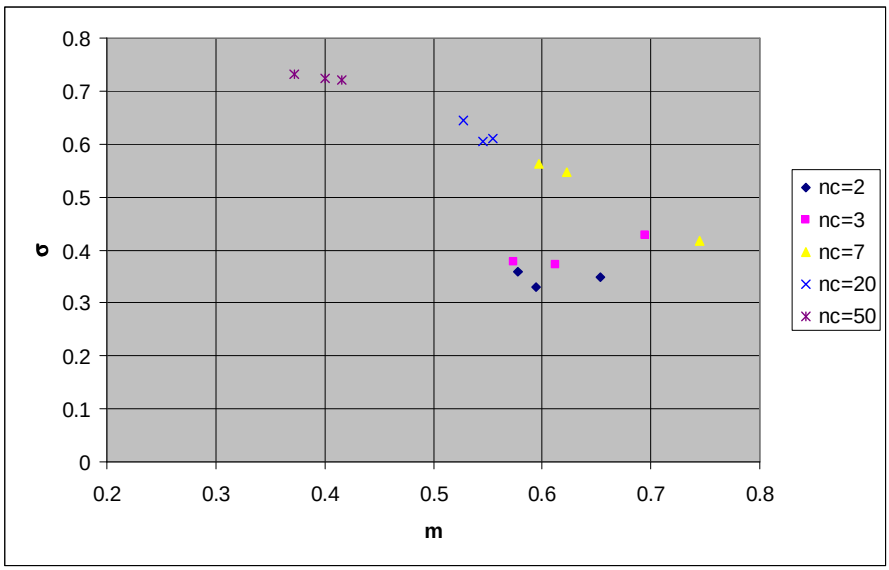

Figure 19 : Evolution des caractéristiques de l'ALM dans le plan (m,σ) pour différentes images de speckle et différentes valeurs du nombre de cellules illuminées n_c.

Cette approche met en évidence une disposition particulière des caractéristiques spatiales du speckle dans le plan (m, σ), le caractère relatif des valeurs m et σ en fontion de la résolution des images mais surtout une modification de la structure de l'ALM autour de la valeur $n_c = 3$ ou 7 sur la Figure 19 mais plus précisément autour de la valeur $n_c = 4$ ou 5 **[61]**, **[62]**. Ces résultats de caractérisation spatiale apportent finalement des éléments nouveaux pour qualifier la transition gaussienne.

Cette démarche a été également appliquée pour l'étude des singularités de phase et les résultats obtenus mettent en exergue des caractéristiques spatiales très différentes pour les maxima et minima **[62]**.

Outre la description spatiale du speckle, l'utilisation du critère ALM pour qualifier le speckle invite à engager des travaux mettant en regard une caractéristique de diffusion spatiale de la lumière à des caractéristiques physiques des objets étudiés.

3) Perspectives

La qualification spatiale de la répartition d'intensité constitue un outil complémentaire à la description et la compréhension du speckle. Par exemple, les caractéristiques spatiales de la répartition des maxima et des singularités sont différentes **[62]**. Il est cependant tout à fait envisageable d'utiliser d'autres niveaux d'intensité ou encore de construire un arbre sur des points correspondant à des niveaux d'intensité donnés.

Cette description de la répartition spatiale peut être utilisée pour caractériser des figures de speckle générées de différentes manières : speckle généré par une surface, par un volume d'un matériau, par la turbulence atmosphérique… Dans le cas du speckle généré par une surface et la turbulence atmosphérique, l'étude de la répartition d'intensité pourrait à terme fournir des informations utiles pour améliorer la qualité de la combinaison cohérente de sources laser. Dans le domaine des sources laser femtoseconde de forte puissance, la qualification de la répartition spatiale des différents filaments est actuellement utilisée comme outil de caractérisation de

l’influence de la turbulence atmosphérique selon qu’elle intervient avant ou après la création des filaments.

Plus généralement, cette démarche peut également être utilisée dans le domaine de l’imagerie pour caractériser des surfaces rugueuses ou la surface de la mer et déterminer les typologies d'organisations représentatives d'une variabilité statistique.

> Le besoin pressant d'un univers logique et cohérent est profondément ancré dans l'inconscient humain. Mais l'univers réel est toujours à un pas au-delà de la logique.
>
> F. Herbert, *Dune*.

V. Perspectives

Les travaux que j'ai réalisé sur les plans d'expériences numériques "Space Filling Design" ont mis en évidence l'intérêt d'un nouveau critère basé sur l'utilisation de l'arbre de longueur minimale construit sur les points des plans numériques pour déterminer leur qualité intrinsèque aussi bien en basse dimension qu'en grande dimension. Ce critère s'est avéré particulièrement performant et robuste en grande dimension contrairement aux critères classiques et souligne les insuffisances des plans construits sur les suites à faible discrépance en grande dimension. De plus, les résultats des analyses de sensibilité globale de systèmes optiques interférentiels bien connus soulignent la cohérence entre les qualités intrinsèque et extrinsèque des plans d'expériences numériques SFD. Les perspectives issues de ces acquis doivent porter désormais sur l'élaboration de plans numériques de grande qualité intrinsèque pour des dimensions supérieures à plusieurs centaines.

L'étude de l'influence des incertitudes sur les paramètres caractéristiques des systèmes optiques interférentiels met en exergue que les interactions constituent les éléments clefs à maîtriser pour la conception robuste de tels systèmes. De plus, nos résultats montrent qu'il n'est pas possible de déterminer une hiérarchisation absolue des facteurs intrinsèques les plus critiques dans un tel système : la criticité des paramètres et de leurs interactions dépend non seulement des critères de performance ou des fonctions de mérite utilisés mais surtout des processus de fabrication et de contrôle mis en œuvre. L'étude de la compensation des défauts des couches minces réalisées lors de

la fabrication d'un filtre interférentiel par les couches restant à déposer, constitue un prolongement naturel des travaux réalisés. De même, la connaissance des interactions entre les fibres pour la combinaison cohérente de faisceaux laser ouvre dorénavant le champ à l'étude de l'influence temporelle des bruits de phase résiduels ou de la turbulence atmosphérique sur la performance de la combinaison cohérente. L'évaluation de multiples architectures est désormais possible comme, par exemple, la robustesse de la combinaison cohérente de structures guidantes variées, qui peuvent être plus complexes (fibres microstructurées par exemple), sur lesquelles seraient déposés des filtres multidiélectriques.

Les acquis concernant la caractérisation spatiale du speckle ouvrent plusieurs axes de recherche. Dans un premier temps, la description de différents types de speckle au moyen de l'ALM (speckles surfaciques, speckles volumiques, speckle généré par la turbulence atmosphérique) s'avère indispensable pour identifier l'ensemble des possibilités de cette démarche. Il s'agit alors d'établir les correspondances entre les paramètres physiques et statistiques (rugosité de surface, force de la turbulence…) et les caractéristiques obtenues dans le plan (m, σ). La construction de métamodèles représentatifs de l'influence de défauts de régularité d'une structure diffractive est désormais envisageable, ce qui permettra d'identifier les architectures les plus robustes à de tels défauts. De manière générale, le potentiel de l'ALM pour caractériser des surfaces rugueuses, des surfaces de mer et la turbulence atmosphérique ainsi que les images obtenues en éclairage cohérent ou incohérent doit être évalué pour déterminer les typologies d'organisations représentatives de la variabilité statistique de ces phénomènes optiques. Enfin, en relation avec la combinaison cohérente de sources laser fibrées et la compensation de la turbulence atmosphérique, la caractérisation spatiale du speckle observée sur l'objet éclairé par la source laser constitue t-elle un moyen complémentaire d'informations permettant d'accroître l'efficacité des boucles de contre-réaction de chacune des fibres ? La réponse à cette question nécessite, là encore, d'apprécier les systèmes optiques interférentiels en relation avec les incertitudes introduites par les adaptations proposées pour obtenir des conclusions fiables.

Bien que les termes de complexité et systèmes complexes soient très largement employés, il subsiste de nombreuses variations sémantiques. Toutefois, de manière générale, il ressort systématiquement qu'un système complexe est un système composé d'un grand nombre d'entités en interaction variée et simultanée qui engendrent des comportements non linéaires [63], [64]. A ce titre, les relations entre les incertitudes sur les paramètres des systèmes optiques interférentiels comportant un grand nombre d'éléments, et les performances de ces systèmes soulignent la difficulté de leur analyse du fait de leur complexité. Inversement, la poursuite de l'étude des incertitudes dans les systèmes interférentiels peut contribuer de manière efficace à l'exploration et la compréhension d'autres types de systèmes complexes aussi bien par la modélisation que par la réalisation de démonstrateurs.

Enfin, les cartographies des interactions entre les fibres dans le cas de la combinaison cohérente, obtenues à partir de différents seuillages sur les coefficients d'interaction, s'apparentent à l'étude des réseaux prenant en compte des paramètres géographiques et sociaux et des systèmes multi-agents [65]. L'étude dynamique de ces systèmes interférentiels bidimensionnels pourrait alors contribuer, à terme, à l'étude de la dynamique de systèmes biologiques ou sociétaux.

VI. Références

[1] M. Françon, *La granularité laser (speckle) et ses applications en optique*, Masson, Paris, 1978.

[2] P. Smigielski, "Interférométrie de speckle", Techniques de l'ingénieur, r6331, 2001.

[3] M. Tilsch, K. Hendrix, "Optical Interference Coatings Design Contest 2007: triple bandpass filter and nonpolarizing beam splitter", Applied Optics 47, C55-C69, 2008.

[4] T. M. Shay, V. Benham, J. T. Baker, A. D. Sanchez, D. Pilkington, C. A. Lu, "Self-Synchronous and Self-Referenced Coherent Beam Combination for Large Optical Arrays", IEEE J. Sel. Topics Quantum Electron. 13, 480-486, 2007.

[5] A. Azarian, O. Vasseur, B. Bennaï, L. Lombard, G. Canat, V. Jolivet, Y. Jaouën, P. Bourdon, "Global sensitivity analyses of coherent beam combining of fiber amplifier arrays by the use of numerical space filling designs", Proc. SPIE 7914, 79141G, 2011.

[6] E. Hecht, *Optique*, Pearson Education France, Paris, 2005.

[7] A. Saltelli, K. Chan, E.M. Scott, *Sensitivity Analysis*, Wiley, New York, 2000.

[8] A. A. Giunta, S. F. Wojtkiewicz, M. S. Eldred, "Overview of modern design of experiments methods for computational simulations", in Proceedings of the 41st AIAA Aerospace Sciences Meeting and Exhibit, AIAA-2003-0649, 2003.

[9] T. J. Santner, B. J. Williams, W. I. Notz, *The Design and Analysis of Computer Experiments*, Springer, New York, 2003.

[10] G. G. Wang, S. Shan, "Review of metamodeling techniques in support of engineering design optimization", J. Mech. Des. 129, 370-380, 2007.

[11] J. Goupy, *La Méthode des plans d'expériences : optimisation du choix des essais et de l'interprétation des résultats*, Dunod, Paris, 1988.

[12] G. Sado, M. C. Sado, *Les plans d'expériences : de l'expérimentation à l'assurance qualité*, Afnor technique, Paris, 1991.

[13] J.-J. Droesbeke, J. Fine, G. Saporta, *Plans d'expériences : applications à l'entreprise*, Technip, Paris, 1997.

[14] J.-P. Gauchi, "Plans d'expériences optimaux : un exposé didactique", MODULAD 33, 139-162, 2005.

[15] V. Feuillard, *Analyse d'une base de données pour la calibration d'un code de calcul*, Ph. D. Thesis, Université Pierre et Marie Curie, 2007.

[16] J. Franco, *Planification d'expériences numériques en phase exploratoire pour la simulation des phénomènes complexes*, Ph. D. Thesis, ENSMSE, 2008.

[17] M. Sergent, R. Phan-Tan-Luu, J. Elguero, "Statistical Analysis of Solvent Scales. Part 1", Anales de Quimica Int. Ed. 93, 3-6, 1997.

[18] Package R 'DiceDesign', http://cran.r-project.org/, 2012.

[19] C. Dussert, G. Rasigni, M. Rasigni, J. Palmari, "Minimal spanning tree: A new approach for studying order and disorder", Physical Review B 34, 3528-3531, 1986.

[20] F. Wallet, C. Dussert, "Multifactorial comparative study of spatial point pattern analysis methods", J. Theor. Biol. 187, 437-447, 1997.

[21] F. Wallet, C. Dussert, "Comparison of spatial point patterns and processes characterization methods", Europhysics Lett. 42, 493-498, 1998.

[22] J. Franco, O. Vasseur, B. Corre, M. Sergent, "Un nouveau critère basé sur les arbres de longueur minimale pour déterminer la qualité de la répartition spatiale des points d'un plan d'expériences numériques", Chimiométrie 2007, Lyon, 2007.

[23] J. Franco, O. Vasseur, B. Corre, M. Sergent, "Minimum Spanning Tree : A new approach to assess the quality of the design of computer experiments", Chemometrics and Intelligent Laboratory Systems, 97, 164-169, 2009.

[24] J. Loeppky, J. Sacks, W. Welch, "Choosing the sample size of a computer experiment: a practical guide", Technometrics 51, 366–376, 2009.

[25] P. Bratley, B. L. Fox, H. Niederreiter, "Implementation and tests of low-discrepancy sequences", ACM Trans. Model. Comput. Simul. 2, 195-213, 1992.

[26] S. Kucherenko, B. Feil, N. Shah, W. Mauntz, "The identification of model effective dimensions using global sensitivity analysis", Reliability Engineering & System Safety 96, 440-449, 2011.

[27] S. Tarantola, W. Becker, D. Zeitz, "A comparison of two sampling methods for global sensitivity analysis", Computer Physics Communications 183, 1061-1072, 2012.

[28] X. Wang, K.-T. Fang, "The effective dimension and quasi-Monte Carlo integration", Journal of Complexity 19, 101-124, 2003.

[29] O. Roustant, J. Franco, L. Carraro, A. Jourdan, "A radial scanning statistic for selecting space-filling designs in computer experiments, in mODa 9 – advances in model oriented design and analysis", Proceedings of the 9th International Workshop in Model-Oriented Design and Analysis held in Bertinoro, Italy, June 14–18, Springer, Heildeberg, 189–196, 2010.

[30] O. Vasseur, A. Azarian, V. Jolivet, P. Bourdon, "Capability of high intrinsic quality Space Filling Design for global sensitivity analysis and metamodelling of interference optical systems", Chemometrics and Intelligent Laboratory Systems 113, 10-18, 2012.

[31] M. Born, E. Wolf, *Principles of optics*, Pergamon Press, London, 1980.

[32] H. A. Macleod, *Thin-film optical filters*, Adam Hilger, Bristol, 1986.

[33] O. Vasseur, M. Claeys-Bruno, M. Cathelinaud, M. Sergent, "High dimensional sensitivity analysis of complex optronic systems by experimental design: Applications to the case of the design and the robustness of optical coatings", Chin. Opt. Lett. 8 Supplement, 21-24, 2010.

[34] Package R 'Sensitivity', http://cran.r-project.org/, 2012.

[35] M.A.F. Martins, R. Requião, R.A. Kalid, "Generalized expressions of second and third order for the evaluation of standard measurement uncertainty", Measurement 44, 1526–1530, 2011.

[36] O. Vasseur, M. Cathelinaud, M. Claeys-Bruno, M. Sergent, "Global sensitivity analysis of bandpass and antireflection coatings manufacturing by numerical space filling designs", Applied Optics, C117-C123, 2011.

[37] O. Vasseur, M. Cathelinaud, "Investigation of manufacturing processes by numerical sensitivity analysis", Proc. of SPIE 8168, 81680A-1, 2011.

[38] M. Désenfant, P. Pernot, O. Vasseur, "Is there a link between correlation and interaction ?", 15ème Congrès International de Métrologie, Paris, 2011.

[39] C. Vassallo, *Théorie des guides d'ondes électromagnétiques*, Eyrolles, Paris, 1985.

[40] C. Vassallo, "Polarisation independent antireflection coatings for semiconductor optical amplifiers". Electron. Lett. 24, 61-62, 1988.

[41] C. Vassallo, *Optical waveguides concepts*, Elsevier, Amsterdam, 1991.

[42] O. Vasseur, *Calcul et réalisation de traitements optiques multicouches pour diodes laser. Etude de l'influence des défauts de structure des couches sur les performances des diodes traitées*, Ph. D. Thesis, Université d'Aix-Marseille III, 1990.

[43] F. Favre, D. Le Guen, "82 nm of continuous tunability for an external cavity semiconductor laser". Electron. Lett. 27, 183-184, 1991.

[44] P. Mascher, M. G. Boudreau, S. G. Wallace, J. R. Roscoe, S. Murugkar, G. Balcaitis, C. Wettlaufer, and H. K. Haugen, Optical coatings for improved semiconductor diode laser performance, Proc.-Electrochem. Soc. 98, 56-67, 1998.

[45] O. Vasseur, "Reflectivity of dielectric coatings deposited on the end facet of a weakly guiding fiber", J. Opt. Soc. Am. A 12, 77-83, 1998.

[46] H. Kihm and S.-W. Kim, "Oblique fiber optic diffraction interferometer for testing spherical mirrors", Opt. Eng. 44, 125601, 2006.

[47] V. Pervak, M. K. Trubetskov, and A. V. Tikhonravov, "Robust synthesis of dispersive mirrors", Opt. Express 19, 2371-2380, 2011.

[48] P. Bourdon, V. Jolivet, B. Bennai, L. Lombard, G. Canat, E. Pourtal, Y. Jaouën, O. Vasseur, "Coherent beam combining of fiber amplifier arrays and application to laser beam propagation through turbulent atmosphere", Proc. SPIE 6873, 687316, 2008.

[49] V. Jolivet, P. Bourdon, B. Bennaï, L. Lombard, D. Goular, E. Pourtal, G. Canat, Y. Jaouën, B. Moreau, O. Vasseur, "Beam shaping of single-mode and multimode fiber amplifier arrays for propagation through atmospheric turbulence", IEEE J. Sel. Topics Quantum Electron. 15, 257-268, 2009.

[50] B. Bennaï, *Mise en phase de lasers à fibre : Etude de l'influence de la turbulence atmosphérique et de l'utilisation de fibres faiblement multimodes*, Ph. D. Thesis, Télécom ParisTech, 2010.

[51] A. Azarian, P. Bourdon, L. Lombard, Y. Jaouën, O. Vasseur, "Orthogonal coded modulations for active coherent beam combination", communication acceptée à IEEE Photonics Conference 2012.

[52] L. Lombard, A. Azarian, K. Cadoret, P. Bourdon, D. Goular, G. Canat, V. Jolivet, Y. Jaouën, O. Vasseur, "Coherent beam combination of narrow linewidth 1.5µm fiber amplifiers in long pulse regime", Opt. Lett. 36, 523-525, 2011.

[53] L. Daniault, M. Hanna, D. N. Papadopoulos, Y. Zaouter, E. Mottay, F. Druon, P. Georges, "Passive coherent beam combining of two femtosecond fiber chirped-pulse amplifiers," Opt. Lett. 36, 4023-4025, 2011.

[54] A. Houard, M. Franco, B. Prade, A. Durécu, L. Lombard, P. Bourdon, O. Vasseur, B. Fleury, C. Robert, V. Michau, A. Couairon, and A. Mysyrowicz, "Femtosecond filamentation in turbulent air", Phys. Rev. A 78, 033804, 2008.

[55] B. Bennaï, P. Bourdon, V. Jolivet, L. Lombard, G. Canat, O. Vasseur, Y. Jaouën, "Coherent combining efficiency assessment for few-mode fibers with higher-order mode content", LEOS Annual Meeting Conference Proceedings, LEOS '09, 789-790, 2009.

[56] X. Wang, P. Zhou, H. Zhao, Y. Ma, X. Xu and Y. Zhao, "Coherent beam combining of high-order-mode fiber lasers with active phase control", J. Opt. 13, 015704, 2011.

[57] J. W. Goodman, "Some fundamental properties of speckle", J. Opt. Soc. Am. 66, 1145-1150, 1976.

[58] O. Vasseur, *L'image dans la technoscience : De son utilisation et de son influence dans les sciences appliquées*, Ph. D. Thesis, Université Toulouse 2, 2006.

[59] J. W. Goodman, *Speckle phenomena in optics : theory and applications*, Roberts and Company Publishers, 2006.

[60] J. Sorrentini, M. Zerrad, C. Amra, "Statistical signatures of random media and their correlation to polarization properties," Opt. Lett. 34, 2429-2431, 2009.

[61] O. Vasseur, I. Bergoënd, X. Orlik, "A Gaussian transition of an optical speckle field studied by the Minimal Spanning Tree method", Journal of the European Optical Society 5, 10052, 2010.

[62] O. Vasseur, I. Bergoënd, D. Upadhyay, X. Orlik, "The Minimum Spanning Tree method applied to the study of optical speckle fields: spatial characterization of a Gaussian transition and its phase singularities", Proc. of SPIE 8171, 81710B-1, 2011.

[63] H. A. Simon, "The Architecture of Complexity", Proceedings of the American Philosophical Society 106, 467-482, 1962.

[64] Philip Anderson, "Complexity Theory and Organization Science", Organization Science 10, 216-232, 1999.

[65] N. Ronald, V. Dignum, C. Jonker, T. Arentze, H. Timmermans, "On the engineering of agent-based simulations of social activities with social networks", Information and Software Technology 54, 625-638, 2012.

VII. Sélection de publications

Global sensitivity analyses of coherent beam combining of fiber amplifier arrays by the use of numerical space filling designs

Adrian Azarian*[a], Olivier Vasseur[a], Baya Bennaï[a], Laurent Lombard[a], Guillaume Canat[a], Véronique Jolivet[a], Yves Jaouën[b], Pierre Bourdon[a]
[a]Département d'optique théorique et appliquée, ONERA, The french aerospace lab, Chemin de la Hunière, 91761 Palaiseau, France;
[b]Telecom ParisTech, CNRS, UMR 5141, 46 Rue Barrault, 75634 Paris, France

ABSTRACT

We perform sensitivity analyses on two different array configurations of coherently combined fiber amplifiers to study the impact of residual phase errors onto the combining efficiency. The arrays studied are: a square of 16 fibers and a hexagon of 19 fibers. For the hexagon, two different shaped wavefronts are studied. In this method a global analysisis performed: we modify simultaneously all the phase errors using numerical space filling designs. Then, the construction of a metamodel makes it possible to investigate more precisely the role of each fiber and specially the role of interactions between fibers onto the combination with less runs than classical approaches. Results exhibit different behaviors and specially interactions between fibers with respect to the array configurations and with respect to the two different shaped wavefronts. Finally, we demonstrate that we can study arrays of more than 100 fibers.

Keywords: coherent combining, computer experiments, sensitivity analysis, fiber laser, phase errors

1. INTRODUCTION

High power is required to increase range and sensitivity in many applications. However, the ultimate power available by a single laser amplifying chain is limited by nonlinear effects and damage threshold [1-3], especially in the case, where the amplifying medium is a fiber. Coherent beam combining (CBC) of fiber lasers [4-6] is an efficient way of power scaling while maintaining good beam quality. In coherent beam combining, several lasers, operating at the same wavelength, are packaged together into an array. Relative phase differences between the elements of the array need to be precisely controlled in order to achieve constructive interferences between the waves, leading to the highest possible power density in the intensity pattern. Therefore it is crucial to know the sensitivity of the system towards phase differences between laser sources and the robustness towards deficient phase-locking of one or more fibers. In the case of an array with a large number of fibers (around 100), we can assume that the role of a single fiber has a little influence on the combining efficiency. Therefore, we can presume that the role of interactions between fibers or groups of fibers will be as important or more important than the role of a single fiber.

Despite the increasing power of computers over the past decade, classical approaches (like Monte-Carlo) to study systems with such a large number of parameters are still too time consuming. Moreover, these approaches do not permit to exhibit all the interactions between parameters. The use of numerical designs is an effective method to study the outputs of a system all over the domain of variation of the inputs, enabling metamodel construction and high dimensional code exploration by a limited number of code runs. In this communication, we apply this approach of using numerical designs to the case of coherent beam combining to exhibit the most critical fibers and interactions between fibers onto the combination.

In a first part, we explain our methodology and present its advantages compared to other methods. We also present the type of design chosen to perform our sensitivity analyses and the cases that we analyze: a square of 16 fibers and a hexagon of 19 fibers. Then, we present the results of our sensitivity analyses which show differences between the studied cases. We also present results on an array with 100 fibers. Finally we are able to conclude on the role of interactions between emitters and on the role of single fibers in a coherently combined array.

*adrian.azarian@onera.fr, phone: +33 180386421, www.onera.fr

Fiber Lasers VIII: Technology, Systems, and Applications, edited by Jay W. Dawson, Eric C. Honea,
Proc. of SPIE Vol. 7914, 79141G · © 2011 SPIE · CCC code: 0277-786X/11/$18 · doi: 10.1117/12.874727

2. DESCRIPTION OF THE SENSITIVITY ANALYZING METHOD

2.1 Overview of existing sensitivity methods

To obtain a high combining efficiency, the influence of phase errors needs to be determined. Various methods have been used by different authors [7-9] to determine the required phase accuracy. A numerical method is used to propagate the uncertainties of the phases at the output of the emitters onto the final result (Strehl ratio, size of the central lobe…). Even if this method does not explicitly calculate a standard deviation of the final result, it provides the largest acceptable phases uncertainty value. But in order to have a precise value of the final result standard deviation, when using a numerical approach, it is necessary to use a Monte-Carlo method. The issue of this method is the number of computer runs, which increases tremendously with the number of fibers in the array. Another method calculates the final result standard deviation analytically as a function of the standard deviations of the phases, as in [9]. However, these two methods do not provide interactions or synergies between specific fibers, and do not reveal the most critical fiber or interactions between fibers on the combining efficiency.

In order to assess these interactions, different methods have been developed in the field of statistics. In particular, response surface methodology, which explores the relationship between several "explanatory variables" (input of the system) and one or more "response variables" (output of the system). Within this methodology, the basic approach is to use a factorial design, as described in [10-11], which yields to information about the most important features of the problem studied. In our case however, due to the complexity of the CBC model, we cannot apply directly this methodology and need to build a surrogate model (or metamodel), which approximates the behavior of the simulation model and will exhibit the interactions. The surrogate model is constructed by computing the response of the simulator to a limited number of well chosen data points. In order to have the best point distribution (and therefore the most accurate metamodel), we use design of experiments called numerical space filling designs, which spread the computer runs evenly throughout the studied region.

2.2 Numerical space filling designs

In this subsection, we will develop the type of designs that we choose. As explained in the previous part, the point distribution in the design is a critical aspect of the sensitivity analysis quality. In order to illustrate our point, we will present different types of designs in 2 dimensions: 2 variables, x_1 and x_2, which can vary between 0 and 1.

To analyze the sensitivity of a system, the basic idea is to use a factorial design (figure 1.a), where the variables are changed one at the time. In this example, the variables take five different values. But in an n-dimensional space, the number of points of the design N is equal to $N = 5^n$. Therefore, to study a system with 100 variables, the number of points in the design is around $N = 5^{100} \approx 10^{70}$, so that it is impossible to use these designs in our case. Moreover, previous work from Franco et al. [12] showed that these kinds of designs are not well-suited for the analysis of system with a high number of variables and for the construction of metamodels. Indeed, if the projection of the design on a 2-dimensional subspace shows points alignments, the design is less effective if the code is a function of a linear combination of the two variables on which the design was projected.

To overcome the problem of point alignments, a space filling design (figure 1.b) should be used, where x1 and x2 can take any value and where the distribution of the points shows no alignments. A precise study of space filling designs can be found in [12]. Their intrinsic quality was characterized using a method to classify the designs in different groups and the authors demonstrate that designs with a quasi-periodical distribution are well suited for metamodel construction. These designs were also applied to the case of interference filters [13] and pointed out the interest of quasi-periodical point distributions. Finally, we will use these types of designs which have proven to be the best designs in the case of optical interference systems.

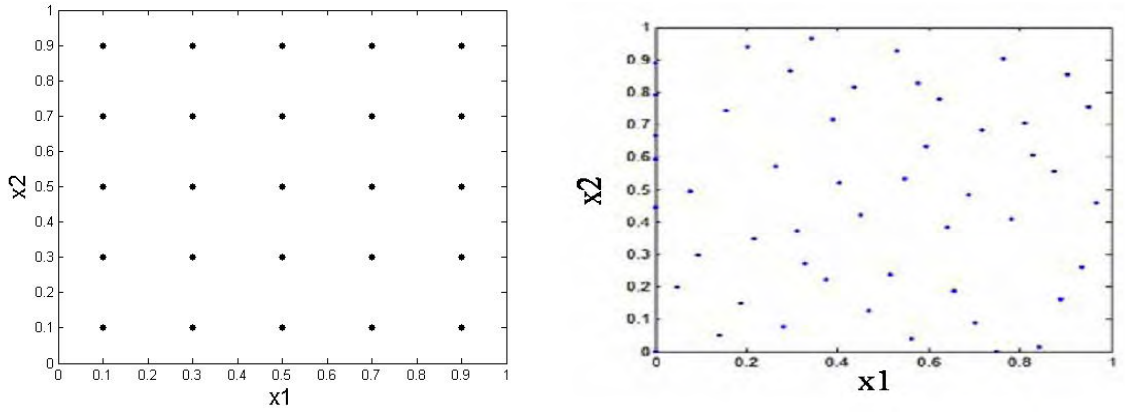

(a) (b)

Figure 1. (a): Example of a factorial design where the variables can take only 5 different values. (b): Example of a space-filling design.

2.3 Presentation of the arrays studied and metamodel construction

In this section we will discuss the model used to describe the coherent beam combination and present the 3 cases that will be studied.

Case 1: square array and associated far field when all the phases equal 0 on figure 2. Fill factor=29.5%, distance between fibers=0.003 meters.

Case 2: hexagonal array and associated far field when all the phases equal 0 on figure 3. Fill factor=19.2%, distance between fiber: horizontal=0.004 meters, diagonal=0.0045 meters.

Case 3: hexagonal array and associated far field of a hollow dark shaped wavefront (the phases of the fibers at the boarder are equal to π, and equal to 0 in the center) on figure 4. Fill factor=19.2%, distance between fibers: horizontal=0.004 meters, diagonal=0.0045 meters.

In all cases, the optical axes of lasers emitted from each array element are parallel to each other, meaning that there is no tilt error. Moreover, the optical power of the light emitted by each fiber is the same, meaning that there is no amplitude error. The far field is calculated by computing the Fourier transform of the near field:

$$I = \left| FT\left(\sum_n E_n(x,y) e^{i\varphi_n} \right) \right|^2 \tag{1}$$

where E_n is the near field with Gaussian shape of the fiber number n and φ_n is the associated phase at the output of the fiber. In this model, the criterion used to qualify the combination is the Mask Encircled Power (MEP), which is defined as the fraction of power contained in a fixed angular aperture with respect to the total amount of power (eq. 2). The aperture is indicated on the far field on figures 2, 3 and 4. In the case of an airy pattern, the domain defined for the MEP is a disk, and for the hollow dark beam, the domain is in-between two disks.

$$MEP = \frac{\iint_{aperture} I(x,y)\,dxdy}{\iint_{total} I(x,y)\,dxdy} \tag{2}$$

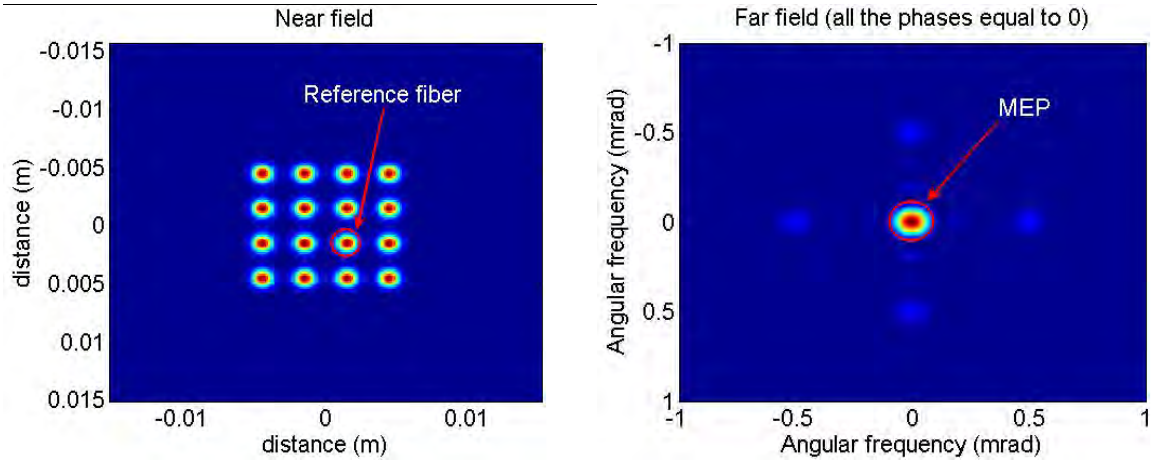

Figure 2. Case 1: Near field of a square array of 16 fibers and associated far field when all the phases are equal to 0. Normalized intensity (red=1, blue=0)

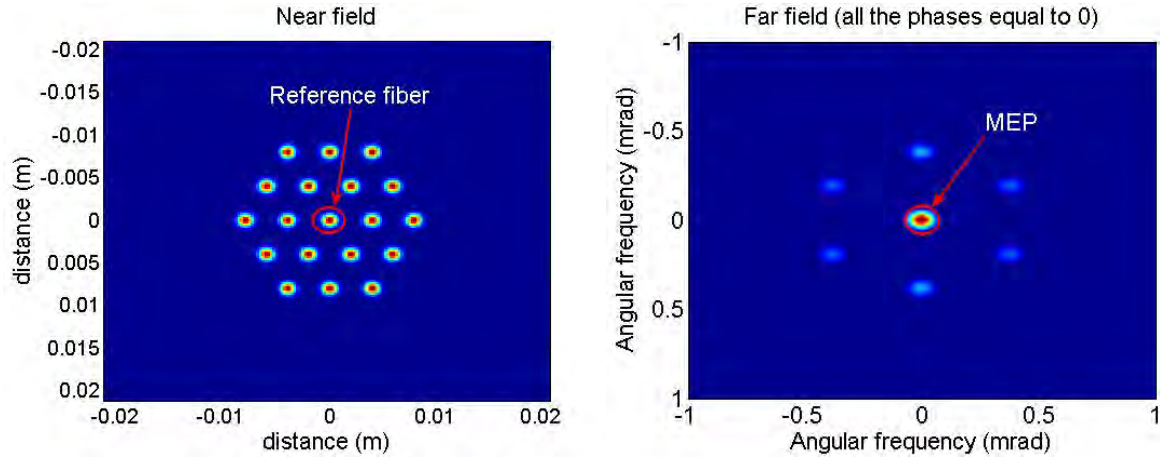

Figure 3. Case 2: Near field of a hexagonal array of 19 fibers and associated far field when all the phases are equal to 0. Normalized intensity (red=1, blue=0)

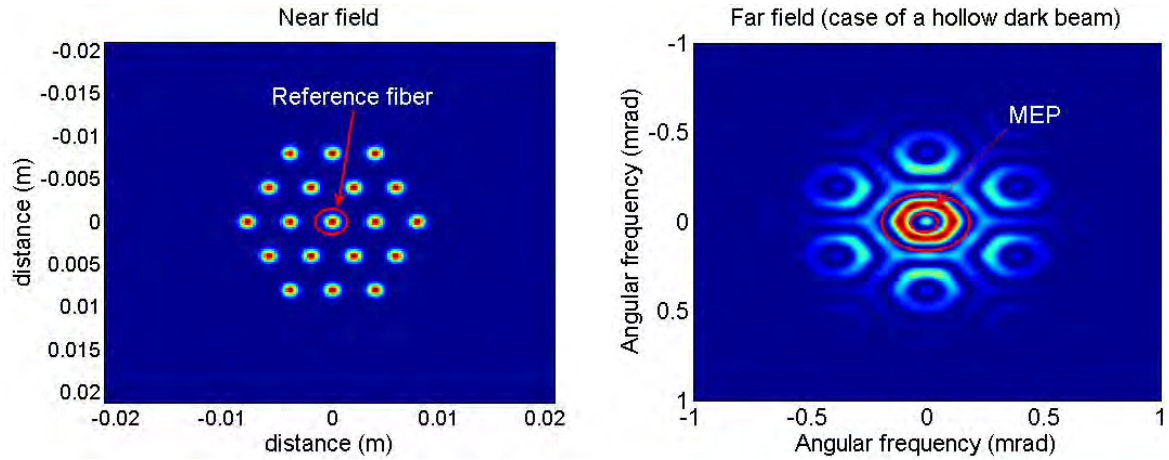

Figure 4. Case 3: Near field of a hexagonal array of 19 fibers and associated far field when the phases are equal to 0 in the center of the hexagon and π at the boarder, leading to a hollow dark beam. Normalized intensity (red=1, blue=0)

In order to simplify the analysis of the MEP model, we use a metamodel defined as a second order polynomial function defined by:

$$MEP = a_0 + \sum_{i=1}^{n} b_i \delta\varphi_i + \sum_{i=1}^{n} c_i \delta\varphi_i^2 + \sum_{1 \le i < j \le n} d_{ij} \delta\varphi_i \delta\varphi_j \quad (3)$$

The goal of the analysis is to compute and to compare the coefficients b_i, c_i and d_{ij} for the 3 cases.

This definition (eq. 3) requires that the MEP has only one maximum, which is insured by a reference fiber (shown on fig. 2, 3 and 4) which phase will be equal to 0. Indeed, the MEP is at its maximum when all the phases are equal (in case 1 and 2) and when the phases are equal in the center and that the phase difference between the center and the boarder is equal to π (in case 3). Therefore, fixing the value of one phase to 0 enables to have only one maximum. Note that the polynomial regression is thus made on the deviation of the phases $\delta\varphi$ with respect to the reference value 0 (or π in case 3).

It is then possible, just by analyzing the different coefficients of the polynomial function, to compare the different cases and to find out which fibers are more critical than others.

Here is a summary of the sensitivity analysis method:

1) Creation of a space filling design, where each point is a set of phases

2) Computation of the MEP using equation 1 and 2, while using the phases defined by the design

3) Making a polynomial regression on the previously calculated MEP

4) Analyzing the coefficients of the polynomial function

3. SENSITIVITY ANALYSES RESULTS

3.1 Results

We considered phase variations of $\pm\frac{\pi}{10}$. The regression has in each case a good quality with a determination coefficient R^2 greater than 0.95. Table 1 summarizes the results of the sensitivity analysis of the 3 cases. The fibers are numbered from 1 to 15 (case 1) and from 1 to 18 (case 2 and 3) from left to right and from the top to the bottom. For the interactions, only the interactions with fiber 1 are listed, because the behavior with any other fiber is the same. Figure 5 shows, as an example, the interactions in case 2.

With this description of the contribution of each fiber and interactions between fibers onto the MEP, we have now a good insight of the general behavior of these different cases. The square array has the simplest behavior, with an almost purely quadratic metamodel and no fiber is more critical than another. Thus, when designing a control-loop to correct the phases, no particular attention is needed, because every fiber has the same importance. Conversely, the hollow dark beam has a complex behavior and has to deal with high interactions. The fibers at the boarder of the hexagon are more critical on the combination. Thus, the design of the control-loop will have to take into account these critical fibers to enhance the combination process.

Table 1. Presentation of the most important coefficients.

	Most important coefficients	Remarks
Case 1	- the quadratic coefficients c_i have the same value and 10 times more than interactions d_{ij}	- linear coefficients negligible - interactions between closest neighbors. But small value compared to quadratic coefficients
Case 2	- c_5, c_6, c_9, c_{10}, c_{13}, c_{14} - $d_{1,2}$, $d_{1,4}$, $d_{1,5}$	- higher quadratic coefficients in the center of the hexagon - figure 5 shows the interactions between the fiber 1 (upper left) and the others and fiber 2 (upper center) and the others - a fiber interacts more with its closest neighbors
Case 3	- b_3, b_{16} - c_1, c_3, c_8, c_{11}, c_{16}, c_{18} - $d_{1,2}$, $d_{1,3}$, $d_{1,4}$, $d_{1,5}$, $d_{1,6}$, $d_{1,8}$, $d_{1,9}$	- higher quadratic coefficients at the boarder of the hexagon - some fibers do not interact at all

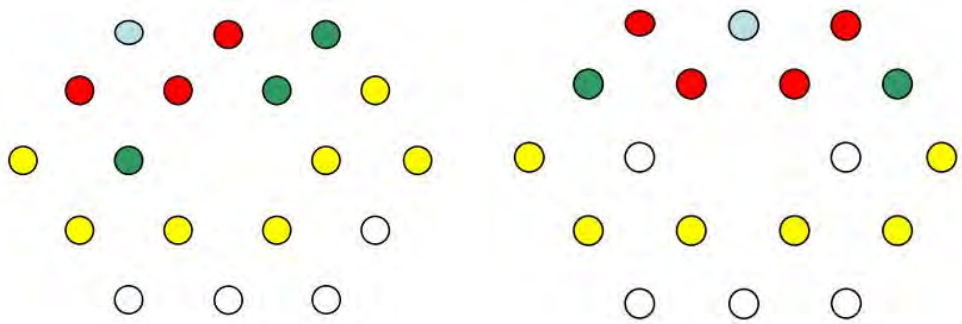

(a) (b)

Figure 5. Interactions between (a): fiber on the upper left and the others (b) fiber on the top center and the others. Red: high interactions. Green: 2-3 times less than red. Yellow: 6-10 times less than red. White: 50-60 times less than red.

3.2 Case of higher dimensions

We use the same of type of space filling designs to analyze a square of 100 and it will be compared with the previous results.

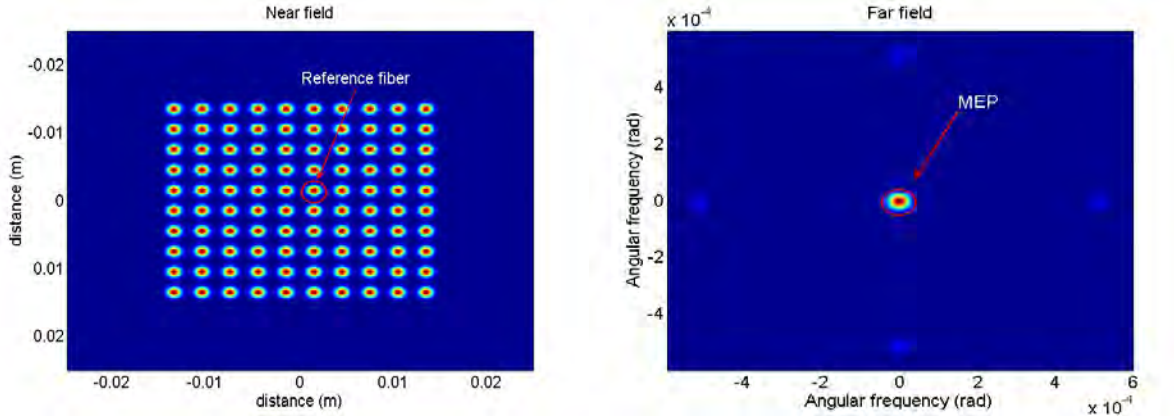

Figure 6. Near field of a square array of 100 fibers and associated far field when all the phases are equal to 0. Normalized intensity (red=1, blue=0).

The linear coefficients are negligible. The quadratic coefficients are dominant, and their values are 2 times higher in the center of the array than on the boarder. The interaction coefficients are around 10 times smaller than the quadratics. The general behaviour of this square is different than the square of 16 fibers: fibers in the centre are more critical than on the boarder of the square, but in both cases, interactions are not dominant.

4. CONCLUSION

In order to analyze the sensitivity of coherent beam combining to the phase noise, we proposed to use numerical space-filling designs to construct a metamodel, enabling us to exhibit the most critical interactions between phase errors at the output of the fibers. Different designs were analyzed and the design with the best point distribution was chosen. The constructed metamodel had in each case a good quality and pointed out that some interactions between fibers have the same importance as fibers alone, confirming the assumption made in the introduction. It also showed different behaviors of the system with respect to the geometrical arrangement of the array of fibers, and the shaped wavefront, leading to a better comprehension of the combination of beams and offering a guide for designing a control-loop to correct the phase errors. In addition, we demonstrate that our methodology can be used to study arrays of more than 100 fibers, while keeping a reasonable computational time.

It appears that the hollow dark beam, which can be of interest when delivering high power on a remote surface, has the most complex behavior and specially the most complex interactions. This wavefront will be complicated to manage in an experiment. The two other cases showed similar behaviors but, even though the hexagonal configuration is better with respect to the size of its central lobe, it also is more sensitive and has to deal with more complex interactions. Finally, the square array has the simplest behavior with an almost purely quadratic metamodel.

Further work will analyze more in detail cases with more than 100 fibers with different geometrical arrangements of the array, different wavefronts and also different criteria with propagation through turbulent atmosphere which will allow us to find the less sensitive configuration with the best combining efficiency.

REFERENCES

[1] Betts, R.A., Tjugiarto, T., Xue, Y.L. and Chu, P.L., “Nonlinear refractive index in erbium doped optical fiber: theory and experiment”, IEEE journal of quantum electronics, 27(4), 908-913 (1991).

[2] Dawson, J.W., Messerly, M.J., Beach, R.J., Shverdin, M.Y., Stappaerts, E.A., Sridharan, A.K., Pax, P.H., Heebner, J.E., Siders, C.W. and Barty, C.P.J., “Analysis of the scalability of diffraction-limited fiber lasers and amplifiers to high average power”, Optics express, 16(17), 13240-13266 (2008).

[3] Jaouën, Y., Canat, G., Grot, S. and Bordais, S., “Power limitation induced by nonlinear effects in pulsed high-power fiber amplifiers”, C.R. Physique, 7(2), 163-169 (2006).
[4] Shay, T.M., Benham, V., Lt. Spring, J., Capt. Ward, B., Ghebremichael, F., Culpepper, M.A., Sanchez, A.D., Baker, J.T., Sgt. Pilkington, D., Berdine, R., “Self-referenced locking of optical coherence by single-detector electronic-frequency tagging”, Proc. SPIE 6102, (2006).
[5] Jolivet, V., Bourdon, P., Bennaï, B., Lombard, L., Goular, G., Pourtal, E., Canat, G., Jaouën, Y., Moreau, B. and Vasseur, O., “Beam shaping of single-mode and multimode fiber amplifier arrays for propagating through atmospheric turbulence”, IEEE journal of selected topics of quantum electronics, 15(2), 257-268 (2009).
[6] Fan, T.Y., “Laser beam combining for high-power, high-radiance sources”, IEEE journal of selected topics of quantum electronics, 11(3), 567-577 (2005).
[7] Zhou, P., Chen, Z., Wang, X., Li, X., Liu, Z. and Xu, X., “Tolerance and tilt error for coherent combining of fiber lasers”, Chinese optics letters, 7(1), 39-42 (2009).
[8] Li, Y., Qian, L., Lu, D., Fan, D. and Wen, S., “Coherent and incoherent combining of fiber array with hexagonal ring distribution”, Optical Fiber Technology, 15(3), 226–232 (2009).
[9] Nabors, C.D., “Effects of phase errors on coherent emitter arrays”, Applied optics, 33(12), 2284-2289 (1994).
[10] Box, G.E., Hunter, J.S., and Hunter, W.G., [Statistics for Experimenters: Design, Innovation, and Discovery], 2nd Edition, Wiley, New-York (2005).
[11] Saltelli, A., Chan, K. and Scott, E.M., [Sensitivity analysis], Wiley, New-York (2000).
[12] Franco, J., Vasseur, O., Corre, B., Sergent, M., “Minimum spanning tree: a new approach to assess the quality of the design of computer experiments”, Chemometrics and intelligent laboratory systems, 97, 164-169 (2009).
[13] Vasseur, O., Clayes-Bruno, M. Cathelinaud, M. and Sergent, M., “High-dimensional sensitivity analysis of complex optronic systems by experimental design: application to the case of the designs and the robustness of optical coatings”, Chinese optics letters, 8(s1), 21-24 (2010).

Chemometrics and Intelligent Laboratory Systems 97 (2009) 164–169

Contents lists available at ScienceDirect

Chemometrics and Intelligent Laboratory Systems

journal homepage: www.elsevier.com/locate/chemolab

Minimum Spanning Tree: A new approach to assess the quality of the design of computer experiments

J. Franco [a,b,*], O. Vasseur [c], B. Corre [d], M. Sergent [e]

[a] Total EP/GSR/TG/G&I, CSTJF Avenue Larribau 64018 Pau Cedex, France
[b] Ecole des Mines de Saint-Etienne, Département 3MI, 42000 Saint-Etienne, France
[c] ONERA DOTA, Chemin de la Hunière, 97761 Palaiseau Cedex, France
[d] Total EP/GSR/COP/EM, CSTJF Avenue Larribau 64018 Pau Cedex, France
[e] Université Paul Cézanne Aix Marseille III, LMRE, 13397 Marseille Cedex 20, France

ARTICLE INFO

Article history:
Received 19 December 2007
Received in revised form 26 March 2009
Accepted 30 March 2009
Available online 6 April 2009

Keywords:
Computer experiments
Space-Filling Designs
Measures of uniformity
Minimum Spanning Tree

ABSTRACT

In the computer experiment setting, if the relationship between the response and inputs is unknown, then the purpose is to use designs that spread the points at which we observe the response evenly throughout the region. These designs are called Space-Filling Designs. Different measures or metrics quantify how a set of points is spread out. In this paper, we present two types of measures of uniformity: discrepancy and point-to-point measures which take into account the distances between the pairs of points. However these criteria of quantification do not permit the qualification of the distribution. Thus, we discuss a new approach to assess the quality of computer experiments. This approach is based on a graph constructed from the set of points of the experimental design. This graph, called Minimum Spanning Tree, allows us to deduce two parameters—the mean and the standard deviation of the edges length—which characterize the points distribution to be studied.

1. Introduction

Various industries use computer simulators instead of laboratory experiments to study complex phenomena (for example, oil production forecast). These codes become more and more realistic with a larger input data set. However, due to the complexity of the mathematical system underlying the computer simulation tools there are, unfortunately, often no explicit input–output formulas known. Although computer power has significantly increased during the last years, the evaluation of a particular setting of the design parameters may still be very time-consuming. In order to take advantage of this simulation, the simulator is often replaced by a *metamodel* or surrogate simulator (or proxy) to approximate the relationship between the code and the design parameters. These metamodels are built using *designs of experiments* that have a considerable effect on their accuracy. Since computation time and as the number of significant simulations is limited, the question regarding the set of experiments to evaluate becomes important.

With the exception of stochastic codes which implement a Monte-Carlo based method, computer experiments are determinist, i.e. they give the same response under the same conditions. In this context, the theory of experimental designs initiated by Fisher [3] is not necessarily appropriate and leads to both major changes.

Firstly, realistic simulation involves strong nonlinearities and/or non-parametric models. Secondly, a metamodel is constructed on data generated from a complex deterministic simulation in which the random variation that exists in the real systems is not represented. Therefore, there is little point in repeating an experiment under the same conditions since no new information is acquired.

In general, if the relationship between the response and inputs is not known, the purpose is to use designs that spread the points evenly throughout the region. These designs are called Space-Filling Designs (Chen [1]). The second requirement results from the observation that codes often depend only on a few influential variables, which may be either direct factors or 'principal components' composed of linear combinations of these variables. Therefore dealing only with these influential factors is sufficient and more efficient. Hence, it is desirable that the space-filling property should be also satisfied in the projection onto subspaces. Experimental designs with too regular structures with points lined, such as factorial designs, must be avoided because they have bad projective properties on subspaces. For instance, the experimental design represented on the Fig. 1 is reduced at 3 points instead of 9, if the code depends on the relation $X_1 + 3X_2$.

There are a number of ways to define what it means to spread points evenly throughout a space. In this paper, we present two types of measures of uniformity: discrepancy and point-to-point measures which take into account the distance between pairs of points. We will

* Corresponding author. Total EP/GSR/TG/G&I, CSTJF Avenue Larribau 64018 Pau Cedex, France.
E-mail address: jessica.franco@total.com (J. Franco).

0169-7439/$ – see front matter © 2009 Elsevier B.V. All rights reserved.
doi:10.1016/j.chemolab.2009.03.011

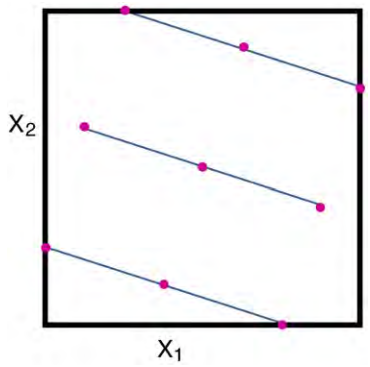

Fig. 1. Consequences of bad projective projections properties with a Latin Hypercube maximin.

point out that these criteria are insufficient to conclude about the uniform distribution of points. Furthermore, we have developed a new approach which is more informative than the above methods. It is based on the graph theory and called the Minimum Spanning Tree (MST). We will see in Section 2.2 that this approach allows the assessment of the quality of points repartition in multidimensional space and to sort out the different designs according to their structure: grid, random sample, agglomerates… For example with this measure, we can say if the experimental design is a good compromise between a random sampling and a factorial design. In Section 3, examples of MST applications within the setting of experimental designs are presented. Finally, we will conclude the paper with a brief discussion and further research.

2. Criteria of quality for point samples in hypercubes

2.1. Uniformity measures

There are a number of ways to define what spreading points evenly throughout a region means. We will briefly present two types:

- discrepancy comparing the point's distribution with respect to the uniform one.
- point-to-point uniformity measure determining how uniformly the points are distributed.

We will see that these measures cannot be studied separately to conclude about uniformity.

2.1.1. Discrepancy

The L_p discrepancy (Niederreiter [13]) is a measure of the difference between the empirical cumulative distribution function of an experimental design and the uniform cumulative distribution function. In other words, it is a measure of the non-uniformity of a design. The empirical distribution function $\hat{F}_N$ for N i.i.d. observations is obtained experimentally from the points of design and is defined as

$$\hat{F}_N(x) = \frac{1}{N}\sum_{i=1}^{N} I_{X_i \le x}$$

where $I_{X_i \le x}$ is the indicator function, equal to 1 if $X_i \le x$ and equal to 0 otherwise.

If we consider the empirical distribution function $\hat{F}_N$ of points $x_1,\ldots,x_N$, we can define the L_∞ discrepancy by $D_N(X) = \sup_{x\in[0,1]} |\hat{F}_N(x) - F_U(x)|$ with F_U the uniform distribution function on [0,1].

Remark. $D_N(X)$ is Kolmogorov–Smirnov statistic for testing fit to the uniform distribution.

Among L_p discrepancy, L_2 discrepancy is used most frequently since it can be expressed analytically and is much easier to compute (Hickernell [7]). A design is called uniform if it minimizes the discrepancy. Therefore, in order to conclude and to know if a design is uniform, we must compute discrepancy and compare this with other discrepancy's designs.

Moreover, discrepancy does not permit the measurements of the designs quality. Indeed, we do not want to only measure the uniformity but also how the points are spread throughout a region.

For example, if we calculate the L_∞ discrepancy of different designs in 2-D with the same number of points, then the factorial design has the highest discrepancy even if these points are, nevertheless, evenly spaced (cf. Table 1 and Fig. 2). The minimal discrepancy is naturally obtained by Halton sequence (Halton [5]). However, the weak discrepancy does not guarantee that the points are evenly spread.

2.1.2. Point-to-point measures

The purpose of these criteria, which are based on the distance between pairs of points (Gunzburger [4]), is to evaluate whether a design is close to a regular uniformed mesh.

We note dist(x_i , x_k) the Euclidean distance between the points x_i and x_k such as

$$\mathrm{dist}(x_i, x_k) = \left[\sum_{j=1}^{d} |x_{ij} - x_{kj}|^2\right]^{1/2}.$$

▪Coverage measure

Definition. Let $X=\{x_1,\ldots,x_N\} \subset [0,1]^d$ a set of N points, the coverage measure λ is defined by

$$\lambda = \frac{1}{\bar{\gamma}}\left(\frac{1}{N}\sum_{i=1}^{N} (\gamma_i - \bar{\gamma})^2\right)^{1/2}$$

with $\gamma_i = \min_{i \neq k} \mathrm{dist}(x_i, x_k)$ the minimal distance between a point and his nearest neighbour and $\bar{\gamma} = \frac{1}{N}\sum_{i=1}^{N} \gamma_i$ the mean of the γ^i.

For a regular mesh, $\gamma_1 = \cdots = \gamma_N = \bar{\gamma}$ so that $\lambda = 0$. Thus, the weaker the λ is, the closer the points are to the regular mesh.

▪The mesh ratio

We consider the ratio between the maximum distance of a point to its nearest neighbour and the minimum distance of a point to its nearest neighbour.

Definition. Let $X=\{x_1,\ldots,x_N\} \subset [0,1]^d$ a set of N points, the mesh ratio R is given by

$$R = \frac{\max_{i=1,\ldots,N} \gamma_i}{\min_{i=1,\ldots,N} \gamma_i}$$

with $\gamma_i = \min_{i \neq k} d(x_i, x_k)$.

For a regular mesh, $\gamma_1 = \cdots = \gamma_N$ so that $R = 1$. Thus, the smaller R is, the more regular the mesh is.

▪ Maximin and Minimax distance

Johnson et al. [8] were first to formally define the concepts of *maximin* and *minimax* distance which are described below and which enable to generate Space-Filling Designs.

Table 1
The L_∞ discrepancy for three types of designs: random sampling, Halton sequence, factorial design with $N = 16$, 25, 36 and 49 in 2D.

	Random sampling	Halton sequence	Factorial design
$N=16$	0.34	0.17	0.44
$N=25$	0.21	0.14	0.36
$N=36$	0.20	0.10	0.31
$N=49$	0.16	0.08	0.27

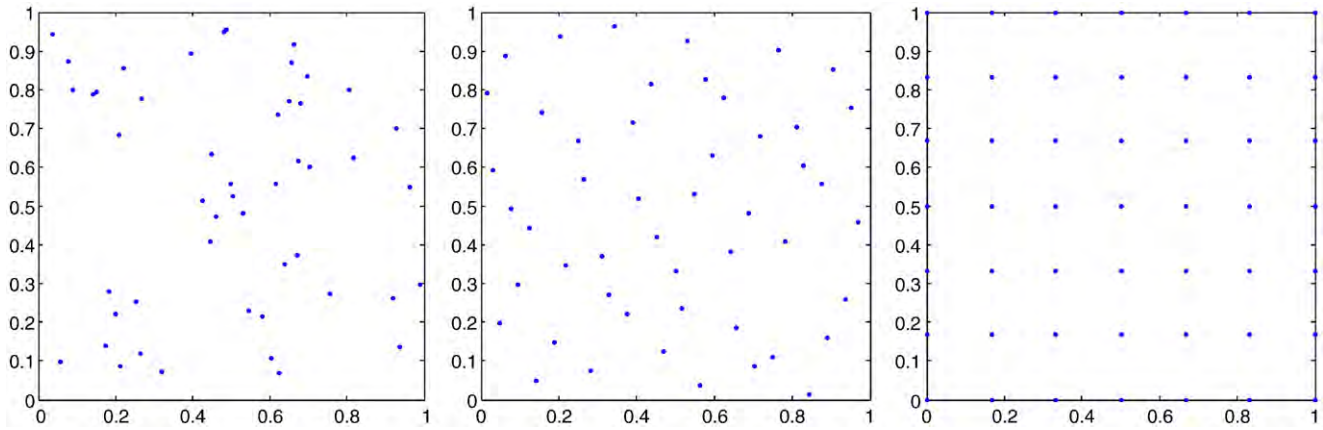

Fig. 2. From left to right. Illustration of random sampling, Halton sequence and factorial design with $N=49$ in 2 dimension studied above.

Definition (Chen [1]). We define the criterion by

$$\text{MINDIST} = \min_{x_i \in X} \min_{\substack{x_k \in X \\ i \neq k}} d(x_i, x_k)$$

where $X=\{x_1,\ldots,x_N\} \subset [0,1]^d$ is a set of N points.

This measure is equivalent to the smallest distance between two points.

Maximin distance seeks to maximize the minimum distance between any pair of points, i.e. MINDIST. A higher MINDIST should correspond to a more regular scattering of design points.

Definition. We define the criterion by

$$\text{MAXDIST}(D,X) = \sup_{x_i \in D} \min_{x_k \in X} d(x_i, x_k)$$

where D is a set of points that belongs to experimental region and $X=\{x_1,\ldots,x_N\} \subset [0,1]^d$ is a set of N points.

Minimax distance seeks to minimize the maximum distance between non design points and the nearest neighbour design point i.e. MAXDIST. Generally, D is a regular grid where this is not always possible in particularly in large dimension.

Remark. These criteria are equivalent except for *MAXDIST*.

Calculating these criteria for different designs of the above example (Table 1 and Fig. 2).

Of course, the best results are obtained by factorial designs (Table 2).

Remark. The set of points D can play a role on MAXDIST. For example, a factorial design at 3 levels involves MAXDIST = 0.16, whereas a factorial design at 6 levels involves MAXDIST = 0. This result is not generally true for designs other than grids.

Conclusion. It is necessary to consider these two types of criteria in order to determine the quality of experimental design. However, these criteria are specifically in order to compare designs and not to qualify designs. This is why, in the next section, we introduce a criterion which can qualify the point distribution of a design by taking into account both, uniform distribution and filling up the space.

Table 2
Point-to-point criteria for three designs: random sampling, Halton sequence and factorial design with $N=16$, 25, 36 and 49 in 2D.

	Random sampling				Halton sequence				Factorial design			
	λ	*R*	Mind	Max*d*	λ	*R*	Mind	Max*d*	λ	*R*	Mind	Max*d*
$N=16$	0.49	7.51	0.04	0.40	0.18	1.81	0.16	0.35	0	1	0.33	0.26
$N=25$	0.45	5.48	0.04	0.34	0.17	1.80	0.12	0.27	0	1	0.25	0
$N=36$	0.53	15.23	0.02	0.24	0.19	2.06	0.10	0.17	0	1	0.20	0.14
$N=49$	0.54	17.76	0.01	0.28	0.22	2.81	0.05	0.17	0	1	0.17	0

2.2. Methods to analyze the topology (spatial relationships) of set objects

We seek to quantify a distribution of points in multidimensional space by two parameters which allow various experimental designs to be distinguished beyond a qualitative analysis, generally amounting to the value of a criterion.

There are many methods to analyze the topology of set objects. We shall quote the most common:

- Statistics methods
- Distance function
- Statistical geometry

We do not rely on the two first methods which go back to using the distance criteria and discrepancy described above, but also notions of probability, volumetric uniformity measures, distance distribution function between one point and its nearest neighbours, or covariance distribution function estimation and/or anisotropy. With regard to this last point, the variogram techniques used by geostatisticians will be considered.

We focus on geometric algorithms, and a method based on a graph which is called the Minimum Spanning Tree.

2.2.1. Geometric algorithms

The algorithmic geometry uses a wide variety of methods based on the partition of space. This leads to a characterisation for each point the influence zone and the relation with its neighbours.

Probably the best technique known is the Voronoï diagram, a collection of geometrics objects based on a partition of space into cells, each of which consists of the points closer to one particular object than to any others. This method allows to obtain characteristic values, such as:

- Measures (area, volume, perimeter…) of each area influence,
- Form factors,
- First statistical moments
- etc.

There are many methods on this topic, e.g. the Delaunay graph. The Delaunay triangulation is a triangulation of the convex hull of the points in the diagram in which every circumcircle of a triangle is an empty circle. It is the dual graph of the Voronoï diagram. In the same way, this triangulation can be characterized by the length of each edge and the number of neighbours, but also statistical moments….

We can also mention:

- Gabriel graph
- Relative neighbourhood graph

- ...
- and Minimum Spanning Tree interesting us.

2.2.2. Basic concepts on graph theory

Some basic definitions.

A *simple graph* $G(V,E)$ can be thought of as a set of vertices (nodes) $V=\{v_1, v_2, \ldots, v_n\}$ and set E unordered pairs of distinct elements of V called edges with a number called weight (in this paper Euclidean distance) assigned to each edge.

A *path* is a sequence $\mu=(u_1, u_2,\ldots, u_q)$ of consecutive edges in a graph and the length of the path is the number of edges crossed.

A graph is *connected* if there is a path connecting every pair of vertices.

A *tree* is a simple graph connected without a cycle.

A *Minimum Spanning Tree (MST)* is a tree which contains all of the nodes and where the sum of the weights of the edges is minimal. Depending on the starting point, there may be more than one MST for a given set of points, but all the MSTs have the same edge-length histogram (Zahn [18] and Dussert [2]), where the edge length considered here is the Euclidean distance (Fig. 3).

2.2.3. MST properties

Consider a set of N points which are randomly distributed with uniformed intensity in a d-dimensional region with a volume of V.

Hammersley et al. [6] were the first to show that the expected length of each connection in the MST constructed for a Poisson process tends, when $N\to\infty$, to:

$$L_{G_\infty} = \alpha_d \left(VN^{d-1}\right)^{1/d}$$

where α_d depends on the dimension d and the problem solved.

If $d=2$, then:

$$L_{G_\infty} = \alpha_2 (VN)^{1/2}$$

And the mean length is given by:

$$M_A = \alpha_2 \frac{(VN)^{1/2}}{N-1}$$

We can also calculate:

- Mean μ and the standard deviation σ of the edges length may be used as characteristics for the corresponding distribution

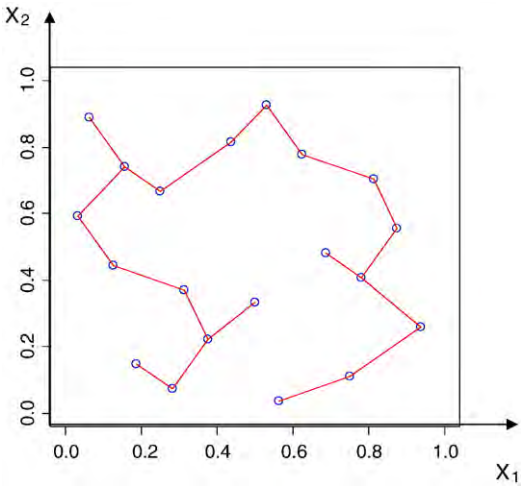

Fig. 3. The Minimum Spanning Tree.

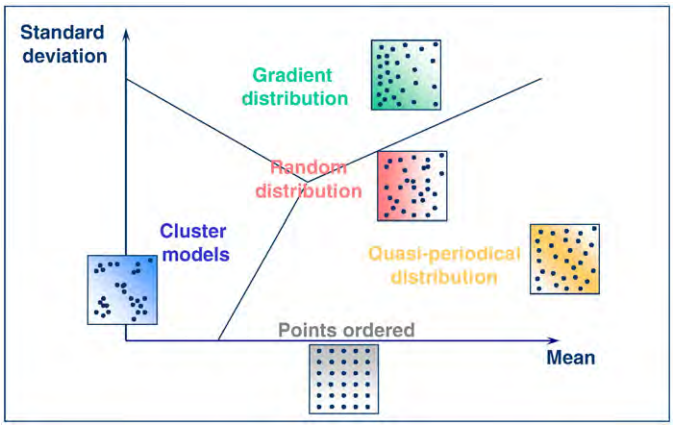

Fig. 4. Characterization of distributions in the (μ,σ) plane.

- But also edge-length histogram, higher-order statistical moments and quantiles,
- Distribution of the angles between edges and a given axis, which is a measurement of the anisotropy of the distribution of points in the space,
- etc.

2.2.4. Application and discussions

Algorithms, as those by Kruskal [10] or Prim [14], allow to calculate the MST. In these algorithms, the MST is grown from a single node by adding the closest node to current tree at each stage along with the edge corresponding to that closest distance. Depending on the starting point there may be more than one MST for a given set of points, but all of the MST's have the same length-edge histogram. It follows the statistical information deduced from the histogram, such as its first two moments: the average and the standard deviation.

In the (μ,σ) plane, all distribution of points can be plotted and easily compared with well-characterized distributions (for example, perfectly ordered or random ones) as shows the Fig. 4.

In plotting the mean and the standard deviation, it is possible to repair the location of experimental designs in this plane. For example, the area corresponding to a relatively high average and a low standard deviation is the area of "points ordered". To check this, it is easy to see that the Minimum Spanning Tree of a factorial design (*cf.* Fig. 5) provides a specific value of mean because the points are regularly spaced and a standard deviation equal to zero because all the edges have the same length. With this plane, it is possible to distinguish different areas such as cluster distributions with a low mean but also the random distributions with a mean and a standard deviation between these cluster designs and points ordered. The quasi-periodical distributions are so a good compromise (low standard deviation but

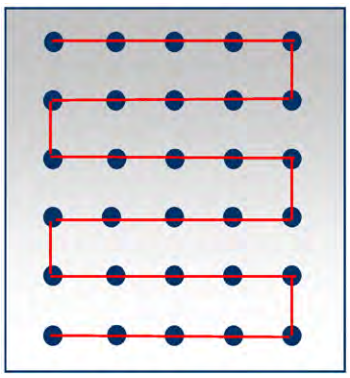

Fig. 5. A Minimum Spanning Tree of a factorial design.

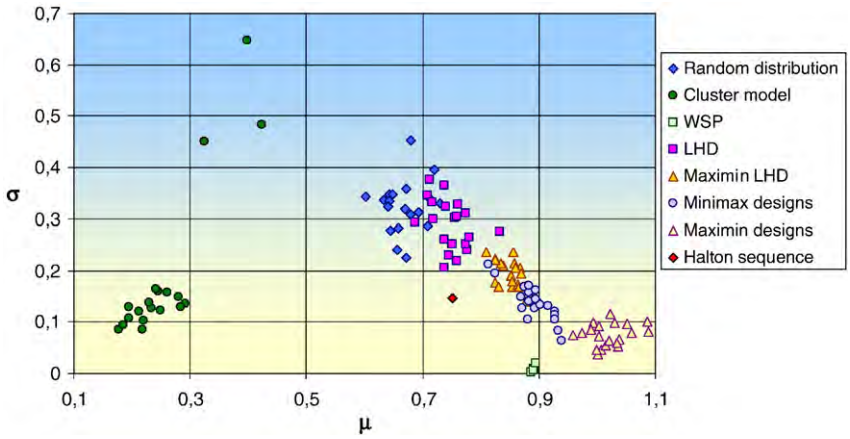

Fig. 6. Representation of the average and standard deviation of the edge length for the various designs with 20 points in 2-D.

non zero and high mean) between random distributions and points ordered where there will be bad projective properties.

Wallet and Dussert [17] have tested the five most used methods of topographical analysis (nearest neighbour distribution, radial distribution, Voronoï paving, quadratic count and Minimum Spanning Tree graph). This comparison highlighted that the method using the MST (mean μ and standard deviation σ of the edges length) involved the smallest standard deviation for every point's distribution tested (random point process, hard disks model and cluster models) and offers the best discrimination power and stability.

The use of two distinct parameters, namely μ and σ, leads to a more informative two-dimensional classification which then allows for a comparison of distributions by taking a simple reading in the (μ,σ) plane. Moreover, it is possible to use others parameters such as histogram, angles distribution, which has allowed for us to use this criterion to study Space-Filling Designs.

3. Applications of criterion based on MST on Space-Filling Designs

The purpose of these applications is to illustrate the theory presented above and to show the efficiency of this criterion for experimental designs in dimensions greater than 2, in the case where we do not know the theoretical values of the average edge length and standard deviation for the uniform random distribution.

The experimental designs studied here are:

- Latin Hypercubes Designs (LHD) (Mc Kay et al. [11]) and LHD maximin which are the designs the most commonly used in computer experiments
- WSP Designs (Sergent [15] and Sergent et al. [16])
- Minimax designs (Johnson et al. [8])
- Halton sequences (Halton [5])
- Maximin designs (Johnson et al. [8])

These designs are compared with a uniformed random distribution and with cluster models built using the Neyman and Scott [12] process.

For each type of experimental designs, 20 of these have been simulated in order to confirm the results. Designs of experiments tested here have 10 points for each dimension in order to take place in the setting of computer experiments.

Remark. As noted above, the theoretical results presented are asymptotic. This is why the obtained results have been verified.

In 2-dimension. The corresponding values of uniform random distribution, namely $\mu = 0.662$ and $\sigma = 0.311$ (Dussert et al. [2]), have been corroborated by Monte Carlo simulations of random distributions generated using the linear congruential method (Knuth [9]).

It is a must that the required experimental designs are to be in quasi-periodical distribution area (cf. Fig. 4) which is the best compromise between discrepancy (uniform distribution) and point-to-point measures (filling up the space).

Fig. 6 shows that LHDs are not the quasi-periodicals region of (μ,σ) plane. Although the points in such design have projections that are evenly spread out over the values of each variable input separately, we would not regard them as evenly spread out over the entire unit square. The maximin distance applied to LHDs allows improving

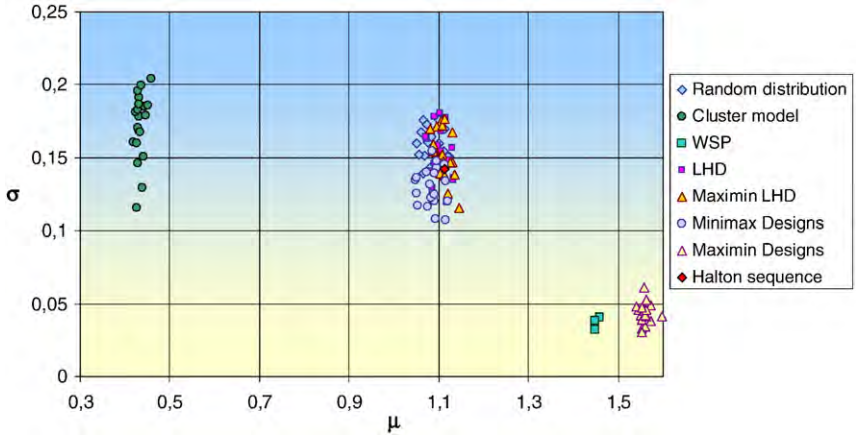

Fig. 7. Representation of the average and standard deviation of the edge length for the various designs with 100 points in 10-D.

the uniformity over the entire unit square. The minimax designs are interesting because they are not $\sigma \neq 0$ and a mean of the edges length equivalent to WSP designs appear as very regular.

Fig. 7 shows the incapacity of minimax designs to fill the space in high dimension.

The LHDs, whatever they are, do not have good properties for space-filling in high dimension because the excess of constraints would make them closer to their random sampling, as is often the case. Only the WSP designs are robust.

4. Conclusions and further research

A new approach to the qualification for Space-Filling Designs based on Minimum Spanning Tree has been studied. The sorting and qualifying of any distribution using cartography, with an average edge length and standard deviation for the corresponding distribution, is permitted due to the criterion.

The (μ,σ) plane is partitioned in three areas allowing us to disconnect models:

- cluster
- gradients
- random
- quasi-periodicals
- perfectly ordered

The further works will focus on the study of the robustness of various Space-Filling Designs in high dimension, and to discuss from which dimension it becomes difficult to have points distributed evenly in the space and, at times, on the margins of 1-dimension.

References

[1] V.C.P. Chen, K.L. Tsui, R.R. Barton, J.K. Allen, A review of design and modeling in computer experiments, Handb. Stat. 22 (2003) 231–261.
[2] C. Dussert, G. Rasigni, M. Rasigni, J. Palmari, Minimal spanning tree: a new approach for studying order and disorder, Phys. Rev., B 34 (5) (1986) 3528–3531.
[3] R.A. Fisher, The arrangement of field experiments, J. Minist. Agric. 33 (1926) 503–513.
[4] M. Gunzburger, J. Burkardt, Uniformity measures for point samples in hypercubes, www.csit.fsu.edu/~burkardt/pdf/ptmeas.pdf.
[5] J.H. Halton, On the efficiency of certain quasi-random sequences of points in evaluating multi-dimensional integrals, Numer. Math. 2 (1960) 84–90.
[6] J.M. Hammersley, J.H. Halton, J. Bearwood, The shortest path through many points, Camb. Philos. Soc. Proc. 55 (1959) 299–327.
[7] F.J. Hickernell, A generalized discrepancy and quadrature error bound, Math. Comp. 67 (1998) 299–322.
[8] M.E. Johnson, L.M. Moore, D. Ylvisaker, Minimax and maximin distance designs, J. Statist. Plann. Inference 26 (1990) 131–148.
[9] D.E. Knuth, The Art of Computer Programming, vol. 2, Addison-Wesley, New-York, 1969.
[10] J.B. Kruskal, On the shortest spanning subtree of a graph and travelling salesman problem, Proc. Am. Math. Soc. 7 (1956) 48–50.
[11] M.D. Mc Kay, R.J. Beckman, W.J. Conover, A comparison of three methods for selecting values of input variables in the analysis of output from a computer code, Technometrics 21 (1979) 239–245.
[12] J. Neyman, E.L. Scott, Statistical approach to problems of cosmology, J.R. Stat. Soc. B 20 (1958) 1–43.
[13] H. Niederreiter, Point sets and sequences with small discrepancy, Monasth. Math. 104 (1987) 273–337.
[14] R.C. Prim, Shortest connection networks and some generalizations, Bell Syst. Tech. J. 36 (1957) 1389–1401.
[15] M. Sergent, Contribution de la Méthodologie de la Recherche Expérimentale à l'élaboration de matrices uniformes: Application aux effets de solvants et de substituants, Ph D Thesis, 1989, Université Aix Marseille III.
[16] M. Sergent, R. Phan-Tan-Luu, J. Elguero, Statistical analysis of solvent scales. Part 1, An. Quim. Int. Ed. 93 (1997) 3–6.
[17] F. Wallet, C. Dussert, Comparison of spatial point patterns and processes characterization methods, Europhys. Lett. 42 (1998) 493–498.
[18] C. Zhan, Graph-theoretical methods for detecting and describing gestalt clusters, IEEE Trans. Comput. C-20 (1) (1971).

Chemometrics and Intelligent Laboratory Systems 113 (2012) 10–18

Contents lists available at ScienceDirect

Chemometrics and Intelligent Laboratory Systems

journal homepage: www.elsevier.com/locate/chemolab

Capability of high intrinsic quality Space Filling Design for global sensitivity analysis and metamodelling of interference optical systems

O. Vasseur *, A. Azarian, V. Jolivet, P. Bourdon

Onera - The French Aerospace Lab, F-97761 Palaiseau, France

ARTICLE INFO

Article history:
Received 4 February 2011
Received in revised form 9 May 2011
Accepted 10 May 2011
Available online 16 May 2011

Keywords:
Computer experiments
Space-Filling Designs
Minimum Spanning Tree
Minimal Spanning Tree
Thin film coatings
Optical filter
Sensitivity analysis
Complex systems

ABSTRACT

In the field of computer experiments, when the relations between the outputs and the inputs of the computer code are complex, the Space Filling Designs (SFD) are used to study the outputs all over the domain or to build metamodels. It is necessary that the points of these designs are distributed as uniformly as possible in the domain of interest. The methodology of Minimum Spanning Tree (MST) was proposed to evaluate the quality of the distribution of the points of an experimental design in a multidimensional space. We introduce here the results obtained in high dimensional case (dimension higher than 20) and we point out the bad quality of the classical designs or the designs based on low discrepancy sequences but mainly the advantages of WSP designs. Empirical results point out the need to qualify SFD in the original space due to the insufficiency of the conclusions obtained using projections onto 2D subspaces. We define the intrinsic quality of SFD as the characteristic of the distribution of the points in the space. Likewise, the extrinsic quality of SFD describes the performances of the results obtained by the use of SFD on an application case. The results obtained with different SFD in the case of interference optical system sensitivity analysis are presented. Finally, the intrinsic quality of SFD is assessed by MST criterion and is proved to be in accordance with the results of the interference optical system sensitivity analysis. So, this study can be considered as an empirical step to connect intrinsic quality and extrinsic quality of SFD designs.

1. Introduction

In the field of computer experiments, models or simulations of complex phenomena is getting more and more realistic. Although computer power has highly increased over the last years, models or simulations including numerous parameters, are still very time consuming. The use of numerical designs is an effective method to explore codes with a high dimensional space of parameters and to build metamodels, which approximate the code and the relationship between inputs and outputs of this code. Due to the computation time of the original model or simulator, the number of runs for building the metamodel must be limited and the set of computer experiments must provide the maximum of information of the code. In general, when the relationship between the response and inputs of the code is not explicit, the purpose is to use designs that uniformly spread the points all over the domain. These designs are called Space-Filling Designs (SFD).

In the case of the dimension of the input parameter space less than 10, Franco et al.[9] pointed out that classical criteria are insufficient to conclude about the uniform distribution of points and proposed to use Minimum Spanning Tree (MST) (Beardwood et al.[4]) criterion, which is more informative than the classical methods. Indeed, Dussert et al. [6] showed that the construction of a MST on a set of points in dimension 2 allows to qualify the distribution of the points (ordered, random, cluster…) and Wallet et al.[39] compared the five most used methods of topographical analysis (nearest neighbour distribution, radial distribution, Voronoï paving, quadratic count and minimal spanning tree graph) to conclude that the method using the MST offers the best discrimination power and stability. By the use of MST criterion, Franco et al.[9] pointed out that the designs which uniformly spread the points all over the domain belong to the quasi-regular distributions. So, we define the intrinsic quality of SFD as the characteristic of the distribution of the points in the space and a good intrinsic quality corresponds to a quasi-regular point distribution.

We firstly summarize the MST methodology and we expose the first intrinsic qualification of SFD designs in the case of high dimension space ($\dim \geq 20$). Using additional results obtained by projections onto 2-D subspaces, we point out the complementarities of MST methodology and the Radial Scanning Statistic (RSS) (Roustant et al.[27]) on a first hand and the need to analyse the SFD designs in the original space to qualify them precisely on the second hand.

In a second part, we apply the different designs which have been sorted by the MST criterion to the study of sensitivity analyses (Saltelli et al.[28]) and metamodels of interference optical systems. By this way, we define the extrinsic quality of SFD which describes the performances of the results obtained by the use of SFD on an application case. These empirical results on applications cases confirm the intrinsic quality of the designs determined by the MST criterion.

* Corresponding author. Tel.: +33 0 1 80 38 63 53; fax: +33 0 1 80 38 63 45.
E-mail address: Olivier.Vasseur@onera.fr (O. Vasseur).

0169-7439/$ – see front matter © 2011 Elsevier B.V. All rights reserved.
doi:10.1016/j.chemolab.2011.05.008

2. Intrinsic quality analysis of high dimensional numerical designs "Space Filling Designs" by minimal spanning tree

2.1. MST methodology

Consider a set of N points which are randomly distributed in a d-dimensional region with a volume of V. An edge-weighted linear graph $G=(X,E)$ is composed of a set of points $X=\{x_1, x_2, \ldots x_N\}$ called nodes and a set of node pairs $E=\{(x_i, x_j)\}$ called edges, with a number called weight (the Euclidean distance in our case) assigned to each edge. A graph is connected if there is a path connecting every pair of nodes and a tree is a connected graph without closed loops. A Minimal Spanning Tree (MST) is a tree which contains all the nodes with a minimal sum of the edge weights (Zhan [40]). It can be noticed that for a set of N points (corresponding to a number of edges of $N-1$) which are randomly distributed d-dimensional region, the total length of the MST is asymptotically given by $L_{G_\infty}=\alpha_d(VN^{d-1})^{1/d}$ where α_d depends on the problem solved (Beardwood et al.[4]). So the mean length of an edge is given by:

$$M=\alpha_d\frac{(VN)^{1/2}}{N-1} \quad (1)$$

In our study, the points of all designs are generated in the domain $[0;1]^d$ and the normalized values of m and σ of the MST (mean m and the standard deviation σ of the edge length) constructed from a given set of data in our case are obtained by dividing the original lengths by the expression following the normalization process proposed by Hoffman and Jain [12]:

$$\frac{N^{(d-1)/d}}{N-1} \quad (2)$$

Algorithms, as those by Kruskal [17] or Prim [26], allow calculating the MST. In Prim's algorithm, the MST is grown from a single node by adding the closest node to current tree at each stage along with the edge corresponding to that closest distance. Depending on the starting point there may be more than one MST for a given set of points, but all of the MST's have the same length-edge histogram (Zahn [40], Dussert et al.[6]). The normalized values of the mean m and the standard deviation σ of the edge length can be used to characterize the distribution of points (ordered, random, cluster…) (Dussert et al.[6]) as shown on the Fig. 1. In the field of topographical analysis, this method presents the advantages of a high discrimination power and stability to characterize spatial point patterns (Wallet et al.[39]).

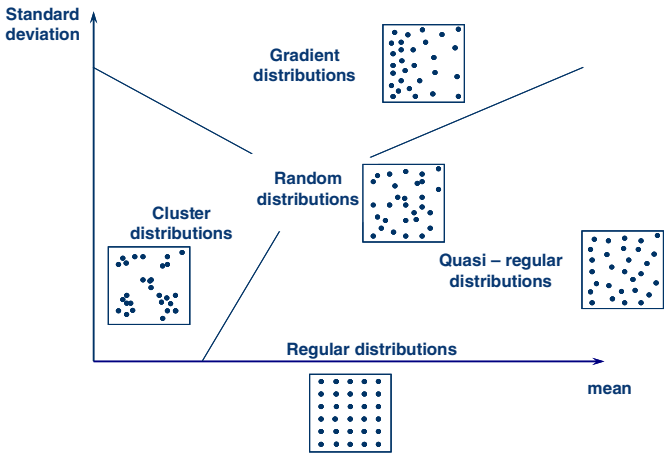

Fig. 1. Points distributions in the (m, σ) plane.

From the MST, the mean m and the standard deviation σ of the edges length may be used as characteristics for the corresponding distribution of the SFD points. On this graphical representation, it is possible to distinguish different areas and mainly the quasi-regular area which is the best area for Space Filling Designs due to the best compromise between a high average length of MST branches to fill the space and a small standard deviation to obtain a sufficient regularity: for example random designs have points too closed and grid designs ($\sigma=0$) are too regular. Moreover with perfect ordered structure ($\sigma=0$), the points are not evenly spread across the projection of the experimental space onto all subspaces (Franco et al.[9]).

2.2. Qualification of SFD in high dimensional spaces

The quality of a large part of numerical designs in dimensions less than 10 was presented by Franco et al.[9]: in this case, all the designs are located in the quasi-periodic area when the space dimension is lower than 5 but only WSP designs offer a good robustness. We present here the results obtained in higher dimension case (20-D).

The experimental designs studied here are:

- Latin Hypercube Design (LHD) (Mc Kay et al. [22])
- WSP design (Sergent et al.[30]). The aim of this algorithm is to find, among a set of possible points, a subset of points situated according to a uniform disposition. The points are selected such as they must be at a minimal distance of every point already included in the design and as near as possible to the center of gravity of the included points.
- Low Discrepancy Sequences (LDS): Faure [8], Halton [11], Sobol [32]
- LDS wrap-around design (Marrel [23])

The LHD and LDS designs are built with the lhs, fOptions and DiceDesign packages in R-software [13,14].

All the designs are compared with a random distribution and with cluster arrangements built using the Neyman and Scott [24] process. In dimension 20 the LHDs, LDS wrap-around sequences and Sobol's design are very close to the random area (cf. Fig. 2). The quality of LDS wrap around sequences does not differ than the other LHD and LDS designs so we will neither study them nor apply them on our application cases.

The other classical LDS (except Sobol) have a particular representation in the (m, σ) plane. The histogram analysis of the edge lengths of the MST explains the high values of the standard deviation. For example, the Faure sequence produces a MST whose values of edge lengths are distributed on two values: ~0.35 and ~1.38. Criticisms relating to the LDS designs often underlined the specific characteristics obtained by projections of the points on subspaces (Tan [34]). The insufficiencies of these LDS designs are here highlighted independently of any projection, the MST being built directly on the points of the original space.

The classical space-filling designs that had good properties (quasi-regular distribution) in low dimension are no more in the quasi-regular area, and are, in the best case, closed to the random distribution area as Sobol design.

Only the WSP designs have simultaneously a higher average length of branch and a lower standard deviation than those of the random designs and correspond to the characteristics of the quasi-regular distributions needed to build high quality SFD.

As our application study corresponds to 18-D and 29-D spaces, we present on Fig. 3 results obtained in both dimensions for few designs.

These results are similar to those presented in 20-D and only WSP designs are located in the quasi-regular area in the (m, σ) plane. Thus, for dimensions of space higher than 20, only the WSP designs seem to have an intrinsic good quality to explore the space due to an important edge length between points without perfect order. In conclusion, these results highlight that only the WSP designs present good properties to be used as SFD.

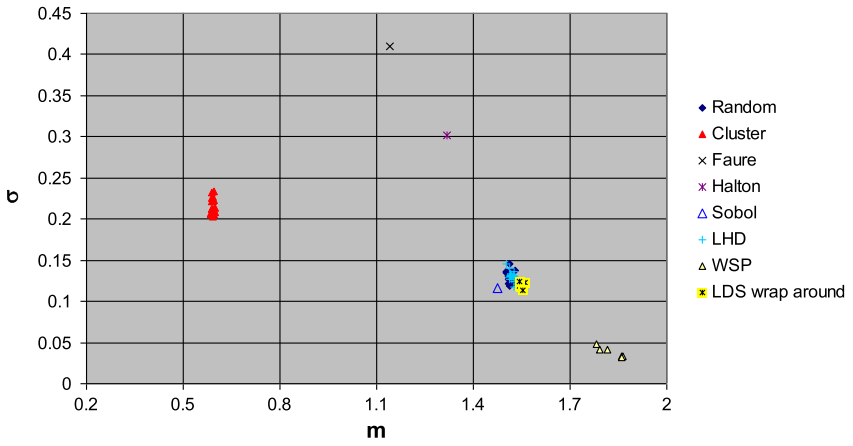

Fig. 2. Representation of the average and standard deviation of the edge length for various designs with 400 points in 20-D.

This methodology based on the (m, σ) plane of the MST appears to be an essential step to determine the intrinsic quality of a design because this quality is determined directly in the original space and can be applied to very high dimensional spaces. In the case of SFD, a high intrinsic quality corresponds to a quasi-regular point distribution. This step can be completed by the use of projections onto subspaces, giving useful information but introducing potential bias or increasing the number of calculations in the case of high dimensional

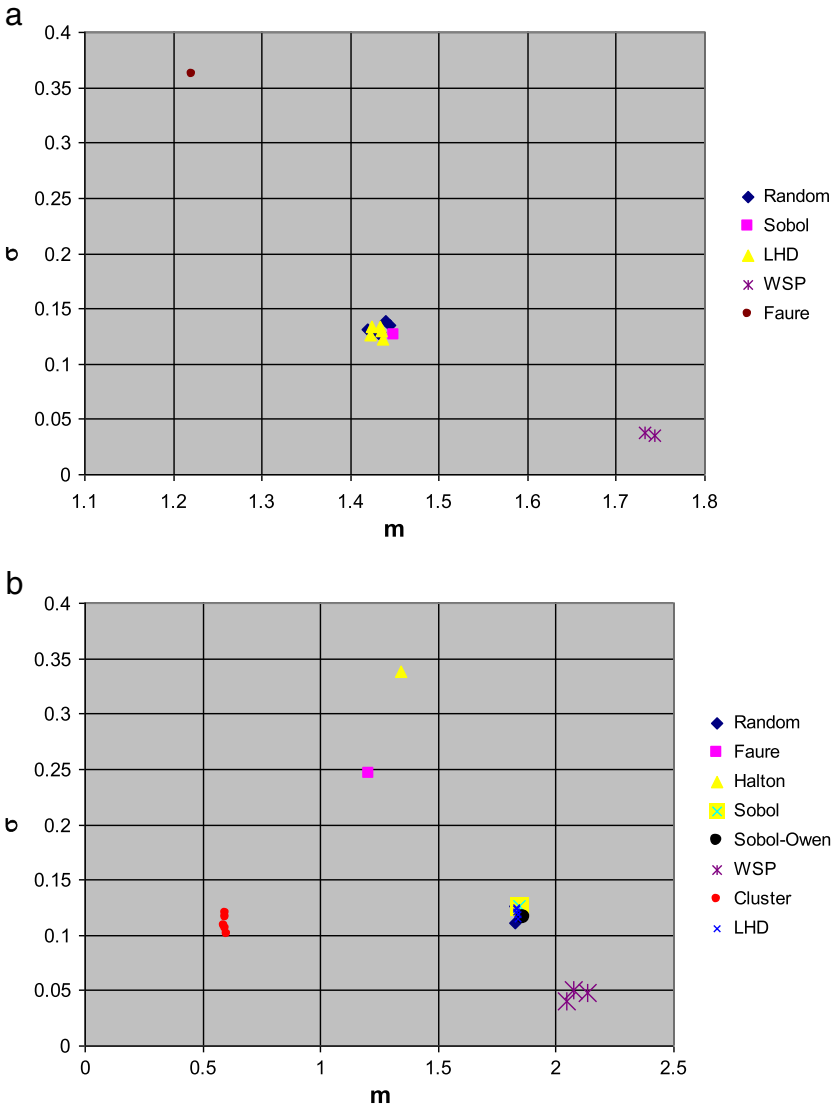

Fig. 3. Representation of the average and standard deviation of the edge length for various designs with 400 points in 18-D (a) and 614 points in 29-D (b).

spaces. For example, the use of all 2-D projections for an d-D space implies $d(d-1)/2$ computer assessments.

2.3. Qualification of high dimensional SFD in 2-D subspaces

Often, it is desired that the space filling property (well distribution of the points in the space) is verified for the projections onto subspaces (Roustant et al.[27]). We present here the results obtained with projections onto 2-D subspaces for the Sobol, Sobol with Owen scrambling (Owen [25], Atanassov et al.[1]), random and WSP 29-D designs using the radial scanning statistic (RSS) (Roustant et al.[27]) and MST criterion.

The quality of a design is determined by the RSS method using the DICE packages in R-software developed in the framework of the DICE consortium [13,14]. This method is based on the analysis of all the 2-dimensional projections of the design. In each of this 2-dimensional projection, the points are projected on a rotated line. For each rotation step of this line, the Greenwood statistic (Greenwood [10], Roustant et al.[27]) is calculated on the projections of all points to qualify the uniformity of the projected points on this line by the analysis of the spacings between the projected points. Finally, the RSS points out the worst 2-dimensional projection and the worst direction in this projection and the higher the statistic is, the less uniform the distribution is. Table 1 presents the results of the RSS. It can be noticed that RSS value are lower for random designs and LHDs: so, these designs can be considered as the best designs for this criterion. Except the Faure design, the worst designs are Sobol and WSP2 for this criterion. Although, the values in the 29 dimension case for the Sobol and for the second WSP designs are almost the same (cf. Table 1), Figs. 4 and 5 show a great difference between these two designs.

In a first step, the Owen scrambling seems to improve the Sobol design due to the lower value of RSS. But Figs. 6 and 7 show bad repartition of the point distribution in the worst pair of dimension (16–23 plane) for the Sobol design and for the Sobol design with Owen scrambling (10–18 plane). In these planes, the point distributions do not correspond to a uniform or a quasi-regular distribution. So, the use of the single RSS value is not always sufficient to assess accurately the quality of a SFD design and a graphic representation of the worst pair of dimensions is needed.

The results obtained with the MST criterion with projections onto 2-D subspaces do not distinguish the quality between random and WSP designs. The results of the Sobol design point out that this design is very inhomogeneous depending on the considered subspace (cf. Fig. 8). In conclusion, the Owen scrambling does not improve the quality of the Sobol design because the main bad characteristics of Sobol design are preserved. The worst pairs of dimension determined by RSS (16–23 plane and 10–18 plane) are identified in the cluster area by the MST criterion (cf. Fig. 8).

It can be noticed that a lot of pair of dimensions of the Sobol design are located in the quasi-regular distribution area but it is not the case in the original space. The same result is obtained with the Sobol design with Owen scrambling. On the contrary, WSP points are randomly distributed onto 2-D subspaces and this design is located in the quasi-regular distribution area in the 29-D space. This empirical observation highlights the essential need to qualify designs in the original space before the analysis the properties onto subspaces.

In fact, both methods (MST and RSS) are analysing two different aspects of a design and are complementary. Using simultaneously both criteria we can conclude that Faure and Halton designs are the designs with the worst quality. Sobol without and with Owen scrambling show point alignments (RSS) and are located in the random area in the (m,σ) plane like LHD in our 29-D original space. Only, the WSP design appears to be the best design. But, due to the difference obtained with projections and direct analysis in the original space with the MST criterion, it seems absolutely necessary to analyse SFD design in the original space.

In the next part, we evaluate the quality of these Sobol, Random, LHD and WSP designs on two application cases.

Table 1
Greenwood statistic given by the RSS on the worst direction in the worst pair of dimension. (*) mean value on 5 designs, because of the random character of these designs.

Design and number of points	RSS value
Faure, 614	0.085
LHD (*), 614	0.0040
Random (*), 614	0.0040
Sobol, 614	0.0298
Sobol with Owen scrambling, 614	0.0169
WSP1, 598	0.0088
WSP2, 598	0.0236
WSP3, 614	0.0044

3. Application of sensitivity analysis and metamodelling of interference optical systems

The purpose of this part is to present the results obtained with different SFD used to perform a sensitivity analysis and to build metamodels of interference optical systems. By this way, it is possible to connect and compare the intrinsic quality of designs determined by the MST with the extrinsic quality of the results corresponding to this application case.

The interference optical systems presented in this paper are based on amplitude splitting, where a primary wave is divided into two or more segments, which travel different paths before overlapping and interfering. Therefore, variation of path length differences and amplitude differences for one of the waves modify the resulting intensity pattern. However, especially when dealing with many interfering waves, it is not obvious which wave parameter or interaction between parameters are the most critical in terms of intensity pattern distortion.

The metamodel that we will use to assess these interactions is a second order polynomial function:

$$f(X_1,\ldots,X_n) = a_0 + \sum_{k=1}^{n} a_k.X_k + \sum_{k=1}^{n} b_k.X_k^2 + \sum_{0<i<j\le n} c_{ij}.X_i.X_j \qquad (3)$$

We chose a second order polynomial function instead of a first order because we know that the response in both cases has an extremum in the center of the domain. The R-square coefficient will guarantee the quality of this polynomial regression. In both cases we look at the interaction coefficients c_{ij} and at the value a_0 to insure of the extrinsic quality of our design (a_0 is the value at the extremum).

3.1. Coherent laser beam combining

The ultimate power density available in a single laser amplifier chain is limited by nonlinear effects and damage threshold in the amplifying medium (Jaouën et al.[15]). In order to overcome this issue, the combination of beams of several lasers packaged into an array is a promising solution for power scaling while maintaining low beam divergence (Fan [7], Shay et al.[31], Jolivet et al.[16]). To increase furthermore the power density, all the array elements have to operate coherently with the same wavelength in order to achieve constructive interferences between the laser emitters. This type of setup is called coherent beam combining. However, the relative optical phases of the electric waves at the output of each emitter have to be controlled in order to maintain constructive interferences between the laser emitters. Therefore, it is crucial to know the sensitivity of the system towards residual phase differences between laser sources in order to study and eventually improve the robustness

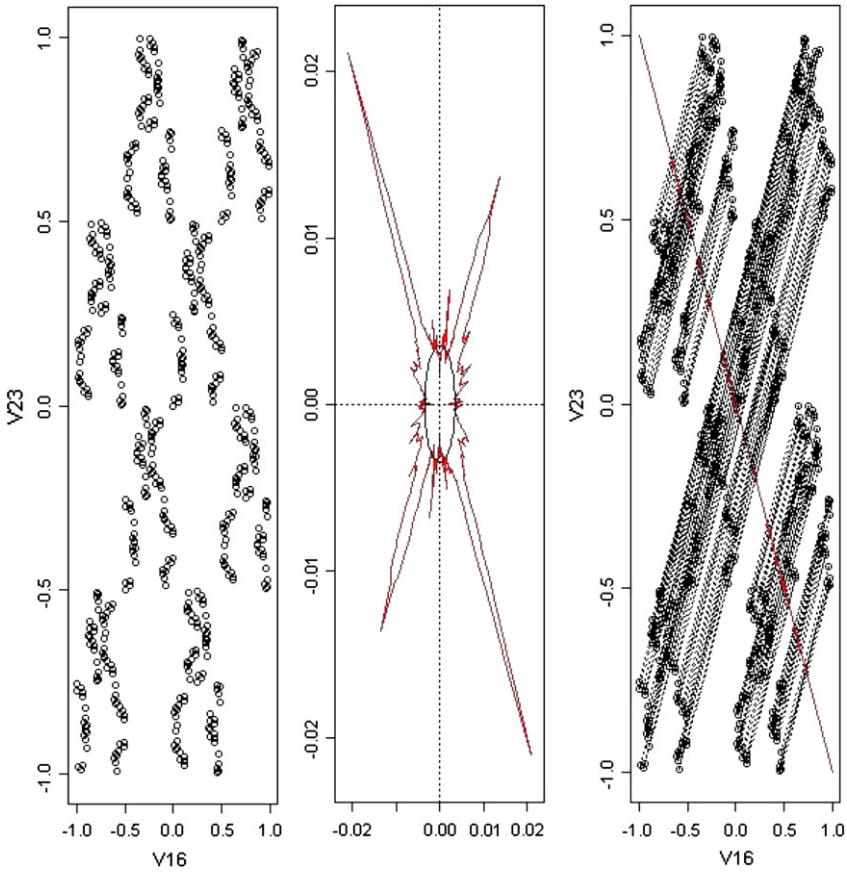

Fig. 4. RSS representation of Sobol 29-D design, 614 points.

of this setup. As an example, we study a hexagonal array of 19 lasers (cf. Fig. 9 a). This configuration guarantees a high fill factor resulting in very efficient coherent beam combining with more than 70% power concentrated in the center of the diffraction pattern.

When phase differences remain (cf. Fig. 9 c), the combining efficiency decreases, resulting in spreading of the power in large areas. Different criteria are used to qualify this efficiency. In this case, we present results with the Mask Encircled Power (MEP) criterion (Scholl [29], Jolivet et al.[16]) which is very convenient for many applications. It is the fraction of power contained in a fixed angular aperture, here a 1 mrad centered circular aperture (cf. Fig. 9 b). The central laser beam in the array will be our reference (cf. Fig. 9 a) and the 18 other lasers will have the following phase variation: $\Delta\phi = \phi_{laser} - \phi_{center}$ with $\phi_{center} = 0$.

We use the previous types of design (random, Sobol and WSP) in dimension 18 to perform sensitivity analyses. The laser in the center will stay with a constant phase equal to zero, while the others have a phase varying in the domain $[-\pi/4; \pi/4]$. When all the phases are equal to 0, the MEP is at its maximum. Therefore, theoretically, the a_0 coefficient should be equal to this maximum MEP value. The error on a_0 is used to assess the quality of the design.

Following the rule proposed by Loeppky et al.[18], the number of point for each design is fixed to the value 200 (around 10 points per dimensions). For all designs, the metamodel has a good quality with an R-square greater than 0.95. After analysis of the metamodel, all designs have the same trend and we performed sensitivity analyses on two different array configurations (a square of 16 fibers and a hexagon of 19 fibers) of coherently combined fiber amplifiers to study the impact of residual phase errors onto the combining efficiency (Azarian et al.[2]). But the error on the a_0 coefficient is lower or around 1% except with the Sobol design which gives an error of roughly 10%.

For the 400 points designs (around 20 points per dimension), all the designs have an error on a_0 less than 1%.

The Sobol sequence with around 10 points per dimension does not deliver accurate results and a greater number of points is preferable. Therefore for the study of the interference filters, we will keep 20 points per dimension for the 29-D case.

3.2. Optical thin film coatings

In optics, bandpass filters are used to select a specific spectral range. Optical thin film coatings are efficient components to select a narrow wavelength bandwidth from an optical signal [20]. Refractive index errors or thickness errors during the manufacturing of these layers can dramatically impair the desired optical properties. Because of the spectral selectivity accuracy that is needed for a bandpass filter, the thickness t and the refractive index n of each layer have to be controlled very precisely during the coating manufacturing.

Due to the interference characteristics of multilayer filters, the optical coatings give the opportunity to evaluate methods which can explore high dimensional space of parameters and mainly in presence of interactions between some parameters. For the coatings production composed with a high number of layers, the sensitivity analysis is an efficient way to determine the most critical layers of an optical coating (Vasseur et al.[38]). Each layer is characterized by its refractive index

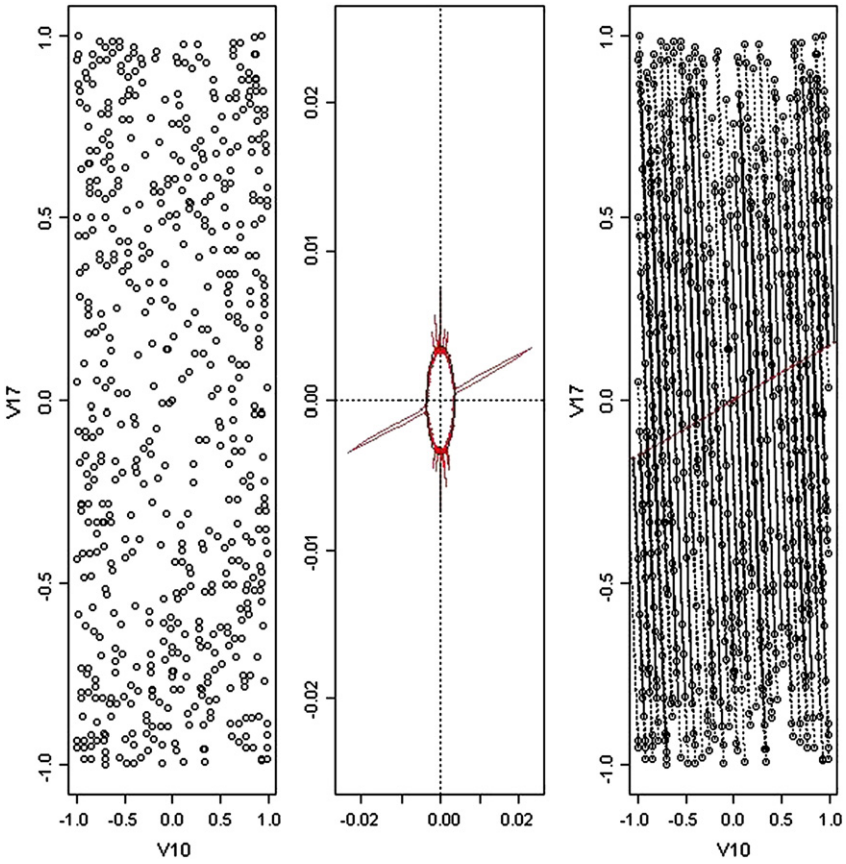

Fig. 5. RSS representation of WSP 29-D design, 598 points.

value *n* and its thickness *t*: thus, for a filter with p layers we can generate up to 2p-dimensions spaces. Refractive index value errors or thickness errors during the manufacturing of these layers can induce dramatic consequences on the wished optical properties (Macleod [19]).

The study of the effect of errors on refractive index values of each layer of the coating on the optical transmittance of the three-cavity bandpass filter composed of 29 layers is presented on Fig. 10 (perfect filter):

Glass/HLHL4HLHLH L HLHL4HLHLH L HLHL4HLHLH/air (1)

where H and L are quarter-wave layers ($n^*t = \lambda_0/4$ at $\lambda_0 = 1\,\mu m$) of high (H: n = 2.35) and low (L: n = 1.3) refractive index values respectively. This coating is an assembly of three basic bandpass filter: HLHL4HLHLH.

In this study, we consider for the monitoring technique that the thickness value of each layer is the same value defined for the perfect filter: thus only the refractive index values of each layer are modified with a maximum error value of ±0.025 and the dimension of the study space is 29. Two examples of the influence of the errors of the refractive index values on the optical properties of the filter are

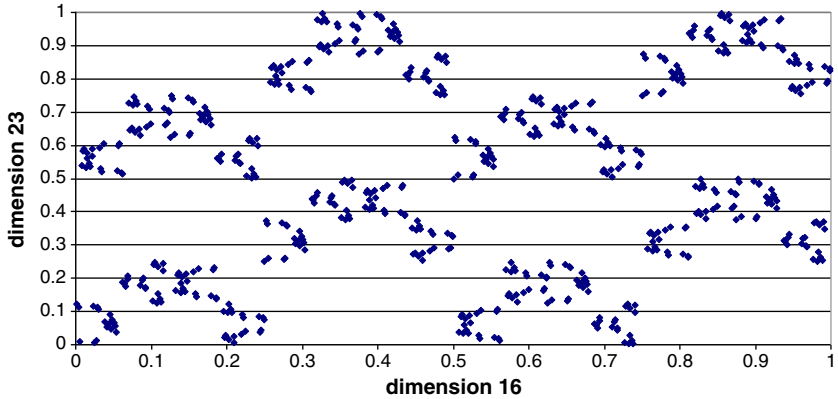

Fig. 6. Point distribution of Sobol design in the worst pair of dimension (16–23 plan). RSS value: 0.0298. MST: m = 0.335 σ = 0.294.

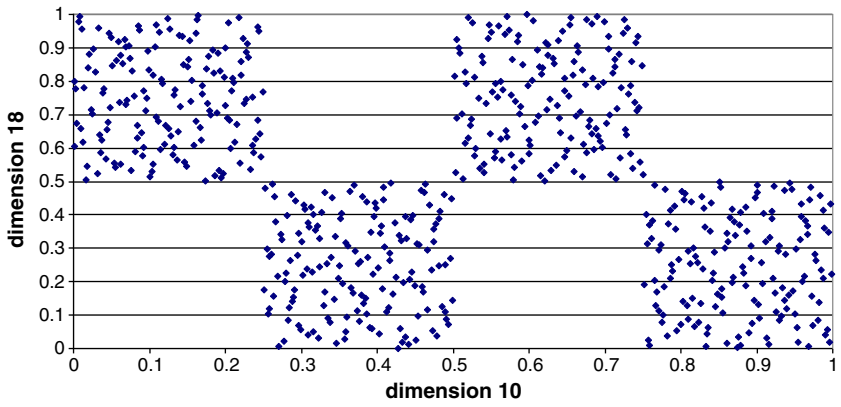

Fig. 7. Point distribution of Sobol design with Owen scrambling in the worst pair of dimension (10–18 plane). RSS value: 0.0169. MST: m = 0.506 σ = 0.170.

presented on Fig. 10: the curves of Filter 1 and Filter 2 show the modifications of the spectral transmittance of the filter due to errors on refractive index values on each layer.

The sensitivity analysis is assessed by the following responses R (merit function):

$$R = \sqrt{\sum_i (T(\lambda_i) - T_p(\lambda_i))^2}$$

where $T(\lambda_i)$ is the transmittance of the filter at the wavelength λ_i in the case of the computer experiment (with error on refractive index values), $T_p(\lambda_i)$ is the transmittance of the perfect filter, and $\lambda_0 = 1$ μm is the designed wavelength of the perfect filter. So, the merit function R evaluates the transmittance influence of the refractive index value errors on the spectral domain [0.9 μm, 1.1 μm].

Due to the knowledge of the optical properties of this filter, the most critical layers or layer interactions belong to the blocks L4HL, which are the fundamental basis of each optical cavity, and between the 4H-layers of these blocks, whose characteristics correspond to the center of the bandpass of each optical cavity.

The most critical layer interactions will be identified by checking the values of the coefficients from the polynomial regression. The quality of the different designs is assessed using the following criteria:

- Value of the R-square obtained with the polynomial regression.
- Identification of the 9 major interaction coefficients c_{ij}: $c_{5,15}$, $c_{15,25}$, $c_{5,25}$, $c_{4,5}$, $c_{5,6}$, $c_{14,15}$, $c_{15,16}$, $c_{24,25}$, $c_{25,26}$. The score highlights the number of major interactions identified by the design, compared to this list. For example, a score of 6/9 means that 6 of the highest interactions identified by the metamodel are within the 9 highest interactions.
- Deviation of a_0 value from 0. In the case of no refractive index error, the value of R is null so the exact value of a_0 is 0.

The results are presented in Table 2. For all designs, the metamodel has a good quality with an R-square greater than 0.96. The WSP designs give the best solutions according to the knowledge of this optical filter.

But in our application case, the results with random designs are better than those of Sobol's design, even if the results are different with random designs. This last observation confirms that a lot of computer runs are required with unoptimized designs or that is necessary to perform several random designs to obtain an average

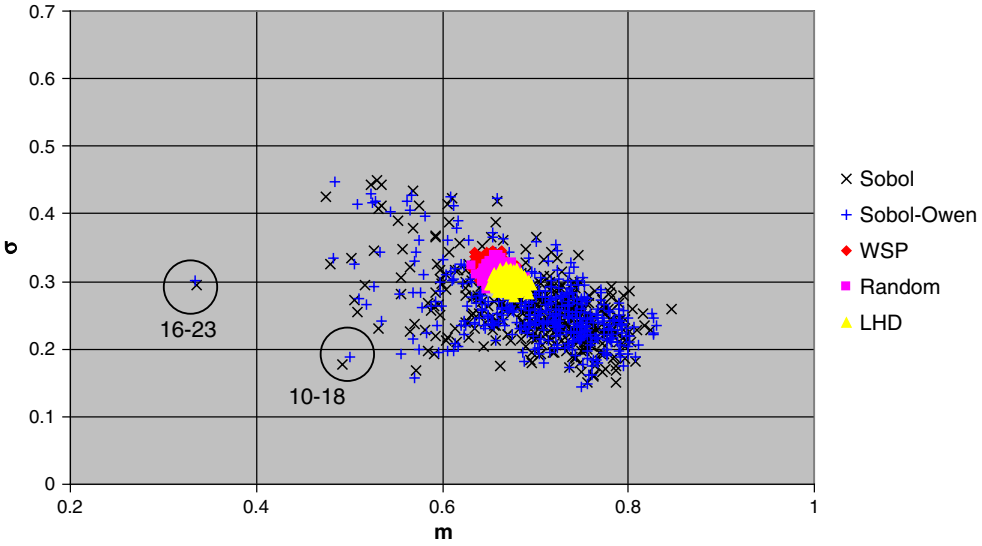

Fig. 8. Representation of the average and standard deviation of the edge length for various projections of 29-D designs with 614 points onto the 406 2-D subspaces. The pairs of dimensions (16–23 plane) and (10–18 plane) of Sobol and Sobol with Owen scrambling designs are indicated by the circles.

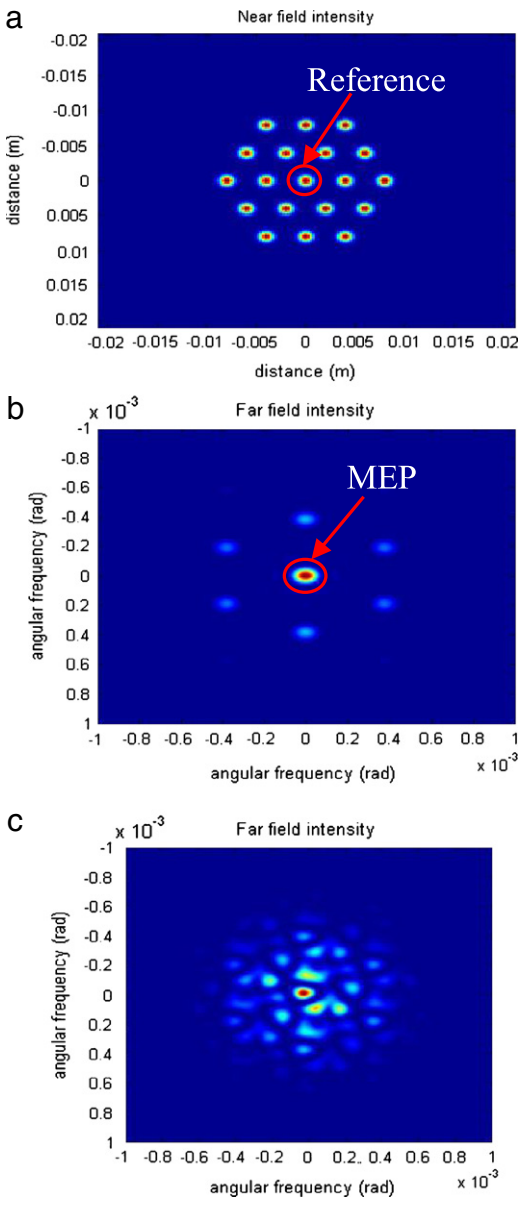

Fig. 9. (a) Near field of the hexagonal array of fibers. (b) Far field when all the phases are equal to 0. (c) Far field when phase differences are not equal to 0.

good result: indeed, 8 coefficients determined for response R with random5 design but only 4 coefficients identified with random2 design.

The results obtained with the good intrinsic quality designs are in agreement with the knowledge of the optical properties of this filter. In conclusion, we can observe that the intrinsic quality of designs determined by the MST criterion corresponds to the quality of the conclusions on the layers interactions of this 29-layers filter and finally the most sensitive and critical layers are well identified. The sensitivity analysis of thin film coatings by experimental designs is very useful to obtain clues about the existence of interactions between the layers of a filter, and especially in the case of high dimensional systems with an adjustable number of layers. The results obtained with the WSP designs are an encouragement to use these designs to perform sensitivity analysis of complex filters (Vassallo [36], Vasseur [37], Sullivan et al.[33]), to compare different monitoring techniques of optical coatings (Macleod [19], Macleod et al.[21], Chun et al.[5], Tikhonravov et al.[35], Badoil et al.[3]) and to explore very high dimensional interference optical systems (more than 100 parameters). There is a good agreement of the intrinsic quality of a design, determined mainly by MST, and the extrinsic quality assessed on cases with a lot of interactions between parameters. Thus we can conclude that the study of systems with a high level of interactions and a large number of parameters should be done using designs with points distributed as evenly as possible. The sensitivity analyses and the metamodels are indeed well connected to the mathematical properties of the designs (point alignments or quasi-periodical point distribution).

4. Conclusions

The criterion of Minimum Spanning Tree allows the classification of any distribution of points using a graph with an average edge length and standard deviation for the corresponding distribution. The qualification of Space-Filling Designs based on MST has been studied in high dimensional space and the insufficiencies of most designs are here highlighted independently of any projection on sub-spaces, the MST being built directly on the points of the original space.

It can be observed that a lot of classical designs do not present good properties when the dimension of the space is higher than 20 and only the WSP designs present the good intrinsic SFD properties. The intrinsic quality of different designs was assessed onto 2-D subspaces by the MST and RSS criteria. In this case, the RSS results based on graphical representation of the worst pair of point projections are useful to exclude bad designs. But, these 2-D results

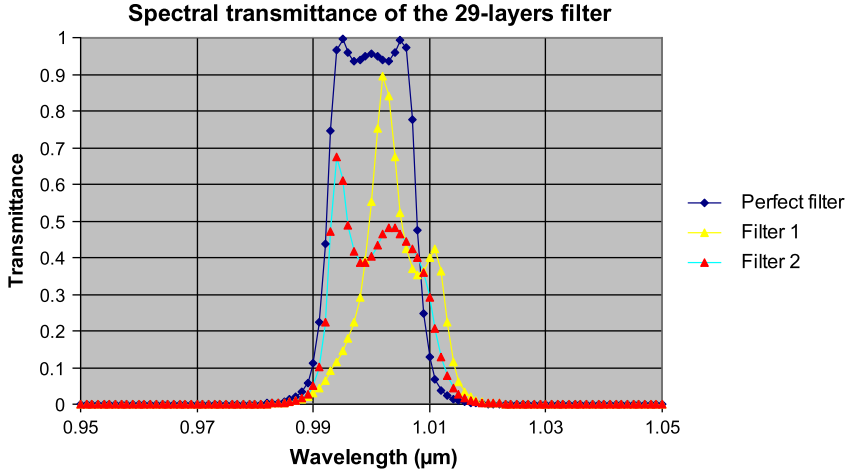

Fig. 10. Spectral transmittance of the perfect filter and of two filters (Filter 1 and Filter 2) with errors on refractive index values.

Table 2
R-square, score obtained by the designs for the identification of the 9 major interaction coefficients and the value of a_0.

Design (614 points)	R^2	Score	a_0 value
Faure	0.98	1/9	1.43
Latin Hypercube 1	0.97	6/9	0.88
Latin Hypercube 2	0.97	5/9	0.90
Latin Hypercube 3	0.97	7/9	0.87
Latin Hypercube 4	0.97	5/9	0.81
Latin Hypercube 5	0.97	6/9	0.89
Random 1	0.97	6/9	0.71
Random 2	0.97	4/9	0.75
Random 3	0.96	7/9	0.82
Random 4	0.97	7/9	0.88
Random 5	0.97	8/9	0.81
Sobol	0.97	6/9	0.68
WSP 1 (598 points)	0.97	7/9	0.30
WSP 2 (598 points)	0.98	6/9	0.02
WSP 3	0.96	6/9	0.53

are not sufficient to qualify correctly SFD and the qualification of SFD in the original space by MST criterion is essential. Indeed, the properties of designs onto projection subspaces do not correspond directly to a good points distribution in the original space.

In the case of coherent laser beam combining, the metamodels built for 19 fibers are very good using designs with approximately 20 points per dimension. In the case of a high number layer of an optical filter, the metamodel and the most critical interactions are well determined by the WSP designs with few computer runs. The employed method is very useful to assess very fast the potential robustness of filters by considering the monitoring strategy.

The results of sensitivity analysis of interference optical systems exhibit the WSP design quality, because of the quality of the metamodel, as well as the ability of assessing interactions. The intrinsic quality and the extrinsic quality show good agreement, which lead to the conclusion that the study of systems with a high level of interactions and a large number of parameters should be done using designs with points distributed as evenly as possible.

Finally, the results of the sensitivity analysis of interference optical systems confirm the intrinsic quality of the SFD and reveal the empirical correlation between the intrinsic and extrinsic qualities of SFD designs.

The quality of the results obtained in the interference optical systems is an encouragement to extend this approach to assess more complex optronic systems and to explore higher dimensional spaces and more complicated interactions.

Acknowledgments

The authors thank M. Claeys-Bruno for building WSP designs and B. Iooss for building LDS wrap around designs.

References

[1] E. Atanassov, A. Karaivanova, S. Ivanovska, Tuning the generation of Sobol sequence with Owen scrambling, Large-Scale Scientific Computing - Lecture Notes in Computer Science, Springer Berlin, 2010.
[2] A. Azarian, O. Vasseur, B. Bennaï, L. Lombard, G. Canat, V. Jolivet, Y. Jaouën, P. Bourdon, Global sensitivity analyses of coherent beam combining of fiber amplifier arrays by the use of numerical Space Filling Designs, Proc. of SPIE, Photonics West, San Francisco, 2011, paper 7914–52.
[3] B. Badoil, F. Lemarchand, M. Cathelinaud, M. Lequime, Interest of broadband optical monitoring for thin-film filter manufacturing, Appl. Opt. 46 (2007) 4294–4303.
[4] J. Beardwood, J.H. Halton, J.M. Hammersley, The shortest path through many points, Camb. Philos. Soc. Proc. 55 (1959) 299–327.
[5] B.J. Chun, C.K. Hwangbo, J.S. Kim, Optical monitoring of nonquarterwave layers of dielectric multilayer filters using optical admittance, Opt. Express 14 (2006) 2473–2480.
[6] C. Dussert, G. Rasigni, M. Rasigni, J. Palmari, Minimal spanning tree: a new approach for studying order and disorder, Phys. Rev. B 34 (1986) 3528–3531.
[7] T.Y. Fan, Laser beam combining for high-power, high-radiance sources, IEEE J. Sel. Topics Quantum Electron. 11 (2005) 567–577.
[8] H. Faure, Discrépance de suites associées à un système de numération (en dimensions), Acta Arith. 41 (1982) 337–351.
[9] J. Franco, O. Vasseur, B. Corre, M. Sergent, Minimum Spanning Tree: a new approach to assess the quality of the design of computer experiments, Chemom. Intell. Lab. Syst. 97 (2009) 164–169.
[10] M. Greenwood, The statistical study of infectious diseases, J. R. Stat. Soc. 109 (1946) 85–110.
[11] J.H. Halton, On the efficiency of certain quasi-random sequences of points in evaluating multi-dimensional integrals, Numer. Math. 2 (1960) 84–90.
[12] R. Hoffman, A. Jain, A test of randomness based on the minimal spanning tree, Pattern Recogn. Lett. 1 (1983) 175–180.
[13] http://cran.r-project.org/.
[14] http://www.dice-consortium.fr/.
[15] Y. Jaouën, G. Canat, S. Grot, S. Bordais, Power limitation induced by nonlinear effects in pulsed high-power fiber amplifiers, C. R. Phys. 7 (2006) 163–169.
[16] V. Jolivet, P. Bourdon, B. Bennaï, L. Lombard, G. Goular, E. Pourtal, G. Canat, Y. Jaouën, B. Moreau, O. Vasseur, Beam shaping of single-mode and multimode fiber amplifier arrays for propagation through atmospheric turbulence, IEEE J. Sel. Topics Quantum Electron. 15 (2009) 257–268.
[17] J.B. Kruskal, On the shortest spanning subtree of a graph and travelling salesman problem, Proc. Am. Math. Soc. 7 (1956) 48–50.
[18] J. Loeppky, J. Sacks, W. Welch, Choosing the sample size of a computer experiment: a practical guide, Technometrics 51 (2009) 366–376.
[19] H.A. Macleod, Turning value monitoring of narrow-band all dielectric thin film optical filters, Opt. Acta 19 (1972) 1–28.
[20] H.A. Macleod, Thin film optical filters, Adam Hilger ltd, Bristol, 1986.
[21] H.A. Macleod, E. Pelletier, Error compensation mechanisms in some thin-film monitoring systems, Opt. Acta 24 (1977) 907–930.
[22] M.D. Mc Kay, R.J. Beckman, W.J. Conover, A comparison of three methods for selecting values of input variables in the analysis of output from a computer code, Technometrics 21 (1979) 239–245.
[23] A. Marrel, Mise en œuvre et utilisation du métamodèle processus gaussien pour l'analyse de sensibilité de modèles numériques, PhD. Thesis, INSA, 2008.
[24] J. Neyman, E.L. Scott, Statistical approach to problems of cosmology, J. R. Stat. Soc. B 20 (1958) 1–43.
[25] O. Owen, Scrambling Sobol' and Niederreiter-Xing Points, J. Complex. 14 (1998) 466–489.
[26] R.C. Prim, Shortest connection networks and some generalizations, Bell Syst. Tech. J. 36 (1957) 1389–1401.
[27] O. Roustant, J. Franco, L. Carraro, A. Jourdan, A radial scanning statistic for selecting space-filling designs in computer experiments, in mODa 9 – advances in model-oriented design and analysis, Proceedings of the 9th International Workshop in Model-Oriented Design and Analysis held in Bertinoro, Italy, June 14–18, Springer, Heildeberg, 2010, pp. 189–196.
[28] A. Saltelli, K. Chan, E.M. Scott, Sensitivity Analysis, Wiley, New-York, 2000.
[29] M. Scholl, Measured spatial properties of the cw Nd:YAG laser beam, Appl. Opt. 19 (1980) 3655–3659.
[30] M. Sergent, R. Phan-Tan-Luu, J. Elguero, Statistical Analysis of Solvent Scales. Part 1, Anal. Quimica Int. Ed. 93 (1997) 3–6.
[31] T.M. Shay, V. Benham, J.T. Baker, A.D. Sanchez, D. Pilkington, C.A. Lu, Self-synchronous and self-referenced coherent beam combination for large optical arrays, IEEE J. Sel. Topics Quantum Electron. 13 (2007) 480–486.
[32] I.M. Sobol', On the distribution of points in a cube and the approximate evaluation of integrals, USSR Comput. Math. Math. Phys. 7 (1967) 86–112.
[33] B.T. Sullivan, G.A. Clarke, T. Akiyama, N. Osborne, M. Ranger, J.A. Dobrowolski, L. Howe, A. Matsumoto, Y. Song, K. Kikuchi, High-rate automated deposition system for the manufacture of complex multilayer coatings, Appl. Opt. 39 (2000) 157–167.
[34] K.S. Tan, P.P. Boyle, Applications of scrambled low discrepancy sequences to exotic options, International AFIR Colloquium Proceedings, 1997.
[35] A. Tikhonravov, M. Trubetskov, T. Amotchkina, Computational experiments on optical coating production using monochromatic monitoring strategy aimed at eliminating a cumulative effect of thickness errors, Appl. Opt. 46 (2007) 6936–6944.
[36] C. Vassallo, Reflectivity of multidielectric coatings deposited on the end facet of a weakly guiding dielectric slab waveguide, J. Opt. Soc. Am. A 5 (1988) 1918–1928.
[37] O. Vasseur, Reflectivity of dielectric coatings deposited on the end facet of a weakly guiding fiber, J. Opt. Soc. Am. A 12 (1998) 77–83.
[38] O. Vasseur, M. Cathelinaud, M. Claeys-Bruno, M. Sergent, Global sensitivity analysis of bandpass and antireflection coatings manufacturing by numerical Space Filling Designs, Appl. Opt. 50 (2011) C117–C123.
[39] F. Wallet, C. Dussert, Comparison of spatial point patterns and processes characterization methods, Europhys. Lett. 42 (1998) 493–498.
[40] C. Zhan, Graph-theoretical methods for detecting and describing gestalt clusters, IEEE T. Comput. C-20 (1971) 68–86.

High-dimensional sensitivity analysis of complex optronic systems by experimental design: applications to the case of the design and the robustness of optical coatings

Olivier Vasseur[1*], Magalie Claeys-Bruno[2], Michel Cathelinaud[3], and Michelle Sergent[2]

[1] *Office National d'Etudes et de Recherches Aérospatiales, Palaiseau Cedex 97761, France*

[2] *Université Paul Cézanne Aix Marseille III, LMRE, Marseille Cedex 20 13397, France*

[3] *Missions des Ressources et Compétences Technologiques, Meudon 92135, France*

[*] *E-mail: Olivier.Vasseur@onera.fr*

Received November 22, 2009

We present the advantages of experimental design in the sensitivity analysis of optical coatings with a high number of layers by limited numbers of runs of the code. This methodology is effective in studying the uncertainties propagation, and to qualify the interactions between the layers. The results are illustrated by various types of filters and by the influence of two monitoring techniques on filter quality. The sensitivity analysis by experimental design of optical coatings is useful to assess the potential robustness of filters and give clues to study complex optronic systems.

OCIS codes: 310.0310, 220.0220, 120.0120.

doi: 10.3788/COL201008S1.0021.

The study of complex optronic systems entails sensitivity analysis with a large number of parameters. Very often the response depends on synergies or interactions between these parameters. Due to interference characteristics of multilayer filters, optical coatings make possible the evaluation of methods that can explore high-dimensional space parameters and the presence of interactions between parts of these parameters. For coatings production with a high number of layers, sensitivity analysis is an efficient way to determine the most critical layers of an optical coating[1]. Refractive index errors or thickness errors during the manufacturing of these layers can induce dramatic consequences on the desired optical properties[2].

We present the advantages of using the method of experimental design[3], which is used for metamodel constructions and high-dimensional code explorations with limited numbers of runs of the code, particularly in the case of coatings with a high number of layers. This methodology is more effective in studying uncertainties propagation (refractive index or thickness values) to determine the influence of errors on the optical properties, and to quantify the interactions between the errors of each layer. The results are illustrated by various types of filters, particularly bandpass filters and multiple half-wave filters. Different designs such as factorial, fractional factorial, and space-filling designs are used to present the results.

Furthermore, we study the influence of two monitoring techniques, and show the most critical coating layers and the dependency of these layers with future manufacturing.

The results show that the study of thin-film filters is very useful in examining the interactions of high-dimensional systems due to the filter's adjustable number of layers, and the existence of interactions between these layers.

Finally, we demonstrate that sensitivity analysis of optical coatings by experimental design is useful in assessing the potential robustness of filters, and gives clues to study complex optronic systems.

The codes to study complex phenomena become more and more realistic with a larger input data set. However, due to the complexity of the mathematical system underlying the computer simulation tools, there are often no explicit input-output formulas. Although computer power has significantly increased in the past years, the evaluation of a particular setting of the design parameters may still be very time-consuming. The simulator is often replaced by a metamodel to approximate the relationship between the code and the design parameters. These metamodels are built using numerical designs of experiments that can indicate interactions between the parameters. The choice of an underlying empirical model (depending on accuracy and interactions level) can be written as

$$Y = C\mathrm{ste} + \sum_i b_i X_i + \sum_{i<j} b_{i,j} X_i X_j + \sum_{i<j<k} b_{i,j,k} X_i X_j X_k + \ldots, \quad (1)$$

where Y is the response of the model, X_i is the ith parameter, b_i is the effect of the ith parameter, and $b_{i,j}$, the interaction between the ith and jth parameters. This model is valid for the levels -1 and $+1$ of the undimensional variables (X_i). In our case, parameters X_i can be thickness, refractive index, or optical thickness.

In our study, we use factorial and fractional factorial designs at two levels for each parameter (low level: -1 or $-$; high level: $+1$ or $+$). The number of runs is 2^n with n parameters for a full factorial design, and 2^{n-p} for a fractional factorial design corresponding to a subset that is $1/2^p$ of the full factorial design 2^n where p is the

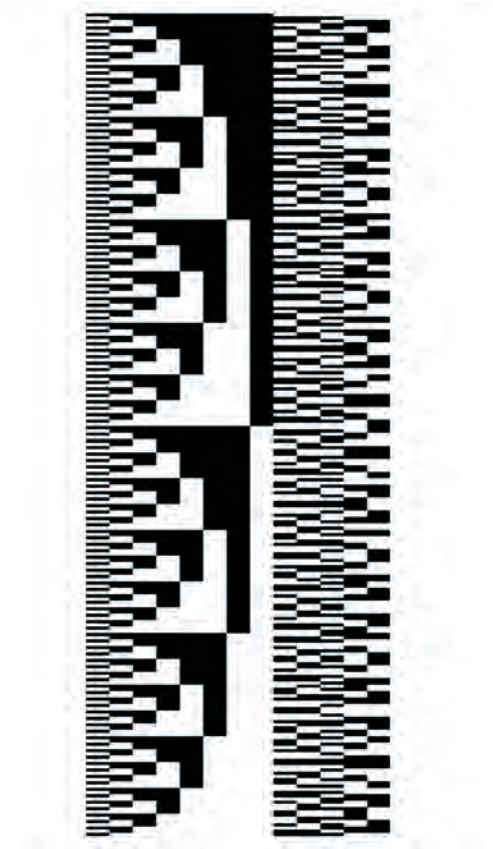

Fig. 1. The 13-layer fractional factorial design $2^{13-5} = 256$ runs. When viewed as pavements, cells with high level (+1) and low level (−1) are in black and white, respectively, where each line corresponds to a run and each column corresponds to a parameter. Several parameters are modified simultaneously.

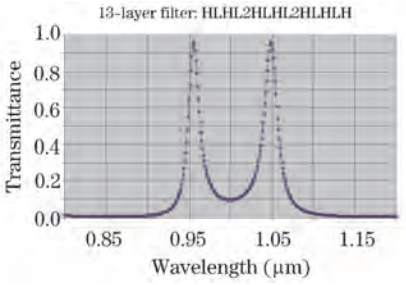

Fig. 2. Transmittance of the perfect 13-layer filter (T_{p}). The high refractive index value is 2.35 and the low refractive index value is 1.3. T_{p} is maximum at λ_1 of about 0.95 μm and λ_2 of about 1.05 μm.

degree of fractionation. Figure 1 presents the 2^{13-5} design to study the sensitivity analysis of a 13-layer filter.

In high-dimensional cases, the number of runs by a full factorial design or a fractional design is too high. There is a need to reduce the number of runs with a good quality of results. The purpose is to use designs that spread the points all over the variation domain of the variables, not only at the limits. These designs are called space-filling designs[4−6].

The study of two monitoring techniques with errors on refractive index values of each layer of the coating are realized with the 13-layer filter (Glass/HLHL2HLHL2HLHLH/air, where H and L are quarter-wave layers at $\lambda_0 = 1$ μm of high and low refractive indices), presented on Fig. 2, and with a fractional factorial design 2^{13-5}.

We consider for the first monitoring technique (MTA) that the thickness value of each layer is the same value defined for the perfect filter. Only the refractive index values of each layer are modified. For the second monitoring technique (MTB), we consider that an optical monitoring technique is used so that the influence of the error on the refractive index value is reduced by a modified thickness of each layer, in order to obtain the optical thickness at λ_0 ($\lambda_0 = 1$ μm) of the perfectly designed filter[7,8]. The error of refractive index is assumed to be 2% for MTA and 5% for MTB . Figure 3 shows the transmittance responses of two examples of the computer experiments.

The sensitivity analysis is assessed by the following $R1$ and $R2$ (merit function) responses:

$$R1 = \sqrt{\sum_i (T(\lambda_i) - T_p(\lambda_i))^2}, \tag{2}$$

$$R2 = \sqrt{(\mathrm{T}(\lambda_1) - \mathrm{T_p}(\lambda_1))^2 + (\mathrm{T}(\lambda_2) - \mathrm{T_p}(\lambda_2))^2}, \tag{3}$$

where $T(\lambda_i)$ is the transmittance of the filter at the wavelength λ_i in the case of the computer experiment (with error on refractive index values); $T_p(\lambda_i)$ is the transmittance of the perfect filter; and λ_1 and λ_2 are the two wavelengths, corresponding to the maxima of the perfect filter. The merit function $R1$ (respectively R2) evaluates the transmittance influence on the domain 0.8−1.2 μm (respectively at λ_1 of about 0.95 μm and λ_2 of about 1.05 μm) due to refractive index errors.

The sensitivity analysis by fractional factorial design gives the major coefficients for the response $R2$ in the case of MTA: $b_{5,9}$ (interaction of layers 5 and 9), $b_{8,9}$, $b_{4,5}$, $b_{9,10}$, and $b_{5,6}$. For the response R1, the difference of each wavelength is modified in the following order: $b_{5,9}$, $b_{8,9}$, $b_{5,6}$, $b_{5,8}$, $b_{6,9}$, $b_{6,8}$, $b_{4,5}$, and $b_{9,10}$. Using this method, we obtain the well-known result for this typical coating; the centers of the bandpass filter are given by the sub-coating L2HL. However, we also obtain the relationship between the layers with errors on refractive index values.

The same analysis for the responses $R2$ and $R1$ in MTB shows that the major coefficients are $b_{6,8}$, $b_{7,8}$, and $b_{6,7}$.

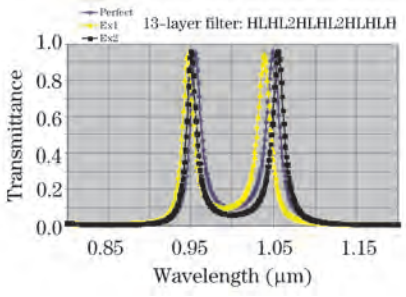

Fig. 3. Transmittance of the perfect filter and two examples, Ex1 and Ex2, of computational runs with error on refractive indices.

Table 1. Critical Layers and Interactions

Optical Coating	Design, Number of Runs	Major Coefficients
9-layer Filter	Factorial, 512	$R1$: $b_{4,5}$, $b_{5,6}$
		$R2$: $b_{4,5}$, $b_{5,6}$
19-layer Filter	Factorial, 512	$R1$: $b_{5,6}$, $b_{4,5}$, $b_{15,16}$, $b_{14,15}$, $b_{5,15}$
		$R2$: $b_{5,15}$, $b_{4,5}$, $b_{5,6}$, $b_{15,16}$, $b_{14,15}$
29-layer Filter	Factorial, 1024	$R1$: $b_{15,16}$, $b_{14,15}$, $b_{4,5}$, $b_{5,6}$, $b_{5,25}$
		$R2$: $b_{5,15}$, $b_{15,25}$, $b_{15,16}$, $b_{14,15}$, $b_{4,5}$
39-layer Filter	Factorial, 4096	$R1$: $b_{25,26}$, $b_{24,25}$, $b_{15,25}$, $b_{15,16}$, $b_{14,15}$
		$R2$: $b_{15,25}$, $b_{5,15}$, $b_{25,35}$, $b_{24,25}$, $b_{25,26}$
39-layer Filter	SFD, 1485	$R1$: $b_{24,25}$, $b_{15,16}$, $b_{25,26}$, $b_{14,15}$, $b_{15,25}$
		$R2$: $b_{15,25}$, $b_{25,35}$, $b_{5,25}$, $b_{5,15}$
55-layer Filter	SFD, 1100	Interactions between Layers:
		6-7-8-20-21-22-34-35-36-48-49-50

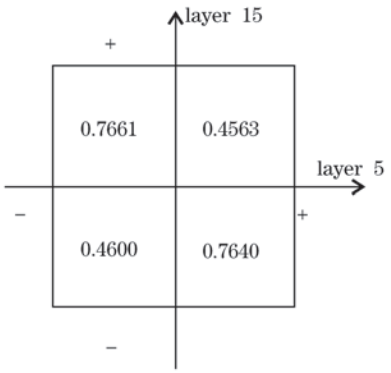

Fig. 4. In the square are given the values of the response $R2$ for each level of layers, 5 and 15 in the case of the 29-layer filter.

To obtain the best filter by this monitoring technique, it is necessary to monitor with high accuracy layers 6, 7, and 8 (LHL) and the influence of the sub-coating L2HL, which is now very low.

Using this example, the results reveal that the most critical layers and the interactions between these layers to obtain the desired optical properties can be achieved by taking into account the characteristics of the monitoring techniques.

Global sensitivity analysis by experimental designs demonstrates the most critical layers of an optical coating and the major interactions between these layers. The criticality of a layer depends on the monitoring technique. Thus, experimental designs are useful in determining the critical difficulties regarding the coating production, with the knowledge of the relationships between layers and monitoring techniques due to stochastic errors. The methodology can be used for other monitoring techniques such as level monitoring[9], optical monitoring of non-quarter-wave layers[10], and broadband optical monitoring[11].

In the sensitivity analysis of optical coatings, the basic filter used is a single Fabry-Pérot filter HLHL4HLHLH with the monitoring technique MTA designed as substrate/HLHL4HLHLH/air.

The high refractive index value is assumed to be 2.35 and the low refractive index value is assumed to be 1.3. The error of refractive index is assumed to be 2.5% for the first monitoring technique and 5% for the second.

The 9-layer filter is studied with a 2-level factorial design ($2^9 = 512$ runs), the 19-layer filter with a two-level fractional factorial design ($2^{19-10}= 512$ runs), and the 29-layer filter with a two-level fractional factorial design ($2^{29-19} = 1024$ runs). The sensitivity analysis of the 39-layer filter is studied with a two-level fractional factorial design ($2^{39-27} = 4096$ runs) and with a space-filling design (SFD), which needs only 1485 runs.

We complete the study by a 55-layer optical coating (four times 13-layer filter) with the MTB.

In Table 1, we present the major coefficients of responses $R1$ and $R2$. These show the most critical interactions between layers and

$$R2 = \sqrt{\left(T(\lambda_0) - T_p(\lambda_0)\right)^2}. \quad (4)$$

As the number of layer increases, the number of interactions between the two layers becomes more crucial and multiplied. All blocks of three layers (L4HL) interact with the others, and we can observe that the coefficient ranks change when the number of layer is higher; the strongest interactions are always from the filter before last.

The interactions between layers can be very strong. For example, Fig. 4 presents the evolution of the response $R2$ for each level (− and +) of layers 5 and 15 in the case of the 29-layer filter; the value modification of $R2$ is around 30%. This interaction graph reveals that the behavior of a layer differs according to the level of the other layer. Moreover, it shows that the response is the same for two different combinations of layers.

The result of MTB with a 55-layer filter extends the previous 13-layer filter result (major influence of the block LHL) in each layer, and reveals the interactions between the layers of different blocks. This is the main perspective of the manufacturing of such filters; it is necessary to monitor each layer during its production, as well as the interactions with the previously deposited layers and the associated errors.

We can observe that the main layers are identified

with an SFD. This result is very interesting because we can obtain good results with a very low number of runs; only 1100 runs are needed to explore a 55-dimension space. The methodology of experimental design adapted to a computer experiment allows us to explore high-dimensional sensitivity analysis of optical coatings, and identify the most critical interactions between layers.

The computational experiments of refractive index errors in optical coatings by experimental design allow us to identify the most critical interactions between layers. The increase of the number of layers in an optical coating is a useful approach to determine the relationship between the parameters in high-dimensional systems. The influence of errors on refractive index values and thickness values should be the next step in the exploration of such high-dimensional spaces.

In conclusion, we proposed the use of experimental design to explore monitoring techniques and determine the most critical layers and interactions in optical coatings. This methodology reveals that the criticality of a set of layers depends on the monitoring technique. In the case of high number of layers, the most critical interactions are determined with a good quality and a low number of computer runs. The method employed is effective in efficiently assessing the potential robustness of filters by taking account of the monitoring strategy. Sensitivity analysis by experimental design of thin-film coatings is very useful to examine high-dimensional systems with interactions resulting from the adjustable number of layers of a filter, as well as the existence of interactions between these layers. Sensitivity analysis of optical coatings is the best way to determine the most effective space-filling designs to explore complex optronic systems.

References

1. A. Saltelli, K. Chan, and E. M. Scott, *Sensitivity Analysis* (Wiley, New York, 2000).
2. H. A. Macleod, *Thin Film Optical Filters* (Adam Hilger Ltd, Bristol, 1986).
3. G. E. P. Box, W. G. Hunter, and J. S. Hunter, *Statistics for Experimenters* (Wiley & Sons, New York, 1978).
4. R. W. Kennard and L. A. Stone, Technometrics **11,** 137 (1969).
5. M. Sergent, "Contribution be la Méthodologie de la Recherche Expérimentale à l'élaboration de matrices uniformes: Application aux effets de solvants et de substituants", PhD. Thesis (University of Aix Marseille III, 1989).
6. M. Sergent, R. Phan-Tan-Luu, and J. Elguero, Anales de Quimica Int. Ed. **93,** 3 (1997).
7. H. A. Macleod, Opt. Acta **19,** 1 (1972).
8. H. A. Macleod and E. Pelletier, Opt. Acta **24,** 907 (1977).
9. A. Tikhonravov, M. Trubetskov, and T. Amotchkina, Appl. Opt. **46,** 6936 (2007).
10. B. J. Chun, C. K. Hwangbo, and J. S. Kim, Opt. Express **14,** 2473 (2006).
11. B. Badoil, F. Lemarchand, M. Cathelinaud, and M. Lequime, Appl. Opt. **46,** 4294 (2007).

Global sensitivity analysis of bandpass and antireflection coating manufacturing by numerical space filling designs

Olivier Vasseur,[1,*] Michel Cathelinaud,[2] Magalie Claeys-Bruno,[3] and Michelle Sergent[3]

[1]Office National d'Etudes et de Recherches Aérospatiales, ONERA DOTA, Chemin de la Hunière, 91761 Palaiseau Cedex, France

[2]Mission des Ressources et Compétences Technologiques, UPS CNRS 2274, 92195 Meudon, France

[3]Equipe ADE2M, Institut des Sciences Moléculaires de Marseille, UMR 6263 Université Paul Cézanne Aix-Marseille III, 13397 Marseille Cedex, France

*Corresponding author: Olivier.Vasseur@onera.fr

Received 23 July 2010; revised 5 October 2010; accepted 8 October 2010; posted 12 October 2010 (Doc. ID 132209); published 15 November 2010

We present the effectiveness of global sensitivity analyses of optical coatings manufacturing to assess the robustness of filters by computer experiments. The most critical interactions of layers are determined for a 29 quarter-wave layer bandpass filter and for an antireflection coating with eight non-quarter-wave layers. Two monitoring techniques with the associated production performances are considered, and their influence on the interactions classification is discussed. Global sensitivity analyses by numerical space filling designs give clues to improve filter manufacturing against error effects and to assess the potential robustness of the coatings. © 2010 Optical Society of America

OCIS codes: 310.0310, 310.4165, 310.5696, 310.3840, 310.6805, 220.4830.

1. Introduction

When the relations between the outputs and the inputs of a computer code are complex, the space filling designs (SFDs) [1–3] are used to study the outputs all over the domain, build metamodels, study the uncertainty propagation, or to determine, by global sensitivity analysis, the most sensitive inputs on the outputs [4–6].

For coating production composed of a high number of layers, the global sensitivity analysis is an efficient way to determine the most critical interactions of layers of an optical coating, with all the layer characteristic parameters varying simultaneously. Indeed, parameters such as refractive index errors or thickness errors during the manufacture of these layers can induce dramatic consequences on the desired optical properties [7]. The global sensitivity analysis methodology is very helpful to determine the influence of errors (refractive index or thickness values) on the optical properties and to quantify the interactions between the errors of each layer with less runs than with Monte Carlo methods [8–10].

We propose using an experimental design method [11] to study optical coatings of quarter-wave layers principally with two-level fractional factorial designs [12] to detect the most important interactions of layers on the optical properties due to errors in the refractive index values, but it is not possible to build a metamodel by the use of two-level fractional factorial designs. In this work, our new results point out the advantages of the use of the SFD to conduct global sensitivity analyses and to simultaneously build metamodels evaluating the influence of uncertainties in manufacturing refractive index values. Indeed, SFDs are more interesting than two-level designs because they spread the computer runs evenly throughout the studied space. The SFD

0003-6935/11/09C117-07$15.00/0

results are compared with those obtained with Monte Carlo calculation, especially in the case of coatings with a high number of layers. The computer designs are built with approximately 20 points per dimension.

The study of the effect of errors in refractive index values of each layer of the coating on the optical properties of the bandpass and antireflection (AR) filters was realized with two monitoring techniques. So, in a first step, the use of these two types of filters illustrates the methodology, but the second goal of this study is to investigate the manufacturing process of these filters in the case of two monitoring techniques. We consider for the first monitoring technique (MT-1) that the thickness value of each layer is the same value defined for the perfect filter, so only the refractive index values of each layer are modified. For the second monitoring technique (MT-2), we consider that an optical monitoring technique is used, so that the influence of the error in the refractive index value is reduced by a modified thickness of each layer to obtain the optical thickness of the perfect designed filter at the wavelength λ_0 [13,14]. The refractive index error is assumed to be 2.5% for both monitoring techniques.

The results of the analysis point out the relationship between these two monitoring techniques and the most critical layer interactions. This knowledge of layer interactions is very helpful in improving optical coating manufacturing or to determine during a process the best potential layers that could correct errors on a previous deposited layer.

The method is described in Section 2, and the results of the bandpass filter and the AR coating are discussed in Sections 3 and 4. Final conclusions and perspectives are presented in Section 5.

2. Method

In this section, we present the methodology of the sensitivity analysis, the underlying metamodel for our study, the characteristics of the filters, and the monitoring techniques.

The sensitivity analysis of optical properties of the filters is assessed by the following merit function F:

$$F = \sqrt{\sum_i (T(\lambda_i) - T_p(\lambda_i))^2} \text{ for the bandpass filter,} \quad (1)$$

$$F = \sqrt{\sum_i (R(\lambda_i) - R_p(\lambda_i))^2} \text{ for the AR coating,} \quad (2)$$

where $T(\lambda_i)$ [respectively, $R(\lambda_i)$] is the transmittance (respectively, the reflectance) of the filter at the wavelength λ_i in the case of the computer experiment (with error in refractive index values), $T_p(\lambda_i)$ [respectively, $R_p(\lambda_i)$] is the transmittance (respectively, the reflectance) of the perfect filter. The calculation of the transmittance and the reflectance for each wavelength λ_i is done by the use of the basic theory of multilayer coatings [7,15], and the incremental step between λ_i and λ_{i+1} for calculation is 1 nm.

These merit functions F evaluate the transmittance influence on the spectral range [0.9–1.1 μm] for the bandpass filter and the reflectance influence on the spectral domain [0.42 μm, 0.75 μm] for the AR coating due to refractive index errors δn_i.

The metamodels, which approximate the relationship between the merit function F, which is the output of the code, and the filter parameters, which are the errors in refractive index values for this study, are built using numerical designs of computer experiments to reveal interactions between the refractive index values of the layers. The underlying empirical model chosen in this study is a second-order polynomial model in order to consider potential curvature in the domain and interaction effects:

$$Y = a_0 + \sum_i b_i X_i + \sum_i b_{i,i} X_i^2 + \sum_{i<j} b_{i,j} X_i X_j, \quad (3)$$

where Y is the response of the metamodel, X_i is the undimensional variable corresponding to the ith parameter. In this paper, we assume that Y is the approximate of the merit function F and the parameters X_i are the errors of the refractive index values of the layer $i(\delta n_i)$, b_i and $b_{i,i}$ quantify the effect of the ith parameter (δn_i) and the curvature on this parameter axis and $b_{i,j}$ the effect of the interaction between the ith and jth parameters $(\delta n_i \delta n_j)$. Y is the multilinear regression built on a set of computer runs where each numerical run computes the F value for a given set of the X_i values.

Let us now consider the study of two monitoring techniques with errors on the refractive index values of each layer on the following optical coatings:

- A three-cavity bandpass filter composed of 29 layers with the filter formula: substrate/ $[(HL)^2\ 4\text{H}\ (LH)^2]^3$/air, where H and L are quarter-wave layers at $\lambda_0 = 1\,\mu$m, respectively, of high ($n_{\text{H}} = 2.35$) and low ($n_L = 1.3$) refractive index values, and with a low refractive index as a coupling layer between the Fabry–Perot filters $[(HL)^2\ 4H\ (LH)^2]$. To explore this 29-dimension space, two SFDs are used with 598 and 614 computer runs and two Monte Carlo designs with 614 computer runs, respectively. We present simultaneously the comparison between the results obtained by numerical SFD and Monte Carlo design and the evolution of the results obtained when using similar designs to appreciate, in this last case, the stability of results.
- An AR coating designed for the visible spectral on the basis of materials with the refractive indices of $n_{\text{L}} = 1.38$, $n_H = 2.30$ with glass featuring $n_s = 1.52$ as the substrate and air as the outer space. We have considered an eight-layer AR described by Baskakov and Tikhonravov [16] with the filter formula: substrate/ $0.259H\ 0.291L\ 0.149H\ 0.074L\ 1.915H\ 0.107L\ 0.311H\ 1.052L$/air at

$\lambda_0 = 0.5\,\mu$m. This filter is studied by a SFD with 159 computer runs.

In the case of the MT-1, corresponding to quartz monitoring [7], which is widespread in the optical coating industry, these two examples of coatings are presented in Figs. 1 and 2 to show the influence of the errors of the refractive index values (maximum error value of 2.5%) on the optical properties of the filter. Thus, the curves of Filters 1 and 2 show the modifications of the spectral transmittance or reflectance of the considered coatings obtained by two computer runs of the calculation set of the SFDs: bandpass filter (Fig. 1) and AR coating (Fig. 2) due to errors in the refractive index values of each layer.

In the case of MT-2, corresponding to optical monitoring, Figs. 3 and 4 show the influence of the errors of the refractive index values on the optical properties of the filter. The curves of Filters 1 and 2 are calculated with the same error values used in Figs. 1 and 2. We notice that the optical monitoring technique is more efficient on a quarter-wave coating.

3. Influence of Monitoring Techniques in the Case of the Bandpass Filter

In this section, divided into two parts, we discuss the results obtained by the global sensitivity analysis of the bandpass filter. We discuss the results corresponding to MT-1 in the first part and those related to MT-2 in the second part. Comparisons between the monitoring techniques are highlighted, and commentaries from the multilayer coating production knowledge complete the discussion.

The merit function F evaluates the transmittance influence of the refractive index value errors on the spectral domain (0.9 and 1.1 μm). The range of the values obtained for the merit function F with all

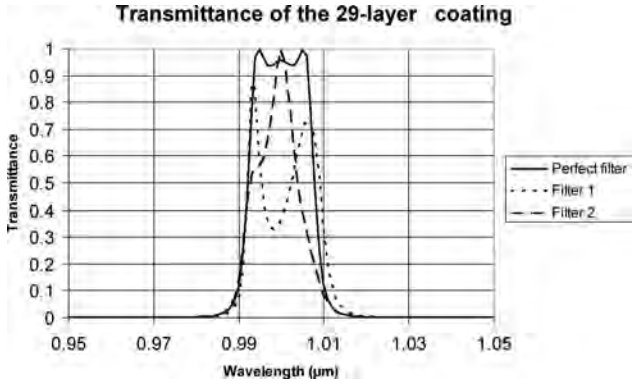

Fig. 1. Transmittance of the perfect bandpass filter and two computer runs (Filters 1 and 2) with errors in the refractive index values (MT-1). The values of δn_i (%) for each layer of Filter 1 are 0.76, −0.29, −1.21, −1.92, 2.09, 0.04, 1.17, 1.91, 1.89, 0.28, −1.04, 1.98, −2.16, −1.32, −1.35, 1.9, 2, 0.99, −2.24, 1.57, 1.61, −2.06, −1.87, −0.98, 1.38, 2.43, −1, −0.29, and −1.13. The values of δn_i (%) for each layer of Filter 2 are 0.64, 0.6, 1.29, −1.68, −1.32, 0.12, 2.11, −2.09, 1.09, −1.59, 2.03, −1.93, 2.04, −2.29, 0.43, 0.24, −0.99, −1.66, 0.7, 2.13, −0.21, 1.55, −0.41, −1.28, 1.32, 2.19, 1.52, 1, and 2.04.

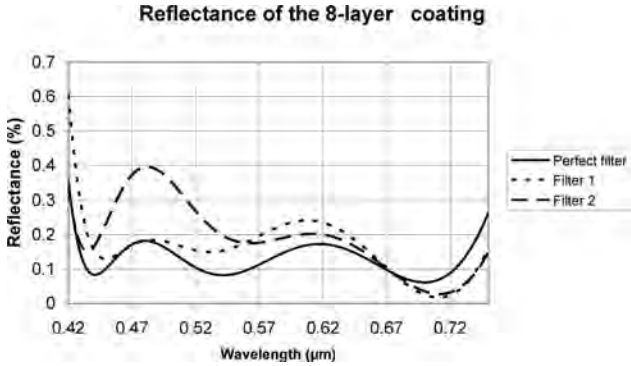

Fig. 2. Reflectance of the perfect AR filter and two computer runs (Filters 1 and 2) with errors in the refractive index values (MT-1). The values of δn_i (%) for each layer of Filter 1 are 0.54, −0.22, −0.28, 1.06, 0.81, 1.25, −0.67, and −0.45. The values of δn_i (%) for each layer of Filter 2 are 0.85, −0.71, −0.7, 0.33, −1.23, 0.22, −0.36, and 0.69.

the designs is [0, 4.30], the mean of the response values is 1.81, and the mean square error is 0.63.

For the bandpass filter, in the case of MT-1, the global sensitivity analysis gives well-known results [7] for this typical coating: the most critical interactions of layers of the bandpass filter are given by the interactions of the layers of the subcoating $L4HL$ and by the interactions between the $4H$ spacer layers of these blocks. All layer interactions are considered in this work, and only significant major coefficients of the interactions of layers are presented in Table 1. But with few computer runs, the relationship between the layers with errors on refractive index values is determined too: the metamodel has a coefficient of determination R square greater than 0.96, so the polynomial regression approximates very well the computed values of the merit function. The value of the coefficient a_o can give a deviation assessment of the metamodel quality: in the case of no refractive index error, the exact value of F is null so the exact value of a_o is 0. In Table 1, we present the best and the worst results obtained with two types of designs: SFD and Monte Carlo. The use of the Monte Carlo method is not as efficient as the SFD: the major interaction coefficient identification is

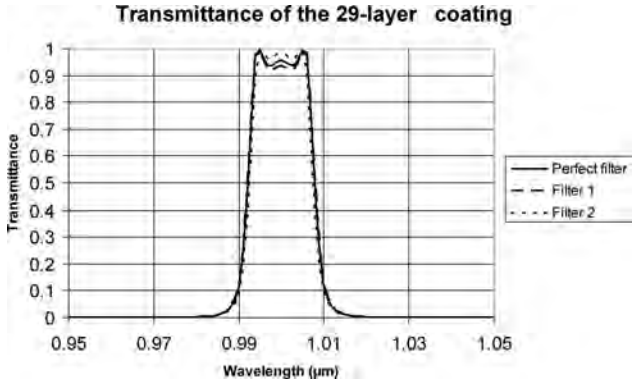

Fig. 3. Transmittance of the perfect bandpass filter and two computer runs (Filters 1 and 2) with errors in refractive index values (MT-2).

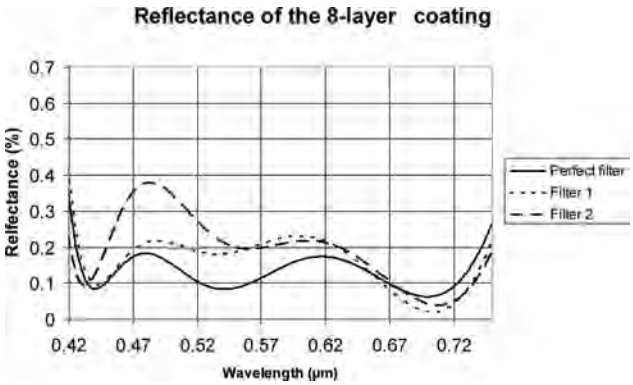

Fig. 4. Reflectance of the perfect AR filter and two computer runs (Filters 1 and 2) with errors in refractive index values (MT-2).

more dependent from the Monte Carlo design, and the deviation coefficients a_o are always greater than those obtained with the SFD. For that reason, the other results of the study were performed only by the use of SFDs. The well-known influence of spacer layers 5, 15, and 25 for this type of coating is observed by the b_i or $b_{i,j}$ coefficients. For example, the major coefficients for the metamodel built by the use of the SFD with 614 runs are given in Table 2. It can be noticed from these results that the major coefficients are square terms ($b_{i,i}$) or interaction terms ($b_{i,j}$). In this polynomial regression, the rank of the first b_i coefficient is higher than 100.

In the case of MT-2, assumed as an optical monitoring, the R square values of the metamodels built with Eq. (3) are greater than 0.98. The range of the values obtained for the merit function F with the two designs is [0, 0.38]. The mean of the response values is 0.11, and the mean square error is 0.06. The global sensitivity analysis for the response F reveals that the major coefficients of the multilinear regression Y correspond to the interaction coefficients of the layers with low refractive index values (Table 3). We can notice slight differences between the major interaction coefficients or a_o given by both SFDs due to the statistic and empiric determination of the metamodel. The results given with these two different SFDs never induce opposite conclusions but confirm the most critical layer blocks.

Table 1. Nine Major Coefficients of Each Design Show the Most Critical Interactions between Layers for MT-1

Method, Number of Computer Runs	Major Interaction Coefficients (Decreasing Order)	Value of a_0
SFD, 614	b_{14-15}, b_{15-16}, b_{4-5}, b_{5-6}, b_{25-26}, b_{15-18}, b_{24-25}, b_{16-21}, b_{13-15}	0.53
SFD, 598	b_{14-15}, b_{15-16}, b_{4-5}, b_{5-6}, b_{24-25}, b_{15-17}, b_{13-15}, b_{15-18}, b_{5-25}	0.02
Monte Carlo, 614	b_{15-16}, b_{14-15}, b_{5-6}, b_{25-26}, b_{15-25}, b_{5-25}, b_{17-24}, b_{4-5}, b_{24-25}	0.81
Monte Carlo, 614	b_{14-15}, b_{15-16}, b_{4-5}, b_{5-6}, b_{15-17}, b_{15-18}, b_{16-20}, b_{11-12}, b_{7-25}	0.75

Table 2. Nine Major Coefficients of the Metamodel for MT-1

Method, Number of Computer Runs	Major Metamodel Coefficient Values (Decreasing Order)
SFD, 614	$b_{15-15} = 2068$, $b_{5-5} = 1129$, $b_{25-25} = 867$, $b_{14-15} = 824$, $b_{15-16} = 768$, $b_{4-5} = 497$, $b_{5-6} = 425$, $b_{25-26} = 344$, $b_{15-18} = 335$

By this example, the results point out the most critical layers and mainly the associated interactions to obtain the desired optical properties by taking into account the characteristics of the monitoring technique. By an optical monitoring technique that reduces the influence of the errors of refractive index values at the control wavelength $\lambda_0 = 1\,\mu$m, the sensitivity analysis points out that the most critical interactions concern layers 6, 8, 10, and 12, where the sixth and eighth layers are of low refractive index of the second mirror of the first Fabry–Perot filter, the tenth layer is the first coupling layer, and the twelfth layer is the second layer of the first mirror of the second Fabry–Perot filter. Generally, the coupling layer is very critical, using an optical transmission monitoring, because the dynamic of the manufacturing signal is about 3% to 4% for this layer, which depends on realization errors of the Fabry–Perot layers. We note that this coupling layer (tenth layer) associated with the sixth, eighth, and twelfth layers appears to be the major block basis of sensitive layers of this three-cavity bandpass filter to obtain good transmission and the desired bandwidth. Also, this analysis confirms that an optical monitor working in transmittance with extremum criterion $\partial T/\partial t = 0$ at λ_0 is the best way to manufacture bandpass filters with quarter-wave layers [17] and to compensate for error realization.

The most critical interactions of layers regarding the possible errors in the refractive index values during the process are extremely dependent on the considered processes MT-1 and MT-2. Independently of the precision of the different supplies involved during manufacturing, modifications in the monitoring strategy can induce specific performance requirements to control the new most sensitive layers. The sensitivity analysis of optical coatings by numerical SFDs is a new method in the design of the coating field, and it is very powerful for assessing the potential robustness of filters by taking into account the monitoring strategy with a limited number of runs

Table 3. Most Critical Interactions between Layers for MT-2

Number of Computer Runs (SFD)	Six Major Interaction Coefficient Values	Value of a_0
614	$b_{6-10} = 48$, $b_{6-12} = 40$, $b_{8-10} = 37$, $b_{8-12} = 45$, $b_{10-12} = 53$, $b_{12-14} = 43$	0.001
598	$b_{6-8} = 50$, $b_{6-10} = 43$, $b_{6-14} = 38$, $b_{8-10} = 50$, $b_{8-12} = 45$, $b_{10-12} = 41$	0.004

of the code. Furthermore, the coefficients and their associated sign can indicate a way to efficiently correct an error on a deposited layer by the following layers, which will be produced.

In the first conclusion, with this example of an optical coating, the strategy to manufacture bandpass coatings can be associated with SFDs and allow manufacturers to define the best monitoring technique for building a specific coating and to appreciate during the manufacturing the possibility of compensating for the errors on previously deposited layers. Global sensitivity analysis by SFD is a new approach in optical coating manufacturing and can provide good results with optical monitoring for bandpass filters, for example, for optic wavelength-division multiplexing telecom filters.

4. Application to the Determination of the Most Critical Interactions in the Case of an Antireflection Filter with Non-Quarter-Wave Layers

In this section, we discuss the results obtained by the global sensitivity analysis of the AR coating. This section consists of two parts. We discuss the results corresponding to MT-1 in the first part and those related to MT-2 in the second part. Perspectives to improve the manufacturing techniques of non-quarter-wave layers are presented.

We notice that all thicknesses of the eight layers of the AR coating are non-quarter-wave AR, and this filter is composed of three very small thickness (t) layers, of the order of 7 nm (third, fourth, and sixth layers) and two of the order of 16 nm (first and seventh layers). The sensitivity analysis is performed by the use of a SFD with 159 points: now, only this one SFD using 159 computer runs is considered to identify the most sensitive layers. In the case of MT-1, the range of values of the merit function F is [0, 0.033] with a mean of 0.013 and a mean square error of 5.5×10^{-3}. In the case of MT-2, the range of values of the merit function F is [0, 0.027] with a mean of 0.012 and a mean square error of 5.1×10^{-3}. All the metamodels have a coefficient of determination R square greater than 0.96, so the polynomial regression approximates very well the computed values of the merit function for this AR filter.

Because of the broadband characteristic of this AR coating, the merit function F evaluates the reflectance influence of the refractive index value errors on the following four spectral ranges: [0.42 μm, 0.75 μm], [0.45 μm, 0.72 μm], [0.45 μm, 0.52 μm], and [0.52 μm, 0.72 μm]. By this way, it is possible to expose the relationship between the criticality of the layers and the global reflectance or a specific spectral domain.

The results obtained for the study of MT-1 are presented in Table 4. Initially, we notice that the highest coefficient corresponds to the first layer (coefficient b_{1-1}), which is known to be very sensitive in the quality of an AR coating. These results point out that for the spectral domains [0.42 μm, 0.75 μm] and [0.45 μm, 0.72 μm], the least critical interaction layer is layer 6. But for these broadband spectral ranges, we note that the other thinnest layers (third and fourth) have the greatest interaction coefficients with the first and the last layers. The interaction between layer 1 and layer 2 is the most important on the optical properties of the perfect filter except in the spectral domain [0.52 μm, 0.72 μm]. In this last domain, the interactions of layer 1 with layers 8 and 7 are the most important but are noted secondly in the case of the reduced spectral domain [0.45 μm, 0.52 μm]. The relationships corresponding to the other thinnest layers (third and fourth), appear only with the first layer, in this short spectral band. So the global sensitivity analysis by SFD allows us to detect the most critical layers for the broadband optical properties and to determine in which spectral subdomains the impact of these interactions is the most crucial. This analysis confirms the classical results related to the AR coating production, where generally the first and last layers are often more prone to errors and can limit optical properties of this type of coating for a given spectral range, but points out simultaneously the new knowledge concerning the most critical interactions between layers.

Table 4. Six Most Critical Coefficients for MT-1 and the Relationship between Layers and Spectral Domains

Spectral Domain	Six Significant Major Coefficients (Decreasing Order)	Value of a_0
[0.42–0.75 μm]	b_{1-1}, b_{1-2}, b_{4-8}, b_{2-2}, b_{7-8}, b_{1-3}	4.5×10^{-3}
[0.45–0.72 μm]	b_{1-1}, b_{1-2}, b_{2-2}, b_{7-8}, b_{1-3}, b_{1-4}	4×10^{-3}
[0.45–0.52 μm]	b_{1-1}, b_{1-2}, b_{1-8}, b_{1-4}, b_{1-3}, b_{1-7}	2.5×10^{-3}
[0.52–0.72 μm]	b_{1-1}, b_{1-8}, b_{1-7}, b_{2-2}, b_{2-7}, b_{4-8}	2.7×10^{-3}

In the case of MT-2, because layers are non-quarter-wave layers at wavelength $\lambda_0 = 0.5\,\mu$m, several direct methods for optical monitoring can be used to manufacture the AR coating. The first is the level monitoring of transmittance or reflectance associated with different sensitive wavelengths for each layer [18]. The second is based on the stop deposition of each layer as soon as the zero value of $\partial T/\partial t$ or $\partial R/\partial t$ for wavelength λ_i is observed. In this case of optical monitoring of non-quarter-wave layers [19], it is necessary to determine, for each layer, the different wavelengths that provide an extremum of transmittance/reflectance when the required thickness is achieved. And the third method possible is optical broadband optical monitoring [20]. To manufacture and to reproduce this eight-AR coating, we specify that layers 1, 3, 4, and 6 are the most critical layers, whichever the optical monitoring technique, because either the dynamics of the optical signal are very low or there are no wavelengths for the extremum method in the spectral range [0.42 μm, 0.75 μm]. If optical thickness errors during production can be compensated for by optical monitoring, it is more complicated to understand the interactions between the layers. The results, corresponding to the sensitivity analysis, are presented in Table 5. As for

the bandpass filter, the optical monitoring technique introduces modifications in the rank of the interactions between layers. Because of the non-quarter-wave layers of this filter, we do not obtain completely different sensitivity analysis results. Indeed, in the broad spectral bands [0.42 μm, 0.75 μm] and [0.45 μm, 0.72 μm], the four major interaction coefficients are the same, and here the interaction between layer 1 and layer 3 is the most important and the fifth, sixth, and eighth layers are less critical. We note also that layer 1 interacts with layers 2 and 4, which is a critical layer in manufacturing the AR coating due to its very thinness. Furthermore, this layer presents high interaction coefficients with layers 1, 2, and 7. For the two spectral ranges [0.45 μm, 0.52 μm], respectively, [0.52 μm, 0.72 μm], we note that the major interactions are between layers 1 and 2 and 4 and 7, respectively. For the second major interactions, Table 5 shows four strong interactions with the first layer, which appears as very sensitive in this first spectral range, and for the last spectral range [0.52 μm, 0.72 μm], there are the fourth and first layers, which are the most sensitive. As for MT-1, the quality of layer 1 is very important because the $b_{1,1}$ coefficient is the highest one, but we notice that in the spectral domains [0.45 μm, 0.52 μm] and [0.52 μm, 0.72 μm] that layer 7 has an effect higher than the second layer due to the rank of the coefficients $b_{7,7}$ and $b_{2,2}$, respectively.

In comparison with MT-1 and MT-2 and for a second conclusion, the SFDs give different interactions between non-quarter-wave layers for a given spectral range. With this study for this broadband AR, it appears in common points that the first layer interacts with the second and third layers, and an essential point is that these three layers are the most sensitive to errors in the manufacture of this eight-AR optical coating. These results can imply that, in the case of non-quarter-wave layers, various monitoring strategies, such as level monitoring, optical monitoring of non-quarter-wave layers, and broadband optical monitoring, should be assessed by this method of global sensitivity analyses to determine the critical difficulties about the coating production. In this way, it could be possible to acquire the knowledge of the relationships between the layers and monitoring techniques due to stochastic errors and to use for a second time the less sensitive monitoring technique associated with the desired optical properties of a thin films filter.

Table 5. Six Most Critical Coefficients for MT-2 and the Relationship between Layers and Spectral Domains

Spectral Domain	Six Significant Major Coefficients (Decreasing Order)	Value of a_0
[0.42–0.75 μm]	b_{1-1}, b_{1-3}, b_{1-4}, b_{1-2}, b_{4-7}, b_{2-4}	4.5×10^{-3}
[0.45–0.72 μm]	b_{1-1}, b_{1-3}, b_{4-7}, b_{7-7}, b_{2-4}, b_{1-2}	4.2×10^{-3}
[0.45–0.52 μm]	b_{1-1}, b_{1-2}, b_{1-8}, b_{1-3}, b_{1-5}, b_{7-8}	2.2×10^{-3}
[0.52–0.72 μm]	b_{1-1}, b_{4-7}, b_{1-4}, b_{1-8}, b_{2-4}, b_{7-7}	3.6×10^{-3}

From the study of these two examples, the approach of experimental design and, more particularly, the SFD, appear as a new method to identify the most sensitive layers of coatings to manufacture. Whatever the monitoring technique used, this method could appear also as an excellent guide to help optical coating production, and, if it associated itself with the synthesis method, SFD could help to choose more stable coating solutions.

5. Conclusion

In this study, a new method is proposed to assess the robustness of filters and to improve the monitoring techniques. Using SFDs to perform global sensitivity analysis, we propose to explore monitoring techniques and determine the most critical layers and interactions in optical coatings. This methodology, which reveals that the criticality of a set of layers depends on the monitoring technique, can be used in the case of quarter and non-quarter optical coatings. In the case of a high number of layers, the most critical interactions are determined with a good quality and are better than those given by the Monte Carlo method. The assessment of the potential robustness of coatings by taking into account the monitoring strategy is very fast, and in the case of broadband filters, the influence of the layers or interactions on specific subdomains can be determined. The quality of the results obtained on the determination of the influence of the interactions of refractive index errors between layers allows us to study the influence of errors on refractive index values and thickness values. This objective should be the next step in exploring higher dimensional spaces and more complicated interactions between the characteristic parameters of optical coatings. The quality of the results obtained in the interference optics is an encouragement for extending this approach to assessing the substrate influence by the study of the relationship between the thin films and a waveguide substrate [21,22] and is mainly an encouragement to study the interactions of parameters in interference complex optronic systems [23,24].

References

1. R. W. Kennard and L. A. Stone, "Computer aided design of experiment," Technometrics **11**, 137–148 (1969).
2. M. Sergent, R. Phan-Tan-Luu, and J. Elguero, "Statistical analysis of solvent scales. part 1," Anales Quimica Int. Ed. **93**, 3–6 (1997).
3. J. S. Park "Optimal Latin-hypercube designs for computer experiments," J. Statist. Plann. Inference **39**, 95–111 (1994).
4. J. R. Koehler and A. B. Owen, "Computer experiments" in *Handbook of Statistics*, S. Ghosh and C. R. Rao, eds. (Elsevier, 1996), Vol. 13, pp. 261–308.
5. A. Saltelli, K. Chan, and E. M. Scott, *Sensitivity Analysis* (Wiley, 2000).
6. T. J. Santner, B. J. Williams, and W. I. Notz, *The Design and Analysis of Computer Experiments* (Springer, 2003).
7. H. A. Macleod, *Thin Film Optical Filters* (Hilger, 1986).
8. P. C. Young, "Data-based mechanistic modelling, generalised sensitivity and dominant mode analysis," Comput. Phys. Commun. **117**, 113–129 (1999).

9. A. A. Giunta, S. F. Wojtkiewicz, and M. S. Eldred, "Overview of modern design of experiments methods for computational simulations," in *Proceedings of the 41st AIAA Aerospace Sciences Meeting and Exhibit*, AIAA-2003-0649 (American Institute of Aeronautics and Astronautics, 2003).
10. G. G. Wang and S. Shan, "Review of metamodeling techniques in support of engineering design optimization," J. Mech. Des. **129**, 370–380 (2007).
11. G. E. P. Box, W. G. Hunter, and J. S. Hunter, *Statistics for Experimenters* (Wiley, 1978).
12. O. Vasseur, M. Claeys-Bruno, M. Cathelinaud, and M. Sergent, "High dimensional sensitivity analysis of complex optronic systems by experimental designs: applications to the case of the design and the robustness of optical coatings," Chin. Opt. Lett. **8**(1), 21–24 (2010).
13. H. A. Macleod, "Turning value monitoring of narrow-band all-dielectric thin film optical filters," Opt. Acta **19**, 1–28 (1972).
14. H. A. Macleod and E. Pelletier, "Error compensation mechanisms in some thin-film monitoring systems," Opt. Acta **24**, 907–930 (1977).
15. M. Born and E. Wolf, *Principles of Optics* (Pergamon, 1970).
16. A. N. Baskakov and A. Tikhonravov "Synthesis of two component optical coatings," Opt. Spectrosc. **56**, 915–919 (1984).
17. P. Bousquet, A. Fornier, R. Kowalczyk, E. Pelletier, and P. Roche, "Optical filters: monitoring process allowing the autocorrection of thickness errors," Thin Solid Films **13**, 285–290 (1972).
18. A. Tikhonravov, M. Trubetskov, and T. Amotchkina, "Computational experiments on optical coating production using monochromatic monitoring strategy aimed at eliminating a cumulative effect of thickness errors," Appl. Opt. **46**, 6936–6944 (2007).
19. B. J. Chun, C. K. Hwangbo, and J. S. Kim, "Optical monitoring of nonquarterwave layers of dielectric multilayer filters using optical admittance," Opt. Express **14**, 2473–2480 (2006).
20. B. Badoil, F. Lemarchand, M. Cathelinaud, and M. Lequime, "Interest of broadband optical monitoring for thin-film filter manufacturing," Appl. Opt. **46**, 4294–4303 (2007).
21. C. Vassallo, "Reflectivity of multidielectric coatings deposited on the end facet of a weakly guiding dielectric slab waveguide," J. Opt. Soc. Am. A **5**, 1918–1928 (1988).
22. O. Vasseur, "Reflectivity of dielectric coatings deposited on the end facet of a weakly guiding fiber," J. Opt. Soc. Am. A **15**, 77–83 (1998).
23. T. M. Shay, V. Benham, J. T. Baker, A. D. Sanchez, D. Pilkington, and C. A. Lu, "Self-synchronous and self-referenced coherent beam combination for large optical arrays," IEEE J. Sel. Top. Quantum Electron. **13**, 480–486 (2007).
24. V. Jolivet, P. Bourdon, B. Bennaï, L. Lombard, G. Goular, E. Pourtal, G. Canat, Y. Jaouën, B. Moreau, and O. Vasseur, "Beam shaping of single-mode and multimode fiber amplifier arrays for propagation through atmospheric turbulence," IEEE J. Sel. Top. Quantum Electron. **15**, 257–268 (2009).

Investigation of manufacturing processes by numerical sensitivity analysis

Olivier Vasseur*[a], Michel Cathelinaud[b]
[a]Onera – The French Aerospace Lab., F-91761 Palaiseau, France;
[b]MRCT, UPS CNRS 2274, F-92195 Meudon, France

ABSTRACT

During the manufacturing of optical coatings, errors in refractive index values or in thickness values of each layer of the coating can induce dramatic consequences on the desired optical properties. Global numerical sensitivity analyses using space filling designs and metamodels were applied in the case of the influence study of different errors on optical filter characteristics to determine the most critical interactions of layers.

We propose to use space filling designs to assess, by computer experiments, the sensitivity of optical filters to the simultaneous errors in the refractive index values and thickness values. In this study, the principal characteristics of space filling designs are presented and are compared to random designs. This comparison allows us to identify the best types of space filling designs to conduct sensitivity analysis with few computer runs.

We will present the first results concerning the global sensitivity analysis of different coatings in the case of simultaneous errors in refractive index values and in thickness values. We consider for this study two monitoring techniques: a quartz monitoring and an optical monitoring. By this way, we will highlight the influence of correlated errors on the most critical interactions classification and give a different perspective to these monitoring techniques.

In conclusion, this computational study gives clues to the understanding of error propagation in manufacturing processes and points out the most critical interactions in coatings to improve the robustness of optical coatings and to reduce the production costs.

Keywords: Optical design and fabrication, System design, Thin films, Materials and process characterization, Multilayer coating design, Refinement and synthesis methods, Sensitivity analysis, Space Filling Design, Computer experiments, Minimal spanning tree, Minimum spanning tree, Metamodel.

1. INTRODUCTION

Four important points are considered in each optical coating application to produce optical coatings: materials, characterization, design modeling and technology deposition for production. Ideally, material coatings for optical applications must exhibit excellent performance with following requirements which are stringent: low optical absorption values, film refractive indices close to bulk values and dense homogeneous microstructures with smooth surfaces and interfaces to reduce light scattering and to secure film characteristics under varying conditions of humidity and temperature, high adherence, hardness and abrasion resistance and high environmental stability.

For the technology deposition, evaporation and sputter deposition and a considerable number of technologically innovative variants of these basic processes are today available for thin film production. Particularly the reactive modes of materials are important to produce the correct stoichiometric compound film. The ion and plasma processes with controlled kinetic particle energy are often preferred in reactive evaporative deposition for densification of the layers and improvement in adherence, hardness, abrasion resistance and stoichiometry. All the ion beam assisted depositions with various broad-beam ion sources, ion plating, are used mainly for the production of various environmental stable dielectric multilayer products in instrument optics and in spatial applications [1].

*olivier.vasseur@onera.fr; phone 33 1 80 38 63 53; fax 33 1 80 38 63 45; onera.fr

Advances in Optical Thin Films IV, edited by Michel Lequime, H. Angus Macleod, Detlev Ristau,
Proc. of SPIE Vol. 8168, 81680A · © 2011 SPIE · CCC code: 0277-786X/11/$18
doi: 10.1117/12.896785

In the case of optical characterization, photometric and ellipsometric techniques are used in situ and/or ex situ, to assess manufactured optical coating component [2]-[4]. In industrial applications, quartz monitoring is often preferred to optical monitoring techniques for economy. But in both cases, the influence of errors during the manufacturing of coatings must be reduced to obtain the desired coatings.

Due to the increase of computer power, the design modeling, which is based on Abeles matrix, can describe very precisely the optical properties (transmittance, reflectance and absorption) of very complicated classical multilayer filters [5]. The calculation power of computers supported the development of the needle method in numerical synthesis [6].

In the case of computer simulators, when the relations between the outputs and the inputs of a computer code are complex, the space filling designs (SFDs) [7]-[10] are used to study the outputs all over the domain, to build metamodels, to study the uncertainties propagation, or to determine by global sensitivity analysis the most sensitive inputs on the outputs [11]-[13]. Indeed, parameters such as refractive index errors or thickness errors during the production of these layers can induce dramatic consequences on the desired optical properties [5]. The global sensitivity analysis methodology is very helpful to determine the influence of errors in refractive indices on the optical properties and to quantify the interactions between the errors of each layer [14], [15].

In this paper, we extend the sensitivity analysis to the case of the influence of errors in refractive index and thickness values of multilayer coatings. We exhibit the most important interactions of layers on the optical properties due to errors in the refractive index values and in the thickness values. To point out the influence of independent errors and correlated errors, we consider two monitoring techniques for the manufacturing process of the filters. In the case of the monitoring technique MT-1, corresponding to a quartz monitoring, the errors in refractive index values are independent. But, for the second monitoring technique MT-2, corresponding to an optical monitoring, the influence of the error in the refractive index value is reduced by a modified thickness of the layer to obtain the optical thickness of the perfect designed filter at the wavelength λ_0. But this new design thickness value is then modified by residual errors in the thickness value. In this case, the errors in refractive index values and in the thickness values are then correlated.

We consider two bandpass filters: a classical two cavities bandpass and a bandpass filter with a very low transmittance in a large spectral domain.

We point out the most critical interactions between layers for both monitoring techniques and exhibit the key points to improve manufacturing processes.

2. METHOD

2.1 Qualification of Space Filling Designs by Minimal Spanning Tree

Consider a set of N points which are randomly distributed in a d-dimensional region with a volume of V. An edge-weighted linear graph G = (X,E) is composed of a set of points $X = \{x_1, x_2, \ldots x_N\}$ called nodes and a set of node pairs $E = \{(x_i, x_j)\}$ called edges, with a number called weight (the Euclidean distance in our case) assigned to each edge. A graph is connected if there is a path connecting every pair of nodes and a tree is a connected graph without closed loops. A Minimal Spanning Tree (MST) is a tree which contains all the nodes with a minimal sum of the edge weights [16].

Depending on the starting point there may be more than one MST for a given set of points, but all of the MST's have the same length-edge histogram [16], [17]. The normalized values of the mean m and the standard deviation σ of the edge length can be used to characterize the distribution of points (ordered, random, cluster...) [17] as shown on the Figure 1. In the field of topographical analysis, this method presents the advantages of a high discrimination power and stability to characterize spatial point patterns [18], [19].

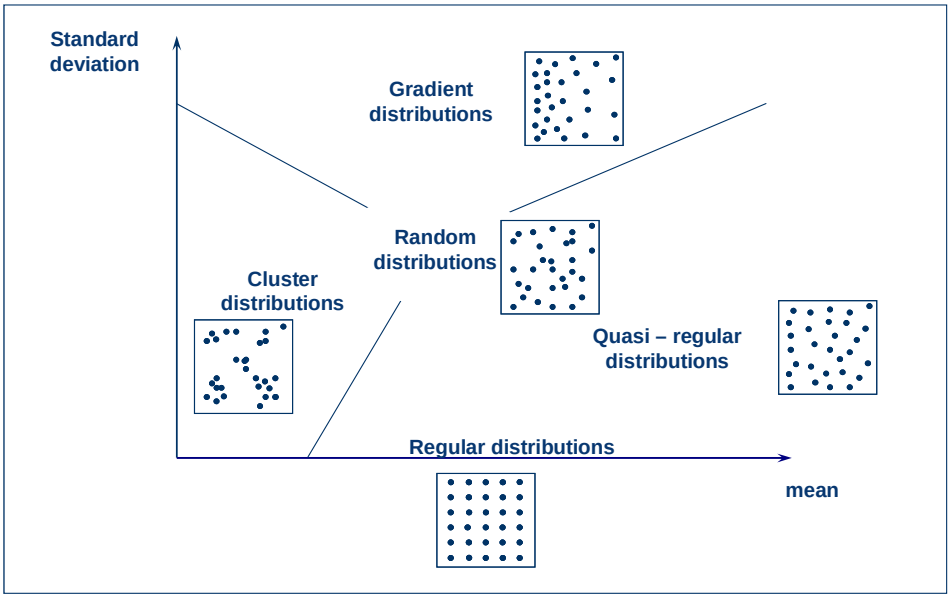

Figure 1: Points distributions in the (m, σ) plane.

From the MST, the mean m and the standard deviation σ of the edges length may be used as characteristics for the corresponding distribution of the SFD points. On this graphical representation, it is possible to distinguish different areas and mainly the quasi-regular area which is the best area for space filling designs due to the best compromise between a high average length of MST branches to fill the space and a small standard deviation to obtain a sufficient regularity: for example random designs have points too closed and grid designs (σ = 0) are too regular. Moreover with perfect ordered structure (σ = 0), the points are not evenly spread across the projection of the experimental space onto all subspaces [20].

The classical space-filling designs that had good properties (quasi-regular distribution) in low dimension are no more in the quasi-regular area in high dimensional spaces, and are, in the best case, closed to the random distribution area [21]. The Figure 2 shows classical SFD and a specific regular SFD in the (m, σ) plane in the case of 29-dimensions (29-D) space: we can notice that classical low discrepancy sequences (Faure, Halton, Sobol) and Latin Hypercube Designs (LHD) are, in the best case, closed to the random distribution.

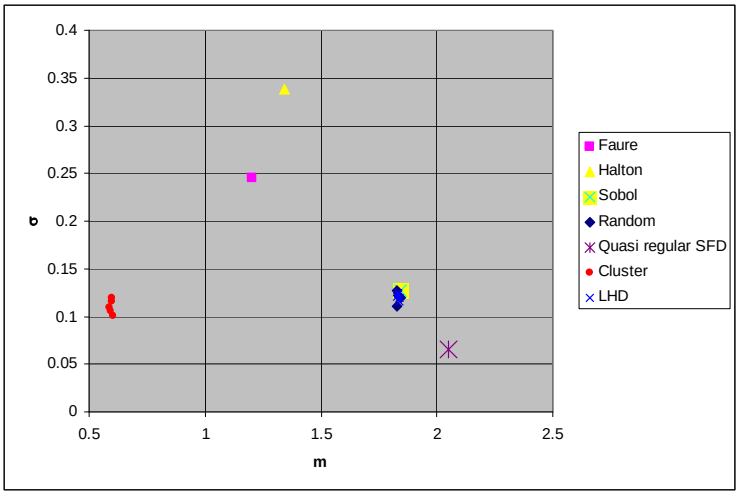

Figure 2: Representation of the average m and standard deviation σ of the edge length for various designs with ~600 points in 29-D space.

Due to this evolution of the quality of classical SFD, we use specific designs which guarantee the quasi-regular distributions and good results with less runs than Monte-Carlo method [21], [22]-[25].

2.2 Sensitivity analysis and metamodel identification

In this section, we present the methodology of the sensitivity analysis, the underlying metamodel for our study, the characteristics of the filters and the monitoring techniques.

The sensitivity analysis of optical properties of the filters is assessed by the following merit function F:

$$F = \sqrt{\sum_i (T(\lambda_i) - T_p(\lambda_i))^2} \qquad (1)$$

where $T(\lambda_i)$ is the transmittance of the filter at the wavelength λ_i in the case of the computer experiment (with errors in the refractive index values or in the thickness values), $T_p(\lambda_i)$ is the transmittance of the perfect filter. The calculation of the transmittance and the reflectance for each wavelength λ_i is done by the use of basic theory of multilayer coatings [5].

These merit functions F evaluate the transmittance influence on the spectral range [1.4-1.6µm] for the 19-layers bandpass filter and the spectral range [0.450-0.9µm] for the 38-layers bandpass filter due to refractive index errors $\delta n = (1+\delta)\cdot n$ and due to thickness errors $\delta t = (1+\delta)\cdot t$ with $|\delta| \leq 0.5\%$.

The metamodels which approximate the relationship between the merit function F, which is the output of the code, and the filter parameters, which are the errors in refractive index and thickness values for this study, are built using numerical designs of computer experiments to reveal interactions between these parameters of the layers.

In the case of errors in refractive index and/or thickness values, the underlying empirical model chosen in this study is a second order polynomial model in order to consider potential curvature in the domain and interaction effects:

$$Y = a_0 + \sum_i b_i \delta_i + \sum_i b_{i,i} \delta_i^2 + \sum_{i<j} b_{i,j} \delta_i \delta_j \qquad (3)$$

where Y is the response of the metamodel, δ_i is the undimensional variable corresponding to the ith parameter. In this paper, we assume that Y is the approximate of the merit function F and the parameters δ_i are the errors of the refractive index or thickness values of the layer i ($\delta n_i = (1+\delta_i)\cdot n_i$ or $\delta t_i = (1+\delta_i)\cdot t_i$) , b_i and $b_{i,i}$ quantify the effect of the ith parameter (δ_i) and the curvature on this parameter axis and $b_{i,j}$ the effect of the interaction between the ith and jth parameters (δ_i δ_i). Y is the multilinear regression built on a set of computer runs where each numerical run computes the F value for a given set of the δ_i values.

Let us now consider the study of two monitoring techniques with errors on refractive index or thickness values of each layer on the following optical coatings:

- A double cavity bandpass filter composed of 19 layers with filter formula: Substrate / $[(HL)^2\ 4H\ (LH)^2]^2$ / air where H and L are quarter-wave layers at λ_0 = 1.5µm respectively of high (n_H= 2.30) and low (n_L=1.3) refractive index values, and with a low refractive index as coupling layer between Fabry-Perot filters $[(HL)^2\ 4H\ (LH)^2]$. To explore the 19-D and 38-D spaces, we built Space Filling Designs with approximately 20 points per dimension.

- A broad bandpass filter with large rejection for long wavelength composed of a multiple cavity filter (15 layers) with formula $(H\ 2L\ H)^2\ (H\ 4L\ H)\ L\ (H\ 2L\ H)$ centred at 540 nm and an adapted 23 layers edge filter with 15 layers and centred at 855.5nm. The refractive index values are the same as the first filter.

In the case of the monitoring technique MT-1, corresponding to a quartz monitoring [5] which is widely spread in optical coating industry, these two examples of coatings are presented on Figures 3 and 4 to show the influence of the errors in the refractive index values (maximum error value of +/-0.5%) on the optical properties of the filter. Thus, the curves show the modifications of the spectral transmittance of the considered coatings obtained by 408 and 826 computer runs of the calculation set of space filling designs: bandpass filter (Fig. 3a) and broad bandpass filter (Fig. 3b) with errors in the refractive index values of each layer.

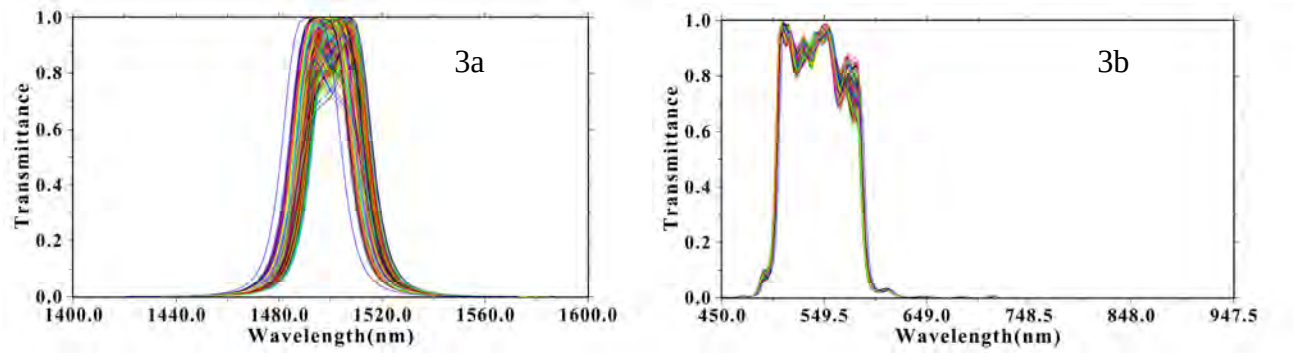

Figure 3: Quartz monitoring technique (MT-1). Influence of errors (+/-0.5%) in the refractive index values: (3a) and (3b) correspond respectively to the transmittance of 408 runs for the first filter (19 layers) and to the transmittance of 826 runs for the broad bandpass filter (38 layers).

In the case of the monitoring technique MT-2, corresponding to an optical monitoring, the Figures 4a and 4b show the influence of the errors of the refractive index values on the optical properties of the filter. The transmittances are calculated with the same error values used on Figures 3a and 3b. We can notice that the optical monitoring technique is very efficient on a quaterwave coating.

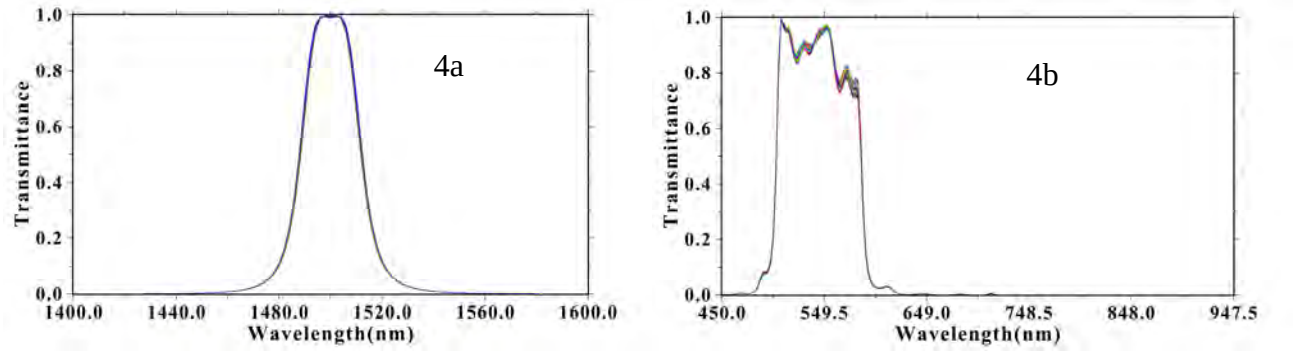

Figure 4: Optical monitoring technique (MT-2). Influence of errors (+/-0.5%) in the refractive index values: (4a) and (4b) correspond respectively to the transmittance of the band-pass filter (19 layers) to the transmittance of the broad bandpass filter (38 layers).

3. INFLUENCE OF THE MONITORING TECHNIQUES AND THE ERRORS IN REFRACTIVE INDICES OR IN THICKNESSES

In this part, we used a SFD with 408 points in a 19-D space for the 19-layers bandpass and a design with 826 points in 38-D space for the 38-layers coating.

3.1 The monitoring technique MT-1, corresponding to a quartz monitoring

All layer interactions are considered in this work, and only significant major coefficients of the interactions of layers are presented on Table 1. All the metamodels have a coefficient of determination R^2 greater than 0.95 so the polynomial regression approximates very well the computed values of the merit function [26].

For the 19-layers filter in the case of monitoring technique MT-1, the global sensitivity analysis give the well-known results for this typical coating: the most critical interactions of layers of the bandpass filter are given by the interactions of the layers of the sub-coating (L 4H L) and by the interactions between the 4H- spacer layers of these blocks. In the case of errors in refractive index values, these results agree those of single cavity and three cavity filters [14], [15].

For interactions between refractive index or thickness layers in the case of the 38 layers, the results in table 1 show that spacer layers are the most important layers and each spacer interacts with the other spacer layers as 10^{th} (4L) and 6^{th} (2L) for the multiple cavity filters.

We can notice that the most critical layers are the same in the case of errors in the refractive index values and in the thickness values. Figures 3a and 3b illustrate evolution of the transmittance with merit function defined in this section.

Table 1: The 6 major coefficients of the metamodel for the monitoring techniques MT-1.

Filter and type of parameters	Major metamodel coefficient values (decreasing order)	The major coefficient value	R^2
19 layers, n	$b_{15\text{-}15}$, $b_{5\text{-}15}$, $b_{5\text{-}5}$, $b_{14\text{-}15}$, $b_{15\text{-}16}$, $b_{15\text{-}17}$	$b_{15\text{-}15} = 325$	0.984
38 layers, n	$b_{10\text{-}10}$, $b_{6\text{-}10}$, $b_{10\text{-}14}$, $b_{14\text{-}14}$, $b_{6\text{-}6}$, $b_{5\text{-}10}$	$b_{10\text{-}10} = 30$	0.995
19 layers, t	$b_{15\text{-}15}$, $b_{5\text{-}15}$, $b_{5\text{-}5}$, $b_{14\text{-}15}$, $b_{15\text{-}16}$, $b_{15\text{-}17}$	$b_{15\text{-}15} = 326$	0.984
38 layers, t	$b_{10\text{-}10}$, $b_{6\text{-}10}$, $b_{10\text{-}14}$, $b_{14\text{-}14}$, $b_{6\text{-}6}$, $b_{9\text{-}10}$	$b_{10\text{-}10} = 31$	0.994

3.2 The monitoring technique MT-2, corresponding to an optical monitoring

All the metamodels have a coefficient of determination R-square greater than 0.95 so the polynomial regression approximates very well the computed values of the merit function.

We can notice that the most critical layers for an optical monitoring are very different from those identified in the case of a quartz monitoring technique. In the case of 19-layers filter, the influence of the refractive index errors is diminished by the optical monitoring technique. The most important interactions concern other layers than those observed with MT-1 (Table 2) : the spacer layers are no more critical layers for example. Figure 4a points out that the 19-layers filter is always well-centered due to the fabrication of the correct optical thickness of the spacer layer by this monitoring technique. This characteristic is translated by low coefficients in the metamodel for these spacer layers. The new layers (8^{th}, 9^{th}, 10^{th}, 13^{th} layers) are less critical due to the low value of the coefficients.

For the 38-layers bandpass filter, composed of four bandpass with a large visible spectral range, we observe that the interactions between the last mirror of second bandpass (7^{th} layer), the first mirror (9^{th} layer) of third bandpass and the coupling layer (8^{th} layer) are the most important interactions.

Table 2: The 6 major coefficients of the metamodel for the monitoring techniques MT-2.

Filter	Major metamodel coefficient values (decreasing order)	The major coefficient value	R^2
19 layers	$b_{8\text{-}9}$, $b_{8\text{-}13}$, $b_{7\text{-}10}$, $b_{9\text{-}13}$, $b_{8\text{-}12}$, $b_{7\text{-}13}$	$b_{8\text{-}9} = -5.1$	0.979
38 layers	$b_{7\text{-}8}$, $b_{8\text{-}9}$, $b_{7\text{-}9}$, $b_{11\text{-}12}$, $b_{9\text{-}9}$, $b_{12\text{-}13}$	$b_{7\text{-}8} = -2.5$	0.996

4. INFLUENCE OF THE MONITORING TECHNIQUES AND THE SIMULTANEOUS ERRORS IN REFRACTIVE INDICES AND THICKNESSES

In this part, we used a design with 826 points in a 38-D space for the 19-layers bandpass and a design with 4000 points in 76-D space for the 38-layers coating.

4.1 The monitoring technique MT-1, corresponding to a quartz monitoring: Independent errors

In this part, the notation of the coefficient is modified as following to show the refractive index and thickness parameters: $b_{ni\text{-}tj}$ means an interaction of the parameter *n* of the i^{th} layer and the parameter *t* of the j^{th} layer. All the metamodels have a coefficient of determination R-square greater than 0.95 so the polynomial regression approximates very well the computed values of the merit function.

We can notice that the most critical layers correspond to the layers identified in section 3.1. But, we can identify interactions between refractive index and thickness of layers too. Figure 5 presents the transmittance of the filters due to errors in refractive index values and thickness values: we can notice that the spectral properties of the filter are very modified by these independent errors.

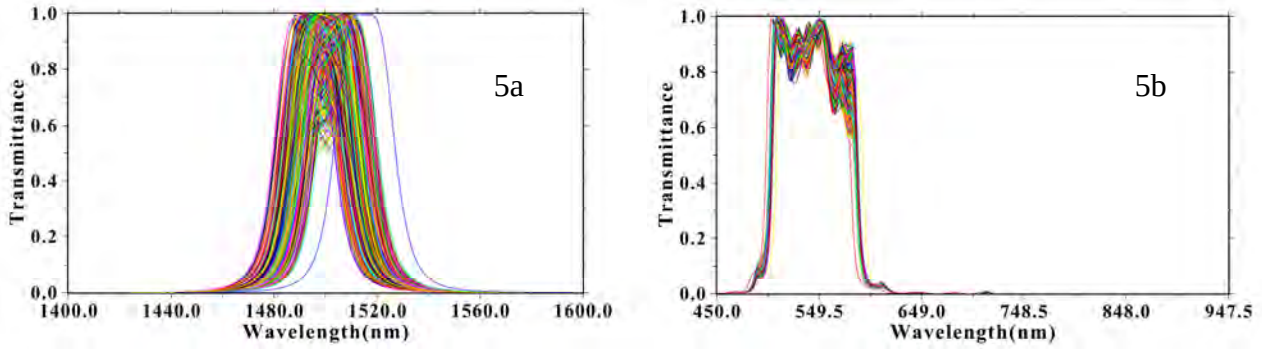

Figure 5: Quartz monitoring technique (MT-1). Influence of errors (+/-0.5%) in the refractive index and thickness values: (5a) and (5b) correspond to the transmittance of 826 runs for the first filter (19 layers) and to the transmittance of 4000 runs for the broad bandpass filter (38 layers).

Due to the results obtained in the section 3, we can assume that the most critical layers are spacer layer parameters with this monitoring technique MT-1. The table 3 confirms this hypothesis but we can now qualify all the interactions between thickness errors and refractive index errors.

Table 3: The 8 major coefficients of the metamodel for the monitoring techniques MT-1.

Filter	Major metamodel coefficient values (decreasing order)	The major coefficient value	R^2
19 layers	$b_{n15\text{-}t15}$, $b_{n5\text{-}t5}$, $b_{n15\text{-}n15}$, $b_{t15\text{-}t15}$, $b_{t5\text{-}t5}$, $b_{n5\text{-}n5}$, $b_{n15\text{-}n16}$, $b_{t5\text{-}t15}$	$b_{n15\text{-}t15} = 367$	0.991
38 layers	$b_{n10\text{-}t10}$, $b_{n10\text{-}n10}$, $b_{t10\text{-}t10}$, $b_{n6\text{-}t6}$, $b_{n6\text{-}t10}$, $b_{n6\text{-}n10}$, $b_{n10\text{-}t6}$, $b_{n14\text{-}t14}$	$b_{n10\text{-}t10} = 42$	0.979

4.2 The monitoring technique MT-2, corresponding to an optical monitoring: Correlated errors

This considered case is a typical case of one channel acquisition optical signal level strategy. For example when we associate a monitoring level as dT/dt =0 [2] at the control wavelength (λ_0) with an acquisition of a spectral broad band of the transmittance at each deposition end of a layer, the repositioning of the control wavelength which is our reference for optical monitoring, is mechanically not the same and implies wavelength changes ($\Lambda_0=\lambda_0\pm\varepsilon$). So, in this case, the process implies correlated errors in refractive index and thickness values and additional residuals errors due to the error in the repositioning of the control wavelength Λ_0. Figures 6a and 6b illustrate correlated errors between refractive index values and thickness values for the two optical coatings.

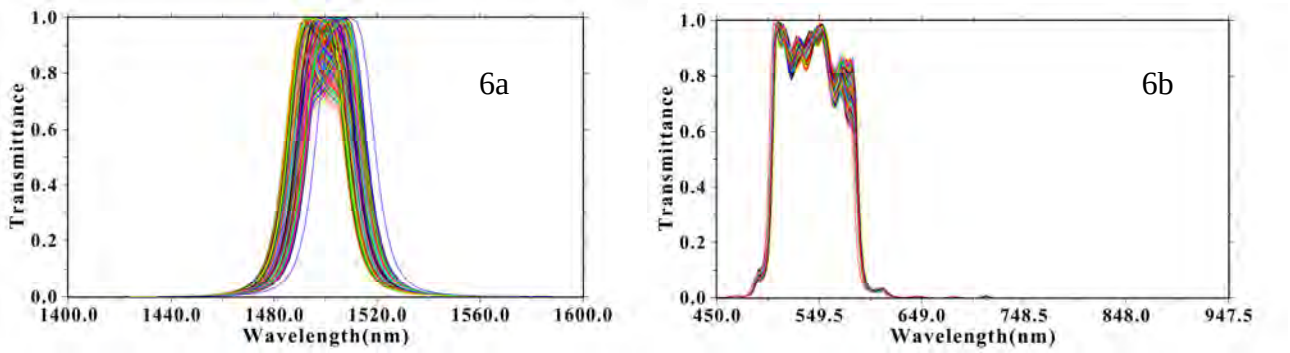

Figure 6: Optical monitoring technique (MT-2). Influence of errors (+/-0.5%) in the refractive index and thickness values: (6a) and (6b) correspond to the transmittance of 826 runs for the first filter (19 layers) and to the transmittance of 4000 runs for the broad bandpass filter (38 layers).

In this case, all the metamodels have a coefficient of determination R-square greater than 0.98 so the polynomial regression approximates extremely well the computed values of the merit function.

We can notice that the most critical layers correspond to the layers identified in section 4.1. But, in this case, it is important to notice that the refractive index values are not the most critical parameters. The major coefficients concern only the thickness values. Table 4 indicates the major coefficient values, and we can notice in comparison of section 3.2 for the two bandpass filters, the critical layers are principally the spacers (6^{th} , 10^{th} ,14^{th} layers), the layers of mirrors for the third and second Fabry-Perot (9^{th}, 11^{th} and 7^{th} layers) and also the coupling layer (16^{th} layer) between broad band mirror and the multiple bandpass for the 38 layers. For the 19 layers filter, we note that the interactions between the spacers (5^{th} and 15^{th} layers) and the layers of mirrors of second bandpass are the most important interactions.

Table 4: The 8 major coefficients of the metamodel for the monitoring techniques MT-2.

Filter	Major metamodel coefficient values (decreasing order)	The major coefficient value	R^2
19 layers	$b_{t15\text{-}t15}$, $b_{t5\text{-}t15}$, $b_{t5\text{-}t5}$, $b_{t15\text{-}t16}$, $b_{t14\text{-}t15}$, $b_{t15\text{-}t17}$, $b_{t4\text{-}t5}$, $b_{t13\text{-}t15}$	$b_{t15\text{-}t15} = 279$	0.996
38 layers	$b_{t10\text{-}t10}$, $b_{t6\text{-}t10}$, $b_{t6\text{-}t16}$, $b_{t10\text{-}t14}$, $b_{t14\text{-}t14}$, $b_{t9\text{-}t10}$, $b_{t10\text{-}t11}$, $b_{t6\text{-}t7}$	$b_{t10\text{-}t10} = 31$	0.989

In conclusion, this monitoring technique MT-2 is very helpful to decrease the influence of the errors in the refractive index values on the optical properties of the filters. Then the knowledge of the most critical interactions between thickness values gives information to improve the coatings manufacturing.

5. CONCLUSION

In this paper, we extend the global sensitivity analysis of thin film coatings to the case of the influence of errors in refractive index values and thickness values of bandpass multilayer coatings. We exhibit for the first time the most important interactions of layers on the optical properties due to errors in the refractive index values and thickness values.

A quartz monitoring technique, which corresponds to the propagation of independent errors, reveals critical interactions between refractive index and thickness parameters of the spacer layers. But, in the case of an optical monitoring technique, which corresponds to the propagation of correlated errors, the most critical interactions concern only thickness parameters. For the production of bandpass coatings and a broadband merit function, the optical monitoring technique is a more efficient technique than the quartz monitoring technique due to correlated errors between refractive index and thickness parameters: in this case of the optical monitoring technique, the most critical interactions concern only thickness parameters. This computational study gives clues to diminish the influence of error propagation in

manufacturing processes and points out that an optical monitoring reduces simultaneously the sensitivity of the coating to the refractive index values and their interactions.

REFERENCES

[1] Pulker, H. K., [Coatings on Glass], Elsevier, Amsterdam (1984).
[2] Vidal, B., "Change of optical properties during the monitoring of quarter wave multilayers" Opt. Comm. 31 (3), 259-262 (1972).
[3] Wilbrandt, S., Kaiser, N., Stenzel, O., "In-situ broadband monitoring of heterogeneous optical coatings" Thin Solid films 502, 153-157 (2006).
[4] Vergohl, M., Malkomes, N., Matthee, T., Brauer, G., Richter, U., Nickol, F.-W., Bruch, J., "In situ monitoring of optical coatings on architectural glass and comparison of the accuracy of the layer thickness attainable with ellipsometry and photometry", Thin Solid Films 392, 258-264 (2001).
[5] Macleod, H. A., [Thin Film Optical Filters], Adam Hilger, Bristol (1986).
[6] Tikhonravov, A V., Trubetskov, M. K., DeBell, G. W., "Application of the needle optimization technique to the design of optical coatings", App Opt. 35 (28), 5493-5508 (1996).
[7] Kennard, R.W., Stone, L.A., "Computer aided design of experiments", Technometrics 11 (1), 137-148 (1969).
[8] Sergent, M., Phan-Tan-Luu, R., Elguero, J., "Statistical Analysis of Solvent Scales. Part 1", Anales de Quimica Int. Ed. 93, 3-6 (1997).
[9] Park, J. S., "Optimal Latin-hypercube designs for computer experiments", Journal of Statistical Planning and Inference 39 (1), 95-111 (1994).
[10] Koehler, J. R., Owen, A.B., "Computer Experiments" in [Handbook of Statistics], vol. 13, Elsevier Science, Amsterdam, 261-308 (1996).
[11] Saltelli, A., Chan, K., Scott, E.M., [Sensitivity Analysis], Wiley, New York (2000).
[12] Santner, T. J., Williams, B. J., Notz, W. I., [The design and analysis of computer experiments], Springer, NewYork (2003).
[13] Azarian, A., Vasseur, O., Bennaï, B., Lombard, L., Canat, G., Jolivet, V., Jaouën, Y., Bourdon, P., "Global sensitivity analyses of coherent beam combining of fiber amplifier arrays by the use of numerical space filling designs", Proc. SPIE 7914, 79141G (2011); doi:10.1117/12.874727.
[14] Vasseur, O., Claeys-Bruno, M., Cathelinaud, M., Sergent, M., "High dimensional sensitivity analysis of complex optronic systems by experimental designs: applications to the case of the design and the robustness of optical coatings", Chinese Optics Letters 8 (s1), 21-24 (2010).
[15] Vasseur, O., Cathelinaud, M., Claeys-Bruno, M., Sergent, M., "Global sensitivity analysis of bandpass and antireflection coatings manufacturing by numerical space filling designs", Appl. Opt. 50 (9), C117-C123 (2011).
[16] Zhan, C., "Graph-theoretical methods for detecting and describing gestalt clusters", IEEE T. Comput. C-20, 68-86 (1971).
[17] Dussert, C., Rasigni, G., Rasigni, M., Palmari, J., "Minimal spanning tree: A new approach for studying order and disorder", Physical Review B. 34 (5), 3528-3531 (1986).
[18] Wallet, F., Dussert, C., "Multifactorial comparative study of spatial point pattern analysis methods", J. Theor. Biol. 187 (3), 437-447 (1997).
[19] Wallet, F., Dussert, C., "Comparison of spatial point patterns and processes characterization methods", Europhysics Lett. 42 (5), 493-498 (1998).
[20] Franco, J., Vasseur, O., Corre, B., Sergent, M., "Minimum Spanning Tree: A new approach to assess the quality of the design of computer experiments", Chemometrics and Intelligent Laboratory Systems 97, 164-169 (2009).
[21] Vasseur, O., Azarian, A., Jolivet, V., Bourdon, P., "Capability of high intrinsic quality Space Filling Design for global sensitivity analysis and metamodelling of interference optical systems", Chemometrics and Intelligent Laboratory Systems doi:10.1016/j.chemolab.2011.05.008 (2011).
[22] Young, P.C., "Data-based mechanistic modelling, generalised sensitivity and dominant mode analysis", Comput. Phys. Commun. 117, 113-129 (1999).
[23] Giunta, A.A., Wojtkiewicz, S.F., Eldred, M.S., "Overview of modern design of experiments methods for computational simulations", in 41st AIAA Aerospace Sciences Meeting and Exhibit, Reno, NV, AIAA, AIAA-2003-0649, 2003.

[24] Wang, G.G., Shan, S., "Review of Metamodeling Techniques in Support of Engineering Design Optimization", J. Mech. Des. 129, 370-380 (2007)
[25] Vasseur, O., Claeys-Bruno, M., Sergent, M., "Quality of high dimensional numerical 'Space filling designs' for the sensitivity analysis of interference optical filters", Procedia - Social and Behavioral Sciences 2, 7761-7762 (2010).
[26] Saporta, G., [Probabilités, analyse des données et statistique], Editions Technip, Paris, 384-385 (1990).

Reflectivity of dielectric coatings deposited on the end facet of a weakly guiding fiber

O. Vasseur

Laboratoire de Physique des Intéractions Photons-Matière, Université d'Aix-Marseille III, Case EC1, 13397 Marseille Cedex 20, France

Received March 24, 1997; accepted June 25, 1997; revised manuscript received August 13, 1997

The computation of the reflectivity of a multilayer dielectric coating deposited on the end facet of single-mode or multimodal fiber is presented. The calculation is done through a plane-wave expansion of the incident fields, and the waveguide is replaced by a homogeneous medium of refractive index n_{eq} while the incident electric (or magnetic) field remains that of the guided mode. The modal reflectivities (coupling factors) between modes are calculated, and the method of computation is accurate enough to satisfy current needs for the design of coatings on fibers and is helpful for the design of coatings deposited on other waveguide structures. © 1998 Optical Society of America [S0740-3232(98)01301-5]

OCIS codes: 230.7370, 060.2270, 310.1620, 120.2440.

1. INTRODUCTION

Because of the importance of traveling-wave semiconductor-laser amplifiers to long distance optical communication, intensive research on antireflection (AR) coating has been conducted.[1]

The rigorous computation[2] of the design and optimization of multilayer coatings deposited at the end facet of a waveguide is too time-consuming, especially in the case of optimization problems. The considerable interest in the semiconductor optical amplifier has motivated the pursuit of less-time-consuming results for the slab fundamental TE and TM modes.[3–11] The approach developed by Vassallo makes it possible to obtain very good performance[12,13] in the case of a weakly guiding slab waveguide and can be applied to the complete three-dimensional problem.[10,14]

The aim of our study was to extend the application of Vassallo's method[9,10,14] to the cases of single-mode fibers and multimodal fibers. This approximate method enables us to determine with good accuracy modal factors at reflection on the end facet of fibers. Furthermore, our study of coatings deposited on fibers is helpful for the design of filters on a laser diode.

2. VASSALLO'S THEORY: THE CASE OF SINGLE-MODE LASER-DIODE OPTICAL AMPLIFIERS

The investigated system is shown in Fig. 1. We assume that the waveguide's refractive index has little variation, i.e., $\Delta = (n_1/n_2 - 1) \ll 1$. Let $\mathbf{e}_0$ and $\mathbf{h}_0$ be the electric and the magnetic fields, respectively, of the incoming guided mode. Let $(\mathbf{E}_r, \mathbf{H}_r)$ and $(\mathbf{E}_t, \mathbf{H}_t)$ be the reflected field (for $z < 0$) and the field in the multilayer part ($z > 0$), respectively, and let $\mathbf{E}(x, y)$ and $\mathbf{H}(x, y)$ be the transverse electric and transverse magnetic components of the total field in the plane $z = 0$. The theory[6–10,14] is based on Maxwell's equations and expansions of exact quantities in terms of the powers of Δ. The plane-wave approach deals correctly with zeroth-order terms and a first-order correction term.

The continuity relations across the plane $z = 0$ are

$$\mathbf{e}_{0,T} + \mathbf{E}_{r,T} = \mathbf{E}_{\mathrm{tr},T} = \mathbf{E}(x, y), \tag{1a}$$

$$\mathbf{h}_{0,T} + \mathbf{H}_{r,T} = \mathbf{H}_{\mathrm{tr},T} = \mathbf{H}(x, y), \tag{1b}$$

where T stands for transverse components.

One can obtain the reflection coefficient R through

$$1 + R = \frac{\langle \mathbf{E}, \mathbf{h}_0 \rangle}{\langle \mathbf{e}_0, \mathbf{h}_0 \rangle}, \tag{2}$$

with

$$\langle \mathbf{A}, \mathbf{B} \rangle = \int_0^{+\infty} \int_0^{2\pi} \mathbf{A}(x, y) \wedge \mathbf{B}^*(x, y) \cdot \mathbf{z} \, dx \, dy,$$

where $\mathbf{B}^*$ is the complex conjugate of $\mathbf{B}$.

The difficulty is then the calculation of $\mathbf{E}$. The use of the impedance and admittance operators Z and Y ($\mathbf{E}_T = Z\mathbf{H}_T$ and $\mathbf{H}_T = Y\mathbf{E}_T$) allows us to write

$$(1 + Z^0_{\mathrm{wg}} Y_{\mathrm{ar}})\mathbf{E} = 2\mathbf{e}_0 - \delta Z Y_{\mathrm{ar}} \mathbf{E} + O(2), \tag{3a}$$

$$Z_{\mathrm{wg}} = Z^0_{\mathrm{wg}} + \delta Z, \tag{3b}$$

where Z_{wg} is the impedance operator in the waveguide, Z^0_{wg} is the impedance operator in a homogeneous medium n_{eq}, δZ is a first-order corrective term, and Y_{ar} is the admittance operator in the multilayer structure.

$\mathbf{E}$ can be expanded as the sum of the main term $\mathbf{E}_0$ and a first-order correction $\delta\mathbf{E}$. The main term $\mathbf{E}_0$ satisfies

$$(1 + Z^0_{\mathrm{wg}} Y_{\mathrm{ar}})\mathbf{E}_0 = 2\mathbf{e}_0. \tag{4}$$

A first evaluation of the reflection coefficient R_0 is then obtained:

$$1 + R_0 = \frac{\langle \mathbf{E}_0, \mathbf{h}_0 \rangle}{\langle \mathbf{e}_0, \mathbf{h}_0 \rangle}. \tag{5}$$

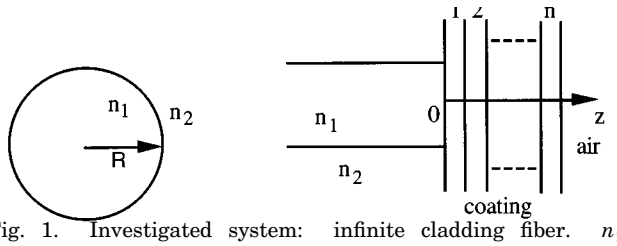

Fig. 1. Investigated system: infinite cladding fiber. $n_2 = 1.48$, $R = 1.37\ \mu$m.

A first-order corrective term δR, due to $\delta\mathbf{E}$, is defined as follows[10]:

$$\delta R = K\langle (n^2(r) - n_{\text{eq}}^2)\mathbf{e}_0, \mathbf{h}_0\rangle, \tag{6}$$

where K is a variable that depends on the multilayer structure.

A significant result is that the corrective term δR vanishes if n_{eq} is chosen such that

$$n_{\text{eq}}^2 = \frac{\langle (n^2(x, y)\mathbf{e}_0, \mathbf{h}_0\rangle}{\langle \mathbf{e}_0, \mathbf{h}_0\rangle}. \tag{7}$$

The practical calculation, proposed by Vassallo, is then summarized as follows[9,10]:

- Computation of the guided mode $(\mathbf{e}_0, \mathbf{h}_0)$.
- Replacement of the waveguide with a homogeneous medium of refractive index n_{eq} [Eq. (7)] while the incident mode is replaced with a plane-wave packet with the same transverse electric field $\mathbf{e}_0$.
- Derivation of the reflected field $(\mathbf{E}_r, \mathbf{H}_r)$ in terms of plane waves.
- The reflectivity is given by the equation

$$R_0 = \frac{\langle \mathbf{E}_r, \mathbf{h}_0\rangle}{\langle \mathbf{e}_0, \mathbf{h}_0\rangle}. \tag{8}$$

3. CALCULATION OF REFLECTIVITY IN THE CASE OF A SINGLE-MODE FIBER

A. Method

Let $n(r)$ be the refractive-index profile of the fiber, and let E (H) be the electric (magnetic) field of the HE_{11} mode.[15,16] The eigenvalue equation of this mode is given[15,16] by (time dependence $i\omega t$):

$$u^4v^4\left(\frac{K_1'(v)}{vK_1(v)} + \frac{J_1'(u)}{uJ_1(u)}\right)\left(n_1^2\frac{J_1'(u)}{uJ_1(u)} + n_2^2\frac{K_1'(v)}{vK_1(v)}\right) - \frac{\gamma^2}{k^2}V^4 = 0, \tag{9}$$

with

$$u = \alpha\mathsf{R}, \qquad v = a\mathsf{R}, \qquad \alpha^2 = k^2n_1^2 - \gamma^2$$

$$a^2 = \gamma^2 - k^2n_2^2, \qquad k = \frac{2\pi}{\lambda}.$$

R is the radius of the fiber, λ is the wavelength, $V^2 = u^2 + v^2 = k^2\mathsf{R}^2(n_1^2 - n_2^2)$, and J and K are Bessel functions.

On the Cartesian axis with polar coordinates, the HE_{11} mode is given as follows[15,16]

Core:

$$E_x = \frac{1}{2}\frac{J_0(\alpha r)}{\alpha}(\gamma A_1 + kB_1) + \frac{1}{2}\frac{J_2(\alpha r)}{\alpha} \times \exp(i2\theta)(-\gamma A_1 + kB_1), \tag{10a}$$

$$E_y = \frac{1}{2}\frac{J_0(\alpha r)}{\alpha}(i\gamma A_1 + ikB_1) + \frac{1}{2}\frac{J_2(\alpha r)}{\alpha} \times \exp(i2\theta)(i\gamma A_1 - ikB_1), \tag{10b}$$

$$H_x = \frac{1}{2}\frac{J_0(\alpha r)}{\alpha}\eta(-ikn_1^2A_1 - i\gamma B_1) + \frac{1}{2}\frac{J_2(\alpha r)}{\alpha} \times \eta\exp(i2\theta)(-ikn_1^2A_1 + i\gamma B_1), \tag{10c}$$

$$H_y = \frac{1}{2}\frac{J_0(\alpha r)}{\alpha}\eta(kn_1^2A_1 + \gamma B_1) + \frac{1}{2}\frac{J_2(\alpha r)}{\alpha} \times \eta\exp(i2\theta)(-kn_1^2A_1 + \gamma B_1). \tag{10d}$$

Cladding:

$$E_x = \frac{1}{2}\frac{K_0(ar)}{a}(\gamma A_2 + kB_2) + \frac{1}{2}\frac{K_2(ar)}{a} \times \exp(i2\theta)(\gamma A_2 - kB_2), \tag{10e}$$

$$E_y = \frac{1}{2}\frac{K_0(ar)}{a}(i\gamma A_2 + ikB_2) + \frac{1}{2}\frac{K_2(ar)}{a} \times \exp(i2\theta)(-i\gamma A_2 + ikB_2), \tag{10f}$$

$$H_x = \frac{1}{2}\frac{K_0(ar)}{a}\eta(-ikn_2^2A_2 - i\gamma B_2) + \frac{1}{2}\frac{K_2(ar)}{a} \times \eta\exp(i2\theta)(ikn_2^2A_2 - i\gamma B_2), \tag{10g}$$

$$H_y = \frac{1}{2}\frac{K_0(ar)}{a}\eta(kn_2^2A_2 + \gamma B_2) + \frac{1}{2}\frac{K_2(ar)}{a} \times \eta\exp(i2\theta)(kn_2^2A_2 - \gamma B_2), \tag{10h}$$

with

$$J_1(u)A_1 = K_1(v)A_2, \qquad J_1(u)B_1 = K_1(v)B_2,$$

$$\frac{A_1}{u^2v^2\left(-\frac{1}{v^2} - \frac{K_0(v)}{vK_1(v)} + \frac{J_0(u)}{uJ_1(u)} - \frac{1}{u^2}\right)} = \frac{-B_1}{\frac{\gamma}{k}V^2},$$

$$\eta = \sqrt{\epsilon_0/\mu_0}.$$

ϵ_0 is the free-space dielectric constant and μ_0 is the free-space permeability. B_1 is chosen for example such that $B_1 = 1/k\mathsf{R}J_1(u)$.

The energy ϕ is given by

$$\phi = \frac{1}{2}\,\text{Re}\left[\int_0^{+\infty}\int_0^{2\pi}\mathbf{E}\wedge\mathbf{H}^*\cdot\mathbf{z}r\,\text{d}\theta\text{d}r\right] = \frac{1}{2}\,\text{Re}\left[\int_0^{+\infty}\int_0^{2\pi}(E_xH_y^* - E_yH_x^*)r\,\text{d}\theta\text{d}r\right], \tag{11}$$

where * and Re mean complex conjugate and real part function, respectively.

The Fourier transform is defined by

$$\widetilde{E_x}(k_x, k_y) = \int_{-\infty}^{+\infty}\int_{-\infty}^{+\infty} E_x(x, y)\exp[ik_x x + ik_y y]\mathrm{d}x\mathrm{d}y \tag{12a}$$

or with polar coordinates

$$\widetilde{E_x}(s, \psi) = \int_0^{+\infty}\int_0^{2\pi} E_x(r, \theta)\exp[irs\cos(\theta - \psi)]r\mathrm{d}r\mathrm{d}\theta. \tag{12b}$$

The reflected field is then obtained on the Cartesian axis[13]:

$$\widetilde{\mathbf{E}'_{x,y,z}} = \begin{pmatrix} (k_x'^2 r_{\mathrm{TM}} + k_y'^2 r_{\mathrm{TE}})\widetilde{E_x} + k_x' k_y'(r_{\mathrm{TM}} - r_{\mathrm{TE}})\widetilde{E_y} \\ k_x' k_y'(r_{\mathrm{TM}} - r_{\mathrm{TE}})\widetilde{E_x} + (k_y'^2 r_{\mathrm{TM}} + k_x'^2 r_{\mathrm{TE}})\widetilde{E_y} \\ r_{\mathrm{TM}}\widetilde{E_z} \end{pmatrix}, \tag{13}$$

where r_{TE} is the reflection coefficient in the transverse electric case, r_{TM} is the reflection coefficient in the parallel electric case, $k_x' = \cos\psi$, and $k_y' = \sin\psi$.

The weakly guiding waveguide could be replaced by a homogeneous medium with an equivalent refractive index n_{eq} (Eq. 7) such that[9,14]

$$n_{\mathrm{eq}}^2 = \frac{\langle n^2(r)\mathbf{E}, \mathbf{H}\rangle}{\langle \mathbf{E}, \mathbf{H}\rangle}, \tag{14}$$

with

$$\langle \mathbf{A}, \mathbf{B}\rangle = \int_0^{+\infty}\int_0^{2\pi} \mathbf{A}(r, \theta) \wedge \mathbf{B}^*(r, \theta) \cdot \mathbf{z}r\mathrm{d}r\mathrm{d}\theta,$$

where $\mathbf{B}^*$ is the complex conjugate of $\mathbf{B}$.

Thus

$$\int_0^{+\infty}\int_0^{2\pi} n^2(r)\mathbf{E} \wedge \mathbf{H}^* \cdot \mathbf{z}r\mathrm{d}r\mathrm{d}\theta = \int_0^{+\infty}\int_0^{2\pi} n_{\mathrm{eq}}^2\mathbf{E} \wedge \mathbf{H}^* \cdot \mathbf{z}r\mathrm{d}r\mathrm{d}\theta. \tag{15}$$

We deduce from Eq. (8) the modal reflectivity

$$R_m = \left|\frac{\langle \mathbf{E}_r, \mathbf{H}_0\rangle}{\langle \mathbf{E}_0, \mathbf{H}_0\rangle}\right|^2, \tag{16}$$

or by using the Parseval–Plancherel theorem,

$$R_m = \left|\frac{\displaystyle\int_{-\infty}^{+\infty}\int_{-\infty}^{+\infty} E_{rx}H_{0y}^* - E_{ry}H_{0x}^*\mathrm{d}x\mathrm{d}y}{\displaystyle\int_{-\infty}^{+\infty}\int_{-\infty}^{+\infty} E_{0x}H_{0y}^* - E_{0y}H_{0x}^*\mathrm{d}x\mathrm{d}y}\right|^2 = \left|\frac{\displaystyle\int_0^{+\infty}\int_0^{2\pi}\widetilde{E_{rx}}\widetilde{H_{0y}^*} - \widetilde{E_{ry}}\widetilde{H_{0x}^*}s\mathrm{d}s\mathrm{d}\psi}{\displaystyle\int_0^{+\infty}\int_0^{2\pi}\widetilde{E_{0x}}\widetilde{H_{0y}^*} - \widetilde{E_{0y}}\widetilde{H_{0x}^*}s\mathrm{d}s\mathrm{d}\psi}\right|^2.$$

It is possible to calculate the power (intensity) reflectivity R_p and the power (intensity) transmissivity T_p by means of the relations

$$R_p = \frac{\mathrm{Re}\left(\displaystyle\int_0^{+\infty}\int_0^{2\pi}\widetilde{E_{rx}}\widetilde{H_{ry}^*} - \widetilde{E_{ry}}\widetilde{H_{rx}^*}s\mathrm{d}s\mathrm{d}\psi\right)}{\displaystyle\int_0^{+\infty}\int_0^{2\pi}\widetilde{E_{0x}}\widetilde{H_{0y}^*} - \widetilde{E_{0y}}\widetilde{H_{0x}^*}s\mathrm{d}s\mathrm{d}\psi}$$

$$\text{and } T_p = 1 - R_p. \tag{17}$$

The use of approximate fields linearly polarized (LP) modes is possible far from cutoff and for non-high-quality antireflection coatings ($R > 10^{-4}$).

B. Results

In the zero guidance limit, R_m is very close to the reflectivity computed by using a single plane wave or with the Gaussian approximation for the LP01 mode.[14] The difference between our reflectivity R_m and the reflectivity R_{pw} computed with a plane wave is always less than 0.51% for the filter presented in Fig. 2 ($\Delta = 0.003$). For other filters and $\Delta \sim 0.003$, the difference is negligible, too. But when the value of Δ is near 5%, our method is useful because the guidance effects are not omitted, unlike with the plane-wave method: Fig. 2 shows the peak transmission modification that is due to Δ. It can be noticed that the greater the value of Δ is, the greater is the difference between the modal reflectivity and the power reflectivity: when $\Delta \sim 0.003$, the difference between R_m and R_{pw} is negligible, but it becomes significant when $\Delta \sim 0.05$ (Fig. 3). Because of the lack of experimental results, it is satisfactory to obtain a good agreement between our model and the well-known cases ($\Delta \sim 0.003$). This agreement could be considered a first step for validation of the model.

The same analysis applied to fibers with index values of semiconductor materials ($n > 3$) is useful for optical-amplifier design. A real laser diode is never a slab, so the study of the filter reflectivity on the fiber can be helpful in choosing the best insensitive antireflection coating ($R < 5.10^{-5}$ was found to be needed at $\lambda = 1.55\ \mu$m in

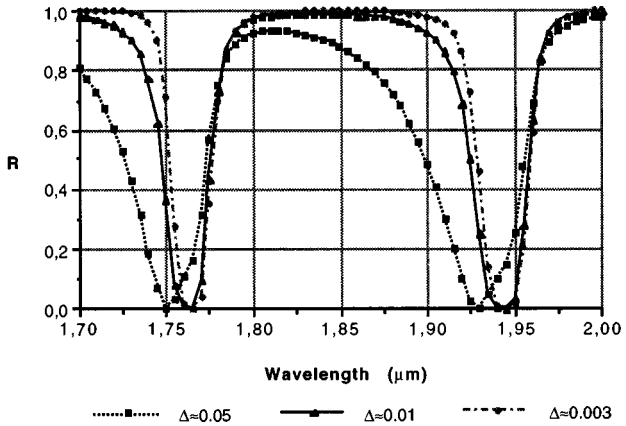

Fig. 2. Δ influence on modal reflectivity. Fiber: $n_2 = 1.48$, R = 1.37 μm; filter:

HBHB2HBHB2HBHBHBHBHB2HBHB2HBHBH

at $\lambda = 1.85\ \mu$m. H means quarter wave of high index, $n_{\mathrm{H}} = 2.25$ at the wavelength given. B means quarter wave of low index $n_{\mathrm{B}} = 1.48$ at the wavelength given. Half-waves are denoted by 2H or 2B. (In Figs. 2–7, commas in axis numbers are to be read as decimals.)

Refs. 12 and 13). The fiber is chosen with the same waveguide parameter V of the slab. Figures 4 and 5 present computation results of the modal reflectivity of a filter defined and used on slab.[12,13] It can be noticed (Fig. 4) that the reflectivities of the four-layer filter on slab and on fiber are very close and are acceptable, so this filter is a solution to the problem of two-waveguide structures, but this is not the case for the best theoretical two-layer filter[8] (Fig. 5). The four-layer filter is insensitive to the waveguide structure, so its behavior helped us to achieve good results (Fig. 4). We think that the computation of filters on slab and on fiber should be the first step in the research of a filter on a waveguide that is neither slab nor fiber because by this method we detect the coatings that are the most insensitive to the waveguide structure. For example, if the section of the active layer is not very large, the waveguide should be regarded as a fiber rather than as a slab. So for optical-amplifier design, the computation of filters on slab and fiber seems to be necessary for choosing the filter that is the most insensitive to the waveguide structure.

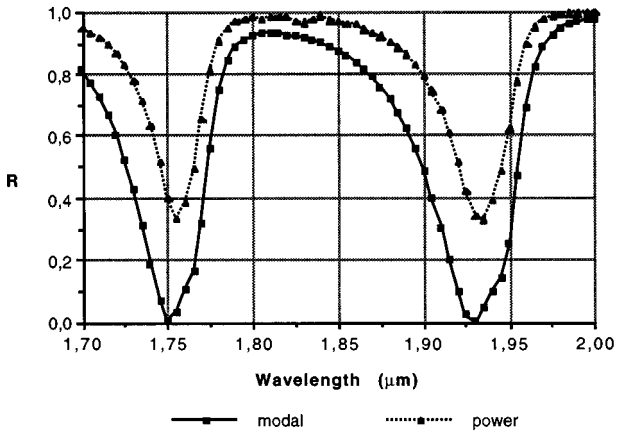

Fig. 3. Modal and power reflectivity. Fiber: $n_1 = 1.55$, $n_2 = 1.48$, R = 1.37 μm. filter:
HBHB2HBHB2HBHBHBHBHB2HBHB2HBHBH
at $\lambda = 1.85$ μm.

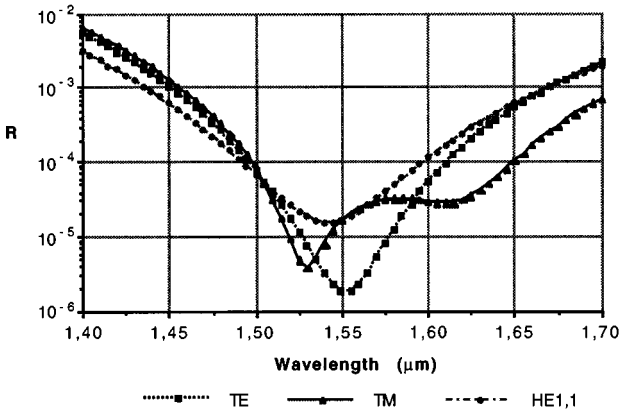

Fig. 4. Four-layer antireflection coatings on slab (TE, TM) and on fiber (HE1, 1). Diode: $n_1 = 3.512$, $n_2 = 3.17$, $d = 0.2$ μm; fiber: $n_1 = 3.512$, $n_2 = 3.17$, R = 0.2 μm; filter: $n_1 = 2.25$, $e_1 = 0.2035$ μm, $n_2 = 1.48$, $e_2 = 0.2349$ μm, $n_3 = 2.25$, $e_3 = 0.0694$ μm, $n_4 = 1.48$, $e_4 = 0.3755$ μm.

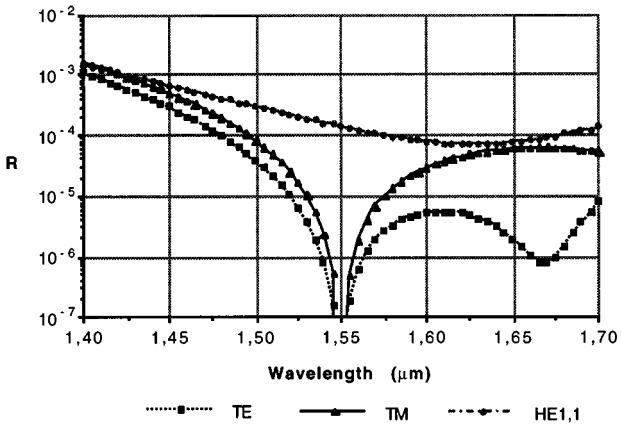

Fig. 5. Two-layer antireflection coatings on slab (TE, TM) and fiber (HE1, 1). Diode: $n_1 = 3.512$, $n_2 = 3.17$, $d = 0.25$ μm; fiber: $n_1 = 3.512$, $n_2 = 3.17$, R = 0.25 μm; filter: $n_1 = 2.4917$, $e_1 = 0.1689$ μm, $n_2 = 1.3924$, $e_2 = 0.3096$ μm.

The study of single-mode fibers shows that this method is useful for computing the modal reflectivity of filters deposited on the end facet of a fiber when Δ is greater than 1%, which is the case for infrared fibers.[17] Furthermore, modal reflectivity computed on single-mode fibers is useful for the study of laser-diode optical amplifiers.

For all these coatings, rigorous field formulas are used to obtain high-precision results, but LP-mode formulas can be used for qualitative results with variation that is always less than that of the coating production.[13,18]

4. CALCULATION OF REFLECTIVITY IN THE CASE OF A MULTIMODAL FIBER

A. Method

The system that we investigated was again, fibers with infinite cladding. As in the single-mode case, it is possible to use the approximate fields, and for the mode near cutoff and high antireflection coatings we should use rigorous fields. A difficulty now appears: the choice of the refractive-index value of the equivalent medium. In the single-mode case, the refractive index n_{eq} is chosen so that the first-order corrective term δR [(Eq. 6)] vanishes. But in this case, each mode i needs a specific refractive index $n_{\mathrm{eq},i}$ [(Eq. 13)]:

$$n_{\mathrm{eq},i}^2 = \frac{\langle n^2(r)\mathbf{E}_i\,,\,\mathbf{H}_i\rangle}{\langle \mathbf{E}_i\,,\,\mathbf{H}_i\rangle}. \tag{18}$$

We can introduce the equivalent index of all propagating modes:

$$n_{\mathrm{eq}}^2 = \frac{\langle n^2(r)\mathbf{E},\,\mathbf{H}\rangle}{\langle \mathbf{E},\,\mathbf{H}\rangle}, \tag{19}$$

where $\mathbf{E} = \Sigma_{i=1}^{n}\,\mathbf{E}_i$ and $\mathbf{E}_i$ is the electric field of the i mode.[16]

The transverse components of the modes are given by the following relations[16]:

Core:

$$E_x = \frac{1}{2}\frac{J_{m-1}(\alpha r)}{\alpha}\exp[i(m-1)\theta](\gamma A_1 + kB_1) + \frac{1}{2}\frac{J_{m+1}(\alpha r)}{\alpha}\exp[i(m+1)\theta](-\gamma A_1 + kB_1), \tag{20a}$$

$$E_y = \frac{1}{2}\frac{J_{m-1}(\alpha r)}{\alpha}\exp[i(m-1)\theta](i\gamma A_1 + ikB_1) + \frac{1}{2}\frac{J_{m+1}(\alpha r)}{\alpha}\exp[i(m+1)\theta](i\gamma A_1 - ikB_1), \tag{20b}$$

$$H_x = \frac{1}{2}\frac{J_{m-1}(\alpha r)}{\alpha}\eta\exp[i(m-1)\theta](-ikn_1^2 A_1 - i\gamma B_1) + \frac{1}{2}\frac{J_{m+1}(\alpha r)}{\alpha}\eta\exp[i(m+1)\theta] \times (-ikn_1^2 A_1 + i\gamma B_1), \tag{20c}$$

$$H_y = \frac{1}{2}\frac{J_{m-1}(\alpha r)}{\alpha}\eta\exp[i(m-1)\theta](kn_1^2 A_1 + \gamma B_1) + \frac{1}{2}\frac{J_{m+1}(\alpha r)}{\alpha}\eta\exp[i(m+1)\theta] \times (-kn_1^2 A_1 + \gamma B_1); \tag{20d}$$

Cladding:

$$E_x = \frac{1}{2}\frac{K_{m-1}(ar)}{a}\exp[i(m-1)\theta](\gamma A_2 + kB_2) + \frac{1}{2}\frac{K_{m+1}(ar)}{a}\exp[i(m+1)\theta](\gamma A_2 - kB_2), \tag{20e}$$

$$E_y = \frac{1}{2}\frac{K_{m-1}(ar)}{a}\exp[i(m-1)\theta](i\gamma A_2 + ikB_2) + \frac{1}{2}\frac{K_{m+1}(ar)}{a}\exp[i(m+1)\theta](-i\gamma A_2 + ikB_2), \tag{20f}$$

$$H_x = \frac{1}{2}\frac{K_{m-1}(ar)}{a}\eta\exp[i(m-1)\theta](-ikn_2^2 A_2 - i\gamma B_2) + \frac{1}{2}\frac{K_{m+1}(ar)}{a}\eta\exp[i(m+1)\theta] \times (ikn_2^2 A_2 - i\gamma B_2), \tag{20g}$$

$$H_y = \frac{1}{2}\frac{K_{m-1}(ar)}{a}\eta\exp[i(m-1)\theta](kn_2^2 A_2 + \gamma B_2) + \frac{1}{2}\frac{K_{m+1}(ar)}{a}\eta\exp[i(m+1)\theta] \times (kn_2^2 A_2 - \gamma B_2), \tag{20h}$$

with

$$J_m(u)A_1 = K_m(v)A_2, \qquad J_m(u)B_1 = K_m(v)B_2,$$

$$\frac{A_1}{u^2v^2\left(\dfrac{J_m'(u)}{uJ_m(u)} + \dfrac{K_m'(v)}{vK_m(v)}\right)} = \frac{-B_1}{m\dfrac{\gamma}{k}V^2}.$$

With the process mentioned above, it is possible to obtain the modal reflectivity $R_{m,i}$, which is the coupling factor of all modes in the mode i, the power reflectivity R_p, and the modal reflectivity $R_{i,j}$ of two specific modes:

$$R_{m,i} = \left|\frac{\langle \mathbf{E}_r, \mathbf{H}_i\rangle}{\langle \mathbf{E}_i, \mathbf{H}_i\rangle}\right|^2 R_p = \frac{\langle \mathbf{E}_r, \mathbf{H}_r\rangle}{\langle \mathbf{E}, \mathbf{H}\rangle} \quad \text{and}$$

$$R_{i,j} = \left|\frac{\langle \mathbf{E}_r^i, \mathbf{H}_j\rangle}{\mathbf{E}_j, \mathbf{H}_j}\right|^2, \tag{21}$$

where $\mathbf{E}_r$ is the total reflected electric field, $\mathbf{E}_r^i$ is the reflected field that is due to the incoming i mode, and $\mathbf{E}_j$ ($\mathbf{H}_j$) is the electric (magnetic) field of the incoming mode j.

As in single-mode case, it is possible to use LP-mode formulas far from cutoff and for non-high-antireflection coatings.

B. Results

The results of the process described above are now applied to various modes and fibers. In computing the reflectivities $R_{i,i}$, it is possible to use every $n_{\mathrm{eq},i}$. The use of n_{eq} instead of $n_{\mathrm{eq},i}$ entails little change in the reflectivity values[19] except when the Δ value is $\sim$0.1 (Fig. 6). In the latter case, the use of first-order corrective terms[14] [Eq. (6) for each mode] is necessary to give good results: the relative difference ΔR $\{\Delta R = [R_{i,i}(n_{\mathrm{eq},i}) - R_{i,i}(n_{\mathrm{eq}})]/R_{i,i}(n_{\mathrm{eq},i})\}$ is less than 85% without first-order corrective terms but less than 24% with them at a wavelength of 1.65 μm. Except for the 1.65-μm domain, the relative difference is less than 5% with the first-order corrective terms but less than 20% without them. It can be noticed that the four-layer filter used on the single-mode fiber is still an antireflection coating: this filter is

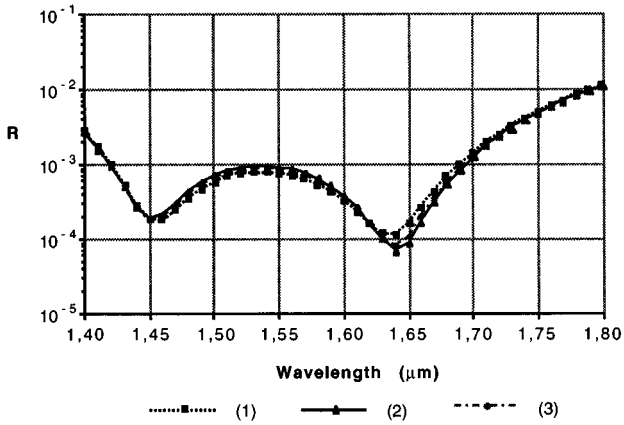

Fig. 6. Equivalent index influence on reflectivity $R_{\mathrm{HE1,1;HE1,1}}$. Fiber: $n_1 = 3.512$, $n_2 = 3.17$, R = 0.9140 μm. filter; $n_1 = 2.25$, $e_1 = 0.2035$ μm, $n_2 = 1.48$, $e_2 = 0.2349$ μm, $n_3 = 2.25$, $e_3 = 0.0694$ μm, $n_4 = 1.48$, $e_4 = 0.3755$ μm. Curve (1) $n_{\mathrm{eq,HE1,1}}$ case, curve (2) n_{eq} case, curve (3) n_{eq}-with-corrective-terms case.

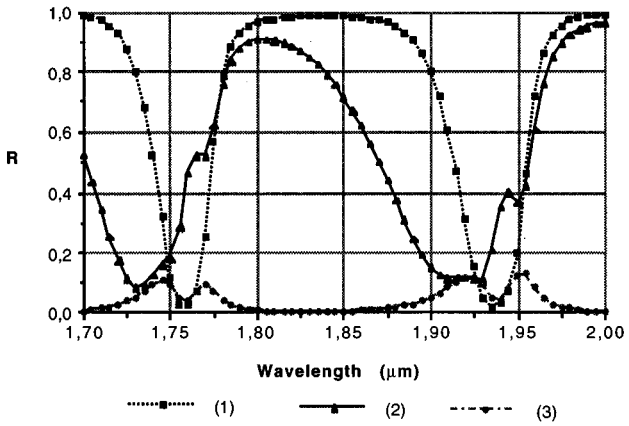

Fig. 7. Modal reflectivities: curve (1) $R_{\mathrm{HE1,1;HE1,1}}$, curve (2) $R_{\mathrm{HE1,2;HE1,2}}$, curve (3) $R_{\mathrm{HE1,1;HE1,2}}$. Fiber: $n_1 = 1.55$, $n_2 = 1.48$, R = 3 μm; filter:

HBHB2HBHB2HBHBHBHBHB2HBHB2HBHBH

at $\lambda = 1.85$ μm.

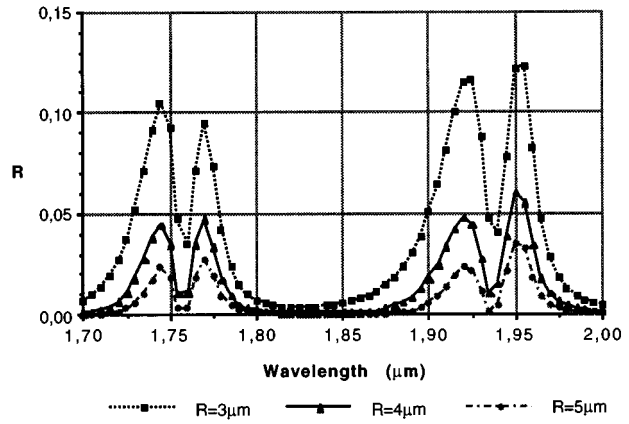

Fig. 8. Modal reflectivities $R_{\mathrm{HE1,1;HE1,2}}$ versus R. Fiber: $n_1 = 1.55$, $n_2 = 1.48$; filter:

HBHB2HBHB2HBHBHBHBHB2HBHB2HBHBH

at $\lambda = 1.85$ μm.

particularly insensitive to the waveguide structure. High-antireflection coatings entail the greatest relative difference. So the case presented here is one of the worst results we have seen: with nonantireflection filters, we observed that the relative differences ΔR are smaller. The results obtained with first-order corrective terms are sufficient for modeling filters, because the trouble introduced by the fabrication tolerance of the coating (index and thickness values) is greater.[13] So when $\Delta < 0.05$, the use of n_{eq} is sufficient for computing reflectivities, but when $\Delta > 0.05$, first-order corrective terms are needed if high-precision computation is required.

The spectral response of a filter for each propagating mode is easy to obtain by the use of $R_{i,i}$, and we observed that when the fiber radius is very large, the results are close to those obtained with ray optics.[20] A good agreement between our approach and well-known results are obtained.

Finally, we present results of the coupling factor $R_{\mathrm{HE1,1;HE1,2}}$ (Fig. 7). The first corrective term entails little change in the results: in this case the difference is less than 0.25%. Although the spectral response of the $HE_{1,1}$ mode looks like the one computed with a plane wave, this is not the case for the $HE_{1,2}$ mode. The smaller the radius of the fiber is, the greater is the coupling factor between these two modes (Fig. 8).

As in the single-mode case, LP modes can be used, because the difference in reflectivity between rigorous and approximate field calculations are negligible and the tolerance due to coating production provides greater variation.

The method we developed to obtain the different reflectivities is simple and very fast. The cpu time is on the same order as with the two-dimensional (slab) case. The response of filters, defined on energy, can be quite different when we are interested in coupling factors of modes. This method gives a simple process for obtaining filters with specific modal (or power) characteristics [Eqs. (20)].

5. CONCLUSION

A simple method, based on the approach of Vassallo, was presented to compute the reflectivity of filters deposited on the end facet of a fiber. This study is based on the optimization of filters on modal reflectivities, which correspond to the reflected modal repartition. In the case of single-mode fibers, this approach can give useful information for semiconductor design. In the case of multimodal fibers, the interactions between specific modes are available. This approach should be extended to fiber junctions: optimization of coupling modal power is important for fiber captor design.

ACKNOWLEDGMENTS

I am grateful to C. Vassallo, E. Rasigni, and F. Wallet for their advice and fruitful discussions on the subject of this paper.

REFERENCES

1. J. Chen, D. Li, and Y. Lu, "Experimental and theoretical studies on monitored signals from semiconductor diodes undergoing antireflection coatings," Appl. Opt. **30**, 4554–4559 (1991).
2. T. E. Rozzi and G. H. Veld, "Variational treatment of the diffraction at the facet of d.h. lasers and dielectric millimeter wave antenna," IEEE Trans. Microwave Theory Tech. **MTT-28**, 61–73 (1980).
3. P. C. Kendall, D. A. Roberts, P. N. Robson, M. J. Adams, and M. J. Robertson, "New formula for semiconductor laser facet reflectivity," IEEE Photon. Technol. Lett. **5**, 148–151 (1993).
4. P. C. Kendall, D. A. Roberts, P. N. Robson, M. J. Adams, and M. J. Robertson, "Semiconductor laser facet reflectivities using free-space rediation modes," IEE Proc. J **140**, 49–55 (1993).
5. C. J. Smartt, T. M. Benson, and P. C. Kendall, "Exact analysis of waveguide discontinuities: junctions and laser facet," Electron. Lett. **29**, 1352–1353 (1993).
6. C. Vassallo, "Rigorous and approximate calculations of antireflection layer parameters for travelling-wave diode laser amplifiers," Electron. Lett. **21**, 333–335 (1985).
7. C. Vassallo, "Antireflection coatings for optical semiconductor amplifiers: justification of a heuristic analysis," Electron. Lett. **24**, 62–64 (1988).
8. C. Vassallo, "Polarisation independent antireflection coat-

ings for semiconductor optical amplifiers," Electron. Lett. **24**, 61–62 (1988).
9. C. Vassallo, "Reflectivity of multidielectric coatings deposited on the end facet of a weakly guiding dielectric slab waveguide," J. Opt. Soc. Am. A **5**, 1918–1928 (1988).
10. C. Vassallo, "Theory and practical calculation of antireflection coatings on semiconductor laser diode optical amplifiers," IEE Proc. Optoelectron. **137**, 193–202 (1990).
11. J. Xu, D. Yevick, and M. Gallant, "Approximate methods for modal reflectivity at optical waveguide facets," J. Opt. Soc. Am. A **12**, 725–728 (1995).
12. F. Favre and D. Le Guen, "82 nm of continuous tunability for an external cavity semiconductor laser," Electron. Lett. **27**, 183–184 (1991).
13. O. Vasseur, "Calcul et réalisation de traitements optiques multicouches pour diodes laser. Etude de l'influence des défauts de structure des couches sur les performances des diodes traitées," Ph.D. thesis (Université d'Aix-Marseille III, Marseille, France, 1990).
14. C. Vassallo, *Optical Waveguide Concepts* (Elsevier, Amsterdam, 1991), pp. 269–308.
15. A. Snyder and J. Love, *Optical Waveguide Theory* (Chapman & Hall, New York, 1983), pp. 238–326.
16. C. Vassallo, *Theorie des Guides d'Ondes Électromagnétiques* (Eyrolles, Paris, 1985), pp. 379–402.
17. J. A. Savage, *Infrared Optical Materials and Their Antireflection Coatings* (Hilger, Bristol, 1985), pp. 150–184.
18. H. A. Macleod, *Thin-Film Optical Filters* (Hilger, Bristol, 1986), pp. 434–443.
19. O. Vasseur, "Analyse modale de la réflexion sur des traitements multicouches déposés en extremité de fibres," in *15èmes Journées Nationales d'Optique Guidée 95* (Société Française d'Optique, Orsay, France, 1995), Paper 32bis.
20. O. Vasseur, "Multilayer coatings for waveguide components," in Proceedings of the International Symposium on Optronics and Defence (Association Aéronautique et Astronautique de France, Paris, 1996), Paper 1.43.

Coherent beam combining of fiber amplifier arrays and application to laser beam propagation through turbulent atmosphere

Pierre Bourdon*[a], Veronique Jolivet[a], Baya Bennai[a], Laurent Lombard[a], Guillaume Canat[a], Emilie Pourtal[a], Yves Jaouen[b], Olivier Vasseur[a]

[a]Departement Optique Theorique et Appliquee, Onera, The French Aerospace Lab, Chemin de la Hunière, 91761 Palaiseau, France
[b]GET Telecom Paris, Centre National de la Recherche Scientifique, UMR 5141, 46 Rue Barrault, 75634 Paris, France

ABSTRACT

Coherent beam combining of fiber amplifier arrays is a promising way to increase power of fiber lasers, and overcome the physical limitations to fiber laser power scaling. We performed the coherent combining of fiber amplifier arrays using active control of the phase of each amplifier. The phase fluctuations in the fiber amplifiers have been measured and their effect on the beam combining process stability evaluated. We extended the coherent beam combining technique to perform wavefront shaping, in order to deliver a high brightness beam after turbulent atmospheric propagation. We present experimental results exhibiting the capability of the modulation multiplexing technique that we implemented to compensate phase fluctuations due to turbulent atmospheric propagation on the laser beam path. Moreover, and for the first time to our knowledge, we demonstrate automatic coherent combining of fiber amplifiers on a diffuse surface, after propagation through turbulent atmosphere, without any external turbulence measurement subsystem.

Keywords: Coherent beam combining, Fiber laser, Fiber amplifier, Phase fluctuation, Turbulence, Laser propagation

1. INTRODUCTION

All-fiber laser systems have already demonstrated high continuous power with very good beam quality and high efficiency, delivering up to 2 kW in a high brightness beam[1]. However, power scaling of fiber lasers is limited by physical effects such as thermal load, nonlinear effects and optical surface damage. The use of large mode area (LMA) fibers with large core enhances the power that can be extracted from fibers, but limits still exist. Beam combining is a promising way to overcome these limits and deliver increased power and brightness from fiber lasers.

Among the numerous techniques that can be pursued to additively overlap power from multiple fiber sources, two have experimentally revealed their potential to combine high power lasers. The first one is spectral combining, an incoherent approach in which lasers emitting different wavelengths are overlapped using a diffractive component such as a diffraction grating[2]. The second one is coherent beam combining with active phase control where same polarization and wavelength lasers are locked to interfere constructively, and deliver most of their added powers in a single lobe of the interference pattern in the far-field[3].

Spectral combining has already demonstrated up to 522 W combined power[2], and coherent combining with active phase control have reached 470 W combined power[3]. Power scaling of these techniques is still going on, with research teams in Europe and in the USA working on kilowatt-class combining.

Anyway, coherent beam combining with active phase control has the ability to perform far more complex tasks than spectral combining. Spectral combining is limited to high-brightness beams overlap, summing powers without impairing beam quality. Whereas coherent combining with active phase control can also perform beam steering or wavefront shaping, as the phase relationship between the combined sources is totally controlled.

*pierre.bourdon@onera.fr; phone (+33) 1 69 93 63 82; fax (+33) 1 69 93 63 45; www.onera.fr

Fiber Lasers V: Technology, Systems, and Applications, edited by Jes Broeng, Clifford Headley,
Proc. of SPIE Vol. 6873, 687316, (2008) · 0277-786X/08/$18 · doi: 10.1117/12.761681

Using coherent combining with active phase control, one can prepare the wavefront from the combined lasers to reverse-match perfectly the turbulent phase fluctuations that the beam will encounter during propagation. This way, the far field brightness can be maximized and the beam quality preserved even after long range turbulent atmospheric propagation. Hughes Research Labs have already demonstrated such experiment for free space communication through turbulent atmosphere[4].

We present here the work conducted at ONERA (the French Aerospace Lab) concerning coherent combining with active phase control of fiber amplifiers arrays. After a description of the modulation multiplexing technique implemented in our laboratory, this technique will be compared with another active combining technique. Experimental results on phase fluctuations measurements and physical origins of these fluctuations are presented. The stability versus these fluctuations and sensitivity of the combining setup are evaluated.

Then, we detail experiments of coherent combining through atmospheric turbulence. The ability of the setup to compensate these fluctuations is demonstrated. Using the modulation multiplexing technique on the backward signal, we succeed in coherently combining fiber lasers in the far-field on a diffuse surface. In real systems, turbulence fluctuation measurement is a main issue to implement these techniques. For the first time to our knowledge, we achieve automatic coherent combining of fiber amplifiers on a diffuse surface, after propagation through turbulent atmosphere, without any external turbulence measurement subsystem.

2. COHERENT COMBINING GENERAL PRINCIPLES AND EXPERIMENTAL SETUP

2.1 Modulation multiplexing technique for coherent beam combining

Coherent combining with active phase control is a classical technique to sum powers from multiple laser sources at the same wavelength and with the same polarization. Due to coherence, these sources interfere in the far field and if let alone, the rapid phase fluctuations of the sources will considerably reduce the average brightness in the combined field.

To perform active phase control, master oscillator power amplifier (MOPA) sources sharing the same master oscillator are generally used. Active phase control of separate laser sources is not feasible, as there is no way to control the absolute value of a laser phase. With MOPA lasers sharing the same MO, only relative phase fluctuations have to be corrected. This can be done easily, as long as a proper technique is used to measure the relative phase difference of each PA chain.

In the experimental setup presented in figure 1, the master oscillator power is splitted into N fiber amplifiers chains producing the overall output power. At the entrance of the fiber amplifiers chains, electro-optic modulators are interfaced to perform the active phase control, and input additional phase differences on each amplifier chain. Only one branch of the amplifiers network is not phase modulated. This branch is used as a reference and all the others will follow the phase fluctuations of the reference output.

Coherent beam combining phase difference analysis is performed through interferometric measurements. In order to get the proper information on the phase difference between the i^{th} branch and the reference, one has to tag the i^{th} branch. This technique was first introduced by the AFRL[5, 6].

At ONERA, we implemented a modulation multiplexing technique where the tagging is done by very low amplitude modulation of the i^{th} branch at a specific ν_i frequency. The overall interference signal is collected on a single photodetector (Fig. 1). Demodulating the interference signal at the specific ν_i frequency results in an output current $i_{error}(t)$:

$$i_{error}(t) \propto E_i J_1(\beta_i)\left[2E_r \sin(\varphi_r - \varphi_i) + \sum_{j=1}^{N-1} E_j J_0(\beta_j)\sin(\varphi_j - \varphi_i)\right] \quad (1)$$

The first order term in $i_{error}(t)$ is proportional to the sine of the phase difference between the i^{th} amplifier chain output and the reference. The second order term depends linearly on the sines of the phase differences of all pairs of amplifier chains outputs.

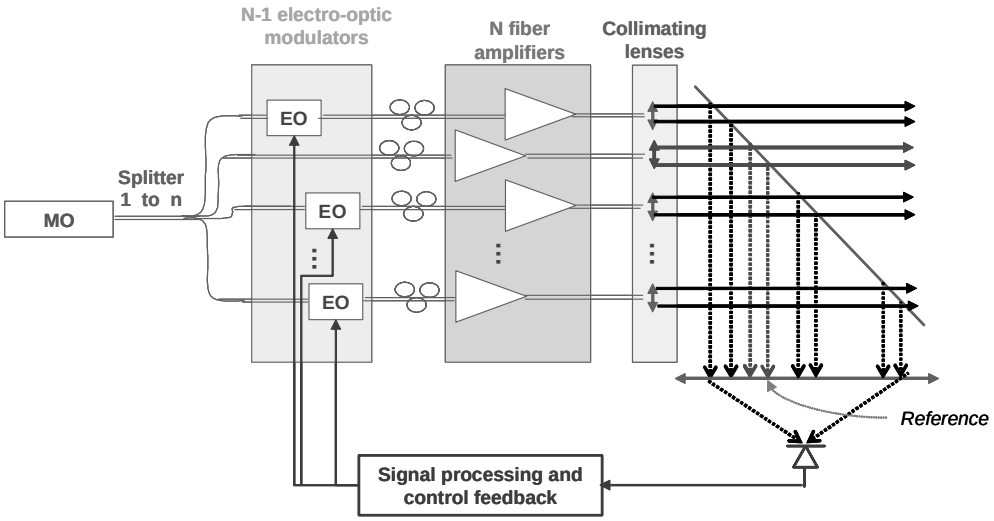

Fig. 1. Modulation multiplexing coherent combining of N amplifying chains.

Coherent combining is obtained through a control feedback loop, using $i_{error}(t)$ as an input, and sending the proper command on the i^{th} electro-optic modulator to verify the condition $i_{error}(t) = 0$. There is N-1 feedback loops in the experimental setup, one for every modulated branch. When all the feedback loops work together, the outputs from the amplifier chains are maintained locked on the reference output phase: coherent combining is achieved and the N beams interfere constructively generating a high brightness beam in the far field.

2.2 Spatial multiplexing technique for coherent beam combining

Another way to tag the i^{th} branch and gather separate information on the phase difference between this specific branch and the reference is to take advantage of the low divergence of the collimated output of an amplifying chain (Fig. 2). Such spatial multiplexing techniques have already been experimentally implemented[7, 8, 9].

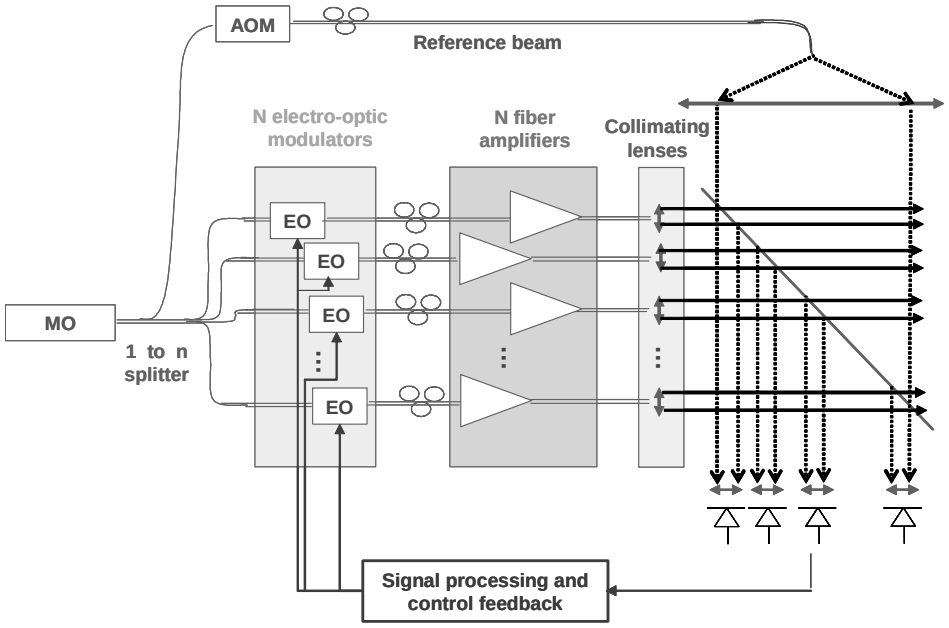

Fig. 2. Spatial multiplexing coherent combining of N amplifying chains.

In this case, a small part of the output beam from each amplifying chain is collected as soon as possible, and mixed with a reference beam either issued from the master oscillator or from one of the amplified chains. The interference signals coming from each branch are well separated spatially and each phase difference can easily be measured as the phase information from multiple branches is not mixed through beams overlap.

The spatial multiplexing techniques are really operative to overlap power from multiple laser sources, and increase overall brightness. Anyway, there is still complexity in this method as N interference signals have to be analyzed with N separate photodetectors.

But the main limitation of this method comes from the need for the output beams from the amplifying chains not to overlap before the interference signal measurement. This means that the phase difference measurement can only be done in the near field with spatial multiplexing techniques.

Modulation multiplexing techniques are comparable in complexity, as even if only one photodetector is required, N-1 feedback loops are needed and N-1 separate modulation frequencies have to be found.

But the main advantage of the modulation multiplexing technique is that the measurement of the interference signal can be done anywhere, in the near field or in the far field indifferently. Further in this paper, we will present results on turbulent atmospheric propagation compensation. Such results can only be obtained using the modulation multiplexing technique, as measurement of the intereference signal in the near field is impossible in this case.

With comparable levels of complexity, the spatial multiplexing and modulation multiplexing techniques differ mainly from their potential to operate on the basis of a signal collected in the near field for the former and anywhere (near field or far field indifferently) for the latter. For this reason, modulation multiplexing reveals higher potential for coherent combining of laser beams, offering more application domains than the spatial multiplexing technique.

2.3 Modulation multiplexing coherent combining experimental setup

We implemented an experimental setup described on figure 3 to coherently combine three 33 dBm polarization maintained Keopsys fiber amplifiers, using a modulation multiplexing technique. The master oscillator is a Koheras DFB polarized fiber laser delivering up to 10 mW at 1550 nm. The MO beam was splitted into three using 50:50 fiber couplers, and two electro-optic modulators were used to perform phase adaptation on two of the branches. The third branch serves as the reference beam.

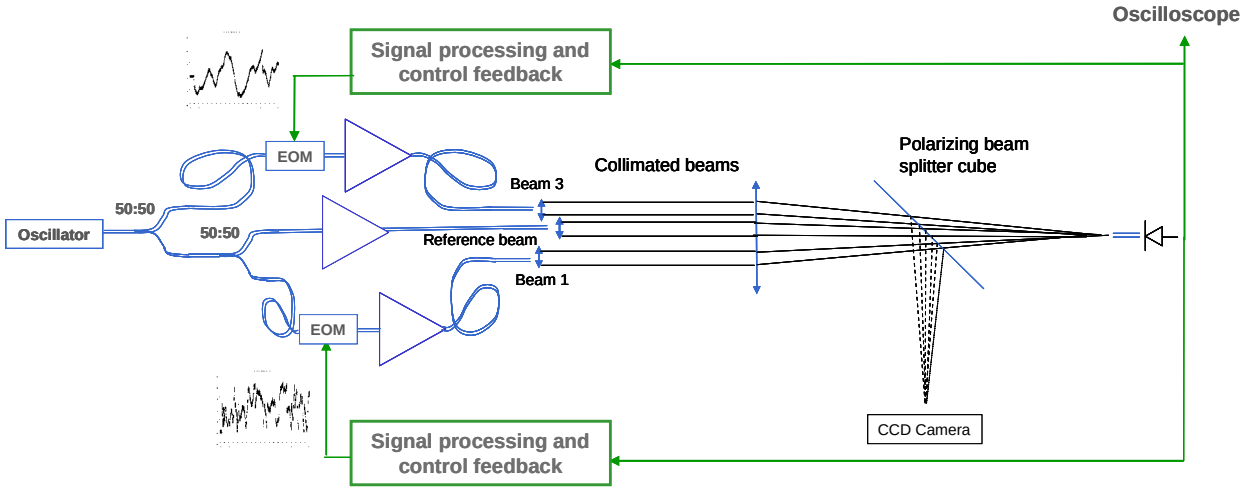

Fig. 3. Modulation multiplexing coherent combining experimental setup.

The fiber amplifier outputs are collimated and the overlapped beams are finally focused on a fibered photodetector to collect the complex interference signal coming from the mixing of the three beams. This signal is sent to two lock-in amplifiers, to perform the demodulation at ν_1 and ν_2 frequencies respectively (ν_1 = 50 kHz, ν_2 = 99 kHz). These lock-in

amplifiers extract the phase difference information specific to each fiber amplifier output. The error current from each lock-in amplifier is then sent as an input for a proportional-integral feedback loop commanding the electro-optic modulator to compensate phase difference with the reference output.

A polarizing beam splitter is placed before the photodetector. The very low flux reflected by the beam splitter is sent on a CCD camera to capture frames of the far-field interference pattern and visualize the coherent combining efficiency.

The feedback loops are implemented using two channels of a FPGA numerical board, with a 10-kHz bandwidth.

3. EXPERIMENTAL RESULTS

We characterized the phase fluctuations of the Keopsys fiber amplifiers used in the MOPA chains. The measurements were performed using an interferometric setup[7]. Interferences are formed between a reference beam coming from the master oscillator and an attenuated beam coming from the output of the fiber amplifier.

The interference spectra were analyzed up to 1 MHz and results are presented on figure 4. Different physical sources of phase fluctuations can be identified in these spectra. The slow low frequency effects up to 10 Hz are due to thermal drift in the fiber amplifiers. These effects are especially strong during the first 30 minutes after the amplifiers are switched on. Temperature in the fibers stabilizes after this warm up period, but temperature drift still exist thereafter. These slow effects are the easiest to compensate through coherent combining.

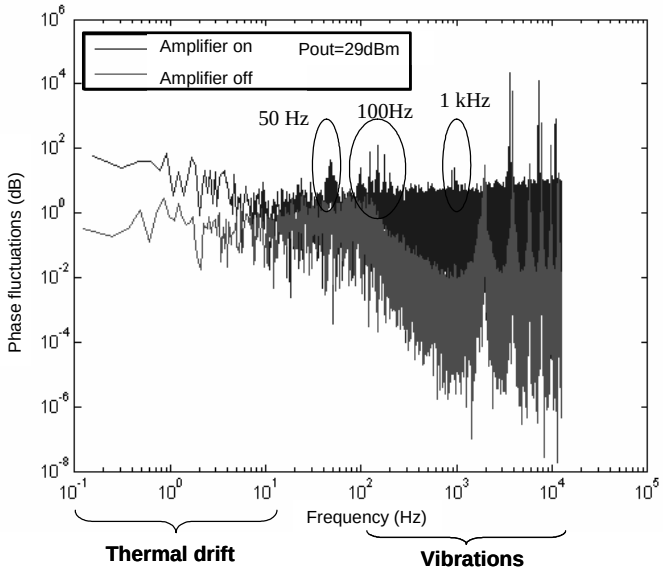

Fig. 4. Keopsys fiber amplifier phase fluctuation measurements: lower curve is obtained when the fiber amplifier is "off", and upper curve when the amplifier is "on", emitting 29 dBm power.

Above 10 Hz, the main effects are due to acoustic vibrations transmitted to the fibers. As the Keopsys amplifiers are commercial products, they are bundled in a box and heat is evacuated through vents using fans. Peaks at 50 Hz, 100 Hz and 1 kHz in the spectra are due to the vibrations induced by the cooling fans in the fibers of the amplifiers. But acoustic waves are also present in the fibers, even when the amplifier and thereby the cooling fans are off. Figure 4 shows strong peaks at 2 kHz and above, corresponding to the frequency and harmonics of resonant acoustic waves in the box containing the amplifier.

When the amplifier is on, the cooling fans induce strong acoustic waves and vibrations. The phase fluctuations resulting from these acoustic frequencies are more difficult to compensate, as the acoustic frequencies can be as high as 10 kHz. Vibrations between 10 kHz and 100 kHz are weaker but can also have to be compensated for.

Above 100 kHz, the phase fluctuations are strongly reduced, and will not have to be considerated when coherent combining is performed.

We coherently combined three fiber laser amplifiers. The far-field fringe patterns with and without active phase control are shown on figure 5. When the control loop is unlocked, the fringe pattern is blurred because of phase fluctuations. When all beams are phase-locked with the reference beam, the fringe pattern is well defined and fully stable.

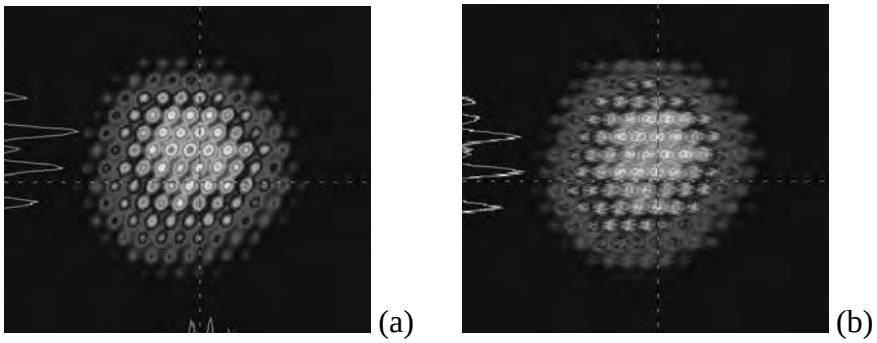

Fig. 5. Far field fringe pattern: a) phase control locked, b) phase control unlocked

Due to the near field geometry, the far field fringe pattern exhibits several interference lobes. As each collimated beam is separated by more than 1 centimetre, the filling ratio in our pupil is only 4%. Figure 6 presents the theoretical far-field pattern simulated with our geometry. If the pupil was more densified, we would have a larger central lobe with higher intensity. This could be done by adding an expanding lens at the output of each fiber amplifier. Our experimental setup allows us to evaluate the influence of a large pupil on the atmospheric turbulence compensation.

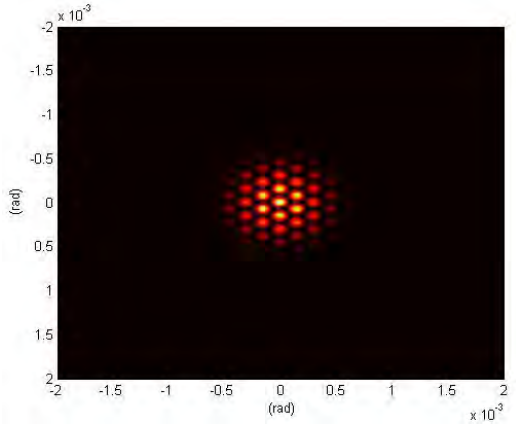

Fig. 6. Theoretical far-field pattern of our system.

The bandwidth of the implemented servo-loop is around 10 kHz. This is high enough to compensate temperature drifts and most of the phase variations measured on figure 4. Sudden vibrations like banging the system have high frequency spectral content and require a much higher bandwidth. Phase correction is made using electro-optic modulators, with a limited phase range of 4π. Since their bandwidths are more than 1 GHz, the snap back is very brief and doesn't impact the system's efficiency. The system's performance should always be assessed on real interference continuous measurements and not on a video signal to avoid sampling and filtering reset time (during snap backs) by video acquisition rate.

The residual phase error of our system is measured using the differential of the interference electric signal between the i^{th} element and the reference. In our configuration, we achieved a stability of $\lambda/30$ rms, no matter which beam is considered for the measurement.

3.1 Atmospheric propagation experiments:

The purpose of coherent combining is to increase power and radiance of laser sources without disturbing beam quality. Beyond compensating phase disturbance between each laser beam inside the laser system, being able to compensate phase disturbances such as atmospheric turbulence during the propagation path will strongly increase the available power and beam quality at distance from the laser system. Turbulence compensation usually requires a measurement of the turbulence induced phase error by an external system, such as an illuminating laser or laser guide star, and adaptive optics. Turbulence compensation have also been shown with stimulated Brillouin scattering phase conjugation[10]. Bruesselbach et al[4] demonstrated turbulence compensation for laser communication through the atmosphere using coherent phase locking of seven fiber amplifiers based on a multi-dither approach and modulation of pump current of the laser diodes pumping the optical amplifiers. This experiment was implemented for a direct link.

We present two experiments of turbulence compensation without an external measurement system. The first one is based on the setup of figure 3 and similar to reference 4, although the multi-dither technique is implemented with electro optic modulators. Atmospheric turbulences are induced with an air blower in the collimated beams zone. The air blower can be set at low flow, generating moderate strength turbulence equivalent to atmospheric propagation over several kilometers. It can also be set at high flow, generating strong turbulence no more comparable with natural turbulence. In the experiments, we managed to compensate moderate turbulence (low flow air blower settings) but the bandwidth of our feedback loop was not sufficient to compensate the strongest turbulences (high flow air blower settings). We obtain a stable far-field fringe pattern when the phase control system is locked. Such atmospheric turbulence compensation without an external measurement system can only be done with active coherent combining systems which analyze phase difference in far field. Therefore, spatial multiplexing techniques are not convenient for such purpose.

This experiment shows that our phase control system is able to compensate atmospheric turbulence without the help of any other subsystem. However, it requires a photodetector in the far field, which is often impossible in real conditions.

The second experiment performs compensation of the onward atmospheric turbulence suffered by the laser beam, using the backward signal received after reflection on a diffuse surface. The amplifiers, master oscillator and signal processing in the experimental set-up have already been described before (figure 3). The output beams are collimated and then focused together on a diffuse surface. A leakage part of the beam is focused on a camera to visualize the far field fringe pattern. The reflected beam comes back in the polarizing beam splitter cube and is focused through a pinhole on the detector. A schematic diagram of the experimental setup is shown on figure 7.

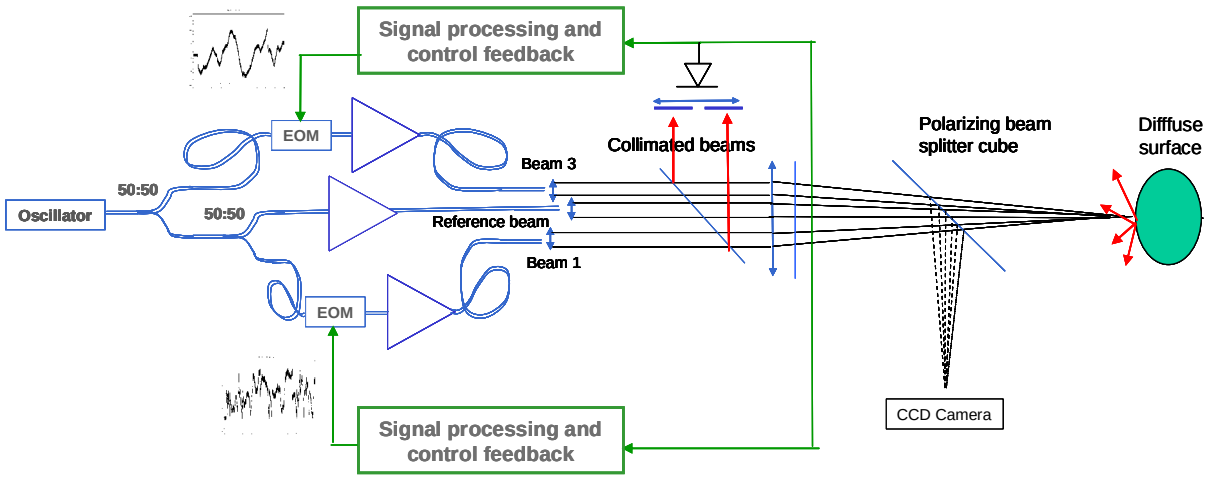

Fig. 7. Experimental setup of coherent combining after propagation through turbulence and reflection on a diffuse surface.

We succeeded in coherently combining the three laser amplifiers on the diffuse surface. Even with turbulence generated by the hot air blower (low flow air blower settings), the fringe pattern on the diffuse surface remains stable. We tested four different places for the turbulent zone: in the collimated beams zone in front of the emitting lenses (i), in the focused part of the beam just before the surface (ii), and just before the detector, in the collimated beams zone (iii) and in the focused reflected beam (iv). When moderate strength turbulence was generated in any of these four zones, we managed to compensate them. When the active phase control is unlocked, we observe rapid fluctuation of the pattern in each case.

The system compensates only turbulence found on the onward path, but not on the backward path of the beam, ensuring the highest brightness on the diffuse surface. Indeed, when generating turbulence in zones (iii) or (iv) (located on the backward part of the beam only) at a stronger level of turbulence (high flow air blower settings), we still observe perfect phase locking on the diffuse surface.

4. CONCLUSION

We have performed coherent combining of fiber amplifiers in a high brightness beam using the modulation multiplexing technique. This technique has revealed a strong potential for many applications, as the interference signal driving the active phase control can be acquired either in the near field or in the far field.

Coherent combining has been extended to wavefront shaping in experiments of propagation through turbulent atmosphere. These experiments demonstrated that coherent combining can be maintained through low to medium turbulence strength, exhibiting the feasibility of coherent combining of laser sources through turbulent atmosphere with the modulation multiplexing technique.

Finally and for the first time to our knowledge, automatic coherent combining of fiber amplifiers on a diffuse surface have been demonstrated. With the modulation multiplexing technique, coherent combining on a surface can be performed after propagation through turbulent atmosphere, without any external turbulence measurement subsystem.

5. ACKNOWLEDGEMENTS

The authors want to thank Bernard Moreau, Anne Durecu, Vincent Michau, Laurent Mugnier, Thierry Fusco, Frederic Cassaing and Cyril Petit for fruitful discussions.

This work was partially funded by Delegation Generale pour l'Armement and Region Ile-de-France.

REFERENCES

[1] V. Gapontsev, D. Gapontsev, N. Platonov, O. Shkurikhin, V. Fomin, A. Mashkin, M. Abramov and S. Ferin, *"2 kW CW ytterbium fiber laser with record diffraction-limited brightness"*, Conference on Laser and Electro-Optics Europe (2005).

[2] T. H. Loftus, P.R. Hoffman, A.M. Thomas, M. Norsen, R. Royse and E. Honea, *"522-W spectrally beam combined fiber laser with near-diffraction limited-beam quality"*, Proc. SPIE vol. **6453**-28 (Photonics West 2007).

[3] J. Anderegg, S. Brosnan, E. Cheung, P. Epp, D. Hammons, H. Komine, M. Weber and M. Wickham, *"Coherently coupled high power fiber arrays"*, Proc. SPIE vol. **6102**-30 (Photonics West 2006).

[4] H. Bruesselbach, S. Wang, M. Minden, D.C. Jones and M. Mangir, *"Power-scalable phase-compensating fiber-array transceiver for laser communications through the atmosphere"*, JOSAB **22(2)**, 347-353 (2005).

[5] T.M. Shay, V. Benham, J.T. Baker, B. Ward, A.D. Sanchez, M.A. Culpepper, D. Pilkington, D.J. Nelson and C.A. Lu, *"First experimental demonstration of self-synchronous phase locking of an optical array"*, Opt. Express **14(25)**, 12015-12021 (2006).

[6] T.M. Shay, V. Benham, J.T. Baker, A.D. Sanchez, D. Pilkington and C.A. Lu, *"Self-synchronous and self-referenced coherent beam combination for large optical arrays"*, IEEE J. Select. Topics in QE **13(3)**, 480-486 (2007).

[7] S.J. Augst, T.Y. Fan and A. Sanchez, *"Coherent beam combining and phase noise measurements of ytterbium fiber amplifiers"*, Opt. Lett. **29(5)**, 474-476 (2004).

[8] C.X. Yu, J.E. Kansky, S.E.J. Shaw, D.V. Murphy and C. Higgs, *"Coherent beam combining of a large number of PM fibers in a 2D fiberarray"*, CThAA6, Conference on Laser and Electro-Optics (2006).

[9] S. Demoustier, A. Brignon, E. Lallier, J.P. Huignard and J. Primot, *"Coherent combining of 1.5μm Er-Yb doped single mode fiber amplifiers"*, CThAA5, Conference on Laser and Electro-Optics (2006).

[10] H. Bruesselbach, D.C. Jones, D.A. Rockwell, R.C. Lind *"Real-time atmospheric compensation by stimulated Brillouin scattering phase conjugation"*, JOSAB **12(8)**, 1434-1447 (1995).

Beam Shaping of Single-Mode and Multimode Fiber Amplifier Arrays for Propagation Through Atmospheric Turbulence

Véronique Jolivet, Pierre Bourdon, Baya Bennaï, Laurent Lombard, Didier Goular, Emilie Pourtal, Guillaume Canat, Yves Jaouën, Bernard Moreau, and Olivier Vasseur

(Invited Paper)

***Abstract*—We report experimental results and theoretical analysis of coherent beam combining with active phase control fiber beam shaping. An original optical configuration for target-in-the-loop single-mode fiber amplifier coherent combining through turbulence is presented, with a $\lambda/15$ residual phase error. The experimental results and theoretical analysis demonstrate that detection subsystem aperture reduction is paramount to lower sensitivity to backward turbulence when using a detector in the laser emitter plane. In this configuration, coherent combining is achieved on a remote scattering surface with sole compensation of the onward turbulence. We also present a numerical model capable of assessing the combining efficiency in the case of high-power multimode large-mode-area (LMA) fiber amplifiers. Preliminary theoretical investigations point out that multiple-transverse-mode combining can result in severe wavefront distortion. In the case of multimode LMA fibers, control of the transverse modes phase relationship has to be achieved to preserve combining efficiency.**

***Index Terms*—Laser arrays, optical fiber amplifiers, optical propagation.**

I. Introduction

BEAM combining of high-power fiber lasers is being considered a promising technique to overcome laser power scaling limits such as thermal load, nonlinear effects in the laser medium, and damage threshold of optical components [1]. Both incoherent and coherent combining techniques have been demonstrated recently, with overall power close to half a kilowatt [2], [3].

Manuscript received October 8, 2008; revised December 5, 2008. Current version published April 8, 2009. This work was supported in part by French Région Ile de France and by Délégation Générale pour l'Armement.

V. Jolivet, P. Bourdon, B. Bennaï, L. Lombard, D. Goular, G. Canat, B. Moreau, and O. Vasseur are with the Département Optique Théorique et Appliquée, Office National d'Etudes et de Recherches Aérospatiales (ONERA), The French Aerospace Lab, Palaiseau 91761, France (e-mail: veronique.jolivet@onera.fr; pierre.bourdon@onera.fr; baya.bennai@onera.fr; laurent.lombard@onera.fr; didier.goular@onera.fr; guillaume.canat@onera.fr; bernard.moreau@onera.fr; olivier.vasseur@onera.fr).

E. Pourtal was with the Département Optique Théorique et Appliquée, Office National d'Etudes et de Recherches Aérospatiales (ONERA), The French Aerospace Lab, Palaiseau 91761, France. She is now with THALES, 78990 Elancourt, France (e-mail: emilie.pourtal@onera.fr).

Y. Jaouën is with TELECOM ParisTech, 75634 Paris, France (e-mail: jaouen@telecom-paristech.fr).

Color versions of one or more of the figures in this paper are available online at http://ieeexplore.ieee.org.

Digital Object Identifier 10.1109/JSTQE.2008.2011141

Incoherent techniques rely on the brilliance of the primary beams to obtain large combined power density [4], [5]. Many coherent techniques imply the use of a self-organized beam coupling process offering no direct control on the combined beam profile [6]–[9]. Coherent beam combining (CBC) with active phase control has been proposed not only for laser power scaling, but also for other purposes such as beam steering [10] and wavefront shaping [11].

This versatile CBC method is therefore particularly useful for long-range operation of deployed laser systems. For such field applications, it is mandatory to compensate for atmospheric turbulence that affects the laser beam during its propagation, considerably fading the far-field power density. Adaptive optics is extensively used to cancel the deleterious effects of atmospheric aberrations, and deliver high power density on a remote surface after turbulent propagation. The various optical systems dedicated to overcoming the wavefront distortions experienced by laser beams, in optical media and in turbulent atmosphere, have been called coherent optical adaptive techniques (COATs) [12]. These wavefront correction techniques are usually achieved using deformable mirrors. These classical adaptive optics components have been used since the 1970s to perform experimental demonstration of COAT [13], [14]. More recently, CBC through turbulence with active phase control has been experimentally demonstrated [11], [15], [16]. First experiment was designed for laser communication through the atmosphere. Coherent phase-locking of seven fiber amplifiers based on a frequency-tagging multidither approach was achieved, using modulation of the optical amplifier diode pump current. The detection subsystem was located in the target plane [11]. Another demonstration with 48 passive fibers was experimentally conducted and relied on a multidither control loop maximizing the power in the bucket on a detector placed in the target plane [15].

However, most outdoor applications of laser systems require that the highest power density be delivered on a surface from afar. As the target plane is out of reach, it is necessary to remotely control the power deposited on the target. Therefore, target-in-the-loop techniques have been developed using the backscattered signal coming from the target. Experiments conducted with deformable mirrors in the 1970s used the signal backscattered from a bright (or glint) point on the target. The near-field wavefront was then distorted to maximize the glint-backscattered signal and, thereby, the far-field power density.

It was only recently that the first experimental demonstration of target-in-the-loop coherent combining of fiber lasers through turbulence using the backscattered signal was presented [16]. This demonstration was done on a scattering target. It involved the use of frequency tagging techniques [in this experiment, self-referenced locking of optical coherence by single-detector electronic-frequency tagging (LOCSET)], thus allowing to extract the phase information from completely overlapped beams. Long-range on-the-field laser systems could benefit from these target-in-the-loop techniques as they do not require secondary turbulence strength measurement subsystem (e.g., laser guide star and wavefront analysis in astronomy), thereby potentially reducing the complexity of COAT systems.

These previous experimental results on turbulence compensation have been supported by numerical studies. Target-in-the-loop wave propagation geometries have been theoretically studied in [17], where a detailed analysis of the impact of the target and atmosphere-induced aberrations on an adaptive system performance has been conducted. The design parameters of a field laser system using CBC for turbulence compensation have been examined thoroughly in [18], and the number of sources and bandwidth requirements for optimized efficiency inferred. More recently, combined beam propagation through turbulence has been theoretically explored in the case of diffraction-limited Gaussian primary beams [19], [20]. Coherent combining and incoherent superposition of laser beams are compared, demonstrating the increase in power density when phase-locking the beams.

However, the diffraction-limited Gaussian beam assumption is not always valid in the case of field systems with long range of operation. High-power laser sources with larger apertures are required (e.g., large-mode-area (LMA) fibers), and the assumption of diffraction-limited Gaussian beams is rarely preserved. Studies have been conducted to evaluate the potential of various beam profiles toward atmospheric propagation [21]. For example, top hat and higher order beams seem to present interesting properties and suffer less than fundamental Gaussian beams from atmospheric turbulence distortion [22], [23].

In this paper, we present both experimental and theoretical results regarding two phenomena that can potentially impair the efficiency of coherent combining laser systems: atmospheric propagation and degraded beam quality primary laser sources.

We report coherent combining wavefront shaping for atmospheric turbulence compensation, and numerical modeling of multiple-transverse-mode coherent combining for efficiency optimization.

The experimental setup we developed to perform CBC of three 1.55-μm eye-safe fiber amplifiers and the frequency tagging active phase control technique is introduced. Efficient CBC is demonstrated. Low- to medium-strength atmospheric turbulence is added and the several kilohertz bandwidth of the setup proves to be sufficient to perform CBC through turbulence. Then, experimental demonstration of target-in-the-loop CBC of fiber amplifiers on a remote scattering target is reviewed in detail. We present an optimized optical configuration for this purpose that we implement experimentally, demonstrating CBC on a remote scattering target with a detector in the laser emitter plane. The theory of frequency tagging CBC is extended to the case of target-in-the-loop experiments. The impact of the detection-subsystem-limited aperture on the sensitivity to backward turbulence is clearly pointed out.

We also present a numerical model for theoretical study of CBC with multiple-transverse-mode primary laser sources. CBC efficiency optimization criteria are introduced and the model is used to evaluate these criteria for various mode compositions in the primary fiber lasers. The influence of the multiple-transverse-mode composition on the combining efficiency is finally discussed.

II. CBC Through Turbulence

A. Principle of Coherent Combining and Experimental Setup

Coherent combining with active phase control is a well-known technique to sum the power of multiple laser amplifiers with same polarization, seeded by a unique master oscillator. Because of their mutual coherence, these laser sources interfere in the far field, thus allowing brightness increase. However, power laser amplifiers induce fluctuating phase differences (thermal drift, mechanical and acoustic vibrations, laser gain, and nonlinear-effect-induced phase shifts) on the common beam reference delivered by the master oscillator. Without any compensation, these phase fluctuations will considerably reduce the average brightness in the combined field. So, active phase control method is required to lock all the amplifiers in phase. The result is a stable interference pattern in the combined field.

In the experimental setup we developed for CBC, phase difference measurement is performed in the spectral domain, using a modulation multiplexing technique first introduced for fiber lasers by Shay *et al.* [24], [25]. A small-depth phase modulation is added on each path with a unique kth tagging frequency using an electro optic modulator. Through frequency tagging, phase difference measurement between each beam and the reference is achievable. The overall interference signal is collected on a single photodetector. Demodulating the interference signal at the kth modulation frequency results in an output current $i_{k\,\mathrm{error}}(t)$ proportional to the phase difference of the kth path with the reference beam.

The experimental setup we developed for CBC of three fiber amplifiers is shown in Fig. 1. The master oscillator is a Koheras DFB polarized fiber laser, delivering up to 22 mW at 1.55 μm with a linewidth lower than 50 kHz. It is split into three paths that are amplified separately through 2 W polarization-maintaining Keopsys fiber amplifiers. Two paths include electro optic phase modulators applying both the phase difference compensation control and the tagging modulation on each path. The third path is chosen as the reference beam. Three adjacent 12-mm-diameter fiber collimators set in triangle with a focal length of 8 mm are used to handle the fiber amplifier outputs. The collimated beams interfere in the far field where a small detector extracts the interference signal, which is processed at each modulation frequency ($v_1 = 50\,\mathrm{kHz},\ v_2 = 83\,\mathrm{kHz}$) using lock-in amplifiers. Each demodulated output is then sent to a proportional integral (PI) control feedback loop. The adjusted commands are then applied on the electro optic phase modulators

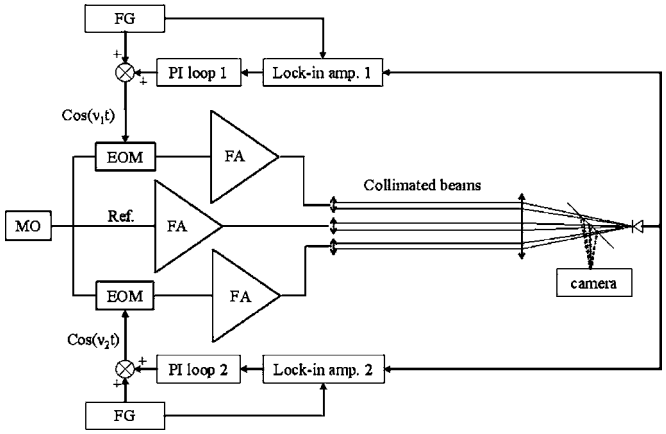

Fig. 1. Experimental setup of coherent combining of three fiber amplifiers (FAs). FG, frequency generator; PI loop, proportional integral feedback control loop; Ref., reference beam; MO, master oscillator; EOM, electrooptic modulator.

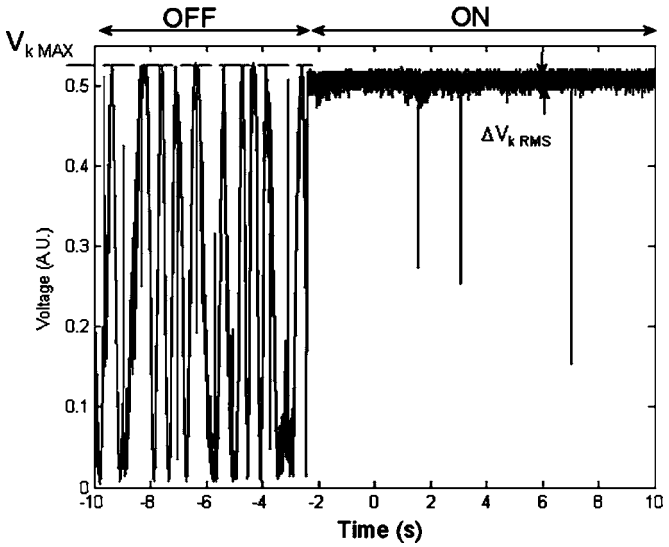

Fig. 2. Interference electric signal between the kth element and the reference. OFF, all control loops inactive; ON, all phase control loops active. 0 V is the destructive interference level and $V_{k\,\mathrm{MAX}}$ the constructive interference level. The three spikes during the active control loops come from the snap back of the electro optic modulator, which can induce phase shifts only in the -2π to 2π range.

and maintain all $i_{k\,\mathrm{error}}(t) = 0$, compensating phase differences with the reference output. The control feedback loops instantaneous response time has been measured and the bandwidth of the feedback loops inferred from this measurement. This bandwidth of several kilohertz is sufficient to balance all the major effects generating phase fluctuations in the amplifiers. A beam splitter is placed before the photodetector. The leakage part reflected by the beam splitter is sent on a charge-coupled device (CCD) camera to capture frames of the far-field interference pattern and visualize the coherent combining efficiency. Atmospheric turbulence induced by a hot air blower can be added on the collimated beam path.

The residual phase error is evaluated from the interference electric signal between the kth element and the reference beam, measured using a separate photodetector. This interference signal is shown in Fig. 2.

When the control loop is inactive, the interference electric signal fluctuates between zero and $V_{k\,\mathrm{MAX}}$ output voltage corresponding to the destructive and constructive interference levels, respectively. When the control loop is active, the interference electric signal reaches $V_{k\,\mathrm{MAX}}$ value with an rms value $\Delta V_{k\,\mathrm{rms}}$. The residual phase error is derived from the differential of the interference electric signal that is equal to

$$V_k = \frac{V_{k\,\mathrm{MAX}}}{2}\left(1 + \cos\,\Delta\varphi_k\right) \tag{1}$$

where $\Delta\varphi_k$ is the phase difference between the kth and reference beams. The rms phase error is therefore

$$\Delta\varphi_{k\,\mathrm{rms}} = 2\sqrt{\frac{\Delta V_{k\,\mathrm{rms}}}{V_{k\,\mathrm{MAX}}}}. \tag{2}$$

Using this experimental setup, we coherently combined three fiber laser amplifiers with a residual phase error of λ/30 rms, no matter which beam is considered for the measurement.

B. Coherent Combining and Turbulence Compensation: Phase-Locking on a Direct Link

As mentioned in Section I, Bruesselbach *et al.* [11] and Kansky *et al.* [15] previously reported atmospheric turbulence compensation using coherent phase-locking and a detector in the target plane.

We performed similar experiments with our system, adding turbulence on the collimated beam path with a hot air blower. The product of the refractive index structure parameter C_n^2 and the propagation distance L is $C_n^2 L = 1.2 \times 10^{-10}$ m$^{1/3}$, measured through a centroid displacement method. The experimental beam propagation is equivalent, for most of the turbulence effects, to kilometric range atmospheric path through a C_n^2 of 1.2×10^{-13} m$^{-2/3}$. The result is a stable interference pattern in the far field when turbulence is added, with a residual phase error of λ/23 rms. This experiment demonstrates that a several kilohertz bandwidth and three laser sources are sufficient to compensate for both watt-power-level fiber laser and low- to medium-atmospheric-turbulence phase fluctuations.

However, these setups require a photodetector in the target plane, which is often unfeasible in real conditions. Coherent adaptive optics techniques have been facing the same difficulty. As a solution, optical configurations have been developed with a detector close to the laser emitter plane receiving the backscattered signal from the target [12]. Such target-in-the-loop configurations can also be used to perform coherent combining of laser sources through turbulence. In this case, the main issue is to succeed in compensating only for the onward turbulence and not the whole-trip phase errors present in the laser beam phase. A way to solve this issue is to use a pinhole limiting the system aperture as we proposed and experimentally demonstrated

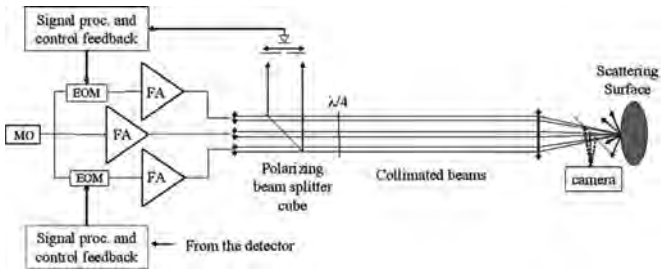

Fig. 3. Experimental setup of coherent combining on a scattering surface after propagation through turbulence. Amplifiers and signal processing are the same as in Fig. 1. The detector is a New Focus low-noise 125-MHz photoreceiver (general purpose receiver, ref.: 1811FC-125 MHz).

in [16]. We present shortly quantitative experimental results and a theoretical analysis of this target-in-the-loop setup.

III. Target-in-the-Loop Experiment

A. Phase-Locking on a Scattering Surface With the Detector in the Laser Emitter Plane, Using the Backscattered Signal and Compensating the Sole Onward Turbulence

We experimentally achieved compensation of the onward atmospheric turbulence encountered by the combined laser beam, using the backward signal received after scattering on a remote surface. The target-in-the-loop setup (Fig. 3) includes the same emitting laser system, but instead of locating the detector in the far field, we replace it by a scattering surface and move the detector next to the laser system. We add a circulator made of a polarizing beam splitter cube and a λ/4 beam plate. This way, the photodetector receives the backscattered signal. The collimated beams from the fiber amplifiers pass through the cube and the beam plate, interfere in the far field on the scattering surface, and are backscattered toward the detector through a pinhole. Rather than the conventional positioning between the lens collecting the backscattered signal and the photodetector, we use an original optical configuration where the pinhole is placed before the lens. As the turbulence strength is the same as in Section II-B, the Fried's parameter r_0 value is 30 mm derived from the measured $C_n^2 L$. Thus, the pinhole of 1 mm diameter reduces the aperture of the detection subsystem below Fried's parameter. The signal processing and control loop have already been described.

Without the pinhole, the phase relationships between beams coming from the different amplifiers are blurred by turbulence during the backward propagation to the detector. Therefore, the coherent combining will be performed in the detector plane and the interference pattern will be stable there but not on the scattering surface. Inversely, as it will be theoretically demonstrated in Section III-B, with a sufficiently small pinhole in place, light scattered by the Lambertian surface is spatially filtered and phase relationships between beams coming from the different amplifiers are preserved during the backward propagation to the detector. Thus, coherent combining results in a stable interference pattern on the scattering surface. The pinhole size and position have to be properly chosen to reduce the aperture of the detection subsystem. The pinhole spatial filtering prevents the turbulence on the backward path from impacting the detection and phase difference measurement process. Coherent combining is performed just as if the detector was placed in the plane of the scattering surface. It should be noted that the efficiency of the combining process in this configuration does not suppose any specific property of the scattering surface (glint start or high contrast in surface reflectivity is not necessary).

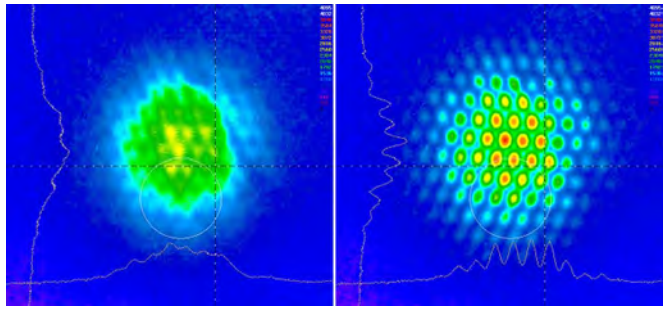

Fig. 4. Far-field fringe pattern on the scattering surface with control loop off (left) and on (right) and turbulence added on the onward and backward path, acquired using a Spiricon phosphor-coated CCD camera. Due to a low fill factor of the pupil (only 4%) in the near-field geometry, the far-field fringe pattern exhibits several interference lobes. Numerical simulations show that the overall power in the central lobe is 7%.

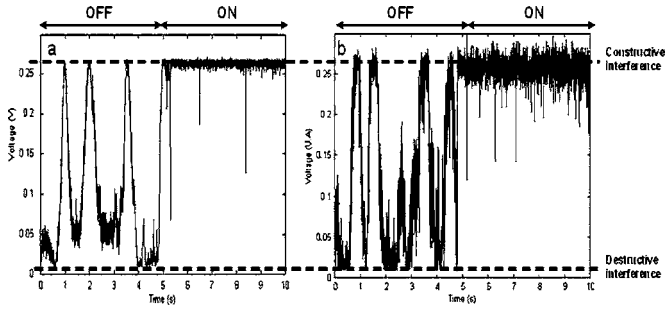

Fig. 5. Interference electric signal between one modulated element and the reference. (a) Target-in-the-loop experiment without turbulence. (b) Target-in-the-loop experiment with low- to medium-strength turbulence; OFF, all control loops inactive; ON, all phase control loops active. Residual phase error measurement is performed from this signal as described in Fig. 2 and (2).

With this experimental setup, we obtain a stable fringe pattern on the scattering surface, even when the beams suffer turbulence on the onward and backward paths (see Fig. 4).

The residual phase error measured using the interference electric signal between one modulated element and the reference is λ/28 rms without turbulence and λ/15 rms when turbulence is added (Fig. 5). With the same configuration and an optimized fill factor (36%), numerical simulations show that the λ/15 residual phase error will result in 68% of overall power in the central lobe and a degradation of the Strehl ratio of 11% when compared with perfect phase-locking.

To illustrate that the setup is insensitive to backward turbulence, we chose a strong level of turbulence ($C_n^2 L = 2.4 \times 10^{-9}$ $\mathrm{m}^{1/3}$, corresponding to kilometric range atmospheric propagation through a C_n^2 of 2.4×10^{-12} $\mathrm{m}^{-2/3}$) generating phase fluctuations beyond the system locking capability. The pinhole diameter (1 mm) is still below the Fried's parameter

($r_0 = 5.5$ mm). Even with this strong turbulence level induced only on the backward path (i.e., between the polarizing cube and the detector), the far-field fringe pattern is stable.

We therefore validated experimentally target-in-the-loop phase-locking of three laser amplifiers on a scattering surface, with sole compensation of the onward turbulence, using a detector in the laser emitter plane.

B. Theory

Comprehensive analysis of this target-in-the-loop experiment requires some theoretical developments. We extend thereafter the self-referenced LOCSET theory described by Shay *et al.* [25] and take into account both propagation through turbulence and presence of a scattering target in the loop.

The reference beam optical field $E_u(t)$ and the ith array beam optical field $E_i(t)$ at the output of the laser are given by

$$E_u\,(t) = E_{u0}\cos\left(\omega_{\mathrm{L}}t + \phi_u\right) \tag{3}$$

and

$$E_i\,(t) = E_{i0}\cos\left(\omega_{\mathrm{L}}t + \phi_i + \beta_i\sin\left(\omega_i t\right)\right) \tag{4}$$

where E_{u0} and E_{i0} are the field amplitudes for the unmodulated reference beam and for the ith-phase-modulated beam, respectively, ω_{L} is the laser frequency, ϕ_u and ϕ_i are the optical phases of the unmodulated and the ith beams, respectively, β_i is the phase modulation amplitude, and ω_i the RF modulation frequency for the ith array element.

As we use collimated laser beams, we assume that the diameter of each primary beam is smaller than the Fried's diameter. With this assumption, the reference and ith-phase-modulated beams propagate to the scattering surface mainly suffering from onward-turbulence-induced uniform phase differences $\Delta\phi_u$ and $\Delta\phi_i$, respectively.

Then, the laser beams interfere on the remote scattering surface. We reference with an index s the scattering areas present inside the laser-illuminated area. The sth scattering area sends back a fraction of laser power η_s^2, and induces a phase shift φ_s [26].

The unmodulated and ith-phase-modulated optical fields backscattered by the sth scattering area can be written as

$$E_{s\_u}\,(t) = \eta_s E_{u0}\cos\left(\omega_{\mathrm{L}}t + \phi_u + \Delta\phi_u + \varphi_s\right) \tag{5}$$

and

$$E_{s\_i}\,(t) = \eta_s E_{i0}\cos\left(\omega_{\mathrm{L}}t + \phi_i + \beta_i\sin\left(\omega_i t\right) + \Delta\phi_i + \varphi_s\right). \tag{6}$$

Fig. 6 describes the path followed by the optical rays coming from one single scattering area when the aperture of the photodetector is limited by a pinhole placed before the collecting lens. Only those areas that scatter light inside the solid angle delimited by the pinhole will contribute to the backscattered signal on the photodetector. We assume that the number of contributing scattering areas is M.

Basic ray tracing considerations show that light scattered by a single contributing area at a given position in the scattering plane is collimated by the far-field focusing lens in a single direction. Light from a different contributing scattering area will be collimated in a different direction. The pinhole selects a channel of optical rays for each direction of propagation. Therefore, all the optical rays coming from a given contributing scattering area have to pass through the same cylindrical channel, whatever the laser beam they originate from. If the pinhole is small enough, all the cylindrical channels inside the field of view of the photodetector have their diameter lower than the Fried's diameter of the atmospheric turbulence. Hence, all the optical rays inside a given propagation channel suffer from the same backward-turbulence-induced phase shift. We denote by $\Delta\varphi_s$ this backward-turbulence-induced uniform phase shift suffered by the rays coming from scattering on the sth contributing area and confined inside the sth propagation channel.

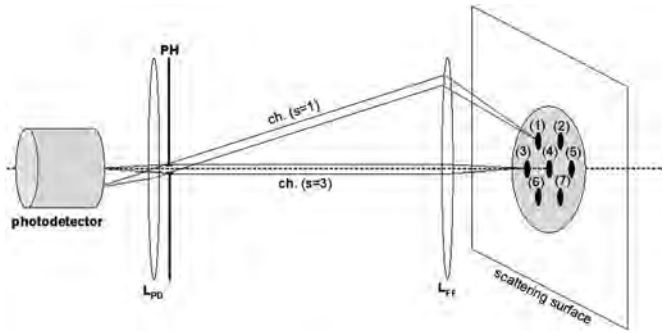

Fig. 6. Ray tracing schematic of backscattered light from the remote surface. (1), (2), . . . , (7) are the contributing scattering areas on the scattering surface. $\mathrm{L_{FF}}$: far-field focusing lens; $\mathrm{L_{PD}}$: photodetector collecting lens; PH: aperture-limiting pinhole. Each contributing scattering area is associated with a propagation channel. The channels denoted by ch. ($s = 1$) and ch. ($s = 3$) are examples of these propagation channels for light backscattered from scattering areas (1) and (3), respectively. Due to the presence of the pinhole, only backscattered light propagating within these channels will reach the photodetector from areas (1) and (3), respectively.

The total optical field coming back to the photodetector through the pinhole $E_{\mathrm{T}}(t)$ is given by

$$E_{\mathrm{T}}\,(t) = \sum_{s=1}^{M} E_{us}\,(t) + \sum_{j=1}^{N}\sum_{s=1}^{M} E_{js}\,(t) \tag{7}$$

with

$$E_{us}\,(t) = \eta_s E_{u0}\cos\left(\omega_{\mathrm{L}}t + \phi_u + \Delta\phi_u + \varphi_s + \Delta\varphi_s\right) \tag{8}$$

and

$$E_{js}\,(t) = \eta_s E_{j0}\cos(\omega_{\mathrm{L}}t + \phi_j + \beta_j\sin(\omega_j t) + \Delta\phi_j + \varphi_s + \Delta\varphi_s). \tag{9}$$

The photodetector current $i_{\mathrm{PD}}(t)$ is proportional to the received intensity and can be written as

$$i_{\mathrm{PD}}\,(t) = R_{\mathrm{PD}}A\sqrt{\frac{\varepsilon_0}{\mu_0}}\left[\sum_{s=1}^{M}\left(E_{us}\,(t) + \sum_{j=1}^{N} E_{js}\,(t)\right)\right]^2 \tag{10}$$

where μ_0 and ε_0 are the magnetic and electric permeabilities of free space, R_{PD} the responsivity of the photodetector, and A the photodetector area.

The phase error control signal is obtained from this photodetector current using coherent demodulation in the RF domain. The photodetector current is multiplied by $\sin(\omega_i t)$ and integrated over a time τ to derive the ith phase error control signal. Proper value of τ is thoroughly discussed by Shay *et al.* [25], where CBC operates only under the assumption that the photodetector is small enough to receive only a portion of the central lobe of the interference far-field pattern. We make a similar assumption that the pinhole and photodetector sizes are both small enough to filter the spatial modulations of the optical intensity, either in the pinhole plane or on the photodetector plane.

Resulting phase error signal is to an excellent approximation

$$S_{Si} = R_{\mathrm{PD}} J_1(\beta_i) \times \sum_{s_1=1}^{M}\sum_{s_2=1}^{M}\left[\begin{array}{l} K_{uis_1s_2}\sin(\phi_u+\Delta\phi_u-\phi_i-\Delta\phi_i+\psi_{s_1s_2}) \\ +\sum_{j=1}^{N} K_{jis_1s_2}\sin(\phi_j+\Delta\phi_j-\phi_i-\Delta\phi_i+\psi_{s_1s_2})\end{array}\right] \tag{11}$$

with

$$K_{uis_1s_2} = \sqrt{P_{us_1}P_{is_2}},\ K_{j\,i\,s_1\,s_2} = J_0(\beta_j)\ \sqrt{P_{js_1}P_{is_2}} \tag{12}$$

and

$$\psi_{s_1s_2} = \varphi_{s_1} - \varphi_{s_2} + \Delta\varphi_{s_1} - \Delta\varphi_{s_2}. \tag{13}$$

where J_0 and J_1 are the Bessel functions of the first kind of order zero and one, respectively, and P_{us} and P_{js} are the optical power backscattered to the photodetector from the sth scattering area and from the unmodulated beam and the jth-phase-modulated beam, respectively.

The double sum over s_1 and s_2 in (11) can be split into two parts: first part S_{Si_I} includes the terms mixing contributions coming from the same scattering area (i.e., $s_1 = s_2$) and second part S_{Si_II} includes the terms mixing contributions coming from two different scattering areas

$$S_{Si\_I} = R_{\mathrm{PD}} J_1(\beta_i) \times \sum_{s=1}^{M}\left[\begin{array}{l} K_{uiss}\sin(\phi_u+\Delta\phi_u-\phi_i-\Delta\phi_i+\psi_{ss}) \\ +\sum_{j=1}^{N} K_{jiss}\sin(\phi_j+\Delta\phi_j-\phi_i-\Delta\phi_i+\psi_{ss})\end{array}\right] \tag{14}$$

$$S_{Si\_II} = R_{\mathrm{PD}} J_1(\beta_i) \times \sum_{s_1\neq s_2}\left[\begin{array}{l} K_{uis_1s_2}\sin(\phi_u+\Delta\phi_u-\phi_i-\Delta\phi_i+\psi_{s_1s_2}) \\ +\sum_{j=1}^{N} K_{jis_1s_2}\sin(\phi_j+\Delta\phi_j-\phi_i-\Delta\phi_i+\psi_{s_1s_2})\end{array}\right]. \tag{15}$$

As $\psi_{ss} = 0$ for all s, (14) can be simplified into

$$S_{Si\_I} = R_{\mathrm{PD}} J_1(\beta_i)\left(\sum_{s=1}^{M}\eta_s\right)\sqrt{P_i} \times \left[\begin{array}{l}\sqrt{P_u}\sin(\phi_u+\Delta\phi_u-\phi_i-\Delta\phi_i) \\ +\sum_{j=1}^{N} J_0(\beta_j)\sqrt{P_j}\sin(\phi_j+\Delta\phi_j-\phi_i-\Delta\phi_i)\end{array}\right] \tag{16}$$

with P_u and P_i being the optical power incident on the photodetector (i.e., having passed through the pinhole) from the unmodulated beam and ith-phase-modulated beam, respectively.

As for (15), it can be written as

$$S_{Si\_II} = R_{\mathrm{PD}} J_1(\beta_i)\sqrt{P_i} \times \left[\begin{array}{l}\sqrt{P_u}\sin(\phi_u+\Delta\phi_u-\phi_i-\Delta\phi_i)\,\Sigma_{\cos} \\ +\sqrt{P_u}\cos(\phi_u+\Delta\phi_u-\phi_i-\Delta\phi_i)\,\Sigma_{\sin} \\ +\sum_{j=1}^{N} J_0(\beta_j)\sqrt{P_j}\sin(\phi_j+\Delta\phi_j-\phi_i-\Delta\phi_i)\,\Sigma_{\cos} \\ +\sum_{j=1}^{N} J_0(\beta_j)\sqrt{P_j}\cos(\phi_j+\Delta\phi_j-\phi_i-\Delta\phi_i)\,\Sigma_{\sin}\end{array}\right] \tag{17}$$

with

$$\Sigma_{\cos} = \sum_{s_1\neq s_2}\sqrt{\eta_{s_1}\eta_{s_2}}\cos(\varphi_{s_1}-\varphi_{s_2}+\Delta\varphi_{s_1}-\Delta\varphi_{s_2})$$

$$\Sigma_{\sin} = \sum_{s_1\neq s_2}\sqrt{\eta_{s_1}\eta_{s_2}}\sin(\varphi_{s_1}-\varphi_{s_2}+\Delta\varphi_{s_1}-\Delta\varphi_{s_2}). \tag{18}$$

As the scattering areas are assumed not to be correlated [26], and as the turbulence phase shifts in two different channels of propagation are not correlated either, $\varphi_{s_1}-\varphi_{s_2}+\Delta\varphi_{s_1}-\Delta\varphi_{s_2}$ is a random variable with uniform distribution of probability over $[-\pi, \pi]$. η_s is also a random variable with an average value η_{s0}.

The part of the target containing the scattering areas contributing to the signal has a surface inversely proportional to the pinhole diameter. Due to the small size of the pinhole, this target contributing part is wide and contains a large number of scattering areas. Therefore, we can apply the central limit theorem and derive that the values of $\Sigma_{\cos}$ and $\Sigma_{\sin}$ are normally distributed around their average values, which are here equal to zero. Thus, $\Sigma_{\cos}$ and $\Sigma_{\sin}$ are both very close to zero, and with the highest probability, negligible when compared with the $(\sum_{s=1}^{M}\eta_s)$ term of (16), so we can neglect the terms from (17) when compared with the similar terms in (16). Consequently, when the pinhole is in place, $S_{Si} \approx S_{Si\_I}$.

This demonstrates that the error signal varies with the phase differences between the laser sources, but only with the phase differences originating from the laser amplifiers and onward-turbulence-induced phase fluctuations. This error signal does not involve phase differences coming from backward turbulence phase fluctuations. Therefore, limiting the aperture of the photodetector allows to phase-lock the laser amplifiers in the

plane of the scattering surface, obtaining a stable interference pattern in this plane.

Without the pinhole, light backscattered from the sth area is no more confined to the sth propagation channel and suffers turbulence-induced phase shifts that are not uniform. Phase differences originating from the propagation of backscattered light through turbulence will modify the error signal. The phase-locking electronics will try to drive the error signal to zero and compensate also for the backward-turbulence-induced phase shifts. Unfortunately, in this case, the laser sources will be phase-locked in the photodetector plane, and not in the scattering surface plane.

This theoretical development shows that the keystone for succeeding in target-in-the-loop phase-locking on the remote target is to reduce the aperture of the photodetector.

Among all the configurations that can be used to reduce this aperture, the one proposed here (i.e., with the pinhole before the backscattered light collecting lens) is particularly suitable. As the pinhole is placed before the lens, the field of view of the photodetector is not reduced, and therefore, the collected optical flux is higher than when limiting the field-of-view and the aperture simultaneously (e.g., placing the pinhole between the collecting lens and the photodetector). The position of the pinhole before the lens also offers a low sensitivity to misalignment, as the pinhole can be placed anywhere before the lens, as long as it intercepts the backscattered optical field. Placing the pinhole off-center will not result in the detection subsystem misalignment.

C. Conclusion

We have extended the self-referenced LOCSET theory [25] to the case of target-in-the-loop experiments. We demonstrated theoretically that reducing the aperture of the detection subsystem was essential to lower the sensitivity to backward-turbulence-induced phase shifts. This aperture reduction allows to achieve phase-locking in the target plane. We proposed positioning of the aperture reducing pinhole before the detection subsystem collecting lens. This original optical configuration is better than classical configurations to optimize the flux received by the photodetector and lower the sensitivity to the pinhole alignment.

We experimentally validated these theoretical results and performed coherent combining of fiber amplifiers using the modulation multiplexing technique. We were able, with a several kilohertz bandwidth, to compensate not only for internal phase fluctuations, but also the low- to medium-strength turbulence on the optical beam path. Finally, we demonstrated automatic phase-locking of fiber amplifiers through turbulent atmosphere on a scattering surface, using a detector in the laser emitter plane and spatial filtering of the backscattered signal with a pinhole properly positioned to limit the aperture of the phase measurement subsystem. Experimental results show that the setup is insensitive to backward turbulence and can achieve efficient real-time compensation of onward turbulence with the modulation multiplexing technique.

IV. Modeling of Multiple-Transverse-Mode Combining

We have shown that atmospheric turbulence is an important factor that affects the efficiency of laser beam combining on a remote target by reshaping the optical wavefront. We have demonstrated both theoretically and experimentally how to compensate for this effect.

But there are other factors that can impair beam combining performance, such as fiber laser array fill factor, tilt, residual phase error, and beam quality of the primary lasers. High-power fiber amplifier most often rely on LMA fibers, as the large core of such fiber sustains larger optical power without damage and nonlinear effects disturbance. These LMA fibers simultaneously guide a few transverse modes and the output beam quality can be affected by the interference of all guided modes. Therefore, coherent combining of LMA fiber amplifiers will result in a reshaped far-field wavefront when compared with combined single-mode fibers.

Coherent combining efficiency assessment can only be performed if all these factors are taken into account. For that purpose, we developed a numerical model of propagation for the computation of the far-field pattern that takes into account few mode beams from LMA fibers. The model is capable of further evolution to take into account atmospheric turbulence propagation effects.

The numerical model is described shortly. Then, we introduce some CBC efficiency criteria that are finally evaluated on various test configurations using the numerical model.

A. Description of the Numerical Model

We developed this numerical model to calculate the intensity profile in the far field in the case of multiple-transverse-mode coherent combining.

The model is not limited to single-mode diffraction-limited beams, but offers the possibility to consider combining of LMA fiber amplifiers emitting simultaneously several transverse modes. The optical field emitted by one LMA fiber amplifier is a linear combination of the linearly polarized LP_{lm} modes that can be guided in the fiber core. The model does not assume that these modes share a common phase inside the same fiber. The composition of the optical field emitted by each fiber amplifier as well as the phase differences between the guided modes are both user-defined. Therefore, it is possible to model any mode composition scenario with the restriction of linear polarization. Of course, some of the mode composition schemes can be technologically unachievable with a genuine fiber amplifier.

The near-field geometry of the fiber output is also user-defined. In the rest of this paper, we assume a regular square lattice near-field geometry (Fig. 7).

Once the near-field geometry and each fiber mode composition are defined, the amplitude and phase profiles of the output optical field are available. Propagation to the far field can be performed by classical beam propagation methods (BPMs). Atmospheric propagation is usually introduced in the model using properly distributed index layers. The optical field is then propagated step by step, layer to layer, up to the far field. Calculation

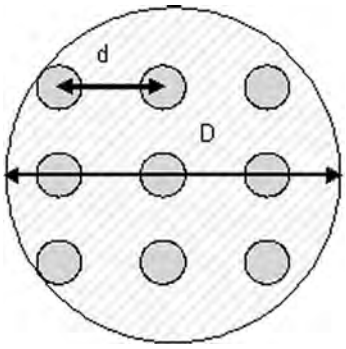

Fig. 7. Example of near-field geometry for the LMA fiber array. d is the distance between two neighbor fibers. The pupil diameter of the array is D.

of all the necessary intermediate optical field profiles with this method can be highly CPU time-expensive.

To reduce the computation time, we have chosen to approximate the LP_{lm} modes emitted by the fibers by Laguerre–Gauss (LG) modes. Indeed, the electric fields of LG and LP modes are very close, and LG mode propagation is fast to compute. Thus, the optical field emitted by the ith fiber is written as a linear combination of LG_{lm} modes

$$E_i(x,y,z) = \sum_{l,m} 2\sqrt{\alpha_{lm}} C_{lm} \frac{\left[(x-x_i)^2+(y-y_i)^2\right]^{l/2}}{w(z)^{l+1}} \cos(l\phi) \cdot \left[L_{m-1}^{l}\left[2\left(\frac{(x-x_i)^2+(y-y_i)^2}{w(z)^2}\right)\right] \exp\left[-\left(\frac{(x-x_i)^2+(y-y_i)^2}{w(z)^2}\right)\right] \cdot \exp\left[-ik\frac{(x-x_i)^2+(y-y_i)^2}{2R_c(z)}\right] \exp\left[-i\left(kz - \psi_{lm}(z) - \varphi_i - \varphi_{ilm}\right)\right] \right] \quad (19)$$

with k being the wave vector modulus, λ the wavelength, (x_i, y_i) the central coordinates of the ith fiber, $L_m^l(u)$ the generalized LG polynomials, α_{lm} the fraction of power in the LG_{lm} mode, and ϕ the polar coordinate angle for the ith element of the array. C_{lm} is a constant

$$C_{lm} = \sqrt{\frac{4P_f}{(\delta_l+1)\pi\varepsilon_0 c}\frac{(m-1)!}{(m-1+l)!}}$$

with P_f being the power delivered by a unique emitter, c and ε_0 the speed of light and electric permeability of free space, and δ_l the Kronecker symbol ($\delta_l = 1$ when $l = 0$ and $\delta_l = 0$ otherwise). The parameter φ_i is the global phase shift induced by amplification and propagation in the ith fiber, φ_{ilm} is the phase of the LP_{lm} mode in the ith fiber, and α_{lm}, φ_i, and φ_{ilm} are user-defined. The parameters of the Gaussian beam are [27]:

1) the wavefront curvature radius $R_c(z) = z[1 + (\frac{z_R}{z})^2]$;
2) the Rayleigh length $z_R = \frac{\pi w_0^2}{\lambda}$;
3) the beam radius $w(z) = w_0\sqrt{1 + (\frac{z}{z_R})^2}$;
4) the Gouy's phase $\psi_{lm}(z) = (2m + l - 1)\arctan(\frac{z}{z_R})$.

The variable w_0 is defined for all LG_{lm} modes using Marcuse's approximation [28] that best approximates the LP_{01} mode with the LG_{01} mode.

We define the total power distribution on the LP_{lm} modes to replicate, as accurately as possible, the power distribution delivered by a real fiber amplifier. In a doped fiber core, the laser gain for each mode is proportional to the overlap integral between the population inversion transverse profile and the mode profile itself. We assume that these overlap integrals are themselves proportional to the overlap integrals between the LP_{01} fundamental mode transverse profile and the mode profile itself. The α_{lm} factors are then calculated so that they are proportional to the overlap integrals between the LP_{lm} transverse profile and the LP_{01} profile, and fulfil the condition $\sum_{l,m} \alpha_{lm} = 1$.

To validate our model approximation, we checked that the LP_{lm} and LG_{lm} modes optical field profiles do not differ significantly. We also compared the far-field intensity profiles obtained with BPM calculation and with the LG mode approach for various mode compositions. The far-field patterns are always comparable, with the same number of interference lobes located at the same positions. Peak values of the lobes slightly differ from BPM calculation to LG model, but not significantly.

The results presented later were obtained using the LG approximation.

The numerical model was first used to obtain extrapolate combining efficiency results for improved fill factor in the experimental configuration described in Section III-A. We reproduced the near-field geometry of the experiment, used single-mode fibers (i.e., only the LG_{01} mode is guided), and tested improved near-field fill factor values, calculating the corresponding fraction of power in the far-field central lobe, and Strehl ratio. As the calculated far-field pattern fits the experimental results [29], we can expect that the extrapolate values are trustworthy. The modeling results have been presented in Section III-A.

Then we used the numerical model to assess multiple-transverse-mode combining efficiency. Modeling results are given in Section IV-C.

B. Coherent Combining Efficiency Assessment Criteria

When designing or comparing coherent combining laser systems, it is necessary to assess the performance level of the combining process. Various criteria are used to qualify beam combining.

The well-known criterion that is widely used in adaptive optics is the Strehl ratio [30]. It is defined as the ratio between the intensity at the center of the coherently combined far-field pattern and the intensity at the center of the Airy spot obtained from uniformly illuminating the system aperture with a constant phase and with the same total power.

The Strehl ratio S is independent of propagation distance and can be expressed from the complex optical field at the aperture (i.e., in the near field) [30]

$$S = \frac{I(r=0,z)}{I_{unif}(r=0,z)} = \frac{\int_0^{2\pi}\int_0^{D/2} |a(r,\theta)\exp[i\phi(r,\theta)]\, r\, dr\, d\theta|^2}{\pi\frac{D^2}{4}\int_0^{2\pi}\int_0^{D/2}|a(r,\theta)|^2 r\, dr\, d\theta} \quad (20)$$

with $a(r,\theta)\,\exp[i\,\phi(r,\theta)]$ being the optical field complex amplitude distribution on the aperture of the laser array and D the aperture diameter.

Zhou *et al.* [31] pointed out that this criterion is not always appropriate to assess the beam quality of a coherently combined fiber laser as it only describes the far-field center intensity level whatever the far-field pattern intensity distribution.

Therefore, it can be interesting to complement the information given by the Strehl ratio criterion.

Another well-known criterion widely used to evaluate coherent combining efficiency is the fraction of power in the central lobe. It measures the percentage of power that is contained in the central lobe of the far-field interference pattern. However, it does not give any information on the size of this central lobe.

The beam propagation factor (BPF) criterion has been proposed by the Defense Advanced Research Projects Agency (DARPA) [32]. This criterion is defined as the fraction of optical power in a far-field bucket defined as 1.44 times the diffraction-limited spot area. The far-field bucket area is then 1.44 A_{DL} with $A_{\mathrm{DL}} = (\pi/4)\,(\theta_{\mathrm{DL}} f)^2$ and the corresponding angular aperture is 1.2 θ_{DL} with $\theta_{\mathrm{DL}} = 2.44\,\lambda/D$, where D is the aperture diameter and f the focal lens of the optical system used to form the far-field spot. Zhou *et al.* [31] studied this criterion and pointed out that it is often more relevant than the Strehl ratio to assess the beam combining efficiency.

We introduce here a new criterion similar to the BPF criterion but that can be more convenient to assess the efficiency of field laser systems involving coherent combining process. We call it the mask-encircled power (MEP) criterion, and define it as the fraction of power in a fixed area in the far field. This area can be chosen to correspond to the minimum size of a target in a given field scenario, taking into account the target width and the maximum range of operation of the system. This criterion is more related than the BPF to the specific application needs of the laser system. As the BPF adapts the bucket size with the laser wavelength and aperture diameter, it does not allow to compare systems on a perfectly fair basis. Moreover, as the effects of atmospheric turbulence are strongly dependent on these wavelength and aperture parameters, MEP seems more relevant to qualify deployed coherent combining laser systems.

All these criteria can generally be evaluated simultaneously, and it is the whole set of values of these criteria that give the most complete information on the beam combining process efficiency.

C. First Numerical Modeling Results

We use the numerical model of multiple-transverse-mode coherent combining to evaluate all the criteria defined in Section IV-B for a four-fiber square array near-field configuration. We focus on two test configurations, the first one to investigate the MEP criterion relevance and the second one to evaluate the impact of multiple-transverse-mode composition on the coherent combining efficiency.

First test configuration involves four single-mode fibers. The four 1-mm-diameter collimated beams are spaced by 3 mm. The fill factor is 41%. Calculated far-field criteria are presented in Table I. The MEP criterion is evaluated for two different values of MEP apertures: one is equal to the 1-μm BPF far-field bucket (i.e., 1.44 A_{DL} for a 1 μm laser) and the other is equal to the 1.5-μm BPF far-field bucket.

TABLE I
COHERENT COMBINING CRITERIA VALUES FOR THREE DIFFERENT WAVELENGTHS

λ (μm)	Strehl ratio (%)	Power in the central lobe (%)	BPF (%)	MEP θ=0.4 mrad (%)	MEP θ=0.6mrad (%)
1	82	57	61	61	80
1.5	82	57	61	56	61
2	82	57	61	46	58

Near-field geometry is a four-single-mode-fiber square array. MEP buckets of 0.4 and 0.6 mrad are considered.

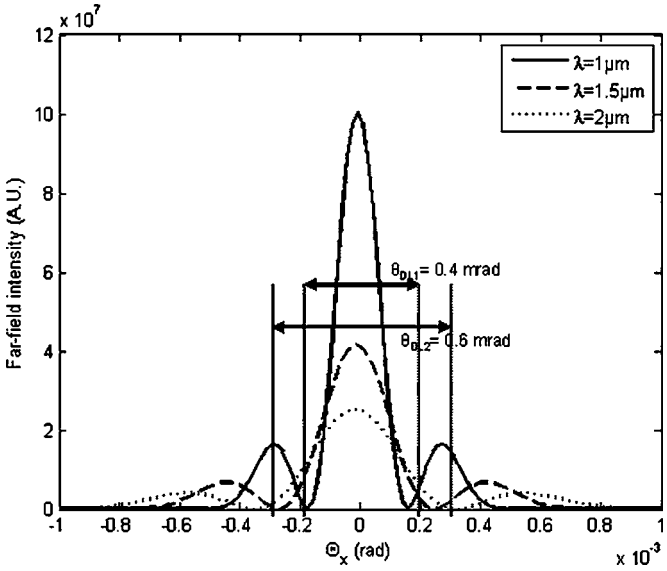

Fig. 8. Far-field intensity along the x-axis for $\lambda = 1$ μm, $\lambda = 1.5$ μm, and $\lambda = 2$ μm. Near-field geometry is a four-single-mode-fiber square array. The two MEP bucket limits are indicated.

As the near-field geometry is the same for the three wavelengths, the Strehl ratio, the power in the central lobe, and the BPF are unchanged. Indeed, even if the far-field spot diameter increases with wavelength, the BPF bucket increases accordingly and the criterion remains constant. The other two criteria do not vary with the far-field spot size either. On the contrary, the reference bucket used to derive the MEP criterion is fixed to a value corresponding to the minimum expected target width. When increasing the wavelength, the far-field pattern and especially the central lobe widens (Fig. 8), thus decreasing the power encircled by this fixed bucket.

The MEP criterion appears to be relevant enough to enable the comparison of different systems for the same application (i.e., same target size and distance) as it can be used to compare the combining efficiencies of various wavelength and pupil diameter systems on a fair basis.

Second test configuration involves four LMA fibers. Each fiber has 10 μm core radius and 0.12 numerical aperture. The fiber core will guide four LP_{lm} modes from LP_{01} to LP_{02}.

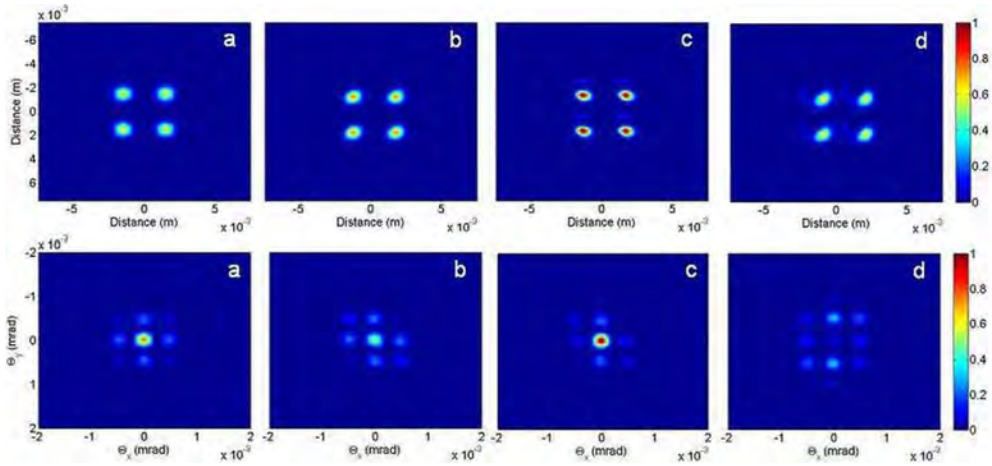

Fig. 9. CBC of LMA fibers near-field (top) and far-field (bottom) intensity profiles. Four different mode compositions are compared. The color bar gives the normalized intensity scale.

TABLE II
COHERENT COMBINING CRITERIA VALUES FOR THREE DIFFERENT MODE COMPOSITIONS IN THE LMA FIBERS

Modes				Strehl ratio	Power in the central lobe	BPF	MEP
LP_{01}	LP_{11}	LP_{21}	LP_{02}	(%)	(%)	(%)	(%)
$\alpha_{01}= 1$ $\varphi_{01}= 0$				61	37	39	39
$\alpha_{01}= 0.67$ $\varphi_{01}= 0$	$\alpha_{11}= 0.33$ $\varphi_{11}= 0$			41	25	27	27
$\alpha_{01}= 0.49$ $\varphi_{01}= 0$	$\alpha_{11}= 0.24$ $\varphi_{11}= 0$	$\alpha_{21}= 0.08$ $\varphi_{21}= 0$	$\alpha_{02}= 0.19$ $\varphi_{02}= 0$	75	45	47	47
$\alpha_{01}= 0.49$ $\varphi_{01}= 0$	$\alpha_{11}= 0.24$ $\varphi_{11}= 0$	$\alpha_{21}= 0.08$ $\varphi_{21}= 0$	$\alpha_{02}= 0.19$ $\varphi_{02}= \pi$	4	4	4.5	4.5

For each configuration, the fractions of power α_{lm} and phases φ_{lm} are indicated. There is no global phase difference between the fibers.

In this numerical modeling session, we assess the impact of the presence of high-order modes on the coherent combining efficiency using the previously defined criteria. We introduce the high-order modes in ascending order and evaluate four mode compositions: a) the fibers only emit the fundamental mode LP_{01} (the high-order modes can be suppressed through fiber coiling); b) the fibers emit a combination of the fundamental mode LP_{01} and the first high-order mode LP_{11}; c) all guided modes are excited and share a common phase; d) all guided modes are excited, and LP_{01}, LP_{11}, and LP_{21} share a common phase and LP_{02} is in phase-opposition with the other modes.

Table II presents the criteria values, and Fig. 9 the near-field collimated beams and far-field interference patterns for the four mode compositions. When compared to mode composition a) (LP_{01} only), composition b) performs worse on all criteria. Indeed, the LP_{11} mode is odd and does not contribute to the central lobe of the far-field fringe pattern. Therefore, the presence of the LP_{11} mode in composition b) spreads power outside of the far-field central lobe and lowers the combining efficiency. Analysis of mode compositions c) and d) is more complex. Although the presence of the LP_{11} and LP_{21} modes should lower the combining efficiency, the addition of LP_{02} mode in phase with the others compensates for this degradation and even improves the combining process performance. However, when the LP_{02} mode is in phase-opposition with the others, its contribution is highly detrimental to the combining efficiency.

This demonstrates the complexity of multiple-order modes coherent combining. Depending on the phase relationship between these modes, their addition can be either beneficial or detrimental to the combining efficiency. Special care has to be taken to control their power and phase, if possible. It should be noted that in real LMA fiber amplifiers, the phase relationship between these modes will fluctuate in time, most often resulting in a lower average combining performance.

V. CONCLUSION

We have theoretically and experimentally demonstrated atmospheric turbulence compensation through coherent combining of fiber amplifiers. We have also theoretically studied the influence of multiple-transverse-mode composition in the primary fiber lasers on coherent combining efficiency and wavefront shaping.

Coherent combining through turbulence using frequency-tagging techniques has been achieved and a $\lambda/15$ rms residual phase error is obtained in a target-in-the-loop configuration. We achieved automatic phase-locking of fiber amplifiers through turbulent atmosphere on a scattering surface, using a detector in the laser emitter plane. The theory of self-referenced LOCSET has been extended to take into account this target-in-the-loop configuration. Through this theoretical approach, we demonstrated that limiting the detection subsystem aperture is essential to make the setup insensitive to backward turbulence and achieve efficient real-time compensation of onward turbulence.

A numerical model of multiple-transverse-mode coherent combining has also been developed. It has been used to assess coherent combining efficiency for various transverse-mode compositions in the primary fiber amplifiers. The combining efficiency depends on the mode composition and phase

relationship. Efficient coherent combining of LMA fibers will imply to extend the active phase control to the phase differences between transverse modes.

Future work is to upgrade the numerical model to include turbulent propagation. Further calculations will be performed to search for optimized mode compositions and study the far-field pattern obtained with high-order transverse modes, like the LP_{07} and LP_{08} modes used by Ramachandran *et al.* [33] to increase the power sustained by fiber amplifiers.

REFERENCES

[1] J. W. Dawson, M. J. Messerly, R. J. Beach, M. Y. Shverdin, E. A. Stappaerts, A. K. Sridharan, P. H. Pax, J. E. Heebner, C. W. Siders, and C. P. J. Barty, "Analysis of the scalability of diffraction-limited fiber lasers and amplifiers to high average power," *Opt. Exp.*, vol. 16, pp. 13240–13266, Aug. 2008.

[2] T. H. Loftus, A. Liu, P. R. Hoffman, A. M. Thomas, M. Norsen, R. Royse, and E. Honea, "522 W average power, spectrally beam-combined fiber laser with near-diffraction-limited beam quality," *Opt. Lett.*, vol. 32, pp. 349–351, Feb. 2007.

[3] J. Anderegg, S. Brosnan, E. Cheung, P. Epp, D. Hammons, H. Komine, M. Weber, and M. Wickham, "Coherently coupled high power fiber arrays," *Proc. SPIE*, vol. 6102, pp. 61020U-1–61020U-5, 2006.

[4] S. J. Augst, A. K. Goyal, R. L. Aggarwal, T. Y. Fan, and A. Sanchez, "Wavelength beam combining of ytterbium fiber lasers," *Opt. Lett.*, vol. 28, pp. 331–333, Mar. 2003.

[5] S. Klingebiel, F. Röser, B. Ortaç, J. Limpert, and A. Tünnermann, "Spectral beam combining of Yb-doped fiber lasers with high efficiency," *J. Opt. Soc. Amer. B*, vol. 24, pp. 1716–1720, Aug. 2007.

[6] D. Sabourdy, V. Kermène, A. Desfarges-Berthelemot, L. Lefort, A. Barthélémy, P. Even, and D. Pureur, "Efficient coherent combining of widely tunable fiber lasers," *Opt. Exp.*, vol. 11, pp. 87–97, Jan. 2003.

[7] H. Bruesselbach, D. C. Jones, M. S. Mangir, M. Minden, and J. L. Rogers, "Self-organized coherence in fiber laser arrays," *Opt. Lett.*, vol. 30, pp. 1339–1341, Jun. 2005.

[8] Y. Huo, P. K. Cheo, and G. G. King, "Fundamental mode operation of a 19-core phase-locked Yb-doped fiber amplifier," *Opt. Exp.*, vol. 12, pp. 6230–6239, Dec. 2004.

[9] L. Michaille, C. R. Bennett, D. M. Taylor, T. J. Shepherd, J. Broeng, H. R. Simonsen, and A. Petersson, "Phase locking and supermode selection in multicore photonic crystal fiber lasers with a large doped area," *Opt. Lett.*, vol. 30, pp. 1668–1670, Jul. 2005.

[10] D. C. Jones, A. M. Scott, S. Clark, C. Stace, and R. G. Clarke, "Beam steering of a fibre bundle laser output using phased array techniques," *Proc. SPIE*, vol. 5335, pp. 125–131, 2004.

[11] H. Bruesselbach, S. Wang, M. Minden, D. C. Jones, and M. Mangir, "Power-scalable phase-compensating fiber-array transceiver for laser communications through the atmosphere," *J. Opt. Soc. Amer. B*, vol. 22, pp. 347–353, Feb. 2005.

[12] T. R. O'Meara, "The multidither principle in adaptive optics," *J. Opt. Soc. Amer.*, vol. 67, pp. 306–315, Mar. 1977.

[13] W. B. Bridges, P. T. Brunner, S. P. Lazzara, T. A. Nussmeier, T. R. O'Meara, J. A. Sanguinet, and W. P. Brown, "Coherent optical adaptive techniques," *Appl. Opt.*, vol. 13, pp. 291–300, Feb. 1974.

[14] J. E. Pearson, W. B. Bridges, S. Hansen, T. A. Nussmeier, and M. E. Pedinoff, "Coherent optical adaptive techniques: Design and performance of an 18-element visible multidither COAT system," *Appl. Opt.*, vol. 15, pp. 611–621, Mar. 1976.

[15] J. E. Kansky, C. X. Yu, D. V. Murphy, S. E. J. Shaw, R. C. Lawrence, and C. Higgs, "Beam control of a 2D polarization maintaining fiber optic phased array with high-fiber count," *Proc. SPIE*, vol. 6306, pp. 63060G-1–63060G-11, 2006.

[16] P. Bourdon, V. Jolivet, B. Bennai, L. Lombard, G. Canat, E. Pourtal, Y. Jaouen, and O. Vasseur, "Coherent beam combining of fiber amplifier arrays and application to laser beam propagation through turbulent atmosphere," *Proc. SPIE*, vol. 6873, pp. 687316-1–687316-9, 2008.

[17] M. A. Vorontsov and V. Kolosov, "Target-in-the-loop beam control: Basic considerations for analysis and wave-front sensing," *J. Opt. Soc. Amer. A*, vol. 22, pp. 126–141, Jan. 2005.

[18] C. Stace, C. J. C. Harrison, R. G. Clarke, D. C. Jones, and A. M. Scott, "Fiber bundle lasers and their applications," presented at the 1st EMRS DTC Tech. Conf., Edinburgh, U.K., 2004, Paper B21.

[19] M. A. Vorontsov and S. L. Lachinova, "Laser beam projection with adaptive array of fiber collimators. I. Basic considerations for analysis," *J. Opt. Soc. Amer. A*, vol. 25, pp. 1949–1959, Aug. 2008.

[20] S. L. Lachinova and M. A. Vorontsov, "Laser beam projection with adaptive array of fiber collimators. II. Analysis of atmospheric compensation efficiency," *J. Opt. Soc. Amer. A*, vol. 25, pp. 1960–1973, Aug. 2008.

[21] O. Korotkova and E. Wolf, "Beam criterion for atmospheric propagation," *Opt. Lett.*, vol. 32, pp. 2137–2139, Aug. 2007.

[22] H. T. Eyyuboglu, "Hermite-cosine-Gaussian laser beam and its propagation characteristics in turbulent atmosphere," *J. Opt. Soc. Amer. A*, vol. 22, pp. 1527–1535, Aug. 2005.

[23] H. T. Eyyuboglu and Y. Baykal, "Hermite-sine-Gaussian and Hermite-sinh-Gaussian laser beams in turbulent atmosphere," *J. Opt. Soc. Amer. A*, vol. 22, pp. 2709–2718, Dec. 2005.

[24] T. M. Shay, V. Benham, J. T. Baker, B. Ward, A. D. Sanchez, M. A. Culpepper, D. Pilkington, D. J. Nelson, and C. A. Lu, "First experimental demonstration of self-synchronous phase locking of an optical array," *Opt. Exp.*, vol. 14, pp. 12015–12021, Dec. 2006.

[25] T. M. Shay, V. Benham, J. T. Baker, A. D. Sanchez, D. Pilkington, and C. A. Lu, "Self-synchronous and self-referenced coherent beam combination for large optical arrays," *IEEE J. Sel. Topics Quantum Electron.*, vol. 13, no. 3, pp. 480–486, May/Jun. 2007.

[26] J. W. Goodman, "Some fundamental properties of speckle," *J. Opt. Soc. Amer.*, vol. 66, pp. 1145–1150, Nov. 1976.

[27] H. Kogelnik and T. Li, "Laser beams and resonators," *Appl. Opt.*, vol. 5, pp. 1550–1567, Oct. 1996.

[28] D. Marcuse, "Loss analysis of single-mode fiber splice," *Bell Syst. Tech. J.*, vol. 56, pp. 703–718, May/Jun. 1977.

[29] B. Bennai, L. Lombard, V. Jolivet, C. Delezoide, E. Pourtal, P. Bourdon, G. Canat, O. Vasseur, and Y. Jaouën, "Brightness scaling based on 1.55 μm fiber amplifiers coherent combining," *Fiber Integr. Opt.*, vol. 27, pp. 355–369, Sep. 2008.

[30] J. R. Leger, "External methods of phase locking and coherent beam addition of diode lasers," in *Surface Emitting Semiconductor Lasers and Arrays*, G. A. Evans and J. M. Hammer, Eds. New York: Academic, 1993, ch. 8.

[31] P. Zhou, Z. Liu, X. Xu, and Z. Chen, "Numerical analysis of the effects of aberrations on coherently combined fiber laser beams," *Appl. Opt.*, vol. 47, pp. 3350–3359, Jun. 2008.

[32] Architecture for diode high energy laser systems (ADHELS) (2006). [Online]. Available: http://www.darpa.mil/mto/programs/adhels/index.html

[33] S. Ramachandran, J. W. Nicholson, S. Ghalmi, M. F. Yan, P. Wisk, E. Monberg, and F. V. Dimarcello, "Light propagation with ultralarge modal areas in optical fibers," *Opt. Lett.*, vol. 31, pp. 1797–1799, Jun. 2006.

Véronique Jolivet received the M.S. degree from the Ecole Supérieure d'Optique, Orsay, France, in 2002, and the Ph.D. degree in physics from the University of Paris XI, Orsay, in 2008.

Since 2002, she has been a Research Scientist at the Département Optique Théorique et Appliquée, Office National d'Etudes et de Recherches Aérospatiales (ONERA), the French Aerospace Lab, Palaiseau, France. Her current research interests include coherent lidars, laser propagation, fiber lasers, and coherent combining.

Pierre Bourdon received the M.S. degree and the Ph.D. degree in physics from the Ecole Polytechnique, Palaiseau, France, in 1990 and 1995, respectively.

From 1995 to 2004, he was a Researcher at the Department Laser, Optique et Thermo optique, Centre Technique d'Arcueil (CTA), Délégation Générale pour l'Armement (DGA). Since 2004, he has been a Research Scientist at the Département Optique Théorique et Appliquée, Office National d'Etudes et de Recherches Aérospatiales (ONERA), the French Aerospace Lab, Palaiseau. He is currently a special advisor on laser sources. His current research interests include fiber lasers, nonlinear optics, optical parametric oscillators, and solid-state lasers.

Dr. Bourdon is a member of the Société Française d'Optique.

Baya Bennaï received the M.S. degree from the Institut de Formation des Ingénieurs de Paris-Sud, Orsay, France, in 2006. She is currently working toward the Ph.D. degree on coherent combining of fiber amplifiers at the Département Optique Théorique et Appliquée, Office National d'Etudes et de Recherches Aérospatiales (ONERA), the French Aerospace Lab, Palaiseau, France.

Laurent Lombard received the M.S. degree from the Ecole Supérieure d'Optique, Orsay, France in 2001, and the Ph.D. degree in physics from the University of Paris XI, Orsay, in 2005.

Since 2006, he has been a Research Scientist at the Département Optique Théorique et Appliquée, Office National d'Etudes et de Recherches Aérospatiales (ONERA), the French Aerospace Lab, Palaiseau, France. His current research interests include high-power fiber laser sources, nonlinear effects in fibers, optical beam processing, lidars, and coherent combining.

Didier Goular received the Electr. Eng. degree from the Conservatoire National des Arts et Métiers (CNAM), Paris, France, in 1990.

Since 1985, he has been at the Département Optique Théorique et Appliquée, Office National d'Etudes et de Recherches Aérospatiales (ONERA), the French Aerospace Lab, Palaiseau, France, where he is engaged in optimization of electronic and signal processing of the coherent optical system.

Emilie Pourtal received the M.S. degree from the Institut d'Optique Graduate School, Orsay, France, in 2004.

She was a Research Associate at the Office National d'Etudes et de Recherches Aérospatiales (ONERA) during the second half of 2007. She joined Thales, Elancourt, France, in 2008.

Guillaume Canat received the M.S. degree from the Ecole Polytechnique, Palaiseau, France, in 2000, the M.S. degree from the Ecole Nationale Supérieure des Télécommunications, Paris, France, in 2002, and the Ph.D degree in physics from Supaéro, Toulouse, France, in 2006.

Since 2004, he has been a Research Scientist at the Département Optique Théorique et Appliquée, Office National d'Etudes et de Recherches Aérospatiales (ONERA), the French Aerospace Lab, Palaiseau. His current research interests include high-power fiber laser sources, nonlinear effects in fibers, and coherent combining.

Yves Jaouën received the D.E.A. degree from the University of Paris VI, Paris, France, in 1989, and the Ph.D. degree in physics from the Ecole Nationale Supérieure des Télécommunications (ENST), Paris, in 1993.

In 1982, he joined the Département Communications et Electronique, ENST (now TELECOM ParisTech), where he is currently a Professor. He gives lectures in the domain of electromagnetic fields, optics, and optical communications systems. His current research interests include high-bit-rate optical communication systems and networks, new characterization techniques for advanced photonic devices, high-power fiber lasers, and optical sensors. He is the author or coauthor of more than 80 papers published in journals and communications.

Bernard Moreau received the M.S. degree from the Ecole Supérieure d'Optique, Orsay, France, in 1969.

He is currently the Deputy Director of the Département Optique Théorique et Appliquée, Office National d'Etudes et de Recherches Aérospatiales (ONERA), the French Aerospace Lab, Palaiseau, France.

Olivier Vasseur received the M.S. degree from the Ecole Nationale Supérieure de Physique de Marseille, Marseille, France, in 1988, the Ph.D degree in physics from the Aix-Marseille III University, Marseille, in 1990, and the Ph.D. degree in sociology from the Toulouse-Le Mirail University, Toulouse, France, in 2003.

From 1992 to 2002, he was at the Délégation Générale pour l'Armement (DGA), where he was engaged in the field of optics and simulation. In 2002, he joined the Département Optique Théorique et Appliquée, Office National d'Etudes et de Recherches Aérospatiales (ONERA), the French Aerospace Lab, Palaiseau, France. He is currently a special advisor on complex optronic systems at DOTA. His current research interests include fiber lasers, optical waveguides, statistics, design of experiments, and complex systems simulation.

Dr. Vasseur is a member of the Société Française d'Optique, the Association Française de Sociologie, and the Société Française de Statistique.

Coherent beam combination of narrow-linewidth 1.5 μm fiber amplifiers in a long-pulse regime

L. Lombard,[1,*] A. Azarian,[1] K. Cadoret,[1] P. Bourdon,[1] D. Goular,[1] G. Canat,[1] V. Jolivet,[1] Y. Jaouën,[2] and O. Vasseur[1]

[1]*Office National d'Études et Recherches Aérospatiales (ONERA), Ch. de la Hunière, 91761 Palaiseau, France*

[2]*Télécom ParisTech, CNRS UMR 5141, 46 rue barrault, 75634 Paris, France*

**Corresponding author: Laurent.Lombard@onera.fr*

Received November 29, 2010; revised December 22, 2010; accepted December 24, 2010; posted January 10, 2011 (Doc. ID 138751); published February 9, 2011

We report what we believe to be the first experimental demonstration of coherent beam combining of two fiber amplifiers in a 100 ns pulse regime using a signal leak between the pulses. Pulses of ~100 W stimulated-Brillouin-scattering limited peak power are combined with 95% efficiency, a residual phase error of $\lambda/27$, and no significant beam quality degradation.

OCIS codes: 140.3538, 060.2320, 140.3298.

Pulsed fiber sources are of strong interest for many applications, such as remote sensing or material processing. In recent years, impressive results have been reported in extracting high energy from pulsed fiber lasers and amplifiers [1]. Producing higher peak power from a single fiber is becoming more challenging owing to fiber damage, thermal limitations, and nonlinear effects such as stimulated Brillouin scattering (SBS). Coherent beam combining (CBC) of fiber amplifiers is a promising technique for overcoming these limitations: an array of fiber amplifiers is actively phase locked and combined into a single beam, while keeping the optical properties of a single fiber, such as good beam quality [2]. CBC of a laser array is also possible but with reduced control of pulse characteristics. Most of the studies concerning CBC have been performed in a CW regime.

CBC in a pulse regime is challenging because phase variation inside the pulses can be expected. In particular, refractive index changes induced by gain depletion (through Kramers–Kronig relations) or nonlinear effects at high peak power can produce fast phase change during the pulse compared to the CBC controller bandwidth. Previous investigation performed in the case of several 10 μs pulses and 1 ns (100 kW peak power) pulses have shown nonnegligible phase variation inside the pulses, with no straightforward compatibility with CBC [3,4]. However, Cheng *et al.* have measured that those phase variations are the same from pulse to pulse and have demonstrated the phase locking between a CW reference and the start of pulses through the addition of a CW leak [4,5].

In this Letter we demonstrate for the first time, to our knowledge, the active CBC of two fiber amplifiers in a 100 ns pulse regime. Pulses are 70 ns, Fourier limited with a frequency repetition rate of 10 kHz. We previously measured a phase variation lower than $\lambda/30$ inside these pulses [6]. This value is compatible with CBC in pulsed operation. The frequency-tagging technique initially proposed for the CW regime [7] has been adapted to the pulse regime by introducing a CW signal leak between the pulses.

CBC by frequency-tagging is a well-known technique used in CW CBC of two or more fiber amplifiers in a master-oscillator-power-fiber-amplifier (MOPFA) configuration. A narrow-linewidth master oscillator is split on several arms, including a phase modulator and one or more fiber amplifiers. CBC is performed by stabilizing amplified signals' interferences at the output to a constructive or a destructive state. In the basic case of two amplifiers, a small phase modulation at frequency F is applied to one of the arms, resulting in a small intensity modulation in the combined beam. This modulation is detected via a single photodetector at the same frequency F. The output is an error signal proportional to the phase difference, $\Delta\varphi$. A simple proportional integrator (PI) controller can then be used to lock $\Delta\varphi$ to 0 and stabilize constructive or destructive interferences on the detector. Modulation multiplexing is used in the case of a large number of amplifiers: each path is controlled using a unique tagging frequency. Note that time multiplexing has also been proposed for CBC [8].

In a pulsed MOPFA architecture, the master oscillator beam is first modulated into pulses with an intensity modulator [e.g., an acousto-optic modulator (AOM)], allowing full control of pulse width, shape, and repetition frequency (PRF). Those low peak power pulses are then amplified by a multistage fiber amplifier. The tagging-frequency technique is not directly applicable to the case of CBC of a pulsed MOPFA. As a rule of thumb, F must be ~100 times the maximum frequency contained in the phase noise to be corrected. Roughly one order of magnitude comes from the low-pass filter of the lock-in amplifier, and the other one comes from the controller integration time. If we want to correct frequencies up to 1 kHz, a tag frequency higher than 100 kHz is required. To directly use the frequency-tagging technique in a pulsed MOPFA, a PRF higher than 200 kHz (Shannon sampling theorem) is then required to achieve correction up to 1 kHz. High-energy fiber amplifiers generally have a PRF of several kilohertz: they are thus not compatible with this solution.

Figure 1 shows the experimental setup of the CBC of the two pulsed fiber amplifiers. Rather than using the information contained in the pulses, we use a signal leak between the pulses for phase stabilization. A 1.5 μm CW seed laser with 15 kHz linewidth is preamplified up to 200 mW and modulated with an AOM to produce 70 ns pulses at 10 kHz with Gaussian-like temporal shape and a low power CW leak. A 50/50 coupler then splits the signal in two arms containing commercial Keopsys pulse

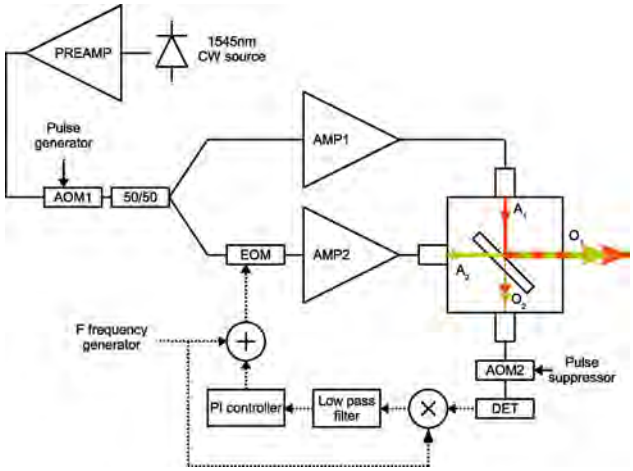

Fig. 1. (Color online) Experimental setup of CBC of two pulsed fiber amplifiers. PREAMP, preamplifier; AMP1 and AMP2, amplifiers; A_1 and A_2, amplifiers' outputs; O_1 and O_2, CBC outputs; DET, photodetector.

fiber amplifiers. One arm also contains a phase modulator [a lithium niobate electro-optic modulator (EOM)] that applies a small phase modulation at frequency $F =$ ~1 MHz. The amplified peak power is limited to ~100 W by SBS arising in the amplifiers [9]. Because fiber lengths inside the amplifiers are somewhat different, the SBS actual peak power limits are 95 W and 123 W, respectively. The signal leak power must be kept as low as possible, because the energy extracted by the leak degrades the performances of the pulses and adds noise. A second AOM is added before the detector to suppress the pulses

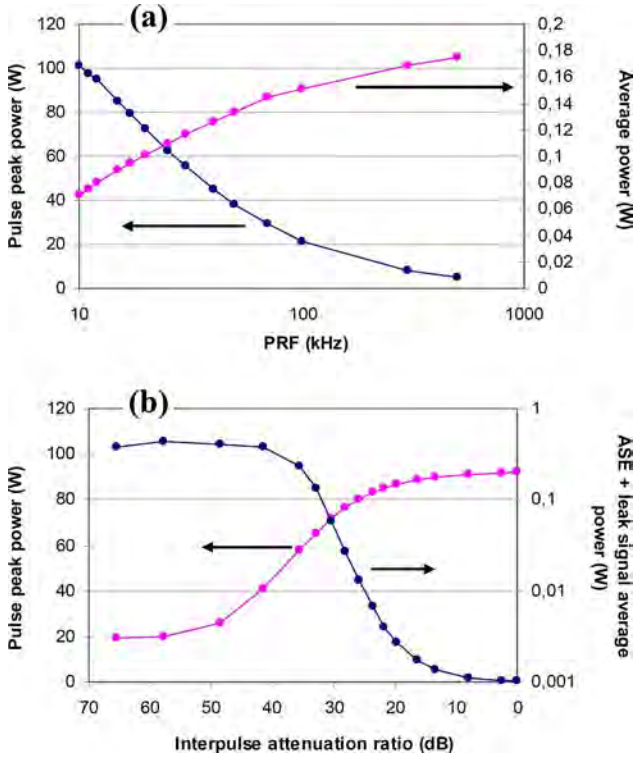

Fig. 2. (Color online) Typical performances of the fiber amplifiers (AMP1 & AMP2). (a) Output pulse peak power and total average power versus PRF; (b) pulse peak power and interpulse average power (ASE + leakage signal) versus interpulse AOM extinction ratio.

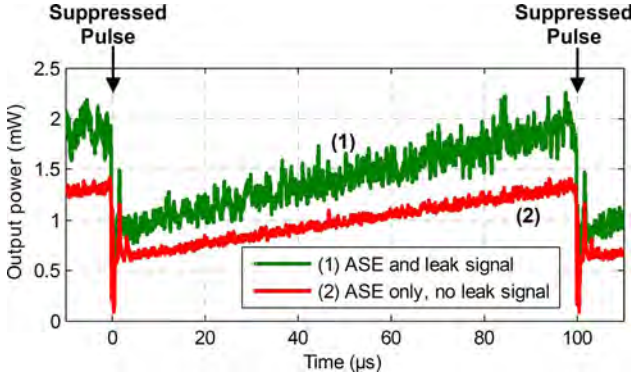

Fig. 3. (Color online) Interpulse signal power in A_2 after pulse suppression over a full 100 μs period. (1) ASE and leak signal, (2) ASE only (leak attenuation >70 dB).

and let only the amplified signal leak reach the detector. The phase stabilization is then performed as in the CW regime, using the amplified leak modulated at F.

Figure 2 shows the typical performances of the fiber amplifiers for a 70 ns pulse signal. The peak and average powers versus PRF are plotted in Fig. 2(a). Below 10 kHz, unwanted SBS effects appear. Figure 2(b) shows the effect of additional interpulse leak on the pulse peak power and on the interpulse signal power [sum of amplified spontaneous emission (ASE) and amplified signal leak] as a function of the AOM extinction ratio for a PRF = 10 kHz. An extinction ratio as low as 40 dB does not affect significantly the output peak power. However, an extinction ratio of 60 dB is chosen to keep the interpulse average power as low as possible. The interpulse average power baseline stems from ASE.

The two amplifiers' outputs (A_1 and A_2) are then collimated with 8 mm aspheric lenses and combined on a bulk beam splitter. Spatial alignment of the two beams is performed by superposing the beams (translation) and removing any fringe pattern (angle). Both beams then overlap along their propagation axis at both outputs, O_1 and O_2. Temporal synchronization of the two beams is achieved by balancing the lengths of the two arms so that the amplified pulses reach the beam splitter at the same time (the <2 ns delay time is small compared to the 70 ns pulse duration). This setup is equivalent to a Mach–Zehnder interferometer with outputs O_1 and O_2 having the same spatial characteristics as A_1 and A_2. Note that the same result could be obtained with a 50/50 fiber coupler in an all-fiber configuration but limited to a much lower peak power to mitigate SBS induced by additional fiber length. This configuration is scalable by cascading bulk beam splitters in a similar way to that described in [10]. Figure 3 shows the interpulse power composed of ASE and signal leak. For comparison, we added the interpulse power in the case of a high extinction ratio (no leak case). The integrated average power ratio is 1.5% in the ASE + leak and 98.5% in the pulses.

CBC is simply achieved by minimizing the leak power at O_2 once the pulse is suppressed, with a frequency-tagging controller developed for CW CBC. The signal can be either minimized or maximized. In the first case, the pulses are constructively combined at the output O_1 (and destructively combined at output O_2). The corresponding measured average output powers at O_1

Table 1. Characteristics of the Fiber Amplifiers Used in a 70 ns Pulse Regime

	Ave. Power (mW)	Peak Power (W)	ASE	ASE + Leak	Ave. Power @ O_1 (mW)	Ave. Power @ O_2 (mW)
AMP1	67	95	1.0%	1.4%	28	39
AMP2	86	123	1.1%	1.5%	50	36

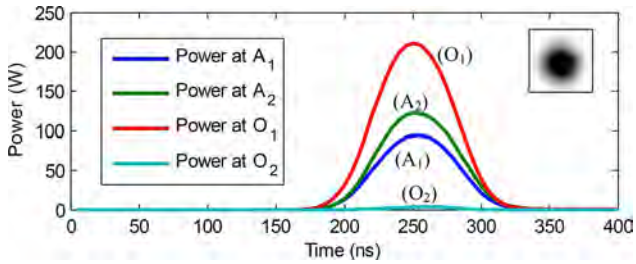

Fig. 4. (Color online) Measured pulse profiles before and after combination (constructive and destructive interferences). Output beam profile is shown as an inset.

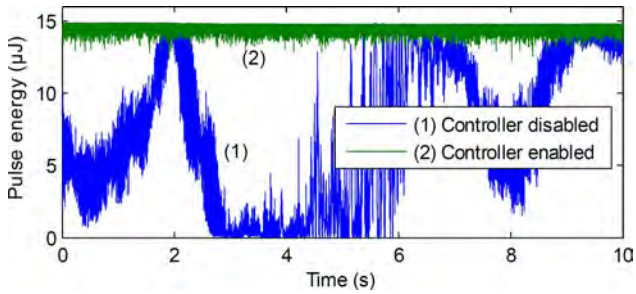

Fig. 5. (Color online) Evolution of combined pulses' energy with controller disabled and enabled.

are 146 mW and 7 mW for constructive and destructive interferences, respectively. The actual reflectivity of the beam splitter for A_1 is 42% (transmission 58%), thus compensating for the slight difference of peak power in the two amplifiers at the O_2 output (see Table 1). This ensures that very low power can be achieved in O_2 when CBC is effective, thus enabling high efficiency in O_1.

Figure 4 shows the pulse profiles in various places. It has a Gaussian shape that is not affected by the amplification. Output peak power is 208 W (O_1 in Fig. 5), to be compared to 218 W = 95 + 123 W (the sum of the A_1 and A_2 pulse amplitudes), thus achieving an average power-combining efficiency of 95%. The few missing percents stem from nonperfect time and spatial overlap as well as the residual phase error. A 10 kHz triggered real-time acquisition board records ~100 points per pulse. The energy of successive pulses is then determined by signal postprocessing. Figure 5 shows the pulse energy evolution over 10 s, with and without the controller running. A residual phase error of $\lambda/27$ is evaluated using the expression

$$\Delta\varphi_{\mathrm{RMS}} = 2\sqrt{\frac{\Delta V_{\mathrm{RMS}}}{V_{\mathrm{MAX}}}}, \tag{1}$$

where $V(t)$ is the energy evolution of the pulses [2]. We have observed that the combined beam quality is similar to those of the two individual AMP1 and AMP2 single-mode beams. The beam combining does not degrade the beam quality.

In conclusion, we have demonstrated the CBC of two SBS-limited fiber amplifiers in the 100 ns pulsed regime. A signal leak between the pulses is used for phase error measurement and correction with the frequency-tagging technique. Using fiber amplifiers with peak power limited to 95 W and 123 W, respectively, we have obtained an output peak power of 208 W with no significant degradation of the beam quality. A power efficiency of 95% and a residual phase error of $\lambda/27$ have been achieved.

The authors acknowledge the financial support of the Triangle de la Physique (Femtocombo project).

References

1. W. Shi, E. B. Petersen, Z. Yao, D. T. Nguyen, J. Zong, M. A. Stephen, A. Chavez-Pirson, and N. Peyghambarian, Opt. Lett. **35**, 2418 (2010).
2. V. Jolivet, P. Bourdon, B. Bennai, L. Lombard, D. Goular, E. Pourtal, G. Canat, Y. Jaouën, B. Moreau, and O. Vasseur, IEEE J. Sel. Top. Quantum Electron. **15**, 257 (2009).
3. J. Martin and J. Mollier, in *Conference on Lasers and Electro-Optics (CLEO)* (Optical Society of America, 2004), paper CTuK4.
4. E. C. Cheung, M. Weber, and R. R. Rice, in *Advanced Solid-State Photonics*, OSA Technical Digest Series (Optical Society of America, 2008), paper WA2.
5. E. C.-T. Cheng, R. R. Rice, M. G. Wickham, and M. E. Weber, "Pulsed coherent fiber array and method," U.S. patent 7,502,395 (March 10, 2009).
6. P. Bourdon, K. Cadoret, L. Lombard, A. Azarian, G. Canat, B. Bennaï, D. Goular, V. Jolivet, Y. Jaouën, and O. Vasseur, Proc. SPIE **7914**, 7914-31 (2011).
7. T. M. Shay, V. Benham, J. T. Baker, B. Ward, A. D. Sanchez, M. A. Culpepper, D. Pilkington, J. Spring, D. J. Nelson, and C. A. Lu, Opt. Express **14**, 12015 (2006).
8. Y. Ma, P. Zhou, X. Wang, H. Ma, X. Xu, L. Si, Z. Liu, and Y. Zhao, Opt. Lett. **35**, 1308 (2010).
9. G. Kulcsar, Y. Jaouën, G. Canat, E. Olmedo, and G. Debarge, IEEE Photonics Technol. Lett. **15**, 801 (2003).
10. R. Uberna, A. Bratcher, and B. G. Tiemann, Appl. Opt. **49**, 6762 (2010).

Femtosecond filamentation in turbulent air

A. Houard,[1] M. Franco,[1] B. Prade,[1] A. Durécu,[2] L. Lombard,[2] P. Bourdon,[2] O. Vasseur,[2] B. Fleury,[3] C. Robert,[3] V. Michau,[3] A. Couairon,[4,*] and A. Mysyrowicz[1]

[1]*Laboratoire d'Optique Appliquée, ENSTA-Ecole Polytechnique, CNRS, F-91761 Palaiseau, France*

[2]*Département d'Optique Théorique et Appliquée, ONERA, 91761 Palaiseau, France*

[3]*Département d'Optique Théorique et Appliquée, ONERA, 92322 Chatillon, France*

[4]*Centre de Physique Théorique, École Polytechnique, CNRS, F-91128 Palaiseau, France*

(Received 6 June 2008; published 5 September 2008)

The influence of air turbulence on femtosecond laser filamentation is studied experimentally and numerically for laser powers of a few critical powers. Air turbulence in the path of the beam prior to filamentation induces a large pointing and formation instability attributed to an increase of the self-focusing distance and higher modulational instability in the presence of turbulence. By contrast, previously formed filaments are robust both in terms of beam pointing accuracy and survival when crossing turbulent air.

DOI: 10.1103/PhysRevA.78.033804 PACS number(s): 42.65.Jx, 42.68.Bz, 42.25.Dd, 42.65.Sf

I. INTRODUCTION

An increasing interest is devoted to the study of femtosecond filamentation. From a fundamental point of view, it provides an interesting system where very strong optical nonlinearities compete to yield remarkably stable structures called filaments, which generate long plasma channels and are able to transmit very high intensities over large distances [1,2]. In turn, this effect has been exploited in many applications such as remote sensing of distant targets, broadband light detection and ranging (LIDAR) detection of pollutants [3], guiding and triggering of electric discharges [4], or generation of THz radiation [5,6]. Many foreseen applications rely on the presence of filaments at very long distances, exceeding hundreds of meters. Therefore an important concern is the influence of air turbulence on the filamentation process and on the filament characteristics.

Air turbulence is usually characterized by a structure constant C_n^2 which determines the intensity of fluctuations of the refractive index [7,8]. Values of C_n^2 between 10^{-15} and 10^{-13} $m^{-2/3}$ represent standard atmospheric turbulence. Air turbulence can influence both the pointing accuracy (transverse filament wandering) and the distance at which filaments are formed (longitudinal filament wandering). The problem of filament wandering along the propagation axis z was investigated by Penano *et al.* who came to the conclusion that air turbulence should lead to an increase of the distance required for filament formation with chirped pulses when the structure constant C_n^2 is increased [9]. In contrast, Kandidov *et al.* showed from numerical simulations with a given $C_n^2=1\times10^{-11}$ $m^{-2/3}$ that the distance at which the intensity in the nonlinear focus reaches the ionization threshold is random for the different realizations (shots) but that on the average, turbulence should lead to a shorter collapse distance [10]. The major difference between the two studies is that Kandidov *et al.* considers pulse power many times exceeding critical power for self-focusing, resulting in multifilamentation of the laser beam. These results highlight the fact that in the presence of turbulence, filaments resulting from self-focusing and collapse of the whole beam exhibit different features from those resulting from modulational instability of the beam inhomogeneity [11]. Self-focusing of the whole beam should prevail for sufficiently weak air turbulence and input powers so as to form only one filament. An understanding of the competition between beam self-focusing and modulational instability in turbulent air is required to achieve control of longitudinal features of filaments, as, e.g., the filamentation length [12] or the filament concatenation [13,14].

Radial pointing stability was studied experimentally and numerically [15]. Measurements of the filament position after 30 and 100 m exhibit random isotropic displacements in good agreement with simulation results. Strong but localized turbulence placed in the zone after the onset of filamentation was found to barely affect the radial stability [16] while extended turbulence does not reduce significantly the survival rate of filaments [17]. It has been argued that the pointing accuracy of already formed filaments should be rather insensitive to turbulence because of the transverse dimension of a filament, smaller by a factor of 10 than the inner scale $l_0=1$ mm characterizing air turbulence. This scenario relies on the concept that the filament behaves as a narrow beam which does not depend on the periphery of the intense core. However, it was established that in the absence of air turbulence, a filament is sustained by an energy flux from the low intensity energy reservoir to the intense core [18]; energy losses via multiphoton absorption would rapidly dissipate the energy of the narrow filament if it was not refilled by this energy flux [19]. Specific experiments have established the validity of this scenario [20,21] and numerical simulations allowed a careful monitoring of the conical energy flux established during filamentation [22,23]. Since the transverse dimension of the energy reservoir surrounding a filament in air is larger than the inner scale of the Kolmogorov spectrum, the low intensity part of the beam must be sensitive to air turbulence; the energy flux and the survival probability of a filament should be correlated to this sensitivity.

No quantitative measurement has been done so far to interpret the interplay between filaments in turbulent air and their energy reservoir. In this work we use well-calibrated turbulence cells to investigate filamentation in air as a func-

*Corresponding author. couairon@cpht.polytechnique.fr

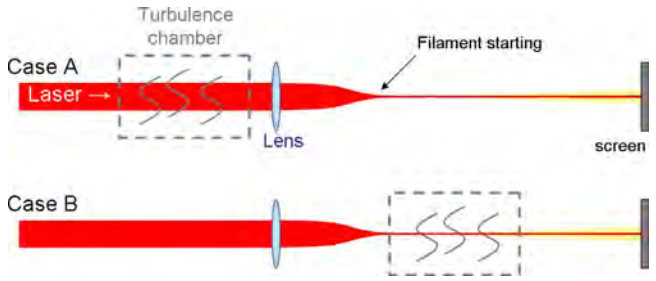

FIG. 1. (Color online) Experimental setup. Case A: turbulence is applied on the beam prior to filamentation and a camera records for each shot the white light spot on a screen placed 7 m after the focusing lens. The distance between the aperture and the entrance of the turbulence cell is 10 cm and the distance between the output plane of the cell and the lens is 30 cm. Case B: turbulence is applied on the filament after the self-focusing of the beam. The distance between the aperture and the lens is 270 cm.

tion of the intensity of turbulence. We study the effect of turbulence on the transverse wandering. We also explore whether turbulence decreases or increases the distance of collapse. We study two cases separately: Turbulence in the path of the beam prior to collapse (case A) and after filamentation (case B). The study is restricted to the case where only a single filament is formed. Numerical simulations are performed for both cases A and B and the effect of transverse wandering is statistically analyzed.

II. EXPERIMENTAL PROCEDURE

The experimental setup is shown in Fig. 1. The laser used is a CPA (chirped-pulse amplifier) Ti:sapphire laser chain delivering 50 fs pulses at 800 nm, with an energy per pulse of 15 mJ maximum at a repetition rate of 100 Hz. The beam has an apertured Gaussian beam resulting in a super-Gaussian profile with a diameter $w_0=1.5$ cm (half width at half maximum). In order to have a single filament, we restricted the initial laser peak power to a few P_{cr}, where P_{cr} ~ 3 GW is the minimum power necessary to form a filament in nonturbulent air at atmospheric pressure, using a 50 fs long laser pulse at 800 nm. It was predicted that atmospheric turbulence increases the power threshold for beam collapse P_c [7,24] by the condition

$$\frac{P_c}{P_{cr}} = 1 + \frac{3}{4}k_0^2 a^2 \left(\frac{aC}{2}\right)^{2/3}, \tag{1}$$

$$C = 4.38 l_0^{-1/3} C_n^2 \left\{1 - \left[1 + 17.5\frac{a^2}{l_0^2}\right]^{-1/6}\right\}, \tag{2}$$

where k_0 denotes the wave number of the laser pulse, $a = w_0/\sqrt{2}$ the width of an initial Gaussian beam $\mathcal{E} = \mathcal{E}_0 \exp(-r^2/2a^2)$, and $l_0=1$ mm, the inner scale of turbulence. For $C_n^2=10^{-13}$ m$^{-2/3}$, the condition (2) gives P_c $\sim 6.4P_{cr}$. Pulses with 3 mJ energy after a circular aperture were used, having therefore peak power of about $18P_{cr}$. This is about three times the required value for collapse in turbulent air with the smallest C_n^2. In order to reduce the distance required for collapse and filamentation, the beam was focused with a 4 m focal lens. Under these conditions, all our experiments led to the observation of a single filament.

The long calibrated turbulence chamber has been described elsewhere [25]. It consists of a 2.3 m long box in which hot air (up to 60 °C) is blown in and out laterally to achieve uniform turbulent flow. The C_n^2 factor defining the turbulence is calibrated inside the chamber with a CT meter, which is a microthermic probe measuring the local temperature structure constant C_T. The C_n^2 is then determined using the relation

$$C_n = \frac{79 \times 10^{-6} P}{T^2} C_T,$$

where P and T are, respectively, the gas pressure (in millibar) and temperature (in Kelvin) in the turbulent chamber [26]. The C_n^2 could be varied between $C_n^2=10^{-13}$ and 10^{-10} m$^{-2/3}$. This corresponds to propagation distances in air of 1 km under typical conditions ranging from very quiet to regular weather. Experiments have been performed by putting the turbulent air region before (case A) or after the onset of filamentation (case B) as shown in the figure.

During the filamentation process the laser pulse experiences a large self-phase modulation, generating a white light emission in the forward direction [1]. This white light continuum is used as a criterion to determine the presence of a filament and to measure its location in the plane perpendicular to the propagation axis. A synchronized charge coupled device (CCD) camera with a BG39 SCHOTT glass filter removing the fundamental component of the pulse around 800 nm took pictures of this white light emission spot on a diffusing screen with a flat spectral reflectivity placed 7 m after the focusing lens (see Fig. 1). The camera is an ANDOR DU434 CCD with an array of 1024×1024 pixels of 13 μm, yielding a resolution of 100 μm on the screen. For each measurement 256 pictures were recorded at 10 Hz. The pointing stability was evaluated by calculating the standard deviation σ of the position of the intensity maximum. Knowing that in the absence of turbulence filament formation occurs for every shot, the counting rate of white light emission corresponds to the probability of filament formation for a beam crossing a turbulence in case A whereas it gives the filament survival rate when it crosses a turbulent region in case B. In each case the position of the white spots is compared to the center of gravity of a low intensity beam (average diameter in the turbulence chamber ~ 1 mm) for which a filament is never formed.

Due to mechanical vibrations in the amplifier of the laser chain, the ir laser beam pointing presents a small instability in the horizontal plane. This is seen, for instance, in Fig. 2(a) showing the superposition of 200 shots of the low intensity beam center in the absence of turbulence. To correct this spatial anisotropy the horizontal spread of the points is reshaped to present the same standard deviation as the vertical one. This treatment is justified by the tacit assumption that the effects of turbulence are isotropic. The resulting distribution is plotted in Fig. 2(b).

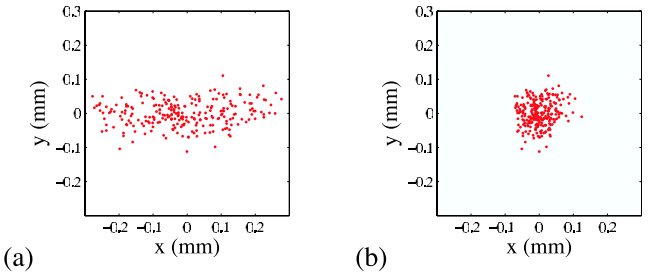

FIG. 2. (Color online) Position of the 100 μJ beam center in the absence of turbulence before (a) and after (b) horizontal reshaping.

III. EXPERIMENTAL RESULTS

A typical result for the beam wandering is shown in Fig. 3. Figure 3(a) shows the positions of the filaments in case A (turbulence before the onset of filamentation); Fig. 3(b) the position of the filaments in case B (turbulence after the onset of filamentation). We performed a systematic statistical analysis of the transverse displacements as a function of turbulence. Figures 4 and 5 show examples for the fluence distribution of white light recorded on the screen (a) and the distribution of the transverse position of the filaments (b) in case A, for $C_n^2=1.7\times10^{-11}$ m$^{-2/3}$ and $C_n^2=2.1\times10^{-13}$ m$^{-2/3}$, respectively. It is well-established that under the assumption of uniform and isotropic turbulence, the vertical and horizontal positions of the hot spots should independently follow a normal distribution law with the same variance, since air turbulence is a stochastic process. This means that the distance from the propagation axis (center of the beam at $r=0$) must be correctly described by a Rayleigh distribution law:

$$\Psi_R(r) = 1 - \exp(-r^2/w_R^2), \tag{3}$$

where w_R characterizes the width of the distribution. This result was established by Chin *et al.* [15] in the case of filaments analyzed after propagation distances of 30 and 105 m in turbulent air. Our experiments partly agree with this result, but also show different distributions interpreted as due to a stronger influence of nonlinear effects than that of turbulence on the transverse wandering. Figures 4(c) and 5(c) show the histogram of the hot spot (i.e., maximum intensity) distances from the axis for strong and very weak

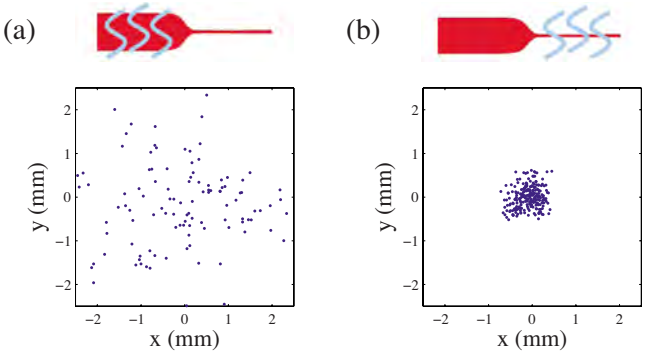

FIG. 3. (Color online) Position of the filament white light spot on the screen in cases A (a) and B (b) for a turbulence parameter of $C_n^2=1.7\times10^{-11}$ m$^{-2/3}$.

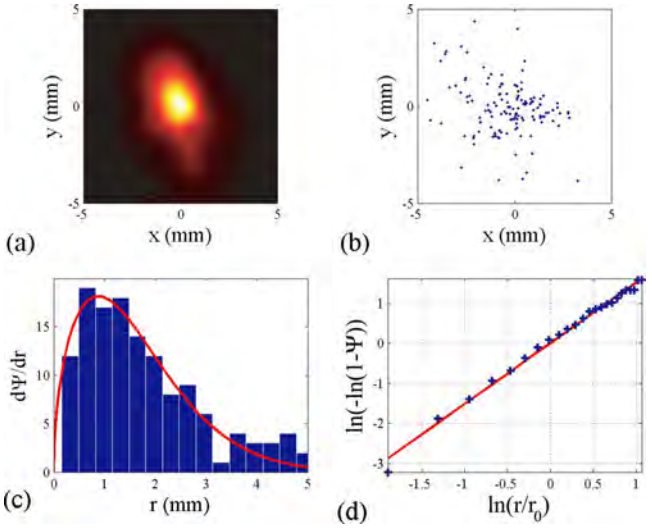

FIG. 4. (Color online) Experimental results for 256 shots in case A with strong turbulence $C_n^2=1.7\times10^{-11}$ m$^{-2/3}$. (a) Example of beam cross section at 7 m beyond the entrance of the turbulence cell. (b) Filament positions after correction of the systematic error in the horizontal direction. 127 (49%) shots were retained for which filamentation occurred. (c) Histogram of the transverse displacements fitted by a Weibull probability distribution [continuous curve in (c) and (d)] with parameters $p=1.52$ and $w_W=1.78$ mm. (d) details the fit procedure which amounts to determining the slope of the function $\ln[-\ln(1-\Psi)]$ of the cumulated number Ψ of filaments found within a circle of radius r.

turbulence. These histograms cannot be fitted perfectly with Rayleigh distribution law. In this case, the best fit of the distribution of filaments was obtained by using a Weibull distribution law:

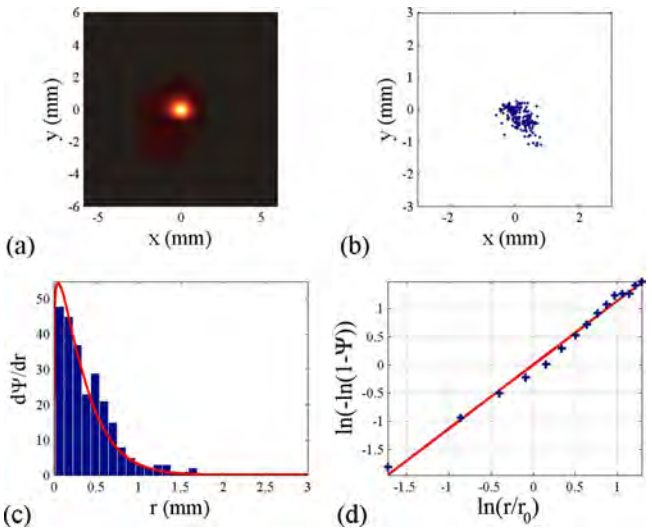

FIG. 5. (Color online) Experimental results presented as in Fig. 4 for 251 shots (98%) in case A with very weak turbulence $C_n^2=2.1\times10^{-13}$ m$^{-2/3}$. The Weibull distribution of transverse displacements [continuous curve in (c) and (d)] has parameters $p=1.13$ and $w_W=0.41$ mm.

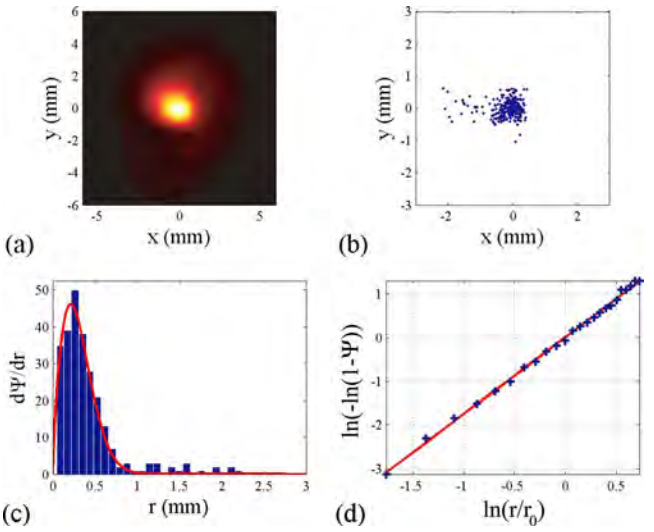

FIG. 6. (Color online) Experimental results presented as in Fig. 4 for 233 shots (91%) in case B with strong turbulence $C_n^2 = 1.7 \times 10^{-11}$ m$^{-2/3}$. The Weibull distribution of transverse displacements [continuous curve in (c) and (d)] has parameters $p = 1.76$ and $w_W = 0.35$ mm.

$$\Psi_W(r) = 1 - \exp(-r^p/w_W^p), \tag{4}$$

which generalizes the Rayleigh distribution law (both coincide for $p=2$). In our statistical analysis, we will fit the distribution of filaments by plotting the quantity $\ln[-\ln(1-\Psi)]$, depending on the cumulated number Ψ of hot spots located within a circle of diameter r, as a function of r for each interval of the histograms [see Figs. 4(d) and 5(d)]. This allows for a determination of the parameters w_W and p for the Weibull distribution, the magnitude of $|p-2|$ indicating the departure from a Rayleigh distribution. The corresponding density of probability $P = d\Psi/dr$ is then compared to the experimental histogram [continuous curve in (c)].

Figures 4 and 5 show that the distribution of the transverse position of the filaments in case A can be well-described by a Weibull probability distribution. This distribution is close to a Rayleigh distribution function only in the case of the strongest intensities of turbulence ($C_n^2 \geqslant 10^{-11}$ m$^{-2/3}$). A decrease of the turbulence intensity leads to a decrease in the averaged amplitude of the transverse wandering of filaments.

Figure 6 shows a similar statistical analysis performed in case B. One can notice that the transverse displacements are much smaller in this case, where the filament is already formed where the beam crosses the turbulent region.

Figure 7 gives results for the pointing stability in cases A and B as a function of the turbulence in the chamber. Also shown is the pointing stability of a similar beam with much lower intensity (black diamonds) propagating linearly in the whole path. According to Ref. [27] for linear propagation the mean square of the transverse displacement δr of the beam on the screen can be expressed as

$$\langle (\delta r)^2 \rangle = 2.91 \int_0^L C_n^2(z) w(z)^{-1/3} dz, \tag{5}$$

where w is the beam width and L is the propagation length in the turbulent medium. This law is shown as a dashed curve

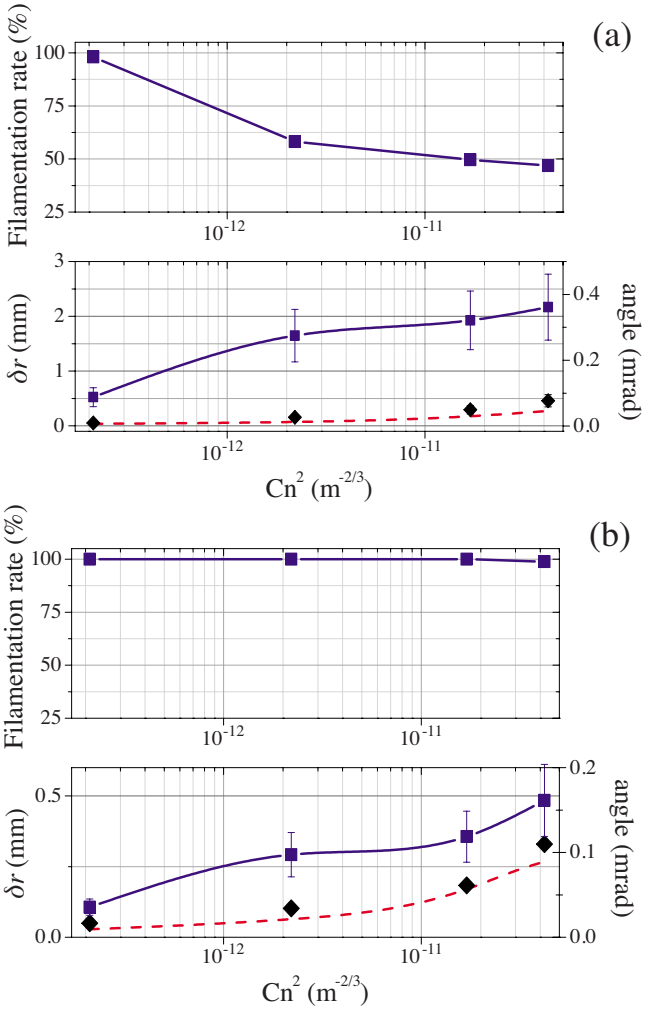

FIG. 7. (Color online) Filamentation rate (top) and average filament deviation $\langle \delta r \rangle$ (bottom) of a 3 mJ laser beam as function of the C_n^2 (in m$^{-2/3}$) in the chamber for case A (a) and B (b). The black diamonds show the deviation for a 100 μJ pulse propagating linearly under the same turbulent conditions, and the dashed red curve is a calculation using formula (5).

in Fig. 7 and fits rather well our measurements with the low intensity beam which were performed as benchmarks for the measurements of the transverse wandering of filaments. In the fully nonlinear regime, one can see that turbulence on the path of the beam prior to the onset of filamentation (case A) has a drastic effect on both the filament survival probability and pointing stability. By contrast the filament survival probability is largely insensitive to turbulence if it is formed before reaching the turbulent cell (case B), but the pointing instability is still larger than for linear beam propagation in the same conditions.

These results are in keeping with the model of the energy reservoir: In case A, the whole beam undergoes the effect of air turbulence before it is focused to form a filament. The energy reservoir is therefore not organized so as to sustain a perfectly cylindrically symmetric energy flow toward the propagation axis, but the filament can still form when turbulence is not strong enough to prevent the energy flux from accumulating power above P_{cr} around an intensity peak of

the beam. This results in a striking effect of turbulence on the filament formation probability rate in case A. Indeed, with the increase of the C_n^2 parameter the probability to form a filament decrease from 97% to 50%. This is in agreement with the conclusions of Penano *et al.* that turbulence increases the distance required for the onset of filamentation in the case of filaments resulting from self-focusing of the whole beam. This result is not expected to be always true; as discussed below, larger beam powers and a regime of modulational instability enhanced by turbulence may lead to the opposite conclusion.

In contrast, in case B, the energy flux is organized in nonturbulent air and is perfectly symmetric at the entrance of the turbulence cell. The strong nonlinear effects occurring in the filament core, in particular multiphoton absorption, act as a driving force which prevails over the effects of turbulence to keep the center of symmetry of the energy flux located on, or close to, the propagation axis. The energy reservoir refilling the central filament is about 1 mm large (corresponding Rayleigh length $\sim$4 m) and is therefore not affected by turbulence, except for a tilt. Therefore once formed the filament is very robust against destruction by turbulence. However, the reason behind this robustness is not explained by an equilibrium of the core of the filament itself but by the fact that much larger propagation distances in turbulent air would be needed to strongly modify the 1 mm large energy reservoir and overcome the effect of the energy flux toward the filament axis.

IV. PROCEDURE FOR NUMERICAL SIMULATIONS

In order to discuss the results, we have performed numerical simulations. The propagation of ultrashort laser pulses and filamentation are described by means of a nonlinear evolution equation for the envelope $\mathcal{E}$ of the laser pulse along the z axis. The derivation of the equations of the model was reviewed in detail [Eqs. (47)–(51) in Ref. [1]]. We included a specific module in our simulation code for the description of the change of refraction index δn due to air turbulence. The propagation equation for the envelope of the laser pulse reads as

$$2ik_0\frac{\partial \mathcal{E}}{\partial z} + \Delta_\perp \mathcal{E} - 2ik_0 N(\mathcal{E}) = 2k_0^2 \delta n \mathcal{E}, \tag{6}$$

where $k_0 = k(\omega_0)$ denotes the wave number corresponding to the central frequency ω_0. The term $\Delta_\perp$ in Eq. (6) represents the transverse Laplacian and accounts for beam diffraction; the third term $N(\mathcal{E})$ in Eq. (6) represents nonlinear effects which usually include the optical Kerr effect, multiphoton absorption, plasma defocusing, plasma absorption, and optical shock terms. Here, we performed a statistical analysis of filamentation in turbulent air and therefore considered only a reduced set of these effects for the bulk of the results, namely the optical Kerr effect with coefficient n_2 and multiphoton absorption with cross section β_K; K denotes the number of photons involved in the process:

$$N(\mathcal{E}) = i\frac{\omega_0}{c} n_2 |\mathcal{E}|^2 \mathcal{E} - \frac{\beta_K}{2} |\mathcal{E}|^{2K-2} \mathcal{E}. \tag{7}$$

Filamentation in the absence of air turbulence exhibits intensities usually saturated at levels which do not exceed a few 10^{13} W/cm^2 due to multiphoton absorption and defocusing due to the plasma generated by multiphoton ionization [28]. The multiphoton absorption cross section corresponds to the multiphoton ionization of oxygen atoms in air, for which $K = 8$ photons are necessary at 800 nm to liberate an electron from an atom with ionization potential of 12.1 eV.

The right-hand side of Eq. (6) includes a source term that accounts for the effect of air turbulence on the refractive index fluctuations in air, described by a stochastic model of phase screens located along the propagation distance [29]. The power spectral density of the refractive index fluctuations is given by the modified von Karman spectrum

$$\psi_n(\kappa) = 0.033 C_n^2 (\kappa^2 + \kappa_0^2)^{-11/6} \exp(-\kappa^2/\kappa_m^2), \tag{8}$$

where C_n^2 denotes the structure constant of atmospheric turbulence characterizing the magnitude of fluctuations, $\kappa_0 = 2\pi/L_0$ and $\kappa_m = 5.92/l_0$, where $L_0 = 15$ cm and $l_0 = 1$ mm, denote the outer and inner scales of turbulence. These scales bound the inertial interval of turbulence where energy of the turbulent fluctuations is transferred from large to small eddies and eventually dissipated by viscosity. Each of the source terms was benchmarked independently by comparison with known analytical cases, or numerical solutions. For instance, the model was checked to correctly reproduce the average displacement of the center of mass of a low power beam in turbulent air [29].

The incoming pulse is assumed to be Gaussian in time and super-Gaussian of order $n = 20$ in space so as to mimic the effect of a circular aperture used in the experiment; its envelope is described by

$$\mathcal{E}(x,y,t,z=0) = \mathcal{E}_0 \exp[-(x^2+y^2)^{n/2}/w_0^n - t^2/t_p^2], \tag{9}$$

where $w_0 = 15$ mm is the beam width, $t_p = 42$ fs is the pulse duration. The input intensity $\mathcal{E}_0^2 \equiv 2^{2/n} n P / 2\pi w_0^2 \Gamma(2/n)$ is computed from the input power $P = E_{in}/t_p\sqrt{\pi/2}$, which is computed from the pulse energy E_{in}. For $P = 18P_{cr}$, the collapse distance of the super-Gaussian beam of order $n = 20$ is obtained on-axis at $z = 119$ m, after formation of a multiple ring profile which does not undergo collapse on itself [33]. The lens is modeled in both experiments by a spatial beam curvature $\exp[-ik_0(x^2+y^2)/2f]$. With the $f = 4$ m lens, collapse of the super-Gaussian beam is obtained at 3.90 m without ring formation.

V. NUMERICAL RESULTS

We performed numerical simulations of the filamentation process in the experimental conditions for both cases A and B. In both cases and for all sets of simulations performed with similar turbulence (C_n^2, l_0, L_0) but different realizations of phase screens, we applied the statistical analysis presented in Sec. III. We show here typical results by using the same order in the presentation.

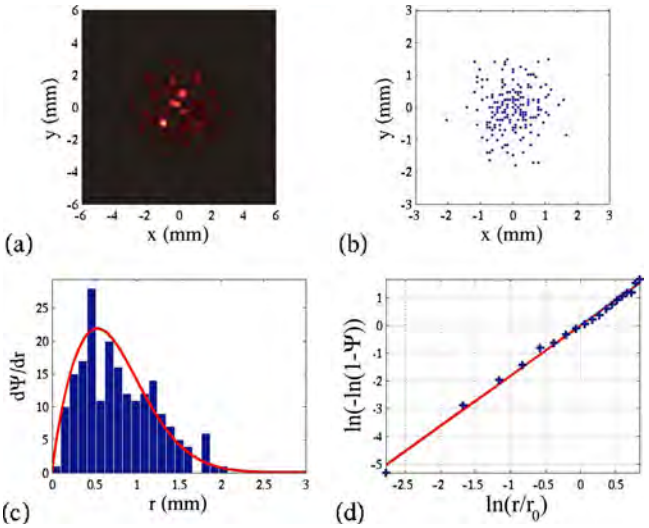

FIG. 8. (Color online) Numerical simulation results presented as in Fig. 4 for 200 shots in case A with strong turbulence $C_n^2=1.7\times10^{-11}$ m$^{-2/3}$. The probability function for the Weibull distribution [continuous curve in (c) and (d)] has parameters $p=1.81$ and $w_W=0.83$ mm.

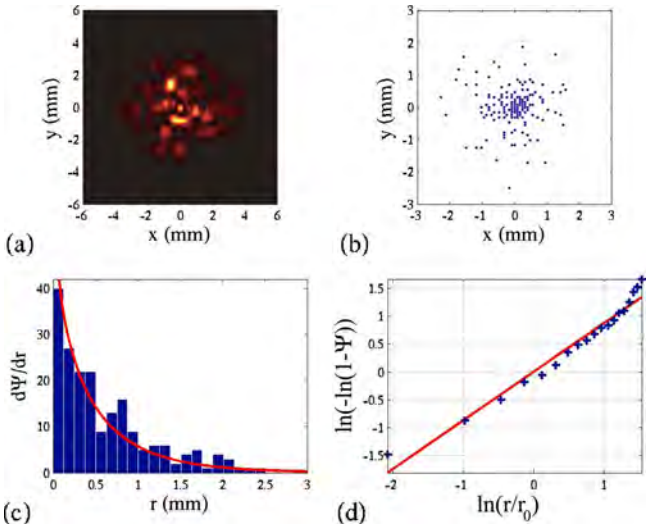

FIG. 10. (Color online) Numerical simulation results presented as in Fig. 4 for 200 shots in case A with the screen at $z=6$ m, weak turbulence $C_n^2=2.2\times10^{-12}$ m$^{-2/3}$. The parameters for the Weibull distribution [continuous curve in (c) and (d)] are $p=1.75$ and $w_W=0.73$ mm.

A. Simulations of case A

Simulation results when the pulse propagates through the turbulence cell before filamentation (case A) are shown in Figs. 8 and 9 for decreasing intensities of atmospheric fluctuations. Simulations were performed from the case of very strong turbulence ($C_n^2=9\times10^{-10}$ m$^{-2/3}$) to that of very weak turbulence ($C_n^2=2.1\times10^{-13}$ m$^{-2/3}$). Each set of simulations represents 200 shots. For very strong ($C_n^2=9\times10^{-10}$ m$^{-2/3}$) or strong (Fig. 8, $C_n^2=1.7\times10^{-11}$ m$^{-2/3}$) turbulence, the distribution of filaments can be correctly described by a Weibull distribution with parameters p slightly smaller than 2, indicating that the pointing instability after the filamentation stage follows the laws expected from homogeneous and isotropic turbulence acting on the whole path. The parameter w_W can be interpreted as a measure of the pointing instability and is observed to decrease when the turbulence strength decreases.

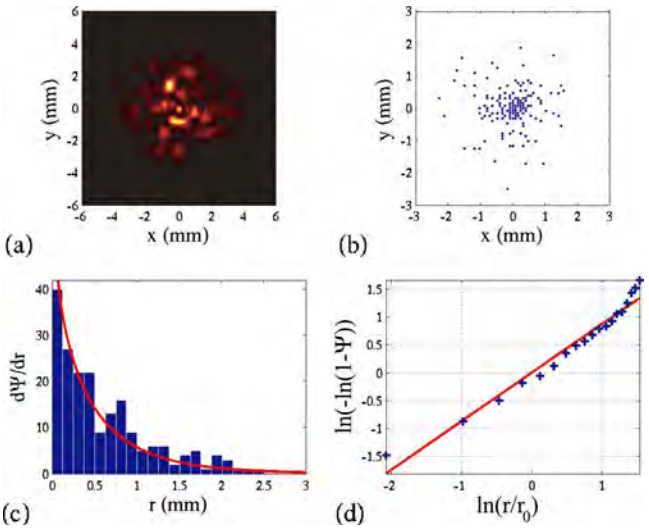

FIG. 9. (Color online) Numerical simulation results presented as in Fig. 4 for 200 shots in case A with the screen at $z=7$ m, weak turbulence $C_n^2=2.2\times10^{-12}$ m$^{-2/3}$. The Weibull distribution [continuous curve in (c) and (d)] has parameters $p=0.87$ and $w_W=0.50$ mm.

For weak (Fig. 9, $C_n^2=2.2\times10^{-12}$ m$^{-2/3}$) or very weak ($C_n^2=2.1\times10^{-13}$ m$^{-2/3}$) turbulence, the distribution of filaments can no longer be described by a Rayleigh-like distribution (i.e., a Weibull distribution with parameter p close to 2). The parameter of the Weibull distribution is indeed smaller than one in both cases, indicating that the probability to find a filament at distance r from the propagation axis is the largest on the axis ($r=0$). A similar distribution is observed experimentally for $C_n^2=2\times10^{13}$ m$^{-2/3}$ (see Fig. 5). This means that after the turbulence cell, the effects of linear focusing by the lens and of self-focusing of the whole beam due to the optical Kerr effect prevail over the effect of weak turbulence in the first propagation stage. This results in a minimal pointing instability which is still decreased as the intensity of turbulence decreases.

B. Competition between turbulence and ring formation

The results above highlight a competition between the effects of weak turbulence and both the linear and nonlinear effects playing a role in filamentation in the absence of turbulence, namely, diffraction and the optical Kerr effect. A striking feature of this competition is visible in Fig. 10 obtained from simulations of experiment A with weak air turbulence (similar results are obtained for very weak turbulence, data not shown). Figure 10(c) shows that the fit with the Weibull distribution function crudely fits the results. The reason for this poor agreement comes from the fact that there are intervals of the histogram in which we obtain an accu-

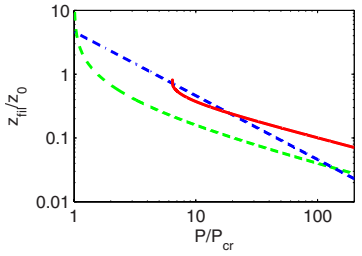

FIG. 11. (Color online) Filamentation distance as a function of P/P_{cr}: distance to observe a gain of 10^4 by MI (dash-dotted curve); collapse distance in nonturbulent air (dashed curve); and collapse distance in turbulent air (solid curve, $C_n^2=10^{-13}$ m$^{-2/3}$).

mulation of filaments. This is also clearly visible on the distribution of filaments [Fig. 10(b)] which exhibits rings where the filaments are preferentially located. These rings are formed because the input beam profiles are super-Gaussians so as to model the effect of the circular aperture. It is known that self-focusing of super-Gaussian beams forms rings [30] and that filaments in nonturbulent air locate preferentially on the largest intensity gradients of the beam [31,32]. A self-similar ringlike solution of the nonlinear Schrödinger equation was shown to exist and to behave as an attractor for the collapse dynamics of super-Gaussian beams [33]. Although the determination of the minimum power above which a ring collapse occurs is still an open question, it was shown that a radially symmetric ring collapse is obtained for input powers above $15P_{cr}$; in the presence of symmetry breaking inhomogeneities in the input beam, multiple filaments are formed as corroborated by experiments [34]. A competition therefore also exists between turbulence and the latter effect. Because of our relatively low powers, we observe a ring formation without any catastrophic ring collapse. For perfect radial symmetry, the filament would finally form on axis after refocusing of the whole beam, even if rings appear. In the presence of weak turbulence, modulational instability is enhanced and filaments form on the intense rings generated during the focusing stage. As shown below, this competition also explains the longitudinal wandering of filaments.

C. Interpretation of the longitudinal wandering of filaments in turbulent air

The competition between self-focusing of the whole beam and modulational instability (MI) was studied by Fibich *et al.* [35] who showed that for input powers smaller than $100P_{cr}$, self-focusing of the whole beam prevails and the collapse distance scales as $1/\sqrt{P}$, whereas for $P>100P_{cr}$, MI prevails and the collapse distance scales as $1/P$. This follows from the amplification rates k_i of small perturbations growing as $\exp(k_i z)$, given by $k_i z_0=k_\perp w_0\sqrt{P/P_{cr}-k_\perp^2 w_0^2/16}$, the propagation distance where z_0, the Rayleigh length associated with the beam of diameter w_0, makes the growth rates dimensionless. The maximum growth rate is $k_i^{max}z_0=2P/P_{cr}$ and yields an amplification by a factor of, e.g., 10^4 over a distance $z=z_0\times 2\log(10)P_{cr}/P$.

Figure 11 shows as a dashed curve the distance z_{fil} at which a filament would form in a nonturbulent atmosphere, as given by Marburger's law for the collapse of optical beams in Kerr media and scaling roughly as $(P/P_{cr})^{-1/2}$ [36]. The dash-dotted line shows the distance required for MI to amplify narrow perturbations by a factor of 10^4; this distance is smaller than the collapse distance z_{fil} for powers above $200P_{cr}$, which means that self-focusing of the whole beam is the prevailing mechanism in the formation of filaments at smaller powers.

In a turbulent atmosphere, the distance required for self-focusing of the whole beam was shown by Petrishchev [24] to be determined by the zeros of the function

$$1+(1-P/P_{cr})(z/z_0)^2+\frac{k^3w_0^4C}{8}(z/z_0)^3=0, \qquad (10)$$

where C is given by Eq. (2). A filament formed in a turbulent atmosphere begins at this collapse distance which is plotted as a function of P/P_{cr} in Fig. 11(b) (solid curve) for $C_n^2=10^{-13}$ m$^{-2/3}$ and the conditions of our experiments. Filaments obtained by self-focusing of the whole beam thus start at larger distances when turbulence is increased. As a result, the power threshold above which MI starts to be the prevailing mechanism to form a filament is smaller than that predicted by using Marburger's collapse distance. Figure 11(b) shows that the solid curve ($C_n^2=10^{-13}$ m$^{-2/3}$) intersects the dash-dotted line (MI) around $20P_{cr}$, which gives a reduction by a factor of 10 for the power threshold to form filaments by MI, in the condition of our experiments. Since the distance required for MI and amplification of turbulence induced noise decreases when turbulence is increased, our conditions belong to the region where self-focusing of the whole beam competes with MI to form filaments. These results also explain the average decrease of the collapse and filamentation distance obtained by Kandidov *et al.* [10] when turbulence is increased. In this respect, we computed the minimal distance for which the peak intensity exceeds a certain threshold, for each of the 200 shots corresponding to each value of the structure constant C_n^2 in case A. Results are shown in Figs. 12 and 13. For strong turbulence, filamentation starts on the average before the nonlinear focus at 390 cm obtained for the same input conditions but without turbulence. For weak turbulence, the average beginning of filamentation is shifted beyond the focus of the lens. This result does not depend on the choice of the intensity threshold to perform these statistics as shown by a comparison of Figs. 12 and 13. However, the filamentation rate defined here as the number of shots for which the peak intensity exceeds the chosen threshold is strongly dependent on the threshold. This is explained by the fact that due to saturation, the peak intensity for a filament in nonturbulent air reaches a few 10^{13} W/cm^2 [28]; the saturation value decreases when the strength of turbulence increases, thus the filamentation rate decreases when C_n^2 increases or when the intensity threshold is chosen larger.

We finally note that our use of the simplest form of MI theories, which applies for perturbations of plane waves, leads to a larger value ($200P_{cr}$ for the threshold above which MI prevails) than the value that would be obtained by considering MI of a Townes profile [37] or MI of a ring solution

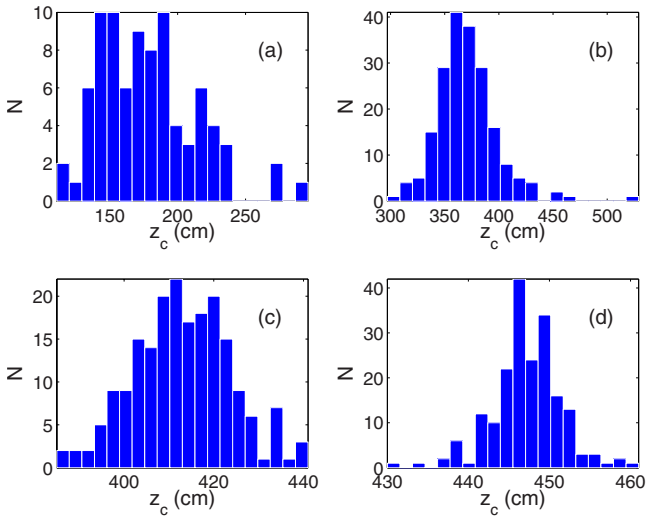

FIG. 12. (Color online) Distribution of filamentation distances, defined as the minimal distance for which the peak intensity exceeds the threshold of 10^{13} W/cm^2 in case A. The focus of the lens is at 400 cm and the collapse distance without turbulence is at 390 cm. The statistics is performed over 200 shots for each C_n^2. (a) $C_n^2=9\times10^{-10}$ m$^{-2/3}$. (b) $C_n^2=1.7\times10^{-11}$ m$^{-2/3}$. (c) $C_n^2=2.2\times10^{-12}$ m$^{-2/3}$. (d) $C_n^2=2.1\times10^{-13}$ m$^{-2/3}$. The peak intensity is below threshold for 57% of the shots in case (a), 1% in case (b), and is above threshold in cases (c) and (d).

[34]. The principle of our analysis would, however, be the same with a different type of beam profile, for which qualitative agreement with our results is expected.

D. Simulations in case B

Figure 14 shows the statistical analysis of simulation results in case B for very strong turbulence. Figure 14(a) clearly shows that the energy reservoir exhibits rings which are the result of several effects, among which diffraction of the apertured input beam, self-focusing of this super-Gaussian-like beam, as well as the competition between diffraction and multiphoton absorption, which acts as a distributed stopper along the filament, thus generating diffraction rings [38]. Turbulence plays a role only after the energy reservoir has been reshaped into rings. Therefore the action of turbulence on the intense core is limited to a moderate tilt of the filament. The larger scale energy flux toward the propagation axis is in principle more sensitive to air turbulence but multiphoton absorption in the filament core prevails in sustaining the energy flux and its symmetry. This leads to an overall weak effect of turbulence on already formed filaments, in agreement with experimental results.

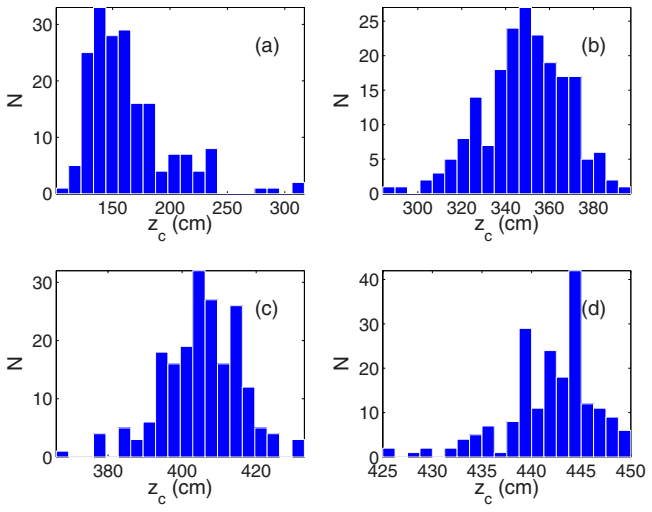

FIG. 13. (Color online) Same as in Fig. 12 but for the threshold of 8×10^{12} W/cm^2. The peak intensity remains below threshold for 7% of the shots for (a) $C_n^2=9\times10^{-10}$ m$^{-2/3}$ and is above threshold for all shots for weaker turbulence (b)–(d).

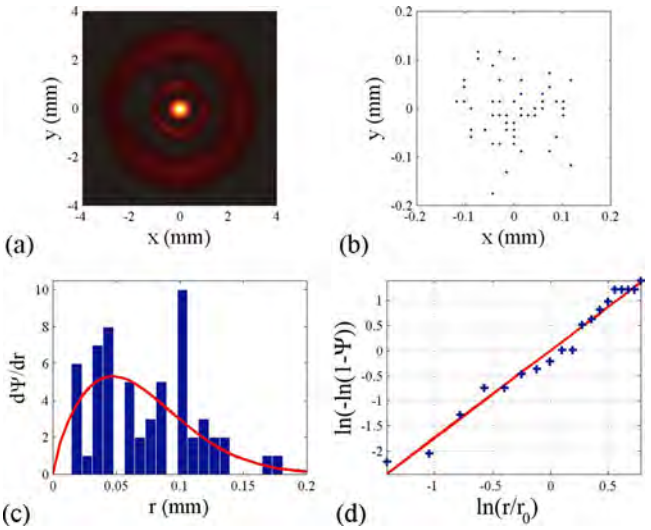

FIG. 14. (Color online) Numerical simulation results presented as in Fig. 4 for 60 shots in case B with the screen at $z=6$ m, very strong turbulence $C_n^2=9\times10^{-10}$ m$^{-2/3}$. The parameters for the Weibull distribution [continuous curve in (c) and (d)] are $p=1.74$ and $w_W=0.077$ mm.

VI. CONCLUSIONS

The influence of air turbulence on the filamentation of ultrashort laser pulses close to one critical power is studied experimentally with a calibrated turbulence chamber reproducing over 2.3 m various atmospherical conditions. The transverse deviation of the filament and its survival rate in the presence of turbulence are accurately measured for different scenarios where the filaments form either in quiet or in turbulent atmosphere. For each case the statistical filament transverse deviation is well-fitted by a Weibull distribution law and the average deviation increases with turbulence. These measurements are well-reproduced by numerical simulations.

Turbulence strongly affects the transverse wandering of filaments even if the average deviation is smaller when the filament is formed in nonturbulent air. When the laser beam undergoes strong turbulence during the initial self-focusing stage as in outdoor experiments, the filamentation rate decreases and a larger filament pointing instability is observed. The decrease of the probability to form a filament in this case

tends to prove that the collapse distance increases in the presence of turbulence. On the contrary, femtosecond filaments generated in air are robust and barely sensitive to turbulence if they are formed in a nonturbulent region. We interpreted the longitudinal wandering of filaments in two different regimes where either modulational instability or self-focusing of the whole beam constitutes the prevailing effect in forming a filament. Self-focusing of the whole beam leads to different scenarios for small powers, strong trubulence, which promotes homogeneous and isotropic filament distributions or for larger powers, weak turbulence, which promotes ring formation and accumulation of filaments on collapsing rings.

ACKNOWLEDGMENT

This work has been partially funded by a DGA grant.

[1] A. Couairon and A. Mysyrowicz, Phys. Rep. **441**, 47 (2007).
[2] G. Méchain, C. D'Amico, Y.-B. André, S. Tzortzakis, M. Franco, B. Prade, A. Mysyrowicz, A. Couairon, E. Salmon, and R. Sauerbrey, Opt. Commun. **247**, 171 (2005).
[3] J. Kasparian, M. Rodriguez, G. Méjean, J. Yu, E. Salmon, H. Wille, R. Bourayou, S. Frey, Y.-B. André, A. Mysyrowicz, R. Sauerbrey, J.-P. Wolf, and L. Wöste, Science **301**, 61 (2003).
[4] A. Houard, C. D'Amico, Y. Liu, Y. B. André, M. Franco, B. Prade, E. Salmon, P. Pierlot, L.-M. Cléon, and A. Mysyrowicz, Appl. Phys. Lett. **90**, 171501 (2007).
[5] C. D'Amico, A. Houard, M. Franco, B. Prade, A. Mysyrowicz, A. Couairon, and V. T. Tikhonchuk, Phys. Rev. Lett. **98**, 235002 (2007).
[6] C. D'Amico, A. Houard, S. Akturk, Y. Liu, J. Le Bloas, M. Franco, B. Prade, A. Couairon, V. T. Tikhonchuk, and A. Mysyrowicz, New J. Phys. **10**, 013015 (2008).
[7] V. E. Zuev, *Laser Beams in the Atmosphere* (Consultants Bureau, New York, 1982).
[8] V. I. Tatarskii, *Wave Propagation in Turbulent Medium* (McGraw-Hill, New York, 1961); *The Effects of the Turbulent Atmosphere on Wave Propagation* (U.S. Departement of Commerce, National Technical Information Service, Springfield, VA, 1971).
[9] J. R. Penano, P. Sprangle, B. Hazafi, A. Ting, D. F. Gordon, and C. A. Kapetanakos, Phys. Plasmas **11**, 2865 (2004).
[10] V. P. Kandidov, O. G. Kosareva, M. P. Tamarov, A. Brodeur, and S. L. Chin, Quantum Electron. **QE-29**, 911 (1999).
[11] V. I. Bespalov and V. I. Talanov, Zh. Eksp. Teor. Fiz. Pis'ma Red. **3**, 471 (1966) [JETP Lett. **3**, 307 (1966)].
[12] A. Couairon, Appl. Phys. B: Lasers Opt. **76**, 789 (2003).
[13] S. Tzortzakis, G. Méchain, G. Patalano, M. A. Franco, B. S. Prade, and A. Mysyrowicz, Appl. Phys. B: Lasers Opt. **76**, 609 (2003).
[14] A. Couairon, G. Méchain, S. Tzortzakis, M. Franco, B. Lamouroux, B. Prade, and A. Mysyrowicz, Opt. Commun. **225**, 177 (2003).
[15] S. L. Chin, A. Talebpour, J. Yang, S. Petit, V. P. Kandidov, O. G. Kosareva, and M. P. Tamarov, Appl. Phys. B: Lasers Opt. **74**, 67 (2002).
[16] R. Ackermann, G. Méjean, J. Kasparian, J. Yu, E. Salmon, and J.-P. Wolf, Opt. Lett. **31**, 86 (2006).
[17] R. Salamé, N. Lascoux, E. Salmon, R. Ackermann, J. Kasparian, and J.-P. Wolf, Appl. Phys. Lett. **91**, 171106 (2007).
[18] M. Mlejnek, M. Kolesik, J. V. Moloney, and E. M. Wright, Phys. Rev. Lett. **83**, 2938 (1999).
[19] M. Kolesik and J. V. Moloney, Opt. Lett. **29**, 590 (2004).
[20] W. Liu, J.-F. Gravel, F. Théberge, A. Becker, and S. L. Chin, Appl. Phys. B: Lasers Opt. **80**, 857 (2005).
[21] A. Dubietis, E. Gaižauskas, G. Tamošauskas, and P. Di Trapani, Phys. Rev. Lett. **92**, 253903 (2004).
[22] D. Faccio, A. Averchi, A. Lotti, P. Di Trapani, A. Couairon, D. Papazoglou, and S. Tzortzakis, Opt. Express **16**, 1565 (2008).
[23] P. Polesana, M. Franco, A. Couairon, D. Faccio, and P. Di Trapani, Phys. Rev. A **77**, 043814 (2008).
[24] V. A. Petrishchev, Izv. Vyssh. Uchebn. Zaved., Radiofiz. **14**, 1416 (1971).
[25] M. Billard, G. Fertin, and J. C. Fontanella, *Atmospheric Turbulence Simulation Cell for Optical Propagation Experiment*, 4th International Symposium on Gas Flow and Chemical Lasers, Stresa (Italy), 1982 (unpublished).
[26] S. S. R. Murty and W. Bilbro, Atmospheric Effects on CO_2, Laser Propagation, NASA Technical Paper 1357, 1978 (unpublished).
[27] R. R. Beland, in *IR/EO Systems Handbook*, edited by F. G. Smith (SPIE Optical Engineering Press, Ann Arbor, 1993), Vol. 2, pp 157–232.
[28] A. Couairon, Phys. Rev. A **68**, 015801 (2003).
[29] J. M. Martin and S. M. Flatte, Appl. Opt. **27**, 2111 (1988).
[30] A. Couairon, S. Tzortzakis, L. Bergé, M. Franco, B. Prade, and A. Mysyrowicz, J. Opt. Soc. Am. B **19**, 1117 (2002).
[31] G. Méchain, A. Couairon, M. Franco, B. Prade, and A. Mysyrowicz, Phys. Rev. Lett. **93**, 035003 (2004).
[32] G. Méchain, A. Couairon, Y.-B. André, C. D'Amico, M. Franco, B. Prade, S. Tzortzakis, A. Mysyrowicz, and R. Sauerbrey, Appl. Phys. B: Lasers Opt. **79**, 379 (2004).
[33] G. Fibich, N. Gavish, and X.-P. Wang, Physica D **211**, 193 (2005).
[34] T. D. Grow, A. A. Ishaaya, L. T. Vuong, A. L. Gaeta, N. Gavish, and G. Fibich, Opt. Express **14**, 5468 (2006).
[35] G. Fibich, S. Eisenmann, B. Ilan, Y. Erlich, M. Fraenkel, Z. Henis, A. L. Gaeta, and A. Zigler, Opt. Express **13**, 5897 (2005).
[36] J. H. Marburger, Prog. Quantum Electron. **4**, 35–110 (1975).
[37] M. A. Porras, A. Parola, D. Faccio, A. Couairon, and P. Di Trapani, Phys. Rev. A **76**, 011803(R) (2007).
[38] D. Faccio, M. Clerici, A. Averchi, O. Jedrkiewicz, S. Tzortzakis, D. G. Papazoglou, F. Bragheri, L. Tartara, A. Trita, S. Henin, I. Critiani, A. Couairon, and P. Di Trapani, Opt. Express **16**, 8213 (2008).

Coherent combining efficiency assessment for few-mode fibers with higher-order mode content

Baya Bennai[1], Pierre Bourdon[1], Véronique Jolivet[1], Laurent Lombard[1],
Guillaume Canat[1], Olivier Vasseur[1] and Yves Jaouën[2]
[1]ONERA/DOTA Chemin de la Hunière 91761 Palaiseau Cedex France
[2]Institut TELECOM Télécom ParisTech 46 rue Barrault 75634 Paris Cedex France
E mail: baya.bennai@onera.fr

***Abstract*— We study coherent combining of few-mode fibers. Experimental and numerical efficiency assessment reveals how coherent combining can be impaired when transverse mode content in a fiber differs significantly from the single-mode case.**

I. INTRODUCTION

Coherent combining of fiber lasers is one of the most promising ways to overcome delivered power limits such as thermal load, nonlinear effects in the laser medium and damage threshold of optical components. In the last few years, combined power has not ceased growing: up to 745 W were obtained for coherently combined fiber array [1], and more than 100 kW has been achieved combining slab lasers [2]. Increasing delivered power can result from either growing number of fibers or scaling power of the laser sources. The last solution is commonly achieved using large mode area (LMA) fibers. Larger core diameter in those fibers results in enhancement of the damage and nonlinear effects power thresholds, and therefore in delivery of higher power. However, most LMA fibers can simultaneously support several transverse modes. Note that it is not always possible to suppress the contribution of high-order modes, especially in the case of Er^{3+}/Yb^{3+} doped fibers due to their high numerical aperture. Besides it has been shown that good beam quality does not guarantee low high-order mode content [3]. In reference [4], we presented a numerical model of coherent combining of single-mode as well as few-mode fibers. The efficiency of coherent combining can be impaired by different parameters such as fiber array geometrical configuration, beam quality of the primary lasers, near-field fill-factor and combining residual phase error. In case of few-mode fibers, coherent combining performances also depend on two other parameters: i) the transverse-mode mixture ratio (i.e. the modal content of the fiber); ii) the phase relationship between the transverse modes in a single fiber. In reference [4], we demonstrated numerically the potentially dramatic impact of the latter on coherent combining efficiency.

In this paper, we investigate more thoroughly how high-order mode content can impair coherent combining efficiency. For that purpose, we developed an experimental setup to measure the residual phase error when combining two different fibers: the first one is a single-mode fiber, and the other one is a few-mode fiber. Various configurations of high-order mode content have been tested. The experimental results are then compared and completed with numerical modelling.

II. EXPERIMENTAL SETUP AND RESULTS

The experimental setup of beam combining is shown in Figure 1. Phase difference measurement is performed in the electrical domain, using the frequency-tagging technique first introduced for fiber array combining by Shay et al. [5]. The master oscillator delivers a few tens of milliwatts at 1.55 µm. It is split into two paths. One is composed of a single-mode fiber and contains an electro-optic modulator applying both the piston difference compensation control and the tagging modulation. The other path is composed of the fiber under test that can be either a standard single-mode fiber -configuration (a)- or a few-mode fiber -configurations (b) and (c). The beams are mixed using a partially reflecting plate, and overlap in free-space. The interference signal is detected using a photoreceiver. A control feedback loop applies the proper command on the electro-optic modulator to maintain the two beams in phase. A leakage part of the beams is reflected by a beam splitter and detected on a CCD camera to capture frames of the far-field interference pattern and visualize the fringe pattern stability.

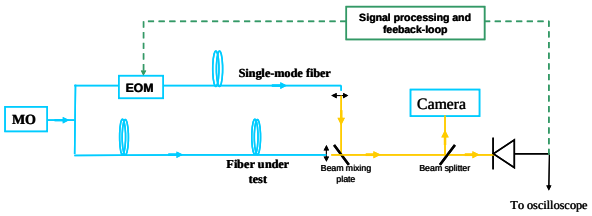

Figure 1. Experimental setup of coherent combining. MO: Master Oscillator, EOM: electro-optic modulator

We use a few-mode fiber with 25 µm core diameter that allows guidance of up to four LP transverse modes. We studied two different configurations. The first one, configuration (b), is obtained when the coupling of the master oscillator beam into the few-mode fiber is optimized through perfect splicing. We assessed that, in this case, more than 80% of the power is coupled in the fundamental LP_{01} mode. The second configuration, configuration (c), is obtained when voluntarily splicing off-center to result in weakened coupling of the MO in the fundamental mode of the few-mode fiber. In

978-1-4244-3681-1/09/$25.00 ©2009 IEEE

this configuration, we assessed that only 60% to 70% of the power was coupled in the fundamental mode. Note that no coiling has been applied to dampen the high-order modes.

The far-field fringe patterns for the different test fibers are shown in Figure 2. In all cases, the beams interfere constructively when the active phase control loop is on. The fringe patterns are stable in position and intensity for both configurations (a) and (b). For configuration (c), although the interference is constructive, we can notice a slow jitter on the position of the fringe patterns.

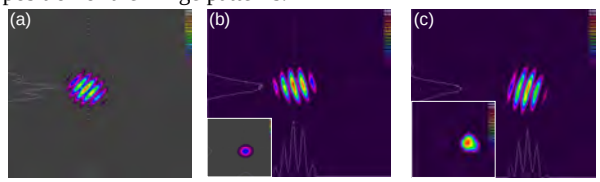

Figure 2. Far-field fringe patterns of a two fibers combining with phase control loop on. The fiber under test is (a) a single-mode fiber, (b) a few-mode fiber mainly containing fundamental mode, and (c) a few-mode fiber with strong high-order mode content. In (b) and (c) the output of the few-mode fiber is shown in inset.

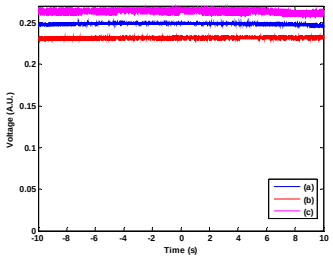

Figure 3. Interference electric signal measured by the photoreceiver.The fiber under test is (a) a single-mode fiber, (b) a few-mode fiber mainly containing fundamental mode, and (c) a few-mode fiber with strong high-order mode content.

To assess the coherent combining efficiency, we measured the residual phase error for the three configurations. As detailed in reference [4], the residual phase error rms value is derived from the electric interference signal presented in Figure 3. . In both configurations (a) and (b), the measured rms values are equal to of ~λ/50, limited by the sensitivity of the phase difference measurement loop. In configuration (c), the measured residual phase error is lower, ~λ/40, and slightly fluctuates in time. Then, we induced thermal gradients in the few-mode fiber by heating it up. We did not notice any disturbance in configurations (a) and (b). Whereas, in configuration (c), the residual phase error could be decreased to ~λ/25 by those thermal disturbances. As the piston phase difference between the fibers is still compensated by the feedback loop, combining is still performed but with a reduced efficiency.

III. NUMERICAL SIMULATIONS

We used the numerical model presented in reference [4] to analyze the former experimental results. The modal content of the few-mode fiber is assumed to be 90% LP_{01} and 10% LP_{11} for configuration (b), and 70% LP_{01} and 30% LP_{11} for configuration (c). As shown in Figure 4. (A), the presence of high-order modes breaks the central symmetry of the fringe pattern, as can also be seen in Figure 2. . Due to stronger side lobes, the power fraction contained in the central lobe, which is 41% in configuration (a), falls to 34% in configuration (c). It also results in a Strehl-ratio decrease from 28% in configuration (a) to 12% in configuration (c). Figure 4. (B) demonstrates the impact of a non-zero phase difference between modes in configuration (c). The higher the phase difference, the more the fringe pattern is shifted off-center. This can explain the pattern jitter and increased residual phase error rms value observed in configuration (c).

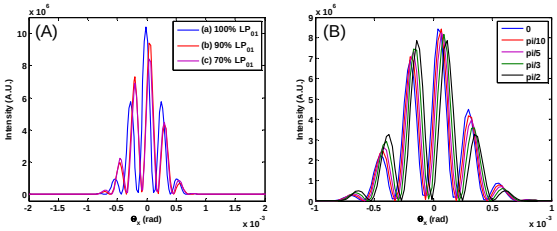

Figure 4. Far-field intensity profiles modelling of two fiber coherent combining. (A) for various modal contents; (B) for various phase differences between LP_{01} and LP_{11} in the few-mode fiber, in configuration (c).

IV. CONCLUSION

We performed coherent combining of a single-mode fiber with various few-mode fiber modal contents. With mainly fundamental modal content, coherent combining appears to operate as efficiently as for a single-mode fiber. As when high-order mode power fraction increases, coherent combining is still performed but with reduced efficiency. According to numerical results, this could be explained by the fluctuation of the phase relationship between the transverse modes supported by the fiber. Future work will include active fibers and more complex transverse mode mixture.

REFERENCES

[1] T.M. Shay, J.T. Baker, A.D. Sanchez, C.A. Robin, C.L. Vergien, C. Zerinque, D. Gallant, C.A. Lu, B. Putford, T.J. Bronder , and A. Lucero, "High power phase loching of a fiber amplifier array," Proc. SPIE, **7195**, 71951M, 2009

[2] S.J. McNaught, "100 kW coherently combined slab MOPAs," Conference on Laser & Electro Optics, paper CThA1, Baltimore, 31-5 June, 2009

[3] S. Wielandy, "Implications of high-order mode content in large mode area fibers with good beam quality," Opt. Ex. Vol. **15**, no. 23, pp. 15402-15409, 2007

[4] V. Jolivet, P. Bourdon, B. Bennaï, L. Lombard, D. Goular, E. Pourtal, G. Canat, Y. Jaouën, B. Moreau and O. Vasseur, "Beam shaping of single-mode and multimode fiber amplifier arrays for propagation through atmospheric turbulence," IEEE J. Sel. Top. Quantum Electron., vol. **15**, no.2, pp. 257-268, 2009

[5] T.M. Shay, V. Benham, J.T. Baker, A.D. Sanchez, D. Pilkington and C.A. Lu, "Self-synchronous and self-referenced coherent beam combination for large optical array," IEEE J. Sel. Top. Quantum Electron., vol. **13**, no. 3, pp. 480-486, 2007

Journal of the European Optical Society - Rapid Publications 5, 10052 (2010) www.jeos.org

A Gaussian transition of an optical speckle field studied by the minimal spanning tree method

Olivier Vasseur ONERA, Theoretical and Applied Optics Department, 91120 Palaiseau, France
olivier.vasseur@onera.fr
Isabelle Bergoënd ONERA, Theoretical and Applied Optics Department, 31055 Toulouse, France
Xavier Orlik ONERA, Theoretical and Applied Optics Department, 31055 Toulouse, France

We propose to study the Gaussian transition of an optical speckle field using the Minimal Spanning Tree method. We perform an analysis of the spatial intensity distribution and show that the maxima of intensity evolve from a cluster distribution in the strongly non Gaussian regime, to a gradient distribution around the transition and then approach the random distribution area when we tend to the Gaussian regime. In the generated minimal spanning trees, we observe that the standard deviation of the edges length exhibits a maximum around the Gaussian transition when about 4 correlation cells of the surface roughness are illuminated. [DOI: 10.2971/jeos.2010.10052]

Keywords: speckle, surface roughness, Gaussian transition, minimal spanning tree, statistical optics

1 INTRODUCTION

An optical speckle field [1] generated by the scattering from a rough surface can contain useful informations about the surface properties especially in the case the incident beam illuminates only a few correlation cells of the surface roughness [2, 3]. However, working with a unique illuminating spot size in such a non Gaussian regime doesn't allow a full characterization of the surface roughness properties. Nevertheless, as it seems to be general in Physics, following a parameter along a transition brings much more information that an observation of the same parameter at a unique point of this transition. Thus, we have recently proposed the idea of studying the transition from the non Gaussian to the Gaussian regime of the speckle field in order to increase the amount of accessible information concerning the surface roughness [4]. Using a Gaussian correlated dephasing screen to modelize the surface roughness, we have shown that, by following such transition generated by a varying illuminating spot size, the speckle contrast was sufficient to discriminate between roughness values in the full range $[0;\lambda]$, λ being the wavelength of the monochromatic illuminating laser. On a practical point of view, such method based on the Gaussian transition study is expected to improve absolute surface roughness and correlation length measurements by speckle analysis [5]–[7].

The probability density function of intensity is helpful to characterize an optical speckle field, however it doesn't contain any information about the spatial distribution of the field. In this paper, we use a new sensitive criterion to characterize this spatial intensity distribution. Our approach is based on a specific graph constructed from the set of points of the local maxima of the intensity distributions in an observation plane. This graph, called Minimal Spanning Tree (MST) [8], allows us to deduce two parameters - the mean and the standard deviation of the edges length - that characterize the distributions of the points (ordered, random, cluster...). We present here the first results of speckle fields characterization obtained by the MST method and we apply it to the study of a Gaussian transition.

2 GENERATION OF NON GAUSSIAN SPECKLE FIELDS

The model consists first in the generation of a random rough surface modelized by a random correlated Gaussian phase screen that exhibits a Gaussian heights distribution. Then, in the case of a Gaussian beam illumination, we calculate the corresponding scattered field at a given distance using the Fresnel diffraction integral [9]. This model has been previously used for the study of the circular Gaussian transition of speckle fields in the near field region [4]. We just propose in this section a brief restatement of the main points.

The discretized and correlated profiles of the surfaces roughness are calculated by the following equation [10] :

$$\mathcal{S}(\xi,\eta) = FT^{-1}\left[\sqrt{FT[\mathcal{A}(\xi,\eta)]}.FT[X(\xi,\eta)]\right], \qquad (1)$$

where :

$$\mathcal{A}(\xi,\eta) = H_{RMS}^2 \exp\left[-\frac{\xi^2+\eta^2}{L_c^2}\right], \qquad (2)$$

with :

- H_{RMS} the standard deviation of the surface heights distribution that will be simply referred as "roughness" in the forthcoming sections

Received July 23, 2010; published September 23, 2010 ISSN 1990-2573

- L_c the correlation length of the surface heights distribution
- $X(\xi,\eta)$ an uncorrelated Gaussian random function with zero mean and standard deviation of unity.

FT denotes here a discrete bidimensional Fourier Transform.

The incident field characterized by a Gaussian amplitude distribution and a wavelength $\lambda = 632$ nm impacts the surface parallel to its normal. Its waist ω_0 is chosen to be located on the mean level of the surface. The scalar field undergoes the dephasing associated to the random correlated Gaussian surface and the scattered field at the distance z in the transverse plane (x,y) is then calculated using the Fresnel diffraction integral :

$$\tilde{E}_{sc}(x,y,z) = \iint_{\mathcal{S}} \tilde{E}(\xi,\eta).\tilde{\mathcal{G}}(x-\xi,y-\eta,z)d\xi d\eta, \qquad (3)$$

with $\tilde{\mathcal{G}}$ the propagator in the paraxial approximation :

$$\tilde{\mathcal{G}}(x-\xi,y-\eta,z) = \frac{e^{ikz}}{i\lambda z}\exp\left[\frac{ik}{2z}\left((x-\xi)^2+(y-\eta)^2\right)\right], \qquad (4)$$

and $\tilde{E}(\xi,\eta)$ the initial Gaussian beam of maximum amplitude unity that has been dephased according to the correlated surface profile $\mathcal{S}(\xi,\eta)$:

$$\tilde{E}(\xi,\eta) = \exp\left[-\frac{\xi^2+\eta^2}{\omega_0^2}\right].\exp\left[ik\mathcal{S}(\xi,\eta)\right]. \qquad (5)$$

The paraxial propagation of the scattered field is performed using the following Fourier Transforms :

$$\tilde{E}_{sc}(x,y,z) = FT^{-1}\left[FT[\tilde{E}(\xi,\eta)].FT[\tilde{\mathcal{G}}(x-\xi,y-\eta,z)]\right]. \qquad (6)$$

This calculation allows the determination of the complex scattered speckle field and its statistics even in the non Gaussian regime where the central limit theorem can't be applied [4].

3 DESCRIPTION OF THE MINIMAL SPANNING TREE METHOD

An edge-weighted linear graph $G = (X,E)$ is composed of a set of points $X = \{x_1, x_2, \ldots\}$ called nodes and a set of node pairs $E = \{(x_i,x_j)\}$ called edges, with a number called weight (the Euclidean distance in our case) assigned to each edge. A tree is a connected graph without closed loops. A Minimal Spanning Tree (MST) is a tree which contains all the nodes with a minimal sum of the edge weights [8]. It can be noticed that for a set of N points (corresponding to a number of edges of $N-1$) which are randomly distributed with uniform intensity in a 2-dimensional region with an area of A, the total length of the MST is asymptotically given by $L_{G\infty} = \alpha_2(AN)^{1/2}$ where α_2 depends on the problem solved [11]. So the mean length of an edge is given by:

$$M_A = \alpha_2\frac{(AN)^{1/2}}{N-1}. \qquad (7)$$

The area A of the sampling window of a data set can be estimated by a normalization of the area H of the convex hull of the data by the following relation:

$$A = \frac{H}{1-(f/N)}. \qquad (8)$$

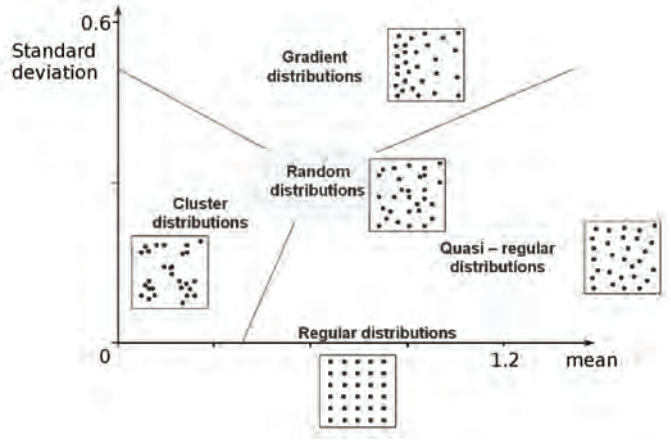

FIG. 1 Points distributions in the (m,σ) plane. Random distributions are built by the use of probability density functions of the continuous uniform distribution to generate the coordinates of the points.

where f is the number of faces of the convex hull [12].

In our study, the convex hull is the smallest square containing all the points. Depending on the starting point there may be more than one MST for a given set of points, but all of the MST's have the same length-edge histogram. The normalized values of the mean m and the standard deviation σ of the edges length can be used to characterize the distribution of points (ordered, random, cluster...) [13]. In the field of topographical analysis, this method presents the advantages of an high discrimination power and stability to characterize spatial point patterns [14]. In the (m,σ) plane, all distribution of points can be plotted and easily compared with well-characterized distributions (for example, perfectly ordered with $\sigma = 0$ or random ones with $m \approx 0.65$ and $\sigma \approx 0.30$) as shown in Figure 1.

4 STUDY OF THE GAUSSIAN TRANSITION BY THE MINIMAL SPANNING TREE METHODS

For a given set of roughness value H_{RMS} and numbers n_c of correlation cells illuminated by a Gaussian beam, we generate, as described in Section 2, 10 random surfaces and the corresponding 10 intensity distributions of the field in the observation plane at the distance $0,75z_R$ from the surface, z_R being the Rayleigh distance. From each intensity distribution, we detect the set of all the points representing a local maximum of the intensity distribution above a threshold. The MST is built on this set of points and provides the location of the spatial intensity maxima distribution in the (m,σ) plane. Figure 2 presents the process along the Gaussian transition of a completely developed speckle ($H_{RMS} = \lambda$), for intensity distributions obtained in the case of the following n_c values : 0.5, 2 and 50.

The windows of analysis has been defined in 2 different ways. When the same square sampling window is used to build the MST's of all the intensity images in the Gaussian transition, the influence of the extension of the speckle in the observation plane is taken into account. When the area of the window is estimated by the normalization of the convex hull of the

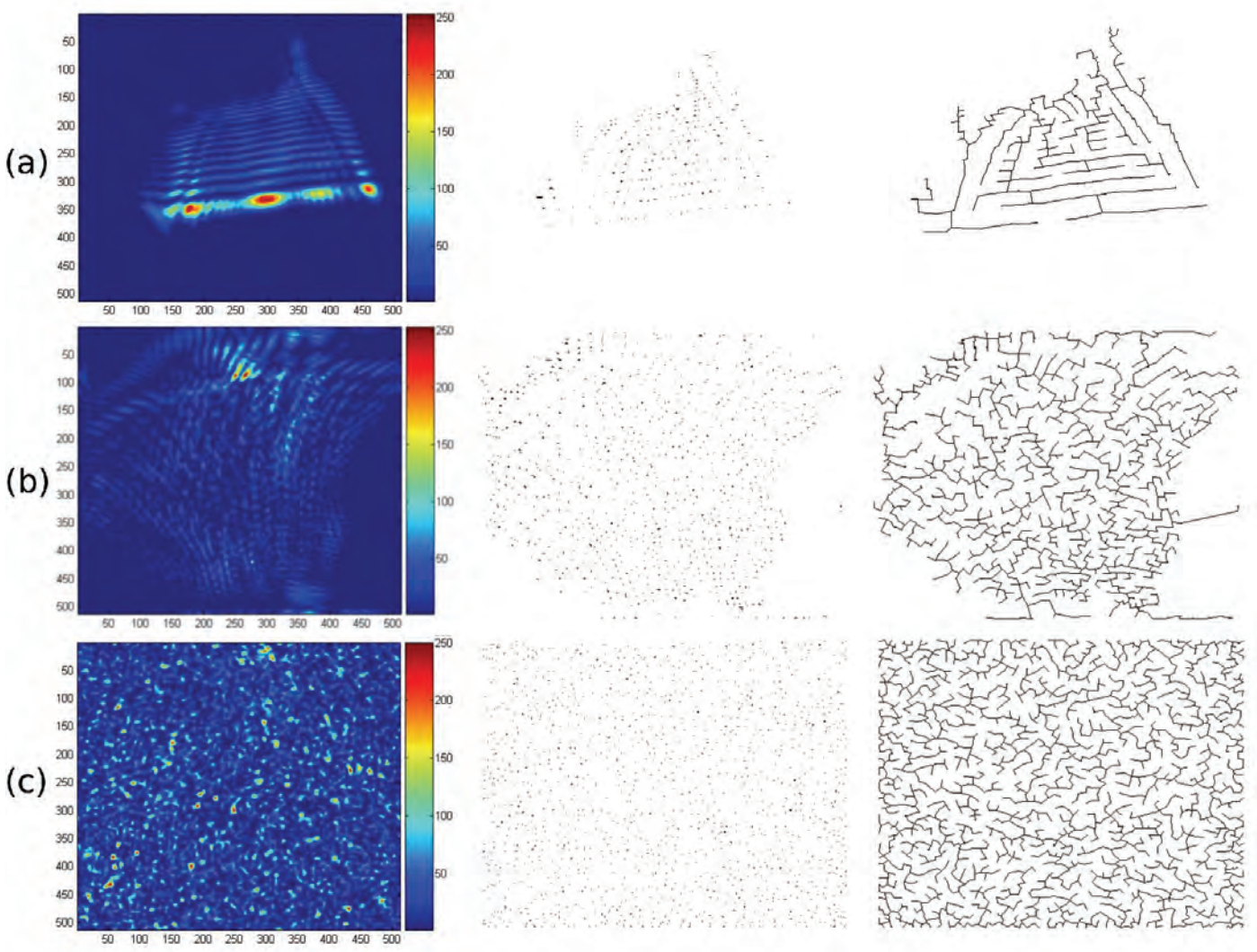

FIG. 2 Process analysis of the spatial intensity distribution by the MST. (a) (b) and (c) correspond respectively to $n_c = 0.5$, 2 and 50 illuminated correlation cells of the surface roughness. The 3 columns display from left to right : the intensity distribution in the observation plane, the points of local maxima and the corresponding MST.

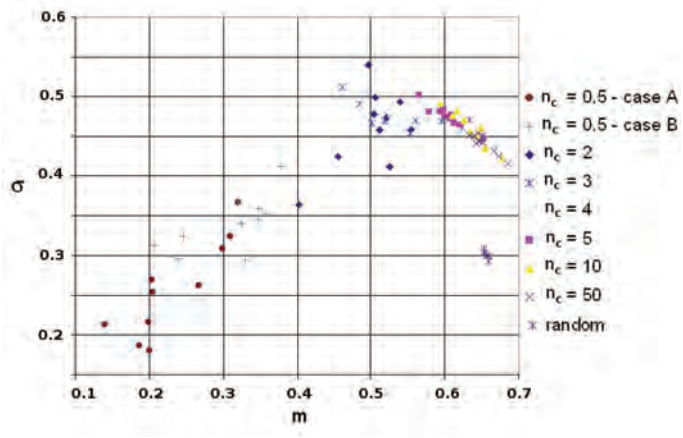

FIG. 3 Representation of the average m and standard deviation σ of MST's edges built on maxima intensity distributions in the Gaussian transition of a speckle field. n_c corresponds to the number of illuminated correlation cells of the surface roughness. In case A, the same square windows of analysis is used whereas in case B, different normalized square windows are used for an intrinsic analysis. We observe a maximum of σ around the Gaussian transition.

data, we obtain an intrinsic analysis of the spatial distribution of points. The results obtained along the Gaussian transition in both cases are presented on Figure 3. All values of $n_c > 0.5$ give the same result in the (m, σ) plane regardless of the definition of the window of analysis. For the case $n_c = 0.5$, when the sampling window is kept constant, the values of the mean length and of the standard deviation obtained (Figure 3, case A) are significantly lower than those calculated using the sampling window estimated by the normalization of the convex hull of the data (Figure 3, case B). This is due to the fact that the set of points of maximum intensity does not reach the border of the analysis window because of the highly non Gaussian illumination conditions giving rise to a more localized repartition of energy. Along the Gaussian transition, we can observe the evolution of the location in the (m, σ) plane due to the increased number of illuminated correlation cells. In the strongly non Gaussian regime and according to the intrinsic quantitative analysis (Figure 3 for $n_c = 0.5$, case B), we observe that the spatial distribution of the maxima of intensity corresponds to the cluster distribution area. When n_c increases (until few units) and reaches the Gaussian transition, the values of m and σ increase to the gradient distribution area. For higher and increasing values of n_c, the location slowly tends

to the random distribution area ($m \approx 0.65$ and $\sigma \approx 0.30$). We point out that the σ value exhibits a clear maximum ($n_c \approx 4$) around the Gaussian transition.

5 CONCLUSION

We have proposed the first results of speckle fields characterization obtained by the use of the Minimal Spanning Tree method. The introduction of a criterion, namely the location in the (m,σ) plane that corresponds to maximum intensity regions, have been used to perform a spatial intensity distribution analysis along the Gaussian transition of an optical speckle field. When we evolve from a strongly non Gaussian regime to the Gaussian one, this location evolves from a cluster distribution to a gradient distribution and then approaches a random distribution. Moreover, the MST method exhibits a maximum of the standard deviation of the edges length around the Gaussian transition when about 4 correlation cells of the surface roughness are illuminated. Both results provide a new and robust way to characterize the correlation length of a surface roughness and its illumination conditions. This method can find further applications such as the study of non circular speckle fields and the spatial distribution of phase singularities in the Gaussian transition. In a more general way, it can improve rough surface or multiple scattering media characterization by speckle field analysis.

References

[1] J. W. Goodman, *Speckle phenomena in optics, theory and applications* (Roberts and Company, Colorado, 2006).

[2] H. Fujii, "Contrast variation of non-Gaussian speckle" Opt. Act. **27**, 409–418 (1980).

[3] M. Deka, S. P. Almeida, and H. Fujii, "Root-mean-square difference between the intensities of non-Gaussian speckle at two different wavelengths" J. Opt. Soc. Am. **71**, 155–163 (1981).

[4] I. Bergoënd, X. Orlik, and E. Lacot, "Study of a circular Gaussian transition in an optical speckle field" J. Europ. Opt. Soc. Rap. Public. **3**, 08028 (2008).

[5] H. Kadano, T. Asakura, and N. Takai, "Roughness and correlation length determination of rough-surface objects using speckle contrast" Appl. Phys. B **44**, 167–173 (1987).

[6] H. Kadano, T. Asakura, and N. Takai, "Roughness and correlation length measurements of rough-surface objects using the speckle contrast in the diffraction field" Optik **80**, 115–120 (1988).

[7] C. Cheng, C. Liu, N. Zhang, T. Jia, R. Li, and Z. Xu, "Absolute measurement of roughness and lateral-correlation length of random surfaces by use of the simplified model of image-speckle contrast" Appl. Opt. **41**, 4148 (2002).

[8] C. Zhan, "Graph-theoretical methods for detecting and describing gestalt clusters" IEEE T. Comput. **C-20**, 68–86 (1971).

[9] R. Grella, "Fresnel propagation and diffraction and paraxial wave equation" J. Opt. **13**, 367–374 (1982).

[10] A. K. Fung, and M. F. Chen, "Numerical simulation of scattering from simple and composite random surfaces" J. Opt. Soc. Am. A **2**, 2274–2284 (1985).

[11] J. Beardwood, J. Halton, and J. Hammersley, "The shortest path through many points" P. Camb. Philos. Soc. **55**, 299–327 (1959).

[12] R. Hoffman, and A. Jain, "A test of randomness based on the minimal spanning tree" Pattern Recogn. Lett. **1**, 175–180 (1983).

[13] C. Dussert, G. Rasigni, M. Rasigni, and J. Palmari, "Minimal spanning tree: A new approach for studying order and disorder" Phys. Rev. B **34**, 3528–3531 (1986).

[14] F. Wallet, and C. Dussert, "Comparison of spatial point patterns and processes characterization methods" Europhys. Lett. **42**, 493–498 (1998).

The Minimum Spanning Tree method applied to the study of optical speckle fields: spatial characterization of a Gaussian transition and its phase singularities.

Olivier Vasseur*[a], Isabelle Bergoënd[b], Debajyoti Upadhyay[b], Xavier Orlik[b]
[a]Onera – The French Aerospace Lab., F-91761 Palaiseau, France
[b]Onera – The French Aerospace Lab., F-31055 Toulouse, France

ABSTRACT

The optical speckle field generated by the scattering of a laser beam on a rough surface contains useful information about the surface properties especially in the case of the incident beam illuminates only a few correlation cells of the surface roughness. The study of the transition from the non Gaussian to the Gaussian regime of the speckle field can increase the amount of accessible information concerning the surface roughness. The probability density function of intensity is helpful to characterize an optical speckle field, but we do not obtain information about the qualification of spatial distribution of the field. To qualify this spatial intensity distribution, we propose to use the Minimum Spanning Tree methodology. From the tree constructed from the set of points of the local maxima of the intensity distributions in an observation plane, we determine the mean and the standard deviation of the edges length of the tree and we qualify the distributions of this points (ordered, cluster, random…).

Using high resolution images, we will present the first results concerning the study of a Gaussian transition of a speckle field by the Minimum Spanning Tree method and some preliminary results about the study of the spatial distribution of phase singularities in this transition.

At the end, we will highlight that this new approach appears to be a very robust way to characterize the correlation length of a surface roughness and its illumination conditions, and offers a new criterion to study the optical speckle field.

Keywords: Speckle, Surface roughness, Gaussian transition, Minimal spanning tree, Minimum spanning tree, Statistical optics, Spatial statistics, Spatial pattern, Point patterns.

1. INTRODUCTION

Following the Gaussian transition of a speckle field [1] using a varying illumination spot size represents a promising method to characterize rough surfaces [2]. Especially, we have shown that, using a Gaussian correlated dephasing screen to modelize the surface roughness, the evolution of the speckle contrast in this statistical transition was sufficient to discriminate between roughness values in the full range [0; λ], λ being the wavelength of the monochromatic illuminating laser. On a practical point of view, such method based on the Gaussian transition study is simple, low cost, non destructive and expected to improve absolute surface roughness and correlation length measurements by speckle analysis [3]-[5]. The probability density function of intensity is helpful to characterize an optical speckle field, however it does not contain any information about the spatial distribution of the field. In a previous paper, we have proposed the use of a sensitive criterion to characterize this spatial intensity distribution [6]. Our approach is based on a specific graph constructed from the set of points of the local maxima and minima of the intensity distributions in an observation plane. This graph, called Minimal Spanning Tree (MST) [7], allows us to deduce two parameters - the mean and the standard deviation of the edges length - that characterize the distributions of the points (ordered, random, cluster...). Using this new methodology applied to the study of the Gaussian transition of a speckle field, we have demonstrated that the spatial distribution of intensity was varying from cluster to gradient and then to a random distribution when we evolved from strongly non Gaussian statistics to Gaussian ones [6]. We present results of speckle fields characterization obtained by the MST method and we apply it to the study of the Gaussian transition and its phase singularities with high resolution 32-bits images.

*olivier.vasseur@onera.fr; phone 33 1 80 38 63 53; fax 33 1 80 38 63 45; onera.fr

Physical Optics, edited by Daniel G. Smith, Frank Wyrowski, Andreas Erdmann,
Proc. of SPIE Vol. 8171, 81710B · © 2011 SPIE · CCC code: 0277-786X/11/$18
doi: 10.1117/12.896569

2. GENERATION OF NON GAUSSIAN SPECKLE FIELDS

The model consists first in the generation of a random rough surface modelized by a random correlated Gaussian phasescreen that exhibits a Gaussian heights distribution. Then, in the case of a Gaussian beam illumination, we calculate the corresponding scattered field at a given distance using the Fresnel diffraction integral [8]. This model was previously used for the study of the circular Gaussian transition of speckle fields in the near field region [2]. We just propose in this section a brief restatement of the main points. The discretized and correlated profiles of the surfaces roughness are calculated by the following equation [9]:

$$S(\xi,\eta) = FT^{-1}\left[\sqrt{FT[A(\xi,\eta)]}.FT[X(\xi,\eta)]\right],$$

where :

$$A(\xi,\eta) = H_{RMS}^2.\exp\left[-\frac{\xi^2+\eta^2}{L_c^2}\right],$$

with :

- HRMS the standard deviation of the surface heights distribution that will be simply referred as ”roughness” in the forthcoming sections
- L_c the correlation length of the surface heights distribution
- X(ξ, η) an uncorrelated Gaussian random function with zero mean and standard deviation of unity.

FT denotes here a discrete bidimensional Fourier Transform.

The incident field characterized by a Gaussian amplitude distribution and a wavelength λ = 632 nm impacts the surface parallel to its normal. Its waist ω_0 is chosen to be located on the mean level of the surface. The scalar field undergoes the dephasing associated to the random correlated Gaussian surface and the scattered field at the distance z in the transverse plane (x,y) is then calculated using the Fresnel diffraction integral :

$$\tilde{E}_{sc}(x,y,z) = \iint_S \tilde{E}(\xi,\eta).\tilde{G}(x-\xi,y-\eta,z)d\xi d\eta\,,$$

with $\tilde{G}$ the propagator in the paraxial approximation :

$$\tilde{G}(x-\xi,y-\eta,z) = \frac{\exp(ikz)}{i\lambda z}.\exp\left[\frac{ik}{2z}\left((x-\xi)^2+(y-\eta)^2\right)\right],$$

and $\tilde{E}(\xi,\eta)$ the initial Gaussian beam of maximum amplitude unity that has been dephased according to the correlated surface profile $S(\zeta,\eta)$:

$$\tilde{E}(\xi,\eta) = \exp\left[-\frac{\eta^2+\xi^2}{\omega_o^2}\right].\exp[ikS(\xi,\eta)]\cdot$$

The paraxial propagation of the scattered field is performed using the following Fourier Transforms :

$$\tilde{E}_{sc}(x,y,z) = FT^{-1}\left[FT[\tilde{E}(\xi,\eta)].FT[\tilde{G}(x-\xi,y-\eta,z)]\right].$$

This calculation allows the determination of the complex scattered speckle field and its statistics even in the non Gaussian regime where the central limit theorem can not be applied [2].

3. DESCRIPTION OF THE MINIMAL SPANNING TREE METHOD

Consider a set of N points which are randomly distributed in a d-dimensional region with a volume of V. An edge-weighted linear graph G = (X,E) is composed of a set of points X = {x1, x2, . . .xN} called nodes and a set of node pairs E = {(xi, xj)} called edges, with a number called weight (the Euclidean distance in our case) assigned to each edge. A graph is connected if there is a path connecting every pair of nodes and a tree is a connected graph without closed loops. A Minimal Spanning Tree (MST) is a tree which contains all the nodes with a minimal sum of the edge weights [7]. It can be noticed that for a set of N points (corresponding to a number of edges of N-1) which are randomly distributed 2-dimensional region, the total length of the MST is asymptotically given by $L_{G_\infty} = \alpha_2 (AN)^{1/2}$ where α_2 depends on the problem solved [10]. So the mean length of an edge is given by:

$$M = \alpha_2 \frac{(AN)^{1/2}}{N-1} \qquad (1)$$

The area *A* of the sampling window of a data set can be estimated by a normalization of the area *H* of the convex hull of the data by the following relation:

$$A = \frac{H}{1-(f/N)} \qquad (2)$$

where *f* is the number of faces of the convex hull [11]. In our study, the convex hull is the smallest square containing all the points.

The normalized values of m and σ of the MST (mean m and the standard deviation σ of the edge length) constructed from a given set of data in our case are obtained by dividing the original lengths by the following expression [11]:

$$\frac{N^{1/2}}{N-1} \qquad (3)$$

In Prim's algorithm [12], the MST is grown from a single node by adding the closest node to current tree at each stage along with the edge corresponding to that closest distance. Depending on the starting point there may be more than one MST for a given set of points, but all of the MST's have the same length-edge histogram [7], [13]. The normalized values of the mean m and the standard deviation σ of the edge length can be used to characterize the distribution of points (ordered, random, cluster...) [13] as shown on the Figure 1. In the field of topographical analysis, this method presents the advantages of a high discrimination power and stability to characterize spatial point patterns [14], [15]. In

the (m, σ) plane, all distribution of points can be plotted and easily compared with well characterized distributions (for example, perfectly ordered with σ = 0 or random ones with m ~ 0.65 and σ ~ 0.30).

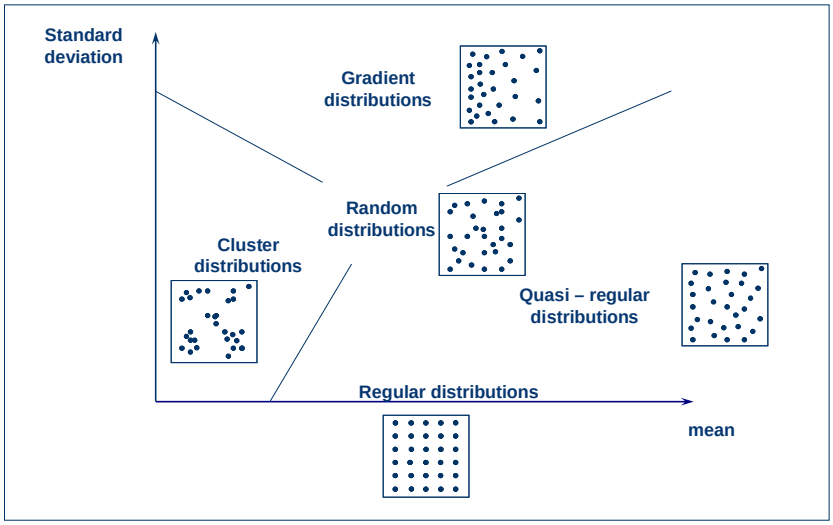

Fig. 1: Points distributions in the (m, σ) plane. Random distributions are built by the use of probability density functions of the continuous uniform distribution to generate the coordinates of the points.

4. ANALYSIS OF THE GAUSSIAN TRANSITION BY THE MINIMAL SPANNING TREE

The first published results [6] obtained by the construction of a MST on intensity maxima pointed out the possibility to study the Gaussian transitions of speckle fields with 8-bits images using varying numbers of correlation cells of the surface roughness illuminated and assessed the influence of the area of square windows. In this study, the window area is the convex hull which contains all the points. We present here the first results obtained with high spatial resolution of the speckle and 32-bits images on one hand and the first results concerning the phase singularities of the Gaussian transition on the other hand.

4.1 Characterization of the speckle by intensity maxima

For a given set of roughness value H_{RMS} and numbers n_c of correlation cells illuminated by a Gaussian beam, we generate, as described in Section 2, 3 random surfaces and the corresponding 3 intensity distributions of the field in the observation plane at the distance 0, $75z_R$ from the surface, z_R being the Rayleigh distance. From each intensity distribution, we detect the set of all the points representing a local maximum of the intensity distribution above a threshold defined as $I_m/2$ where I_m the mean intensity value in the image. It should be noticed that in this study, the value of the threshold has consequently a different value for each image. The MST is built on this set of points and provides the location of the spatial intensity maxima distribution in the (m, σ) plane. Figure 2 presents the process used for the Gaussian transition of a completely developed speckle ($H_{RMS} = \lambda$), for intensity distributions obtained in the case of the following n_c values: 3 and 20.

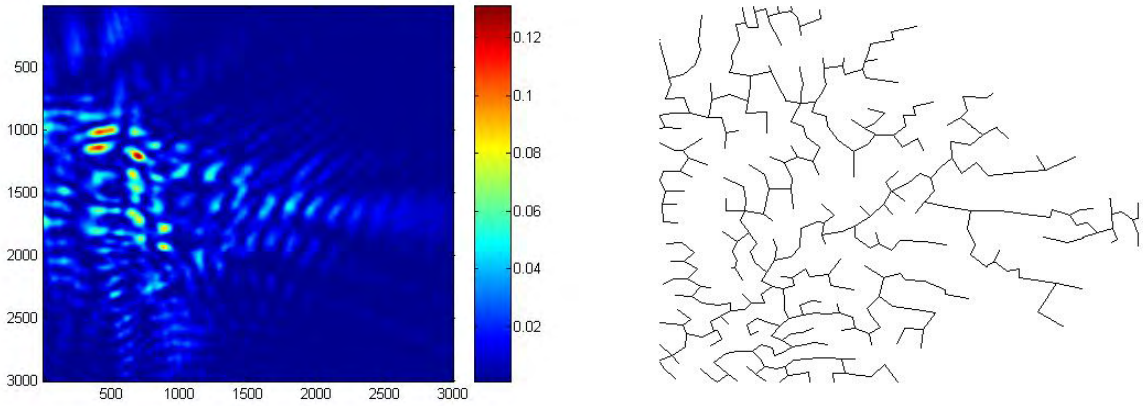

(a) : $n_c = 3$; mean intensity value = $6.6\ 10^{-3}$; MST with 526 nodes (points): m = 0.57, σ = 0.38.

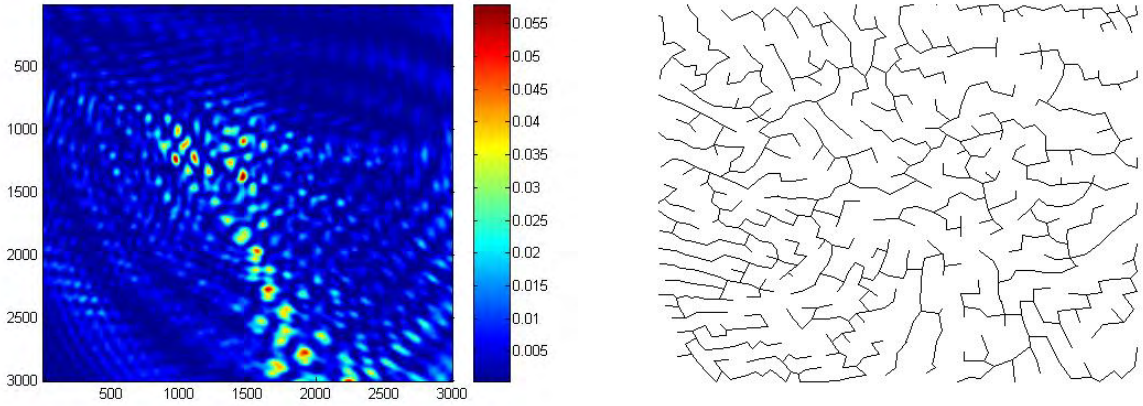

(b) : $n_c = 3$; mean intensity value = $4.5\ 10^{-3}$; MST with 991 nodes (points): m = 0.69, σ = 0.43.

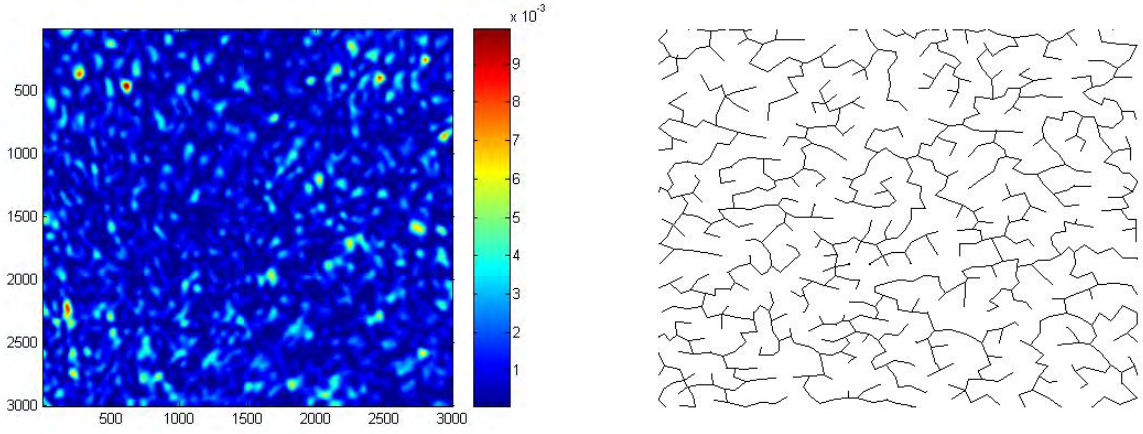

(c) : $n_c = 20$; mean intensity value = 10^{-3}; MST with 1776 nodes (points): m = 0.55, σ = 0.60.

Fig. 2: Process analysis of the spatial maxima intensity distribution by the MST. n_c corresponds to the number of illuminated correlation cells of the surface roughness. Each node corresponds to a local maximum with an intensity higher than $I_m/2$.

Along the Gaussian transition, we can observe the evolution of the location in the (m, σ) plane due to the increased number of illuminated correlation cells on Fig. 3.

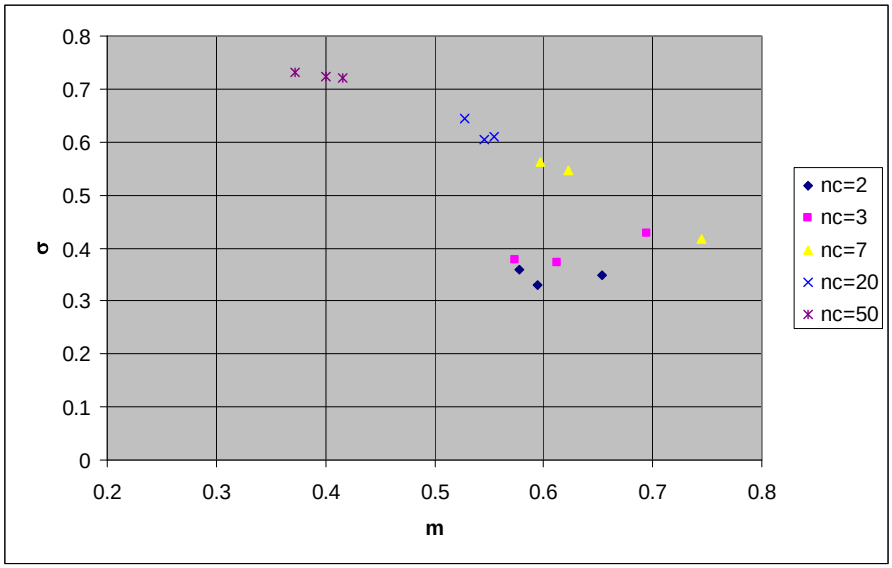

Fig. 3: Representation of the average m and standard deviation σ of MST's edges built on maxima intensity distributions in the Gaussian transition of a speckle field with high resolution images. n_c corresponds to the number of illuminated correlation cells of the surface roughness.

This evolution is different from the evolution obtained with low resolution 8-bits images in the (m, σ) plane (Fig. 4).

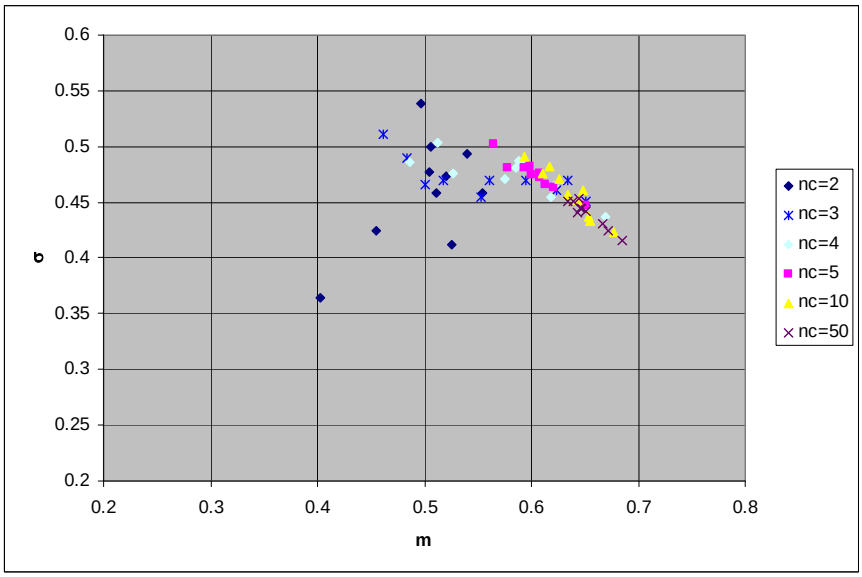

Fig. 4: Representation of the average m and standard deviation σ of MST's edges built on maxima intensity distributions in the Gaussian transition of a speckle field with low resolution 8-bits images [6]. n_c corresponds to the number of illuminated correlation cells of the surface roughness.

In the case of high resolution images and low n_c values, the distribution of intensity maxima is located in the random area and then evolves to the gradient and cluster areas when we tend to Gaussian statistics. But in both cases (high resolution images and 8-bits images) the transition is still located around the n_c value of 4.

4.2 Characterisation of the speckle by singularities

The same process used for the intensity maxima in the section 4.1, is applied for local intensity minima. The threshold for the maximum value of intensity minima is the mean of the intensity I_m in the image. The Fig. 5 show the MST built on these points for the same original images presented on Fig. 2.

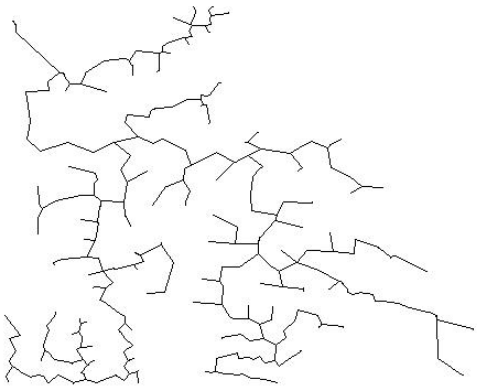

(a) : $n_c = 3$; MST with 1200 nodes: m = 0.27, $\sigma = 0.54$.

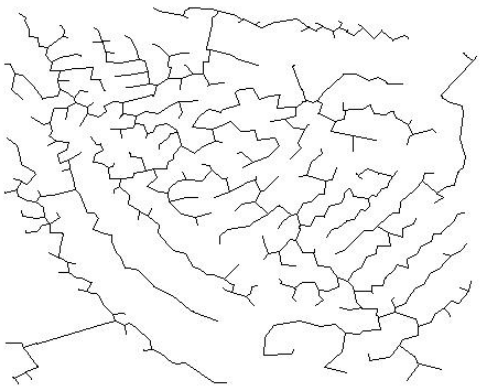

(b): $n_c = 3$; MST with 1752 nodes: m = 0.38, $\sigma = 0.56$.

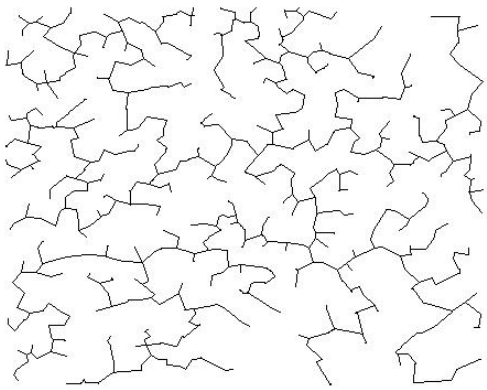

(c) : $n_c = 20$; MST with 4008 nodes: m = 0.27, $\sigma = 0.65$.

Fig. 5: MST built on the spatial minima intensity distribution for the images presented on Fig. 2. n_c corresponds to the number of illuminated correlation cells of the surface roughness. Each node corresponds to a local minimum with an intensity lower than I_m.

As in the case of the local intensity maxima characterization, the different cases of n_c values are are located in various areas. The evolution of the location in the (m, σ) plane due to the increased number of illuminated correlation cells is presented on Fig. 6. This evolution is located near the cluster area and there is no image located in the random area.

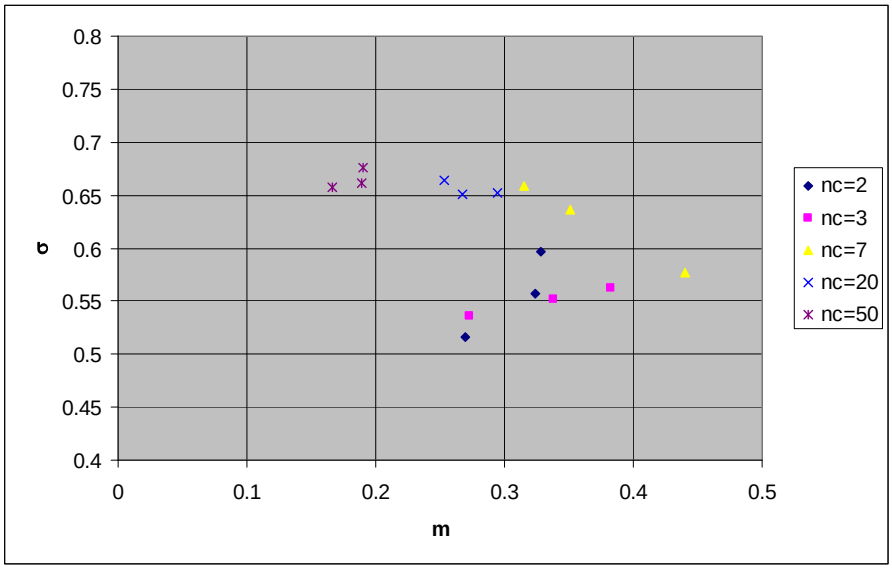

Fig. 5: Representation of the average m and standard deviation σ of MST's edges built on minima intensity distributions in the Gaussian transition of a speckle field. nc corresponds to the number of illuminated correlation cells of the surface roughness.

The study of the singularities confirms the conclusion obtained with the use of intensity maxima: the Gaussian transition is still located around the n_c value of 4. Furthermore, Fig. 3 and Fig. 5 point out that the distributions of local minima and maxima are not similar: the means of edge length of trees have lower values in the case of minima intensity distributions than in case of the maxima intensity distributions.

The detection of the Gaussian transition is possible with different image resolutions. All the results obtained confirm that the MST methodology applied to this detection is not sensitive to the image resolution, to the different values of threshold and to the choice of building a MST on minima or maxima intensities. But, the evolution of m and σ values in the (m, σ) plane depends on the resolution of the images. Consequently, the comparison of speckle images needs the use of similar resolution.

5. CONCLUSION

We have proposed speckle fields characterization obtained by the use of the Minimal Spanning Tree method. The introduction of this criterion that corresponds to local intensity maxima and phase singularities regions, have been used to perform a spatial intensity distribution analysis along the Gaussian transition of an optical speckle field. The influence of the resolution of the images is highlighted. Moreover, the MST method exhibits a specific curvature in the (m, σ) plane when about 4 correlation cells of the surface roughness are illuminated. The method highlights for the first time the different spatial distributions of the intensity maxima and the phase singularities in the speckle images. A new and robust way to characterize the correlation length of a surface roughness and its illumination conditions is provided. This methodology can find further applications such as the study of non circular speckle fields and, in a more general way, can improve rough surface or multiple scattering media characterization by speckle field analysis.

REFERENCES

[1] Goodman, J. W., [Speckle phenomena in optics, theory and applications], Roberts and Company, Greenwood Village (2006).

[2] Bergoënd, I., Orlik, X., Lacot, E., "Study of a circular Gaussian transition in an optical speckle field", J. Europ. Opt. Soc. Rap. Public. 08028 Vol. 3, doi:10.2971/jeos.2008.08028 (2008)

[3] Kadano, H., Asakura, T., Takai, N., "Roughness and correlation length determination of rough-surface objects using speckle contrast" Appl. Phys. B 44, 167-173 (1987)

[4] Kadano, H., Asakura, T., Takai, N., "Roughness and correlation length measurements of rough-surface objects using the speckle contrast in the diffraction field" Optik 80, 115-120 (1988)

[5] Cheng, C., Liu, C., Zhang, N., Jia, T., Li, R., Xu, Z., "Absolute Measurement of Roughness and Lateral-Correlation Length of Random Surfaces by Use of the Simplified Model of Image-Speckle Contrast," Appl. Opt. 41, 4148-4156 (2002)

[6] Vasseur, O., Bergoënd, I., Orlik, X., "A Gaussian transition of an optical speckle field studied by the minimal spanning tree method", J. Europ. Opt. Soc. Rap. Public. 10052 Vol. 5, doi:10.2971/jeos.2010.10052 (2010).

[7] Zhan, C., "Graph-theoretical methods for detecting and describing gestalt clusters", IEEE T. Comput. C-20, 68-86 (1971).

[8] Grella, R., "Fresnel propagation and diffraction and paraxial wave equation" J. Opt. 13, 367-374 (1982).

[9] Fung, A. K., Chen, M. F., "Numerical simulation of scattering from simple and composite random surfaces", J. Opt. Soc. Am. A 2, 2274-2284 (1985).

[10] Beardwood, J., Halton, J. H., Hammersley, J. M., "The shortest path through many points", Camb. Philos. Soc. Proc. 55, 299-327 (1959).

[11] Hoffman, R., Jain, A., "A test of randomness based on the minimal spanning tree", Pattern Recogn. Lett. 1, 175-180 (1983).

[12] Prim, R. C., "Shortest connection networks and some generalizations", Bell Syst. Tech. J. 36, 1389-1401 (1957).

[13] Dussert, C., Rasigni, G., Rasigni, M., Palmari, J., "Minimal spanning tree: A new approach for studying order and disorder", Physical Review B. 34 (5), 3528-3531 (1986).

[14] Wallet, F., Dussert, C., "Multifactorial comparative study of spatial point pattern analysis methods", J. Theor. Biol. 187 (3), 437-447 (1997).

[15] Wallet, F., Dussert, C., "Comparison of spatial point patterns and processes characterization methods", Europhysics Lett. 42 (5), 493-498 (1998).

VIII. Annexe : Planches présentées lors de la soutenance le 07 septembre 2012

Nota : Pour une meilleure lisibilité, le format des références mentionnées au bas des planches a été agrandi lorsque cela était possible.

Habilitation à diriger des recherches

Systèmes optiques interférentiels et incertitudes.

Olivier Vasseur

ONERA
THE FRENCH AEROSPACE LAB

return on innovation

Plan

- Introduction
- Prolégomènes
- Qualité des plans d'expériences numériques Space Filling Design
- Analyse de sensibilité de systèmes optiques interférentiels
- Caractérisation du speckle et de la variabilité spatiale de phénomènes optiques
- Perspectives

Introduction

- Les développements technologiques permettent l'élaboration de systèmes optiques interférentiels comportant un grand nombre de composants :
  - Filtres diélectriques composés de plusieurs dizaines ou centaines de couches minces
  - Combinaison cohérente de plusieurs dizaines ou centaines de sources laser fibrées.
  - Réseaux diffractifs composés d'un grand nombre d'ouvertures
- Evaluation de la robustesse de tels systèmes aux incertitudes de conception ou de fabrication → Enjeu majeur pour déterminer les caractéristiques critiques d'un système :
  - Identification des paramètres critiques
  - Identification des interactions critiques entre des paramètres

Introduction

- Le nombre élevé de paramètres considérés exige de se doter d'outils statistiques efficaces pour explorer des espaces mathématiques de grandes dimensions :
  - Plans d'expériences numériques.
  - Qualité des plans d'expériences numériques Space Filling Design.
- Application des plans d'expériences numériques pour l'analyse de sensibilité de systèmes optiques interférentiels.
- Caractérisation spatiale de la diffusion lumineuse par une surface rugueuse et de la variabilité spatiale de phénomènes optiques.

Introduction

- Les acquis obtenus sont le fruit des synergies de différents domaines et de diverses activités de recherche :
  - Micro-électronique et plans d'expériences (CNET Meylan puis Onera)
  - Optique des couches minces (Institut Fresnel)
  - Optique guidée (Institut Fresnel - CNET Lannion)
  - Simulation comportant un grand nombre de paramètres d'entrée et propagation d'incertitudes, analyse multicritères (DGA). Orientations d'axes de recherche.
  - Perception de l'aléatoire et influence de l'image dans le monde de la technoscience (CERS)
  - Combinaison cohérente de sources laser fibrées et caractérisation du speckle (Onera)
- Thèmes omniprésents dans l'exposé :
  - Le fléau de la dimension
  - Connaisance :
    - Multicritères
    - Synergies de différentes disciplines

Plan

- Introduction
- Prolégomènes
- Qualité des plans d'expériences numériques Space Filling Design
- Analyse de sensibilité de systèmes optiques interférentiels
- Caractérisation du speckle et de la variabilité spatiale de phénomènes optiques
- Perspectives

Prolégomènes : Les interférences lumineuses

- Une interférence optique résulte de l'interaction entre deux ou plusieurs ondes lumineuses qui produit un éclairement global différent de la somme des éclairements des ondes individuelles.

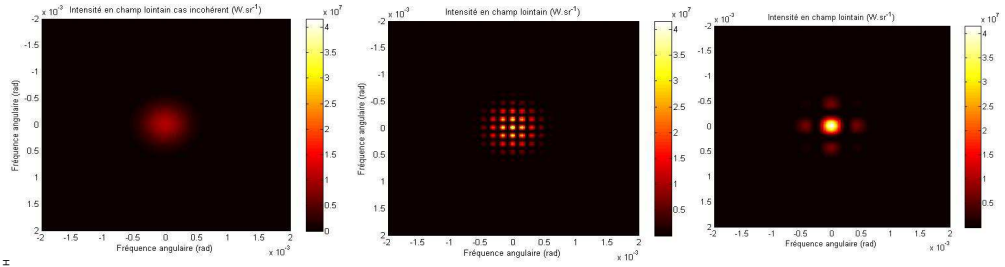

E. Hecht, Optique, Pearson Education France, Paris, 2005
M. Born, E. Wolf, Principles of optics, Pergamon Press, London, 1980
H. A. Macleod, Thin-film optical filters, Adam Hilger, Bristol, 1986

Prolégomènes : Les plans d'expériences numériques

- Définir un plan d'expériences : placer les points d'expérimentation *numérique* dans le domaine de variation des variables d'entrée (facteurs, paramètres).

→ Optimiser l'information requise avec le minimum de points/expérimentations

- Etablir les liens entre :
  - Réponse (sortie du modèle, variable d'intérêt)
  - Facteurs/paramètres/variables :
    - Différentes natures : continus, discrets ou qualitatifs
    - Domaine de variation : [borne inf , borne sup], niveaux

- La qualité de l'information obtenue dépend de la position des points "expérimentaux".

Prolégomènes : Les plans d'expériences numériques

- Historique : Des plans d'expériences du domaine expérimental aux plans d'expériences numériques.
  - De la réplication à l'expérience déterministe.
  - Grand nombre de variables d'entrée, large domaine de variation, plusieurs variables d'intérêt, modèles fortement non linéaires.
  - Plans factoriels, plans factoriels fractionnaires, plans de Box-Behnken, plans de Doehlert → **Space filling designs : répartition uniforme dans l'espace des variables d'entrée** → Remplir le mieux possible l'espace avec peu de points.

- Les objectifs de ces plans :
  - Recherche exploratoire : identification des régions d'intérêt
  - Criblage des facteurs : identification des facteurs influents → simplification du modèle
  - Etude quantitative des facteurs : identification des effets des facteurs et de leurs interactions
  - Construction de métamodèles
  - Optimisation

J. Goupy, La Méthode des plans d'expériences : optimisation du choix des essais et de l'interprétation des résultats, Dunod, Paris, 1988.
J.-J. Droesbeke, J. Fine, G. Saporta, Plans d'expériences : applications à l'entreprise, Technip, Paris, 1997.
T. J. Santner, B. J. Williams, W. I. Notz, The Design and Analysis of Computer Experiments, Springer, New York, 2003.

Prolégomènes : Graphe, Arbre de Longueur Minimale (ALM) et qualification de l'Ordre et du Désordre

- ALM → Histogramme des longueurs de branche → moyenne m et écart-type σ des longueurs de branche.

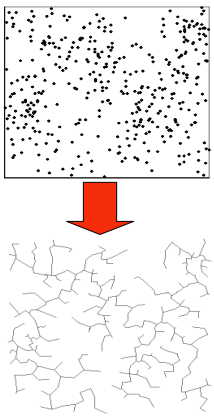

N = 400 points
(Amas)

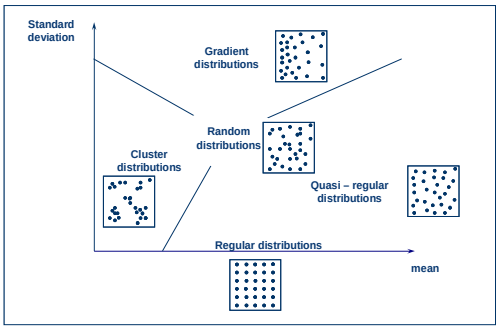

Beardwood J., Halton J.H., Hammersley J.M., "The shortest path through many points", Camb. Philos. Soc. Proc., 55, 1959.
Dussert C., Rasigni G., Rasigni M., Palmari J. & Llebaria A., "Minimal spanning tree : a new approach for studying order and disorder", Phys. Rev. B 34, 3528-3531, 1986.
F. Wallet, C. Dussert, "Multifactorial comparative study of spatial point pattern analysis methods", J. Theor. Biol. 187, 437-447, 1997.
O. Vasseur, L'image dans la technoscience :De son utilisation et de son influence dans les sciences appliquées, Ph.D. Thesis in Sociology, Université Toulouse 2, Juin 2003.

Prolégomènes : Grandes dimensions

- Grandes dimensions : Quelle définition de la dimension ?
  - Nombre de paramètres d'entrée
    - Ex : 10 paramètres.
  - Nombre de termes dans un métamodèle
    - Ex : 10 paramètres et polynômes 2nd degré avec interactions 1er degré → 1 + 10 +10 + 45 = 66

$$f(X_1,...,X_n) = a_0 + \sum_{k=1}^{n} a_k.X_k + \sum_{k=1}^{n} b_k.X_k^2 + \sum_{0<i<j\leq n} c_{ij}.X_i.X_j$$

  - Nombre défini par produit tensoriel
    - Ex : 10 paramètres → 10 bases de 10 vecteurs → 10^{10}

Plan

- Introduction
- Prolégomènes
- Qualité des plans d'expériences numériques Space Filling Design
- Analyse de sensibilité de systèmes optiques interférentiels
- Caractérisation du speckle et de la variabilité spatiale de phénomènes optiques
- Perspectives

Space Filling Designs (SFD)

- Space filling designs : répartition uniforme des points des expériences numériques dans l'espace des variables d'entrée → Remplir le mieux possible l'espace avec peu de points.

- Exploration de l'espace *sans connaissance a priori*.
  - Identification des zones d'intérêt, enrichissement du plan, élaboration de plans spécifiques en tenant compte des connaissances a priori.

- Grande variété de types de plans :
  - Carrés latins (LHDs) et variantes, plans aléatoires (loi uniforme), grilles et plans factoriels, plans à faible discrépance, plans de Strauss, plans WSP…

T. J. Santner, B. J. Williams, W. I. Notz, The Design and Analysis of Computer Experiments, Springer, New York, 2003.
J. Franco, Planification d'expériences numériques en phase exploratoire pour la simulation des phénomènes complexes, Ph. D. Thesis, EMSE, Septembre 2008
J. Santiago, M. Claeys-Bruno, M. Sergent, "Construction of space-filling designs using WSP algorithm for high dimensional spaces", Chemometrics and Intelligent Laboratory Systems 113, 26-31, 2012.

Qualification des SFD : principaux critères

- Différents critères pour apprécier la **qualité intrinsèque** d'un plan :
  - La discrépance mesure la différence entre la fonction de répartition empirique et la fonction de répartition uniforme.
    - Densités de points dans différents volumes
    - Plusieurs discrépances…

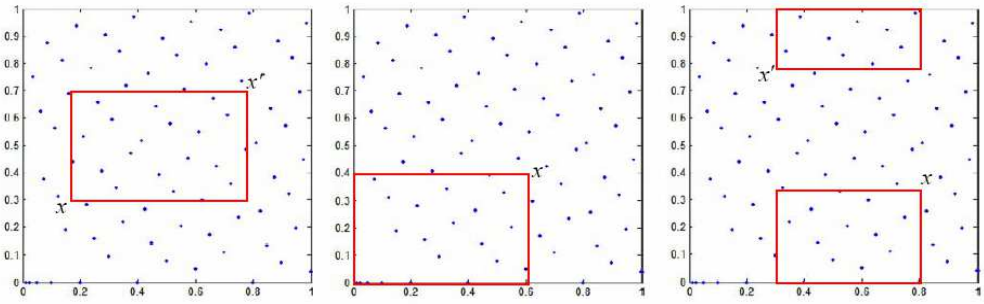

J. Franco, Planification d'expériences numériques en phase exploratoire pour la simulation des phénomènes complexes, Ph. D. Thesis, EMSE, Septembre 2008
V. Feuillard, Analyse d'une base de données pour la calibration d'un code de calcul, Ph. D. Thesis, Université Pierre et Marie Curie, 2007

Qualification des SFD : principaux critères

- Différents critères pour apprécier la **qualité intrinsèque** d'un plan :
  - La distance entre les points du plan :

$$MinDist = \min_{x_i \in X} \min_{x_k \in X, k \neq i} dist(x_i, x_k) \qquad X = \{x_i, ..., x_n\}$$

    - → Maximiser cette distance (critère maximin) : Ecarter les points du plan → Remplir au mieux l'espace
  - Radial Scanning Statistics (RSS) :
    - Projection des points dans tous les sous espaces de dimension 2 (et 3).
    - Projection des points sur une droite, qui tourne sur 180° → Analyse de l'uniformité

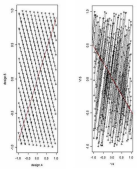

  - ***Arbre de Longueur Minimal :***
    - Qualification de la structure de la répartition des points dans l'espace d'origine.
    - Histogramme des longueurs de branche unique mais l'arbre est (*presque) toujours* unique dans le cas des SFD !

$$L_{G_\infty} = \alpha_d (VN^{d-1})^{1/d} \qquad M_A = \alpha_d \frac{(VN^{d-1})^{1/d}}{N-1}$$

J. Franco, O. Vasseur, B. Corre, M. Sergent, Minimum Spanning Tree : A new approach to assess the quality of the design of computer experiments, Chemometrics and Intelligent Laboratory Systems 97, 164-169, 2009. http://www.dice-consortium.fr/
O. Roustant, J. Franco, L. Carraro, A. Jourdan, "A radial scanning statistic for selecting space-filling designs in computer experiments", in mODa 9 – Advances in Model-Oriented Design and Analysis, Proceedings of the 9th International Workshop in Model-Oriented Design and Analysis held in Bertinoro, Italy, June 14-18, 189-196, Springer, Heildeberg, 2010.

Qualité intrinsèque des Space Filling Designs (SFD)

- La qualité intrinsèque d'un plan est définie par :
  - Espacement suffisant des points → permet de répartir un nombre faible de points dans l'espace → m grand (ou suffisamment grand)
  - Suffisamment régulier mais sans excès → σ non nul et inférieur à celui d'un plan aléatoire

  → Un plan SFD doit être situé dans la zone quasi-périodique du plan (m, σ).

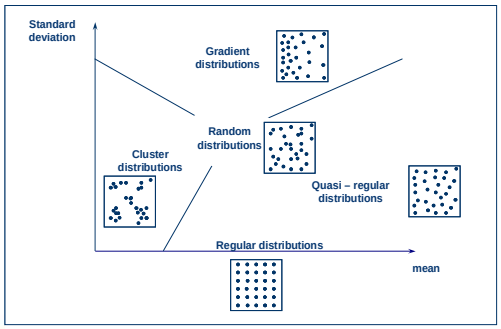

Space Filling Designs (SFD) et critères

- Exemples en dimension 2 avec 36 points :

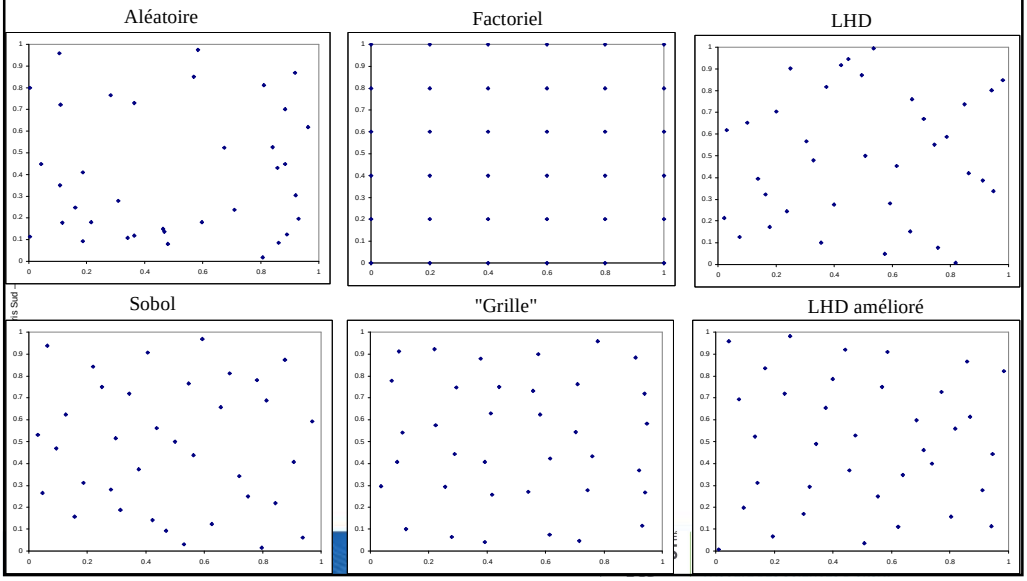

Space Filling Designs (SFD) et critères

- Exemples en dimension 2 avec 36 points :
  - Calcul des différents critères sur les plans SFD.
  - Quel est le meilleur plan (hormis plan factoriel) ?

	MinDist	Discrépance C2	Discrépance L2	m	σ
Factoriel	0.2000	0.1113	0.0338	1.1667	0.0000
Aléatoire	0.0143	0.1296	0.0322	0.6930	0.3076
"Grille"	0.1013	0.0439	0.0147	0.8479	0.1615
LHD	0.0358	0.0280	0.0128	0.6996	0.2527
LHD amélioré	0.0690	0.0247	0.0115	0.8545	0.1472
Sobol	0.0663	0.0370	0.0119	0.7967	0.2262

- LHD et projections :

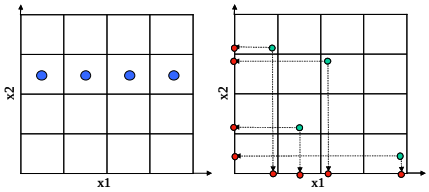

R-package lhs : http://cran.r-project.org/web/packages/lhs/index.html
http://www.dice-consortium.fr/
J. Franco, O. Vasseur, B. Corre, M. Sergent, "Minimum Spanning Tree : A new approach to assess the quality of the design of computer experiments", Chemometrics and Intelligent Laboratory Systems 97, 164-169, 2009.
http://www-mip.onera.fr/projets/JSO-2012/fichiers/presentations/25 janvier/O_Vasseur.pdf

Critères de qualité des Space Filling Designs (SFD)

- Exemples en dimension 2 avec 20 et 36 points (ALM) :

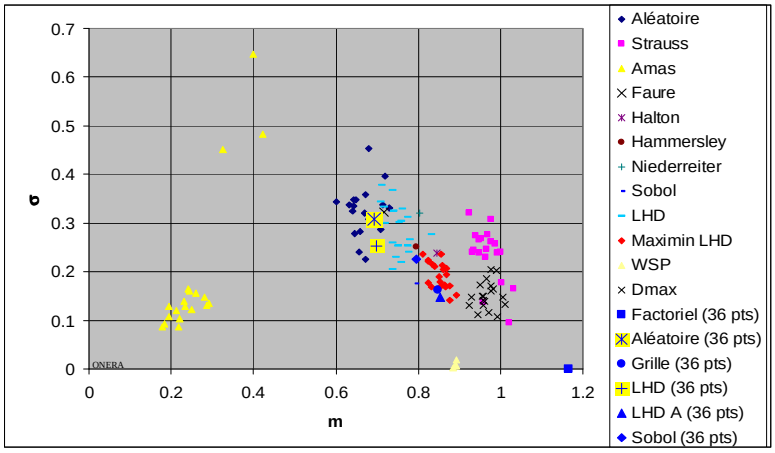

J. Franco, O. Vasseur, B. Corre, M. Sergent, "Minimum Spanning Tree : A new approach to assess the quality of the design of computer experiments", Chemometrics and Intelligent Laboratory Systems 97, 164-169, 2009.

Qualité intrinsèque des Space Filling Designs (SFD)

- Plan (m,σ) en dimension 5 avec N=100 (N~100 : WSP)

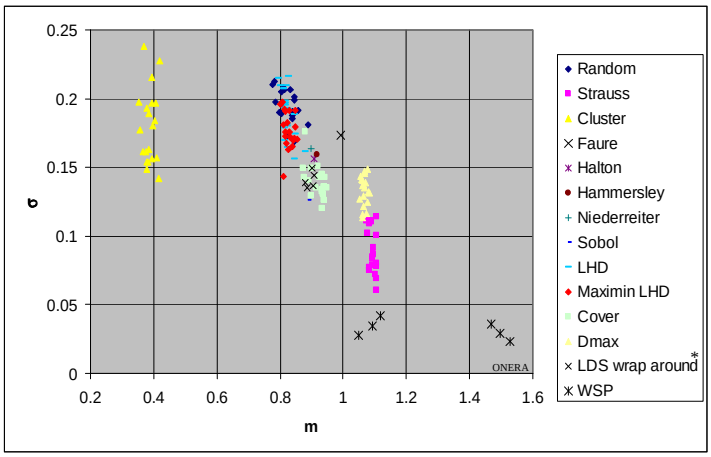

* Marrel A., Mise en œuvre et utilisation du métamodèle processus gaussien pour l'analyse de sensibilité de modèles numériques, Ph. D. Thesis, INSA, Juillet 2008

Qualité intrinsèque des Space Filling Designs (SFD)

- Plan (m,σ) en 20D avec N=400 et 29D avec N=614:

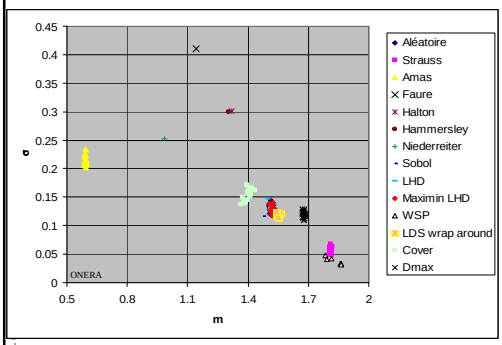

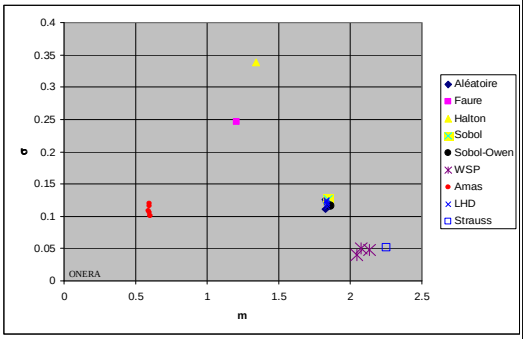

→ Les plans construits sur des suites à faible discrépance ne possèdent pas une bonne qualité intrinsèque en grandes dimensions.

O. Vasseur, A. Azarian, V. Jolivet, P. Bourdon, "Capability of high intrinsic quality Space Filling Design for global sensitivity analysis and metamodelling of interference optical systems", Chemometrics and Intelligent Laboratory Systems 113, 10-18, 2012.
P. Bratley, B. L. Fox, H. Niederreiter, "Implementation and tests of low-discrepancy sequences", ACM Trans. Model. Comput. Simul. 2, 195-213, 1992

Qualification des plans Sobol et WSP 29D : Projections en dimension 2 - Critère ALM.

- Résultats obtenus dans les projections de dimension 2 :
  - Diversité des caractéristiques des plans de Sobol.
  - Le scrambling d'Owen ne modifie pas ces caractéristiques.

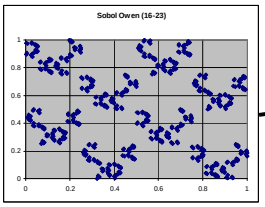

Remarques :
- Plus mauvais plan pour critère RSS
- Nécessité représentation graphique

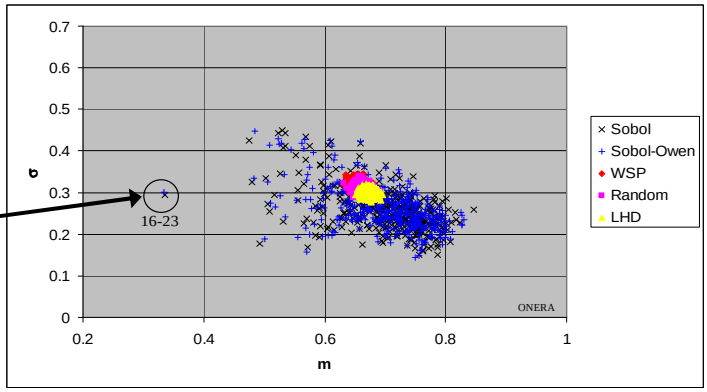

O. Vasseur, A. Azarian, V. Jolivet, P. Bourdon, "Capability of high intrinsic quality Space Filling Design for global sensitivity analysis and metamodelling of interference optical systems", Chemometrics and Intelligent Laboratory Systems 113, 10-18, 2012.

Grandes dimensions et problématiques associées

- Remplir un volume dans un cube unité en grandes dimensions ?
  - avec une loi uniforme pour chacune des composante

Dim 2 :

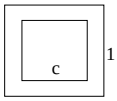

→ Proportion de points dont toutes les coordonnées sont à l'intérieur du volume considéré en fonction de la dimension ?

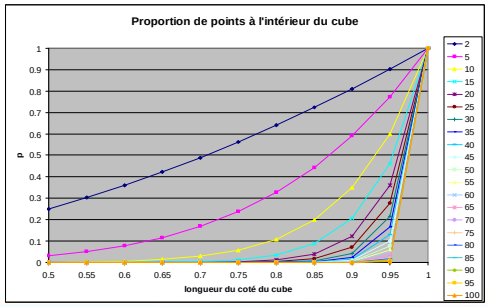

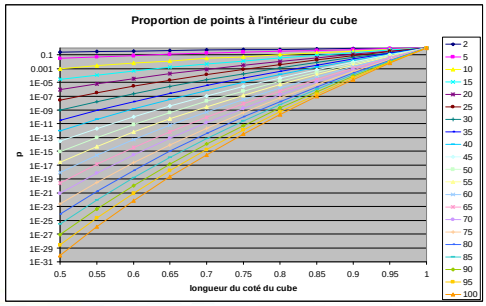

Grandes dimensions et problématiques associées (66D)

- Plans de 3000 points en dimension 66.
- Combien de points dans l'hypercube central de coté 0.9 ?

- Aléatoire : $3000 * 0.9^{66} = 2.86$ → 3 points

- LHD1 : 1
- LHD2 : 7
- LHD3 : 3
- LHD amélioré : 9
- Sobol : 18
- Sobol-Owen : 3
- Sobol-Owen-Faure-Tezuka : 1 !!!

En grandes dimensions, à défaut d'un plan WSP, les plans de type LHD constituent le meilleur choix initial.

*Formules de filtres (passe bande) de 66 à 96 couches communiquée par A. Tikhoravov – Université de Moscou.

Qualité intrinsèque des Space Filling Designs (SFD)

- Selon le critère utilisé, la qualité intrinsèque des plans SFD peut être très différente. **La qualité intrinsèque des catégories de plans SFD est extrêmement dépendante de la dimension de l'espace.**
- Les suites à faible discrépance (y compris les suites de Sobol et le scrambling) ne fournissent pas des plans de très bonne qualité en grandes dimensions.
- A défaut des plans WSP, les plans aléatoires et surtout les variantes des LHD semblent constituer le meilleur choix et possèdent de bonnes propriétés en projection dans les sous espaces de dimension 2.
- Le critère ALM est **très** performant pour évaluer la qualité d'un plan SFD de manière globale dans l'espace original et en projections.

Plan

- Introduction
- Prolégomènes
- Qualité des plans d'expériences numériques Space Filling Design
- Analyse de sensibilité de systèmes optiques interférentiels
- Caractérisation du speckle et de la variabilité spatiale de phénomènes optiques
- Perspectives

SFD et systèmes optiques interférentiels

- Utilisation de différents plans SFD pour le criblage, l'analyse de sensibilité, l'élaboration de métamodèles et l'optimisation de systèmes optiques interférentiels :
  - L'analyse des modifications des propriétés optiques d'un filtre interférentiel lors de sa fabrication et la combinaison cohérente de sources laser fibrées.
  - Caractéristiques :
    - *Grand nombre de paramètres d'entrée (objectif : qq 10^2)*
    - Incertitudes sur ces paramètres + facteurs non contrôlables
    - **Fortes interactions entre facteurs**
    - *Présence de boucles de rétroaction (100ms 19 fibres → 1 jour de calcul).*
    - *Sorties fonctionnelles*

Filtres interférentiels multidiélectriques

- Modélisation des filtres multidiélectriques → réduction de la réalité.

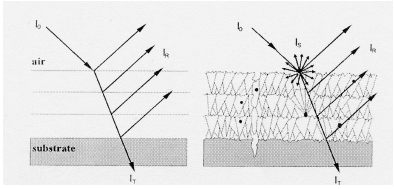

- Exemple de l'évolution du profil spectral lors de la fabrication d'un filtre couches minces.

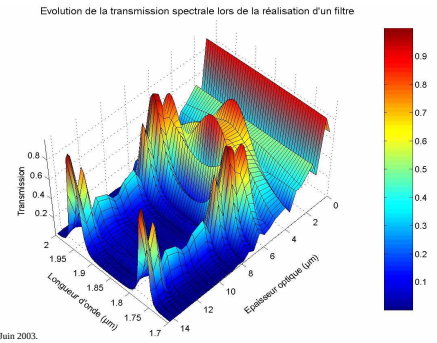

N. Kaiser, Review of the fundamentals of thin-film growth, Applied Optics, 41, 3054, 2002.
O. Vasseur L'image dans la technoscience :De son utilisation et de son influence dans les sciences appliquées, Ph. D. Thesis, Toulouse II, Juin 2003.

O. Vasseur – Soutenance HDR – Université Paris Sud – 07 septembre 2012

La fabrication de couches minces optiques

- Les techniques de dépôts :
  - Electron Beam Deposition
  - Ion assisted deposition
  - Ion plating
  - Dual ion beam sputtering
  - Sputtering
  - …
- Matériaux (oxide, sulfide, …)
- Techniques de contrôle :
  - Quartz
  - Optique

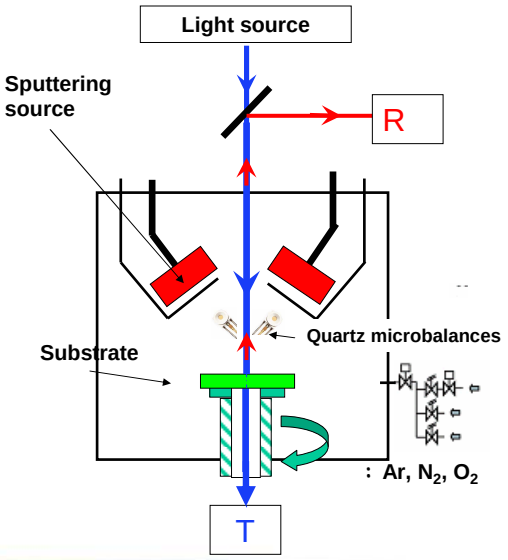

Filtres interférentiels multidiélectriques

- Illustration de la méthodologie sur un filtre composé de **29** couches minces :

  Substrat/HBHB4HBHBH B HBHB4HBHBH B HBHB4HBHBH/air

  - 2 matériaux utilisés → 2 valeurs d'indice
    - H : indice haut n_h, B : indice bas n_b
  - Définition d'un filtre "parfait"
  - λ_c : longueur d'onde de centrage
  - Épaisseur e_i de chacune des couches H, B : $n_i * e_i = \lambda_0/4$

→ **29** variables d'entrée :

- Chaque valeur d'indice peut varier de +/- x%
- Utilisation de plusieurs variables d'intérêt pour l'analyse des effets des variations d'indice sur le profil spectral de type :

$$F = \sum_i (T(\lambda_i) - T_p(\lambda_i))^2$$

Filtres interférentiels multidiélectriques

Influence de la variation des valeurs d'indices sur le facteur de transmission du filtre en fonction de la longueur d'onde (λ_0 = 1µm). Incidence normale

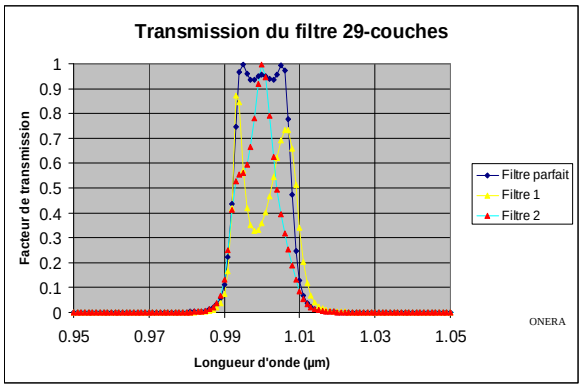

±2,5% d'erreur sur la valeur d'indice

Analyse de sensibilité de filtres interférentiels multidiélectriques et plans SFD

- **Qualité extrinsèque** des SFD :
  - Utilisation d'un métamodèle pour décrire la fonction de mérite :

$$f(X_1,...,X_n) = a_0 + \sum_{k=1}^{n} a_k.X_k + \sum_{k=1}^{n} b_k.X_k^2 + \sum_{0<i<j\leq n} c_{ij}.X_i.X_j$$

  - Dans le cas d'un filtre optique interférentiel "connu", la qualité des résultats obtenus avec les différents plans est appréciée de la manière suivante:
    - Coefficient de détermination: R^2
    - Score : Identification des interactions les plus critiques $c_{i,j}$: $c_{5,15}$, $c_{15,25}$, $c_{5,25}$, $c_{4,5}$, $c_{5,6}$, $c_{14,15}$, $c_{15,16}$, $c_{24,25}$, $c_{25,26}$.
    - Valeur du coefficient a_0 = 0.

O. Vasseur, M. Cathelinaud, M. Claeys-Bruno, M. Sergent, "Global sensitivity analysis of bandpass and antireflection coatings manufacturing by numerical space filling designs", Applied Optics, C117-C123, 2011

Analyse de sensibilité de filtres interférentiels multidiélectriques et plans SFD

- Qualité extrinsèque et qualité intrinsèque des SFD concordantes:

HLHL4HLHLH L HLHL4HLHLH L HLHL4HLHLH

SFD (614 points)	R^2	Score	Valeur a_0
Faure	0.98	1/9	1.43
LHD 1	0.97	6/9	0.88
LHD 2	0.97	5/9	0.90
LHD 3	0.97	7/9	0.87
LHD 4	0.97	5/9	0.81
LHD 5	0.97	6/9	0.89
Aléatoire 1	0.97	6/9	0.71
Aléatoire 2	0.97	4/9	0.75
Aléatoire 3	0.96	7/9	0.82
Aléatoire 4	0.97	7/9	0.88
Aléatoire 5	0.97	8/9	0.81
Sobol	0.97	6/9	0.68
WSP 1 (598 points)	0.97	7/9	0.30
WSP 2 (598 points)	0.98	6/9	0.02
WSP 3	0.96	6/9	0.53

O. Vasseur, A. Azarian, V. Jolivet, P. Bourdon, "Capability of high intrinsic quality Space Filling Design for global sensitivity analysis and metamodelling of interference optical systems", Chemometrics and Intelligent Laboratory Systems 113, 10-18, 2012.

Filtres interférentiels multidiélectriques : Incertitudes sur les valeurs d'indices et d'épaisseurs

- Deux méthodes de fabrication : Cas de variables indépendantes et corrélées :
  - TC Quartz : les incertitudes sur les valeurs d'indice de réfraction n et d'épaisseur des couches e sont indépendantes :

$$n^* = (1+\delta)\cdot n \qquad e^* = (1+\delta)\cdot e$$

  - TC Optique : la valeur de l'indice de réfraction n* est compensée par la modification de l'épaisseur de la couche à la longueur d'onde λ_0 via la relation :

$$e' = \frac{\lambda_0}{4\cdot n^*}$$

Puis : $e^* = (1+\delta)\cdot e'$

O. Vasseur, M. Cathelinaud, "Investigation of manufacturing processes by numerical sensitivity analysis", Proc. of SPIE 8168, 81680A-1, 2011.
M. Désenfant, P. Pernot, O. Vasseur, "Is there a link between correlation and interaction ?", 15ème Congrès International de Métrologie, Paris, 2011.

Filtres interférentiels multidiélectriques : Incertitudes sur les valeurs d'indices et d'épaisseurs

- Cas de variables corrélées – Hiérarchisation des paramètres critiques :
  - n* et e' ou e* → "Disparition" des interactions entre indice et épaisseur – Changement de hiérarchie des facteurs les plus critiques.
    - Exemple de résultat avec n* et e' :

Facteur de transmission du filtre 13 couches en fonction de la longueur d'onde (λ_0 =1µm) - 5% d'erreur sur indice

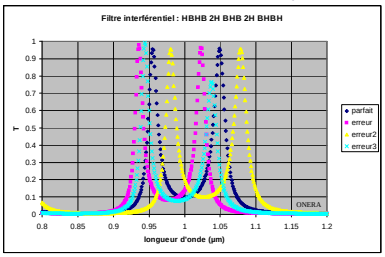

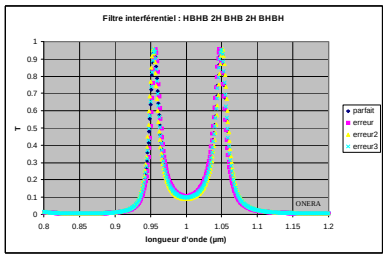

n → n* | n → n* e → e' avec ne=n*e'

HBHB 2H BHB 2H BHBH | HBHB 2H BHB 2H BHBH

O. Vasseur, M. Claeys-Bruno, M. Cathelinaud, M. Sergent, "High dimensional sensitivity analysis of complex optronic systems by experimental design: applications to the case of the design and the robustness of optical coatings", FOCASIA 2009
O. Vasseur, M. Cathelinaud, "Investigation of manufacturing processes by numerical sensitivity analysis", Proc. of SPIE 8168, 81680A-1, 2011..

Filtres interférentiels et optique guidée

- Amplificateurs optiques non résonnants → Réalisation d'antireflets 4 couches en extrémité de diode (n_c=3.512, n_g=3.17, e_d=0.2µm).

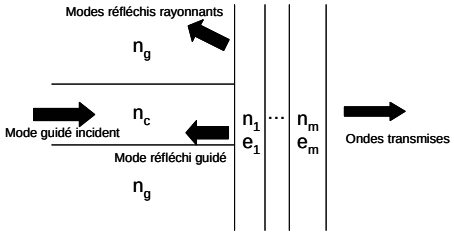

$$n_{eq}^2 = \frac{\left\langle n^2(x,y)\vec{e}_0, \vec{h}_0 \right\rangle}{\left\langle \vec{e}_0, \vec{h}_0 \right\rangle}$$

$$R_m = \left| \frac{\left\langle \vec{E}_r, \vec{h}_0 \right\rangle}{\left\langle \vec{e}_0, \vec{h}_0 \right\rangle} \right|^2 \qquad R_p = \frac{\mathrm{Re}\left[\iint \left\langle \vec{E}_r, \vec{H}_r \right\rangle \right]}{\left\langle \vec{e}_0, \vec{h}_0 \right\rangle}$$

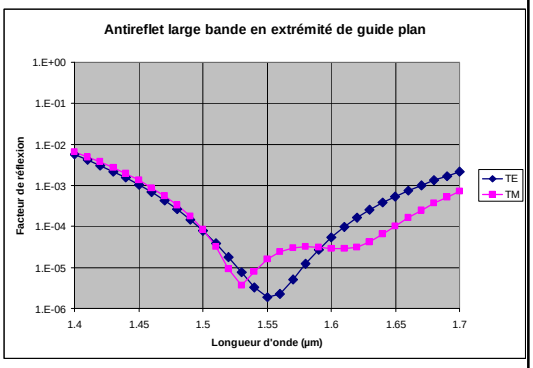

O. Vasseur, Calcul et réalisation de traitements optiques multicouches pour diodes laser. Etude de l'influence des défauts de structure des couches sur les performances des diodes traitées, Ph. D. Thesis, Université d'Aix-Marseille III, 1990.
O. Vasseur, "Reflectivity of dielectric coatings deposited on the end facet of a weakly guiding fiber", J. Opt. Soc. Am. A 12, 77-83, 1998.

Filtres interférentiels et optique guidée : Analyse de sensibilité et influence du critère de décision.

- Variation des valeurs d'indice ($\delta \in [-0{,}01 ; 0{,}01]$) et 100 runs → Les paramètres les plus critiques sont a_1 et a_3 en tenant compte de l'ensemble du domaine spectral :

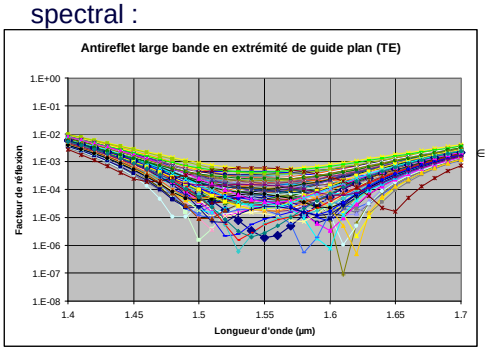

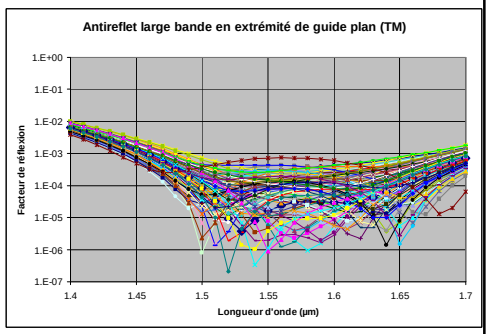

- Pour les 3 longueurs d'onde 1.54 µm, 1.55 µm et 1.56 µm, les paramètres les plus critiques sont : b_1, b_3 , $c_{1\text{-}2}$, $c_{1\text{-}4}$, $c_{2\text{-}4}$

Conclusion

- L'analyse de sensibilité au moyen de plans numériques SFD permet d'identifier les paramètres et interactions les plus critiques en tenant compte des procédés de fabrication.
- La conception robuste de systèmes comportant un grand nombre de paramètres est accessible.
- La connaissance des interactions entre les paramètres les plus critiques permet d'envisager, dans certains cas, de corriger des défauts de fabrication par la modification de la structure du filtre restant à fabriquer.
- La hiérarchisation des plans SFD par l'ALM est corroborée par les résultats obtenus dans l'étude des filtres interférentiels.

Perspectives

- Impact des incertitudes sur d'autres propriétés que la transmission ou la réflexion des filtres est également envisageable.
  - Par exemple, pour l'élaboration de miroirs dispersifs destinés au domaine des lasers femtoseconde, les variables d'intérêt à retenir sont le facteur de réflexion du miroir et la dispersion de la vitesse de groupe.
- Conception robuste de filtres multidiélectriques sur des structures guidantes beaucoup plus élaborées → guides microstructurés.

La combinaison cohérente de sources laser fibrées : La voie vers des lasers de très forte puissance.

- La source laser est composée de N fibres :

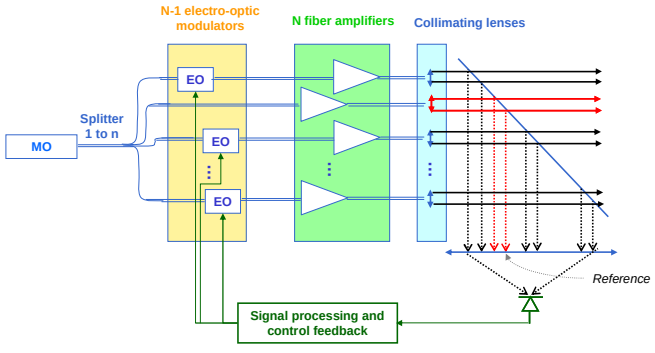

Champ lointain non phasé

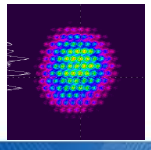

Champ lointain phasé

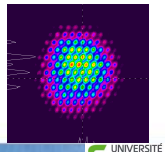

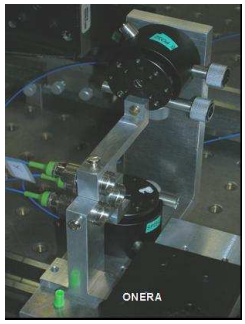

Expérimentation :Combinaison cohérente de 3 sources laser fibrées

La combinaison cohérente de sources laser fibrées

- Les travaux conduits à l'Onera ont permis notamment :
  - de démontrer la combinaison cohérente à distance après propagation en atmosphère turbulente sur une cible non coopérative,

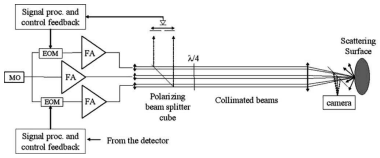

  - d'étudier la combinaison cohérente de fibres faiblement multimodes,
  - de démontrer la combinaison cohérente impulsionnelle,
  - d'ouvrir la voie à des systèmes utilisant les combinaisons cohérente et incohérente d'un grand nombre de faisceaux tout en limitant le nombre de fréquences de modulation utilisées (technique de codage à base de matrice d'Hadamard),

  - **d'initier les travaux d'analyse de sensibilité de ces systèmes** :
    - Différents types de paramètres : positionnement, puissance, bruit de phase…
    - Etude de l'influence des déphasages résiduels et augmentation du nombre de fibres.

P. Bourdon, V. Jolivet, B. Bennaï, L. Lombard, G. Canat, E. Pourtal, Y. Jaouën, O. Vasseur, "Coherent beam combining of fiber amplifier arrays and application to laser beam propagation through turbulent atmosphere", Proc. SPIE 6873, 687316, 2008..
V. Jolivet, P. Bourdon, B. Bennaï, L. Lombard, D. Goular, E. Pourtal, G. Canat, Y. Jaouën, B. Moreau, O. Vasseur, "Beam shaping of single-mode and multimode fiber amplifier arrays for propagation through atmospheric turbulence", IEEE J. Sel. Topics Quantum Electron. 15, 257-268, 2009.
B. Bennaï, Mise en phase de lasers à fibre : Etude de l'influence de la turbulence atmosphérique et de l'utilisation de fibres faiblement multimodes, Ph. D. Thesis, Télécom ParisTech, 2010.
L. Lombard, A. Azarian, K. Cadoret, P. Bourdon, D. Goular, G. Canat, V. Jolivet, Y. Jaouën, O. Vasseur, "Coherent beam combination of narrow linewidth 1.5µm fiber amplifiers in long pulse regime", Opt. Lett. 36, 523-525, 2011.
A. Azarian, P. Bourdon, L. Lombard, Y. Jaouën, O. Vasseur, "Orthogonal coded modulations for active coherent beam combination", communication acceptée à IEEE Photonics Conference 2012

La combinaison cohérente de sources laser fibrées

- Analyse de sensibilité de la mise en phase de 19 fibres aux variations de phases résiduelles:
  - Profil d'intensité en sortie d'une fibre (approximation gaussienne) et en champ lointain

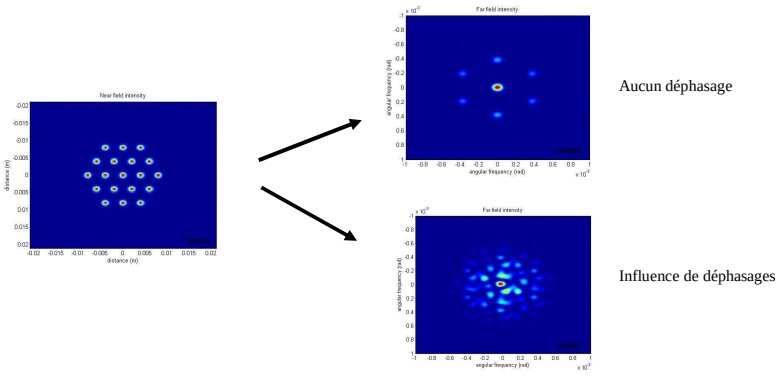

La combinaison cohérente de sources laser fibrées

- Différentes formes de faisceau en champ lointain obtenues pour des réseaux de 19 et 127 fibres disposées en hexagone :

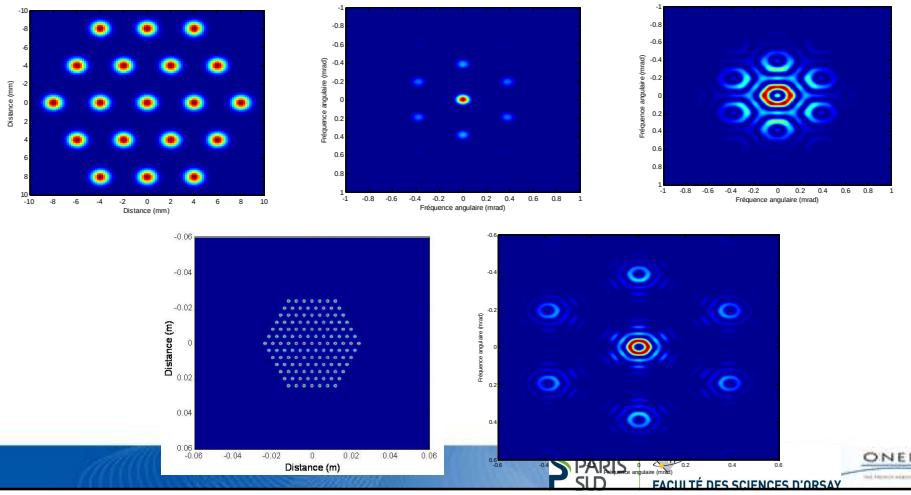

La combinaison cohérente de sources laser fibrées

- Différents critères pour qualifier la mise en phase :
  - Rapport de Strehl : Intensité en champ lointain sur l'axe d'un faisceau issu d'une pupille divisé par l'intensité en champ lointain sur l'axe d'un faisceau issu d'une pupille de même taille uniformément éclairée ayant la même puissance.
    - Peu pertinent car évaluation de l'intensité uniquement sur l'axe.
    - Différents arrangements peuvent conduire à la même valeur.
  - Beam Propagation Factor (BPF) : Fraction de puissance contenue dans une certaine zone A du faisceau par rapport à la puissance totale.
    - Indépendant de la cible.
  - Mask Encircled Power (MEP) : Fraction de puissance contenue dans une zone d'ouverture fixée (par l'application : cible éclairée) divisée par la puissance totale de la source.
    - Indépendant de la pupille du système et représentatif de l'application.
    - Comparaison de différents agencements de combinaison de fibres.

P. Zhou, Z. Liu, X. Xu et Z. Chen, "Numerical analysis of the effects of aberrations on coherently combined fiber laser beams", Applied optics, 47, 18, 3350-3359, 2008
V. Jolivet, P. Bourdon, B. Bennai, L. Lombard, D. Goular, E. Pourtal, G. Canat, Y. Jaouën, B. Moreau, O. Vasseur, "Beam shaping of single-mode and multimode fiber amplifier arrays for propagation through atmospheric turbulence", IEEE J. Sel. Topics Quantum Electron. 15, 257-268, 2009.

Analyse de sensibilité de la combinaison cohérente de sources laser fibrées

- La qualité des résultats obtenus avec les différents plans (dim 18 car une fibre sert de référence) est appréciée de la manière suivante:
  - Métamodèle sous jacent :

$$f(X_1,...,X_n) = a_0 + \sum_{k=1}^{n} a_k.X_k + \sum_{k=1}^{n} b_k.X_k^2 + \sum_{0<i<j\leq n} c_{ij}.X_i.X_j$$

  - Coefficient de détermination R^2.
  - Valeur du coefficient a_0 est maximal lorsque toute les fibres sont en phase.
- Influence du critère de qualification de la mise en phase :
  - Les interactions dépendent du critère retenu :
    - Pour le rapport de Strehl, les coefficients b_i sont équivalents et les autres négligeables.
    - Mise en évidence des paramètres et des interactions les plus critiques avec les autres critères.

Analyse de sensibilité de la combinaison cohérente de sources laser fibrées

- Hiérarchie des interactions de la fibre F avec les autres (MEP) :
  - Rouge : interactions les plus fortes.
  - Vert : interactions 2 à 3 fois inférieures à rouge.
  - Jaune : interactions 6 à 10 fois inférieures à rouge.
  - Blanc : 50 à 60 fois inférieures à rouge.

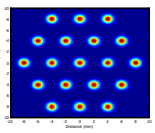

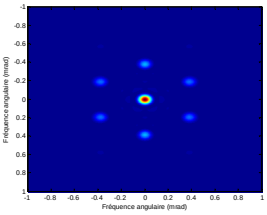

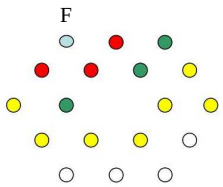

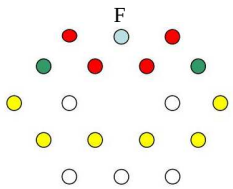

- Hiérarchie dépendante de la sculpture du front d'onde.

Conclusion

- La combinaison d'un grand nombre de sources laser fibrées (>100) met en évidence :
  - la prépondérence des termes b_i dans le cas de la tâche d'Airy, .
  - la prépondérence des termes b_i ainsi que certains $c_{i,j}$ dans le cas d'un anneau.
  - la nécessité de disposer de plusieurs critères
  - la nécessité de développer des outils d'analyse de sensibilité utilisant des entrées et sorties fonctionnelles en grandes dimensions.
  - la possibilité d'étudier les meilleurs compomis entre nombres de fibres, puissance de chacune des fibres, agencement des fibres en relation avec la sculpture du front d'onde et l'application souhaitée.
- La hiérarchisation des plans SFD par l'ALM est corroborée par les résultats obtenus dans le domaine de l'optique interférentielle.

Perspectives

- Analyse de sensibilité de sources laser combinant d'autres structures guidantes :
  - Fibres multimodes, structures guidantes (carré, rectangulaire, microstructurée…) ou modification de la géométrie de l'extrémité des fibres → A étudier. Assemblage de structures variées.
- Conception robuste de systèmes associant de manière incohérente plusieurs sous-ensembles d'amplificateurs laser fibrés combinés de manière cohérente → Enrichier la panoplie des sources laser à large bande spectrale.
- Simulation dynamique de systèmes composés d'éléments en forte interaction et disposant de boucles de contre-réaction en présence de paramètres non contrôlés → Un nouveau challenge.
- Poursuite des études de l'influence des incertitudes de variables corrélées dans les systèmes dynamiques.

Gary M. Smith, Joseph P. Donnelly, Leo J. Missaggia, Michael K. Connors, Shawn M. Redmond, Kevin J. Creedon, David C. Mathewson, Reuel B. Swint, Antonio Sanchez-Rubio and George W. Turner," Slab-coupled optical waveguide lasers and amplifiers", Proc. SPIE 8241, High-Power Diode Laser Technology and Applications X, 82410S, 2012.

Plan

- Introduction
- Prolégomènes
- Qualité des plans d'expériences numériques Space Filling Design
- Analyse de sensibilité de systèmes optiques interférentiels
- Caractérisation du speckle et de la variabilité spatiale de phénomènes optiques
- Perspectives

Caractérisation du speckle

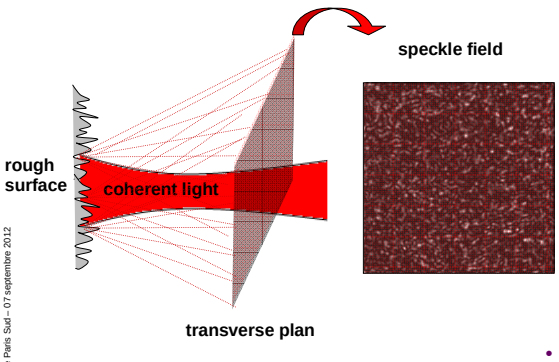

- La loi de distribution de l'intensité est bien connue :

$$p(I) = \frac{1}{I_m}\exp(-\frac{I}{I_m})$$

avec I_m l'intensité moyenne et I > 0

Mais cette loi ne permet pas de qualifier la distribution **spatiale** de l'intensité.

- La contruction de l'ALM sur les maxima et minima permet de caractériser la distribution spatiale de ces extrema (répartition ordonnée, aléatoire, en amas…)

Nombre de cellules illuminées : nc = $\frac{\omega_0^2}{L_{corr}^2}$

ω_0 est le waist de l'amplitude gaussienne du faisceau laser illuminateur

L_{corr} est la longueur de corrélation de la distribution gaussienne de hauteur de la surface éclairée

J. W. Goodman, "Some fundamental properties of speckle", J. Opt. Soc. Am. 66, 1145-1150, 1976.
J. W. Goodman, Speckle phenomena in optics : theory and applications, Roberts and Company Publishers, 2006.

Caractérisation du speckle

- Différentes répartitions spatiales d'intensité ayant la même distribution de densité de probabilité :

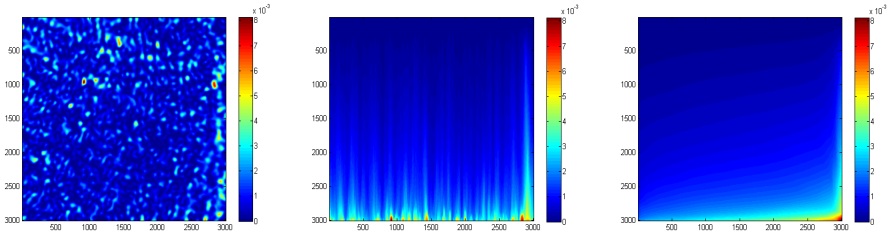

→ Nécessité de caractériser la répartition spatiale des niveaux d'intensité.

ALM et analyse de la transition gaussienne : Maxima d'intensité et singularités

- Exemples d'ALM construits sur les maxima et minima d'intensité pour différents nombre de cellules illuminées par un faisceau gaussien – Seuils : $I_M = \langle I \rangle / 2$, $I_S = \langle I \rangle$.

$n_c=2$

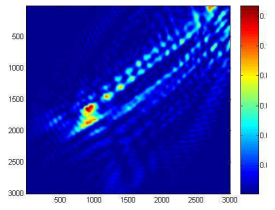

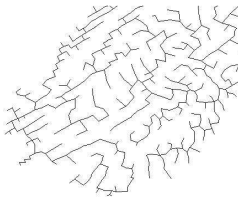

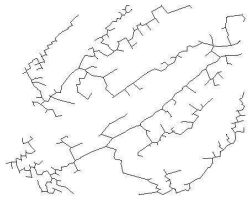

$n_c=3$

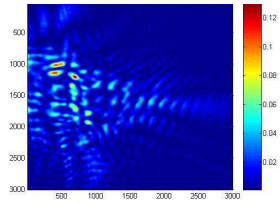

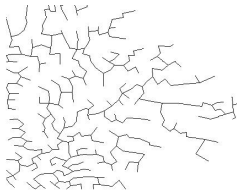

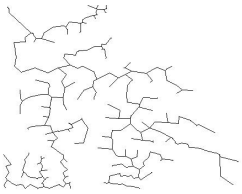

O. Vasseur, I. Bergoënd, D. Upadhyay, X. Orlik, "The Minimum Spanning Tree method applied to the study of optical speckle fields: spatial characterization of a Gaussian transition and its phase singularities", Proc. of SPIE 8171, 81710B-1, 2011.

ALM et analyse de la transition gaussienne : Maxima d'intensité et singularités

- Exemples d'ALM construits sur les maxima et minima d'intensité pour différents nombre de cellules illuminées par un faisceau gaussien – Seuils : I_M = <I>/2, I_S = <I>.

n_c=3

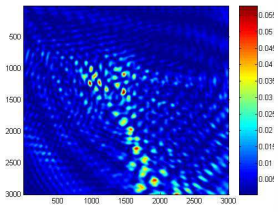

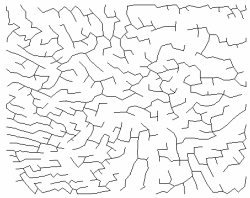

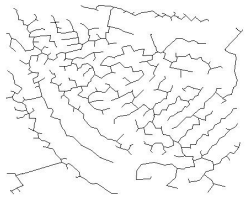

n_c=7

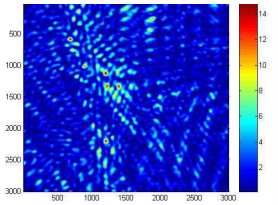

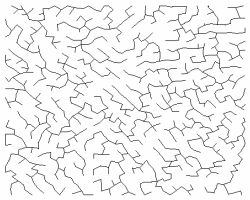

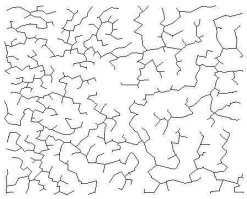

ALM et analyse de la transition gaussienne : Maxima d'intensité et singularités

- Exemples d'ALM construits sur les maxima et minima d'intensité pour différents nombre de cellules illuminées par un faisceau gaussien – Seuils : I_M = <I>/2, I_S = <I>.

n_c=20

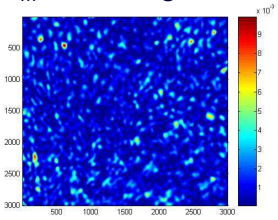

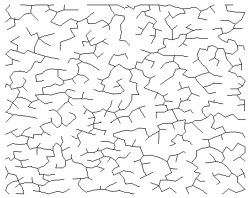

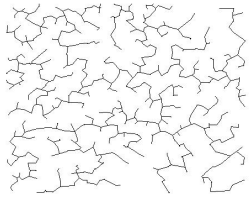

n_c=50

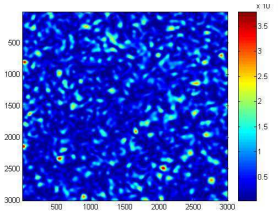

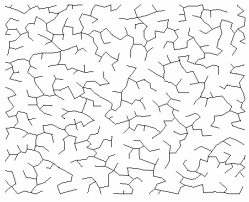

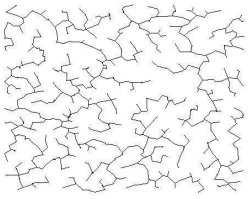

Analyse de la transition gaussienne par l'ALM : Maxima

- Representation dans le plan (m, σ) des différents arbres construits sur les maxima d'intensité – Influence de la résolution des images :

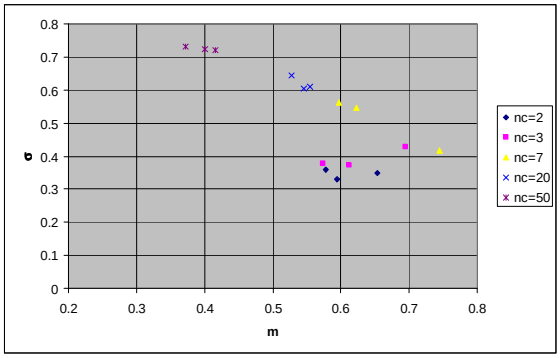

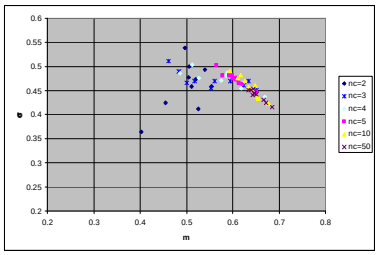

→ Résultats obtenus ont mis en évidence l'intérêt du critère ALM.

O. Vasseur, I. Bergoënd, D. Upadhyay, X. Orlik, "The Minimum Spanning Tree method applied to the study of optical speckle fields: spatial characterization of a Gaussian transition and its phase singularities", Proc. of SPIE 8171, 81710B-1, 2011.
O.Vasseur, I. Bergoënd, X. Orlik, "A Gaussian transition of an optical speckle field studied by the minimal spanning tree method", J. Europ. Opt. Soc. Rap. Public. 10052 Vol. 5, 2010.

Caractérisation de la variabilité spatiale de phénomènes optiques : Maxima

- Autres explorations et applications :

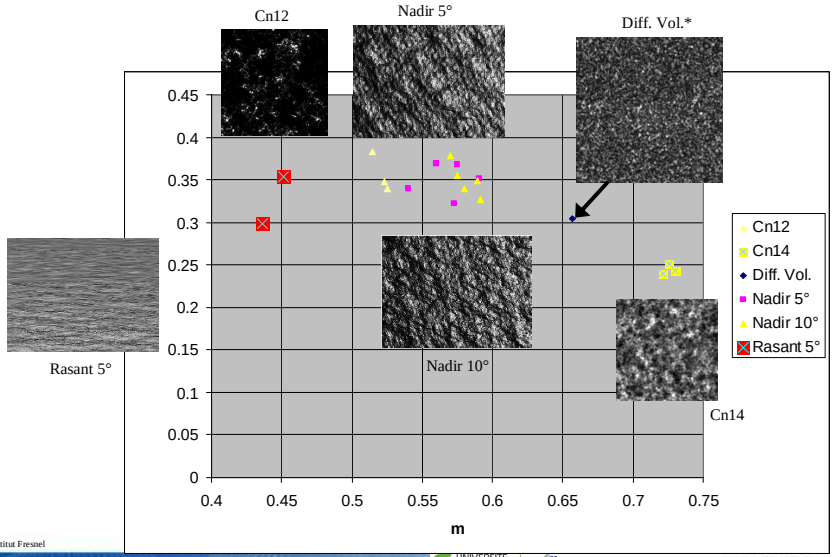

*Image de speckle fournie par l'Institut Fresnel

Conclusion

- L'ALM permet de qualifier la répartition spatiale des intensités et de mettre en évidence la transition gaussienne.
  - Les distributions spatiales des maxima et minima d'intensité sont différentes.
- Les valeurs numériques obtenues avec le critère ALM dépendent de la résolution des images.
- Qualification de la variabilité spatiale d'autres phénomènes optiques est initiée : speckle généré par une surface, par un volume d'un matériau, par la turbulence atmosphérique.

→ **Un nouvel outil pour l'étude spatiale des phénomènes optiques.**

Perspectives

- Etude de la répartition d'intensité du speckle → Informations utiles pour améliorer la qualité de la combinaison cohérente de sources laser.
- Autre application : Qualification de la répartition spatiale des "impacts" de faisceaux laser après propagation en atmosphère turbulente.
- Utilisation dans le domaine de l'imagerie pour caractériser des surfaces rugueuses, la surface de la mer, des surfaces biologiques :
  - Identification des typologies d'organisations représentatives d'une variabilité statistique par l'analyse de la répartition spatiale de niveaux spécifiques dans une image.

Plan

- Introduction
- Prolégomènes
- Qualité des plans d'expériences numériques Space Filling Design
- Analyse de sensibilité de systèmes optiques interférentiels
- Caractérisation du speckle et de la variabilité spatiale de phénomènes optiques
- Perspectives

Conclusion

- Théorie des graphes :
  - ALM → Critère d'appréciation de la qualité des plans d'expériences et de la variabilité et distribution spatiale de phénomènes optiques.
- Plans d'expériences / Chimiométrie :
  - Exploration efficace d'espaces de grandes dimensions pour l'analyse de sensibilité de systèmes optiques interférentiels aux paramètres d'entrée du système (modélisé). Intérêt du critère ALM : plan (m, σ).
- Systèmes optiques interférentiels :
  - Cas d'applications (voire cas d'école) présentant de fortes interactions pour qualifier les plans SFD en grandes dimensions. Pertinence du critère ALM.

→ Acquis et socle pour l'analyse de l'influence des incertitudes dans les systèmes complexes.

Perspectives pour l'optique interférentielle

- Assemblage des différents acquis pour l'étude et la conception robuste de systèmes laser reposant sur la combinaison de sources laser à "guide" :
  - Mode gaussien → Calcul du champ émis par la structure guidante
    - Dans le cas de fibres à saut d'indice → **Evaluation de l'incertitude de modèles**
  - Structure guidante avec traitements optiques en extrémité.
- Sculpture de faisceau et influence de paramètres non contrôlables lors de la propagation → De la robustesse à la résilience du système.
- Qualification du speckle (turbulence atmosphérique et cible) → nouveaux critères pour améliorer l'efficacité du système laser :
  - Inversion : Eclairement de la cible → définition des meilleures corrections de phase à apporter à chaque élément source.
  - Correction dynamique des paramètres de la source en fonction des critères représentatifs de l'application.

→ Analyse multicritère (méthode de surclassement)

B. Roy, Méthodologie multicritère d'aide à la décision, Economica, Paris, 1985.

Perspectives pour l'étude des systèmes complexes

- Prise en compte de sorties vectorielles, matricielles et fonctionnelles.
- Etudes de variables corrélées.
- Construction de plans SFD de qualité en grandes dimensions.

- Acquis des études de l'influence des incertitudes dans les systèmes interférentiels → Contribution à l'exploration et la compréhension d'autres types de systèmes complexes.

- Cartographies des interactions entre les fibres (différents seuillages sur les coefficients d'interaction) → similarités avec réseaux sociaux et des systèmes multi-agents (paramètres géographiques):
  → L'étude dynamique de ces systèmes interférentiels bidimensionnels pourrait alors contribuer, à terme, à l'étude de la dynamique de systèmes biologiques ou sociétaux.

Perspectives scientifiques générales

- Connaissance précise de l'objet → Utilisation de plusieurs critères.
- Choix des critères + Décision → Systèmes complexes → Dépassement des oppositions entre épistémologie et sociologie des sciences :
  - Résultats acquis, subjectivité des acteurs, normativité, modes, consensus…
  - Fond/Forme

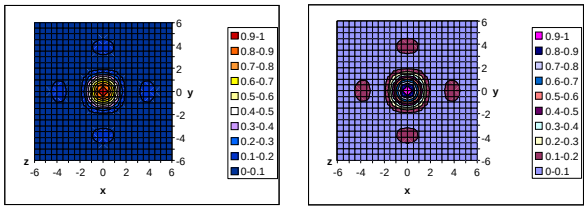

→ Synergies entre sciences physiques et sciences humaines :
  - Rétroaction et systèmes complexes → systémisme et sciences humaines.
  - Développement scientifique et société → Horizon 2020.

B. Latour, La science en action, Gallimard, Paris, 1995.
A. Chalmers, Qu'est ce que la science ? Le Livre de Poche, Paris, 1997.
M. Pastoureau, Bleu, Seuil, Paris, 2002.
O. Vasseur L'image dans la technoscience :De son utilisation et de son influence dans les sciences appliquées, Ph. D. Thesis, Toulouse II, Juin 2003
B. Badie, M-C Smouts, Le retournement du monde – Sociologie de la scène internationale, Dalloz, Paris, 1995.

Merci pour votre attention